Modeling and therapeutic development for the tuberous sclerosis related neoplasm lymphangioleiomyomatosis

Sean Phillip Delaney

A thesis submitted to the Faculty of Graduate and Postdoctoral Studies in partial fulfillment of the requirements for the Doctorate of Philosophy degree in Cellular and Molecular Medicine

Department of Cellular and Molecular Medicine
Faculty of Medicine
University of Ottawa

Abstract

The multisystemic tumors characteristic of the monogenic neoplastic diseases, tuberous sclerosis complex (TSC) and lymphangioleiomyomatosis (LAM), share common signaling aberrations upon the loss of heterozygosity in either the *TSC1* or *TSC2* genes. However, their physical manifestations are vastly different and can generally be classified as being either neurological (TSC) or mesenchymal (TSC & LAM; referred to herein as LAM for simplicity) in origin. In this study, I present a comprehensive stem cell model of LAM utilizing multiple TSC2 knockout (*TSC2*$^{-/-}$) pluripotent stem cell lines differentiated to the putative cell of origin for mesenchymal tumors, neural crest cells (NCCs). *TSC2*$^{-/-}$ NCCs faithfully recapitulate LAM phenotypes and temporal RNA-seq analysis of neural and neural crest differentiation was performed to model disease pathogenesis. Analysis revealed immediate activation of stress response signaling resulting in protein aggregation and lysosome and autophagosome accumulation upon neuralization in *TSC2*$^{-/-}$ cells. This resulted in acute and lasting effects specific to neural progenitor cells (NPCs), that are transient and ameliorated in NCCs. These lineage-specific effects resulted in selective sensitization of NPCs to cell death via proteasome inhibition, suggesting a potential therapeutic avenue for neurological TSC, but not LAM. Thus, a genome-wide CRISPR knockout screen was performed in *TSC2*$^{-/-}$ NCCs. Analysis of synthetic lethal genes reveals pathways previously targeted for LAM, but provides gene-level resolution to the vulnerable nodes within these pathways. Importantly, 18 novel gene targets were identified that display synthetic lethality to *TSC2*$^{-/-}$ cells with high specificity. 3 genes within this list were targetable using commercially available small molecule inhibitors, one of which, FGFR1, shows highly selective lethal targeting of *TSC2*$^{-/-}$ NCCs. Importantly, this model system, paired with the expansive resource of transcriptomic and synthetic lethal data, serves as a foundation for the development of next generation treatment strategies for LAM, and potentially the entire spectrum of TSC manifestations.

Authorization

Adaptations, Figures, Tables:

Acknowledgements

The first and foremost person that I owe much gratitude is Catherine Lawrence. Catherine, leading with laughs in the face of what would otherwise be serious circumstances, your efforts and attitude are simply inspiring. It's contagious too! Research is not easy, and when it is tough, a good hearty laugh will bring you back around; though I do not think anyone can laugh quite as whole-heartedly as you. It has always been a pleasure sharing our work with you and having a good laugh together at Laugh Out LAM. All the work I performed during my studies, in the end, was always for you.

I would also like to thank the Judith R. Raymond Scholarship fund for the substantial support that I have received during my studies. The financial support greatly alleviated much worry and stress that would have otherwise occupied my mind, allowing me to focus on my studies to help advance my research and, in turn, their mission. I also thank the University of Ottawa for the generous bursaries awarded during my studies.

I wish to acknowledge and thank my thesis advisory committee, Dr. Jeff Dilworth, Dr. Bernard Thébaud, and Dr. Steffany Bennett, for their guidance throughout my studies. Your valuable comments, critiques, and suggestions honed the mission of my research project and helped keep me on course within an expansive project.

Very importantly, I would like to thank the members of the Stanford Lab, both past and present. Not quite knowing exactly what I was getting into, I was fortunate to have landed in such a supportive, collaborative, and productive work environment. Working with such colleagues made any hardships endurable, victories that more enjoyable, and it is a pleasure to walk in through the door every day. I would like to especially thank Dr. Lisa Julian for her valuable advice and perspective while working on this project, especially as I was rounding the final bend of my studies. I would also like to

express my deep gratitude to Carole Doré and Angela Raymond for making sure the lab world was always spinning, and Dr. Julien Yockell-Lelièvre for his technical expertise. The amount of help I have received from them, and other members of the lab, both in and outside of work surpasses anything that I could possibly have expected, and I will always be indebted to them.

One person who will undoubtedly have lasting influence in my life is my advisor, Dr. William L. Stanford. Bill, I thank you for bringing me into your lab and providing me with a research project in which I could work with independence to develop my skills as a scientist. Your enthusiasm for pursuing the unknown and pushing the limits of our capabilities has challenged me throughout my PhD project, and I believe has made me a better researcher. You have always pushed for excellence and believed in my capabilities, and I have enjoyed trying my best to deliver. I thank you for your mentorship. Whenever I asked for help or advice, you would, without fail, take the time to properly consider and offer whatever council you could. Throughout all of the challenges I, along with my family, have faced over the years, your patience, understanding, and generosity have been most greatly appreciated. We thank you.

I would also like to thank my father, for always instilling the value of education and his constant support throughout the many long years of university. I wouldn't be in this mess if it wasn't for you, and I'm grateful for it.

Finally, I would like to quite especially thank my wife, Trischa. I thank you for pushing me out of the plane (figuratively), over and over again in life. Your efforts to pull me back into the reality that is the world outside of work have always been appreciated. You give me perspective and remind me of what counts. You are always supportive, always my advocate, and always a comfort when it all seems to spiral. I thank you for your patience throughout these years. I dedicate this to you, and those two wonderful (not so) little knuckleheads of ours.

Table of Contents

List of Tables

List of Figures

List of Abbreviations

aa	amino acids
AML	angiomyolipomas
CaM	calmodulin
CDK2	cyclin-dependent kinase 2
CNS	central nervous system
CRISPR	clustered regularly interspaced short palindromic repeats
crRNA	CRISPR RNA
CtIP	CtBP-interacting protein
dCas9-KRAB	catalytically inactive Cas9-Krüppel-associated box repression conjugate
DEG	differentially expressed gene
DNA-PKcs	DNA-PK catalytic subunit
DSB	double strand break
dSMADi	dual inhibition of SMAD signaling
EB	embryoid body
EB-NCC	embryoid body neural crest differentiation
EMT	epithelial-to-mesenchymal transition
ER	endoplasmic reticulum
ERα	estrogen receptor alpha
FACS	fluorescent activated cell sorting
FC	flow cytometry
FDR	false discovery rate
GAP	GTPase activating protein
gDNA	genomic DNA
GE	genome editing
GEO	Gene Expression Omnibus
hESC	human embryonic stem cell
HIF1α	hypoxia-inducible factor 1-alpha
hPSC	human pluripotent stem cell

HR	homologous recombination
i-proteasome	immunoproteasome
IF	immunofluoresence
IFC	imaging flow cytometry
IHC	immunohistochemistry
iPSC	induced pluripotent stem cell
KSR	Knockout serum replacement media
Ku	Ku70-Ku80 heterodimer
LAM	lymphangioleiomyomatosis
LDN	LDN193189
LOF	loss of function
Log2FC	log2 fold change
miRNA	micro RNA
MMP	matrix metalloproteinase
MMP	matrix metalloproteinases
MOI	multiplicity of infection
MRN	Mre11-Rad50-Nbs1
mRNA	messenger RNA
mTOR	mammalian target of rapamycin
NCC	neural crest cell
ncRNA	non-coding RNA
NCSC	neural crest stem cell
NES	normalized enrichment score
NHEJ	non-homologous end joining
NPC	neural progenitor cell
NIM	neural induction media
NSC	neural stem cell
PAM	protospacer-adjacent motif (PAM)
PARP	poly(ADP ribose) polymerase

PC	principal component
PCA	principal component analysis
PCR	polymerase chain reaction
PEComa	perivascular epitheloid cell tumors
PFA	paraformaldehyde
PR	progesterone receptor
Rab5	Rabaptin 5
Rheb	Ras homolog enriched in brain
RISC	RNA-induced silencing complex
RNAi	RNA interference
ROS	reactive oxygen species
RPA	Replication protein A
RT-qPCR	reverse transcription quantitative PCR
RTK	receptor tyrosine kinase
S-LAM	sporadic LAM
SB	SB431542
SEGA	subependymal giant cell astrocytomas
siRNA	small interfereing RNA
SMA	smooth muscle actin
SMC	smooth muscle cell
SSB	single strand break
ssDNA	single stranded DNA
ssODN	single stranded oligonucleotide
TBC1D7	Tre2-Bub2-Cdc16 1 domain family member 7
TFEB	transcription factor EB
TGF-ß	transforming growth factor beta
TSC	tuberous sclerosis complex
TSC-LAM	TSC associated LAM
TSC1	Hamartin

TSC2	Tuberin
TSC2-/-	TSC2 knockout
TSC2Δ	TSC2 delta exon 11 modification
tSMC	teratoma-derived smooth muscle cell
UV	ultraviolet
VEGF	vascular endothelial growth factor
WB	western blot
WT	wild type

Preface

The research 'story' presented in this thesis could not have been told without the help of many contributions, both intellectually and technically. This thesis contains much work that was the product of a well-orchestrated effort by the TSC & LAM group within the Stanford Lab. The technical support of Carole Doré and Angela Raymond was key to efficiently perform experiments for this project. Application-specific experimental support from Adam Pietrobon and Julien Yockell-Leliévre, PhD, was also essential in advancing our goals. This most notable of these contributions were those of Lisa M. Julian, PhD. As co-first author on nearly all published works of my PhD thesis, we worked very closely together to advance the TSC & LAM research program in the Stanford Lab. This includes the intellectual development of the neural crest cell of origin theory presented in this thesis, which is also a published work (Appendix V). Furthermore, within the TSC & LAM research initiative, our efforts were two-pronged; Dr. Julian's efforts were focused within neurological TSC, whereas my efforts were directed towards modeling mesenchymal TSC and LAM utilizing neural crest cells. Thus, within this thesis and in our most recent manuscript (Appendix II), the work and data derived from neural progenitor cells is the product of Dr. Julian's hard work. Furthermore, raw RNA sequencing and synthetic lethal datasets described in chapters 4 & 5, respectively, were prepared for analysis by Chris Porter at the Ottawa Bioinformatics Facility. Additionally, our collaborator at Carlton University, Hongyu Sun, PhD, performed electrophysiology experiments detailed in Chapter 3, section 3.3.1. Specific contributions are listed in detail at each chapter title page. Thus, unless otherwise stated, all other work described here was performed by the author of this thesis.

CHAPTER 1:

General Introduction

Portions of sections 1.1-1.3 have been adapted from:

Delaney, S.P., Julian, L.M., and Stanford, W.L. (2014). “The neural crest lineage as a driver of disease heterogeneity in Tuberous Sclerosis Complex and Lymphangioleiomyomatosis”. Frontiers in cell and developmental biology *2*, 69.

Original Manuscript:
Conceptualization, **S.P.D.**, L.M.J., and W.L.S.
Visualization, **S.P.D.**
Writing – Original Draft, **S.P.D.** and L.M.J.
Writing – Review & Editing, **S.P.D.**, L.M.J., and W.L.S.

1.1: Tuberous sclerosis complex and lymphangioleiomyomatosis

Tuberous sclerosis complex (TSC) is a rare, multisystem disorder that is the consequence of inherited or spontaneously acquired mutations in either of the *TSC1* or *TSC2* genes. Following only neurofibromatosis type 1, TSC is the most common neurocutaneous disease, occurring in approximately 1 in 6000 births (Kandt 2003, Curatolo, Bombardieri et al. 2008), however, the clinical features of TSC are diverse (Figure 1.1). TSC is typically characterized by the appearance of low-grade tumors and malformations in the brain, heart, lungs, kidneys, eyes, skin, and bone. Cortical tubers are the most prevalent neurological symptom of TSC and account for the majority of the debilitative neurological symptoms, including epilepsy, mental retardation and autism (Goh et al., 2005; Crino et al., 2006; Crino and Tsai, 2012; Webb et al., 1996; Wong, 2006). Interestingly, cortical tubers, along with cardiac rhabdomyomas, are formed during early development and can be detected prenatally (Park, Pepkowitz et al. 1997, Moss, Avila et al. 2001, Henske and McCormack 2012). This suggests that the consequences of *TSC1* or *TSC2* loss during embryogenesis can be realized immediately and affect various developing tissues early on. Other tumors and lesions form during childhood and into adulthood, such as retinal astrocytomas, subependymal giant cell astrocytomas (SEGAs), angiofibromas and hypomelanotic macules in the skin, sub-ependymal nodules/giant-cell tumors, and renal angiomyolipomas (rAMLs). The variability of disease penetrance in TSC patients is also likely affected by the high rate of mosiacism observed in TSC patient populations (Verhoef, Bakker et al. 1999). Thus, both the age of onset and penetrance of disease is diverse, suggesting a highly tissue-specific and complex developmental pathogenesis.

Perhaps the most significant feature of TSC associated with high morbidity and mortality, is pulmonary Lymphangioleiomyomatosis (LAM). LAM is a progressive neoplasm of the lung that occurs in roughly 30% of women with TSC (TSC-LAM), with

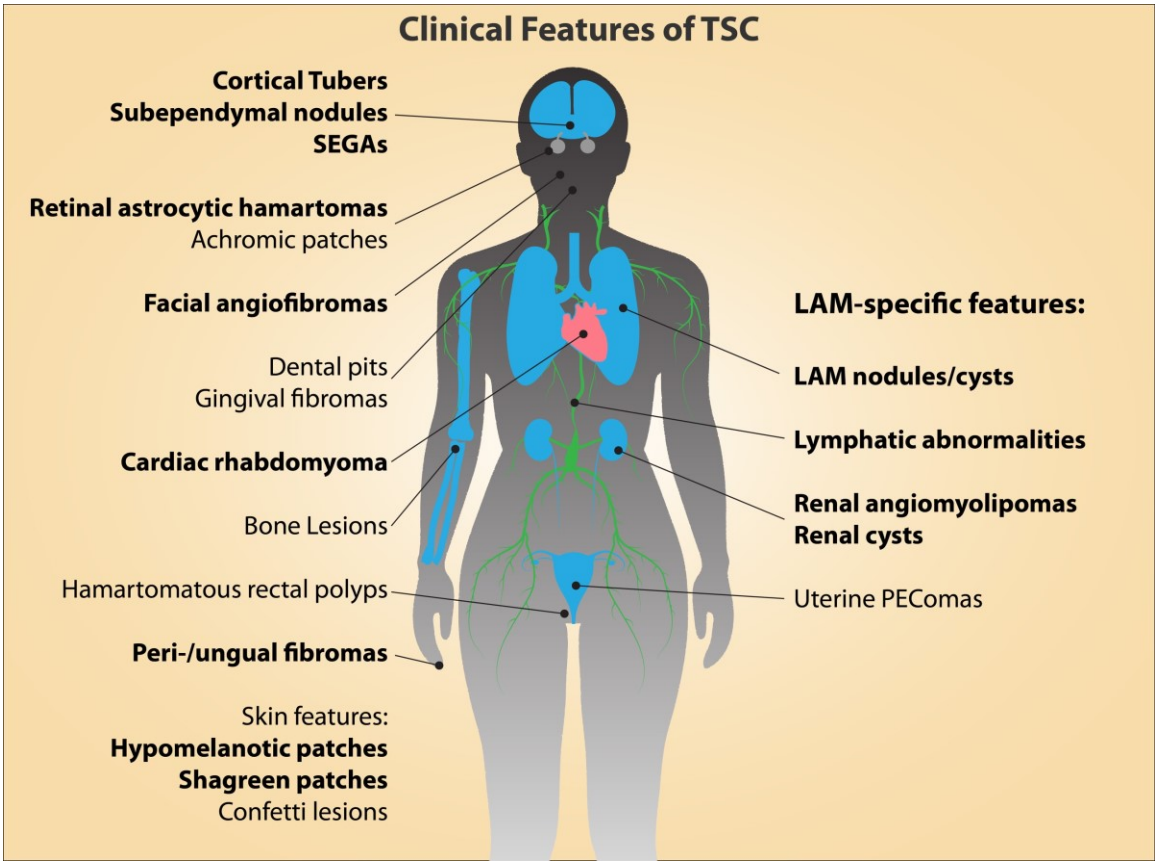

Figure 1.1: The multisystem features of TSC and LAM.
The clinical manifestation of TSC and LAM are diverse and affect multiple organs, organ systems, and tissues. The primary diagnostic features of TSC are indicated in boldface type (Northrup, Krueger et al. 2013). Cortical tubers and cardiac rhabdomyomas occur during fetal development. Facial angiofibromas, hypomelanic macules, and retinal astrocytic hamartomas can be detected in infancy, while other features, such as LAM-specific manifestations, continue to present themselves throughout development into adulthood. Reprint from Delaney et al. 2014. Front Cell Dev Biol. 2:69 (Delaney, Julian et al. 2019).

an average age of diagnosis of about 35 years (Henske and McCormack, 2012). It should be noted that TSC-LAM is often thought to be higher in prevalence within the general population and affects female TSC patients earlier on in life. It is suspected that LAM is often misdiagnosed as other pulmonary complications, such as asthma or emphysema, until more serious symptoms emerge, such as pleural effusion or collapsed lung. LAM is characterized by the presence of multiple neoplastic tumor nodules within the lung interstitium. These LAM nodules are composed of a mix of proliferating smooth muscle-like cells and exceptionally large epithelial cells that express melanocyte markers. LAM primarily affects post-pubescent females and pregnancy often results in the acceleration of disease progression. Thus, hormone signaling is thought to play an important role in disease onset and advancement. Indeed, LAM lung nodules and associated rAMLs express estrogen receptor alpha and progesterone receptor (ERα and PR, respectively), however, the role of hormone signaling in TSC and LAM is not yet clearly understood. The proliferative LAM nodules grow to form cystic lesions, which lead to the destruction of the lung parenchyma, culminating in progressive shortness of breath, chylous pleural effusions, pneumothorax, and eventual respiratory failure (Chu et al., 1999; Kitaichi et al., 1995; Urban et al., 1999). One of the only effective treatments for late stage LAM is lung transplantation; however, LAM cells have been shown to once again populate healthy donor lungs following successful transplantation (Mosser, Herdrich et al. 1976, Karbowniczek, Astrinidis et al. 2003).

LAM also occurs sporadically (S-LAM), where lung nodules present, commonly with TSC-LAM renal and lymphatic manifestations; however, other TSC-associated features (e.g. cortical tubers, SEGAs, skin hamartomas, etc.) are absent in S-LAM (Costello et al., 2000; Moss et al., 2001). In addition to the most characteristic pulmonary manifestations, other common features of LAM include lymphatic abnormalities, such as lymphadenopathy (Chu et al., 1999; Urban et al., 1999), renal rAMLs, and uterine

perivascular epitheloid cell tumors (PEComas). rAMLs are considered benign growths and are composed of adipocytes and, reflecting the composition of the pulmonary LAM nodules, smooth muscle cell-like cells. Fortunately, rAMLs are asymptomatic in most cases, but can affect quality of life depending on their size and position in the kidney (Bissler and Kingswood, 2004). Interestingly, uterine PEComas are also characterized by epithelial-like cells that express both smooth muscle and melanocytic markers, reminiscent of the cell composition of LAM lung nodules (Martignoni et al., 2007; Henske and McCormack, 2012; Hayashi et al., 2011).

Taking both TSC and LAM together, these multisystem diseases are associated with the development of a broad spectrum of pathological lesions, affecting a diverse range of cell lineages and tissues, but retain specificity in their presentation while maintaining variable penetrance. Thus, TSC and LAM, although both monogenic diseases, clearly have highly complex mechanisms of pathogenesis, likely involving developmental and temporal factors, hormone signaling, and perhaps yet unknown stimulus initiating tumor formation.

1.1.1 The TSC Genes

DNA sequencing of patient samples, combined with the finding of multiple animal and cell models of TSC have confirmed that the loss of heterozygosity or second-hit mutations of wild-type (*WT*) *TSC1* or *TSC2* allele drive the formation of TSC lesions (Henske, Scheithauer et al. 1996, Carsillo, Astrinidis et al. 2000, Crino, Aronica et al. 2010, Qin, Chan et al. 2010, Tyburczy, Wang et al. 2014, Blair, Hockemeyer et al. 2018). The tuberous sclerosis complex genes themselves, *TSC1* and *TSC2*, were discovered in the mid-1990s through their association with TSC manifestations(European Chromosome 16 Tuberous Sclerosis 1993, van Slegtenhorst, de Hoogt et al. 1997). Further investigation revealed the protein products of *TSC1* and *TSC2*, hamartin (TSC1)

and tuberin (TSC2), respectively, form an inhibitory complex (TSC1/2) acting on the mammalian target of rapamycin (mTOR) signaling pathway (Plank, Yeung et al. 1998, Garami, Zwartkruis et al. 2003, Inoki, Li et al. 2003). Thus, loss of functional TSC1/2 is thought to drive TSC and LAM tumor formation, as this would lead to hyperactive mTOR signaling leading to uncontrolled growth and proliferation of affected cells. Interestingly, although mutations in both *TSC1* and *TSC2* lead to TSC and LAM, they do not share equivalent representation in patient populations; roughly 70-90% of families identified to carry TSC gene mutations harbor mutations in *TSC2* (Rosset, Netto et al. 2017). Furthermore, genotype-phenotype studies have revealed TSC and LAM patients with mutations in *TSC2* present with more severe phenotypes (Dabora, Jozwiak et al. 2001, Muzykewicz, Sharma et al. 2009). This suggests both *TSC1* and *TSC2* have distinct roles in disease pathogenesis that are independent of their role regulating mTOR signaling as the TSC1/2 complex.

TSC1 was identified in 1997, where its locus was determined to be on chromosome 9 (9q34), encoded by 23 exons resulting in a 130kDa protein (van Slegtenhorst, de Hoogt et al. 1997). TSC1 contains two conserved protein domains, a transmembrane domain (amino acids (aa) 127-144) and a coiled-coil domain (aa 719-998) and has been found to interact and/or bind with 17 unique proteins alone or in complex with TSC2. The most notable function of TSC1 outside of the TSC1/2 complex is its role in actin cytoskeleton organization; through interactions with Rho family GTPases, TSC1 affects cell adhesion, polarity, and migration (Lamb, Roy et al. 2000, Ohsawa, Kobayashi et al. 2013). Further characterization of TSC1 has identified multiple phosphorylation sites (targeted by CDK1, IKKß , and GSK3) that have been shown to regulate its protein-protein interaction with TSC2, both positively and negatively regulating TSC1/2 formation (Astrinidis, Senapedis et al. 2003, Mak, Kenerson et al. 2005, Inoki, Ouyang et al. 2006, Lee, Kuo et al. 2007).

In turn, the *TSC2* gene, was discovered in 1993, and is composed of 41 exons located on chromosome 16p13.3 (European Chromosome 16 Tuberous Sclerosis 1993). *TSC2* encodes 198kDa protein of 1807 amino which contains a number of conserved protein domains including a leucine zipper (aa 75-107), two coiled-coil domains (aa 346-371; 1008-1021), two transcriptional activation domains (aa 1163-1259; 1690-1743), the well-characterized GTPase activating protein (GAP) domain (aa 1517-1674), and a calmodulin/estrogen receptor alpha (CaM/ERα) binding domain (aa 1740-1757) (Tsuchiya, Orimoto et al. 1996, Noonan, Lou et al. 2002, Rosner, Hanneder et al. 2008). Clearly, with such complexity, TSC2 has the potential for a wide array of interactions. Indeed, TSC2 interacts with over 30 proteins/complexes either alone or in complex with TSC1, indicating a complex role for TSC2 in a number of cellular functions (Rosner, Hanneder et al. 2008). Many of these specific interactions are not well characterized, however the intricacy of TSC2's interactions is evident in its variable cellular localization; TSC2 has been found to be localized within the cytosol, the Golgi apparatus, lysosome and vesicle membranes, apical membrane, and the nucleus (Wienecke, Konig et al. 1995, Henry, Yuan et al. 1998, Plank, Yeung et al. 1998, Murthy, Haddad et al. 2000, Lou, Griffith et al. 2001, Wei, Li et al. 2002, Yamamoto, Jones et al. 2002).

The nuclear localization of TSC2, along with the presence of two transcriptional activation domains points to potential transcriptional regulation; however, the extent of its nuclear function has not been clearly elucidated. There are several examples of indirect regulation of gene expression through interaction with a number of proteins. For instance, co-localized in the nucleus with TSC2, SMAD2/3 was shown to interact with the N-terminal region of TSC2 and regulate gene transcription in response to TGFβ1 signaling (Birchenall-Roberts, Fu et al. 2004). Additionally, TSC2 binds directly to ERα through its CaM/ERα binding domain, and subsequently affects ERα-associated signaling (York, Lou et al. 2005, York, Lou et al. 2006). Translocation of TSC2 to the

nucleus is dependent on S6K phosphorylation of the C-terminus of TSC2, which in turn suppresses ERα-mediated translational activity (York, Lou et al. 2006). Studies investigating gene regulatory functions as a direct result of TSC2-DNA binding are lacking. However, one study has shown TSC2 to bind DNA and act as a transcription factor for epiregulin in a human oral squamous cell carcinoma cell line (Pradhan, Rather et al. 2014).

The GAP activity of TSC2 is most often linked to its canonical target, Rheb (Ras homolog enriched in brain), which interacts and activates mTOR under conditions supportive of growth (discussed in more detail in section 1.1.2). However, TSC2 exhibits specific GAP activity to additional proteins, Rabaptin 5 (Rab5) and Rap1 (Wienecke, Maize et al. 1996, Xiao, Shoarinejad et al. 1997). Rap1 has been associated with a number of cellular processes, including cell proliferation, cytoskeletal reorganization, cell motility, and the mediation of epithelial and endothelial cell-cell contact (Asha, de Ruiter et al. 1999, Guvakova, Lee et al. 2014). TSC2 has also been shown to have specific GAP activity towards Rab5 in modulating endocytosis (Xiao, Shoarinejad et al. 1997). Intriguingly, Rap1 has been found to interact directly with phosphatidylinositol 3-kinase (PI3K) catalytic subunit p110, which in turn promotes Rab5 activation and subsequent lysosomal formation, promoting autophagosome formation through the Rab5/Vps34/Beclin 1 complex (Ao, Zou et al. 2014).

An additional role of TSC2 outside of the TSC1/2 complex is the regulation of cell cycle, and subsequent effects on cell proliferation, through interactions with cyclin-dependent kinase 2 (CDK2) and its inhibitor $p27^{KIP1}$. Cyclin D and E bind CDK2 to promote G1 to S phase transition and promote DNA replication, respectively (Sherr and Roberts 1999, Krasinska, Besnard et al. 2008). TSC2 has been found to bind to both CDK2 as well as $p27^{KIP1}$, sequestering the latter from degradation (Rosner and Hengstschlager 2004). In addition, a novel C-terminal variant of TSC2 was identified that

increased proliferation in both LNCaP and HEK293 cells following androgen stimulation (Munkley, Rajan et al. 2014). This C-terminal TSC2 variant does not contain a TSC1 binding domain, nor a complete interaction domain for Rheb inactivation. It appears that this TSC2 isoform acts within the cytosol and independently of mTOR signaling. Mechanistic data regarding the function this isoform in proliferation signaling is lacking, but is nonetheless supportive of the notion that TSC2 plays important regulatory roles in cell cycle and proliferation outside of mTORC1 signaling, which may contribute disease pathogenicity of TSC and LAM.

The molecular etiology of how TSC gene mutations result in TSC and LAM was unclear until the early 2000's when it was first determined that TSC1 and TSC2 form the TSC1/2 complex and act to inhibit mTOR signaling, fulfilling roles as tumor suppressor genes (Plank, Yeung et al. 1998, Garami, Zwartkruis et al. 2003, Inoki, Li et al. 2003). However, the structure of the TSC1/2 complex remained elusive as immunoprecipitation and protein gel filtration experiments revealed several complexes far larger than expected (Nellist, van Slegtenhorst et al. 1999, Hoogeveen-Westerveld, van Unen et al. 2012). Thus, a possible third TSC gene was thought to contribute to the TSC1/2 complex. In 2012, a third member of the TSC1/2 complex was recently identified as Tre2-Bub2-Cdc16 1 domain family, member 7 (TBC1D7; for simplicity, the TSC1/2-TBC1D7 heterotrimeric complex will be referred to as TSC1/2). Although the TSC1/2 complex has been confirmed to consist of these three subunits, the subunit ratio within the heterotrimeric complex are not 1:1:1; the crystal structure of TSC1-TBC1D7 interaction has been determined, however, the composition of the TSC1/2 complex has yet to be confirmed (Qin, Wang et al. 2016). The absence of functional TBC1D7 results in similar molecular signaling phenotypes as a loss of TSC1 or TSC2; interestingly, mutations in TBC1D7 does not result in TSC disease pathogenesis, dispelling the existence of a TSC3 gene (Dibble, Elis et al. 2012, Capo-Chichi, Tcherkezian et al.

2013). This phenotype is most likely attributed to the destabilization of the TSC1/2 complex, but not complete loss of the mTOR regulating function of TSC1/2.

1.1.2 The mTOR pathway and the TSC1/2 complex

Perhaps the most complex, adaptive, and far-reaching signaling network that influences cell homeostasis is the mTOR pathway. The mTOR pathway has an impressive number of signaling inputs and affects a number of downstream signaling events controlling protein synthesis, energy metabolism, autophagy, lipid synthesis, and lysosome biogenesis among other functions (Figure 1.2; extensively reviewed in (Saxton and Sabatini 2017, Valvezan and Manning 2019)). The protein for which this pathway is known, mTOR, nucleates two distinct macromolecular protein complexes, mTOR complex 1 (mTORC1) and mTOR complex 2 (mTORC2). mTORC1-related signaling events have undergone far more investigation than those of its counterpart, mTORC2, as mTORC1 signaling more directly affects cell growth and proliferation signaling cascades; its link to cancer being a likely reason for its extensive characterization (Guertin and Sabatini 2007). Upstream 'sensors' governing mTORC1 activation include growth factor stimulation, nutrient levels, energy status, cellular stress, and oxygen levels, and the majority of these downstream signaling cascades converging at the TSC1/2 complex. The TSC1/2 complex acts to inhibit activation of mTORC1 signaling via the GAP property of TSC2 (Inoki, Li et al. 2003). The TSC1/2 complex acts directly to stimulate the GTP hydrolysis of Rheb, inhibiting its interaction and subsequent activation of mTORC1.

mTORC1 signaling can be seen broadly as a molecular switchboard regulating cellular metabolism, promoting anabolic pathways under conditions favorable leading to increased biomass and subsequent growth and proliferation of cells, or permitting activation of catabolic pathways in stress conditions, most notably lysosomal biogenesis

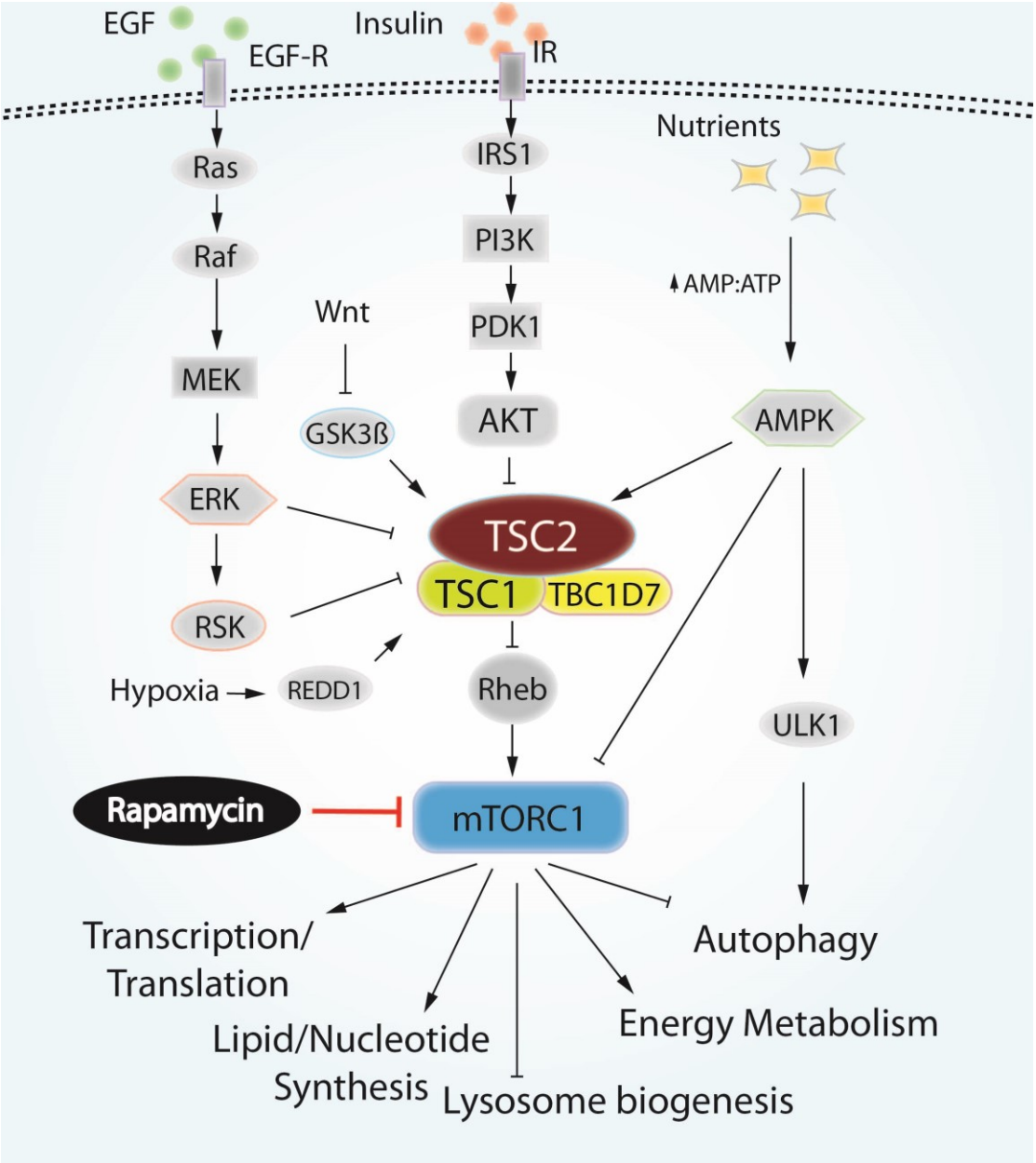

Figure 1.2: Overview of the TSC1/2-mTORC1 signaling pathway
Multiple signaling inputs, including growth factors, hypoxia, energy, and nutrient levels converge through the TSC1/2 complex, a central regulator of mTORC1 activation. Under favorable growth conditions, the formation of the TSC1/2 complex is inhibited, allowing Rheb to activate mTORC1 signaling. mTORC1 then activates number of downstream signaling cascades that support anabolic processes, such as increased transcription/translation, lipid synthesis, and nucleotide synthesis. Concurrently, catabolic processes are inhibited, including autophagy and lysosome biogenesis. Under stress conditions, the GAP activity of TSC2 inactivates Rheb, thereby inhibiting pro-growth mTORC1 signaling cascades and allowing pathways promoting cell survival to proceed.

and autophagy. Although numerous growth factors act to induce mTORC1-mediated cell growth, the availability of metabolic building blocks is most determinate of mTORC1 activation. Upon mTORC1 activation in the presence of ample energy and nutrients, mTORC1 initiates a series of phosphorylation events leading to increased global protein synthesis; mTORC1-mediated phosphorylation of both 4E-BP1 and S6 kinase 1 (S6K) lead to cap-dependent translation through and increased transcription, respectively (Saxton and Sabatini 2017). To facilitate the increase in protein synthesis and biomass, mTORC1 simultaneously initiates ribosomal assembly, nucleotide synthesis, and lipid biogenesis (Porstmann, Santos et al. 2008, Ben-Sahra, Howell et al. 2013, Iadevaia, Liu et al. 2014, Ben-Sahra, Hoxhaj et al. 2016). Furthermore, mTORC1 initiates metabolic programming conducive to anabolic processes, most notably glycolysis through increased expression of the glucose transporter, SLC2A1, and hypoxia-inducible factor 1-alpha (HIF1α) induced expression of glycolytic enzymes (Duvel, Yecies et al. 2010).

Under conditions supportive of cell growth, catabolic pathways are inhibited by mTORC1; however, under stress conditions (nutrient deprivation, low ATP/ADP ratio, hypoxia) mTORC1 quickly acts to curb the consumption of valuable energy reserves and permits the activation of autophagy to break down and recycle macronutrients critical to cell survival (Egan, Kim et al. 2011, Kim, Kundu et al. 2011). Autophagy is directly inhibited through the mTORC1-mediated phosphorylation of Unc-51 Like Autophagy Activating Kinase 1 (ULK1) at Ser 757. This phosphorylation event prevents the interaction of ULK1 with AMP activated protein kinase, which normally acts to phosphorylate and activate ULK1 at Ser 113, Ser 555, and Ser 777 (Egan, Shackelford et al. 2011, Kim, Kundu et al. 2011). mTORC1 also acts to inhibit the formation of lysosomes, a critical component within early autophagy induction, through direct phosphorylation of transcription factor EB (TFEB). TFEB and its related family members regulates the expression of genes involved in lysosome biogenesis and assembly of

autophagic machinery (Sardiello, Palmieri et al. 2009, Settembre, Di Malta et al. 2011). mTORC1-mediated phosphorylation of TFEB prevents its transport into the nucleus, rendering its gene-regulatory function inoperable (Martina, Chen et al. 2012). This negative regulation of lysosome biogenesis is somewhat paradoxical: mTORC1 must first be recruited to the lysosomal surface to activate and enact its metabolic signaling circuitry. This is accomplished through its association with a unique family of small GTPases, the Rag-GTPases. The four Rag-GTPases, Rag A/B/C/D, form heterodimers which change conformation and subsequent active docking states based on nutrient levels, leading to mTORC1 recruitment and retention at the lysosomal surface (Sancak, Peterson et al. 2008, Sancak, Bar-Peled et al. 2010). This anchorage of mTORC1 to the lysosomal surface is required for Rheb-GTPase-mediated activation of mTORC1, and similarly, recruitment of the TSC1/2 complex to the lysosomal surface is required to inhibit its activity (Demetriades, Plescher et al. 2016).

The formation of the TSC1/2 complex is dependent on a number of different phosphorylation events at multiple sites on both TSC1 and TSC2, resulting in a highly dynamic regulatory system upstream of mTORC1. Upon growth factor or cytokine stimulation, activation of the phosphatidylinositol 3-kinase (PI3K) pathway results in the phosphorylation of TSC2 by Akt, Erk, or RSK, each with unique phosphorylation sites (Inoki, Li et al. 2002, Roux, Ballif et al. 2004, Ma, Chen et al. 2005). Phosphorylation of TSC2 by these proteins results in the deactivation of TSC2, inhibiting the formation of the TSC1/2 complex and allowing the activation of mTORC1 signaling. Proinflammatory cytokines also activate mTOR via the IkB kinase β-mediated phosphorylation of TSC1, resulting in dissociation of TSC1/2 (Lee, Kuo et al. 2007). Additionally, in unfavorable growth conditions, such as hypoxia or at energy deficit, AMPK acts to directly phosphorylate TSC2 and promote the GAP activity of TSC2 towards Rheb (Inoki, Zhu et al. 2003). Wnt signaling is also integrated into TSC1/2 signaling, as evident by GSK3-

mediated phosphorylation of TSC2, which is also dependent on and synergistically enhances AMPK-mediated inhibition of protein synthesis via TSC2 (Inoki, Ouyang et al. 2006). Thus, TSC1 and TSC2 function as gatekeepers of the critical, multi-functional cellular signaling network that is mTORC1 signaling. The therapeutic efficacy of rapamycin, a molecular inhibitor of mTOR, in treating many of the manifestations in TSC and LAM (Krueger, Care et al. 2010, Casanova, Maria Giron et al. 2011, Dabora, Franz et al. 2011, DeKlotz, Ogram et al. 2011, McCormack, Inoue et al. 2011, Tiberio, Franz et al. 2011, Bissler, Kingswood et al. 2013, Canpolat, Per et al. 2014, Park, Yun et al. 2014, Franz and Capal 2017) has established elevated mTOR signaling as a key feature driving TSC and LAM tumors.

1.1.3 Molecular characteristics of TSC and LAM tumors

The tumors that arise in TSC are generally comprised of immature cells that exhibit molecular and phenotypic features of either neuronal (central nervous system (CNS) lesions) or mesenchymal differentiation, with LAM manifestations being strictly mesenchymal in nature (mesenchymal TSC and LAM will herein be referred to as LAM for simplicity). The cells that comprise LAM and TSC tumors reflect many common features of hyper-active mTOR signaling; abnormally large or ‘giant’ cells, altered morphology, aberrant migration, abnormal proliferation, increased autophagy and cell survival are common features of the diverse multisystem lesions that patients present with (Crino, Nathanson et al. 2006, Henske and McCormack 2012, Caban, Khan et al. 2017). Furthermore, increased angiogenesis is also a feature of many TSC and LAM lesions (Nguyen-Vu, Fackler et al. 2001, Arbiser, Govindarajan et al. 2002, Kumasaka, Seyama et al. 2004).

Despite the common signaling element of mTORC1 dysregulation, the types of lesions that develop in TSC and LAM are diverse, in terms of both the tissues that are

affected and the molecular characteristics of the aberrant cells. Furthermore, the various types of TSC and LAM-associated tumors exhibit additional behavioral and signaling characteristics that are distinct from one another. For example, LAM cells are uniquely responsive to estrogen and prolactin signaling, and express these receptors on their surface (Terasaki, Yahiro et al. 2010, Yu and Henske 2010, Gao, Yue et al. 2014). They also express markers of smooth muscle cells and melanocytes, cell types not normally found within the lung interstitium. In contrast, the aberrant cells that comprise cortical tubers and SEGAs in TSC patients express markers of early neuronal and glial lineages (Ess, Kamp et al. 2005). Several TSC mouse models have revealed that these tumors result from mTORC1-dependent neural stem cell (NSC)/neural progenitor cell (NPC) expansion and premature differentiation, with subsequent defective maturation and migration (Lopes, Altermatt et al. 1996, Magri, Cambiaghi et al. 2011, Zhou, Shrikhande et al. 2011, Magri, Cominelli et al. 2013). Thus, in CNS TSC lesions, constitutive mTORC1 activation directly affects the self-renewal and differentiation capacity of the cells endogenous to the tissue in which the lesions are found. However, the etiology of mTORC1 hyper-activation to the appearance of mesenchymal lesions in the lungs, kidneys, and uterus is not yet defined. Of note, TSC and LAM are further differentiated by developmental time point of disease presentation; where most TSC features typically present in infancy or during childhood, LAM presents in adulthood. These differences suggest that, despite their common genetic characteristic, tissue specific TSC and LAM lesions exhibit unique pathological mechanisms.

1.1.4 Current treatment options for TSC and LAM

While double lung transplant is currently the gold standard treatment option for late-stage LAM, this approach is not possible in all patients. Furthermore, LAM lesions have been shown to recur in the donor lung in some patients following successful

transplant (Bittmann et al., 2003; Karbowniczek et al., 2003). Thus, although clearly beneficial for most patients, lung transplantation does not address the underlying mechanisms that drive the development of LAM. The mTOR-specific inhibitor rapamycin is a long investigated molecular intervention for treating both TSC and LAM. rapamycin has proven clinically effective for the treatment of most TSC-associated lesions (Bissler et al., 2008; Dabora et al., 2011; Franz et al., 2006; Krueger et al., 2010; DeKlotz et al., 2011; Casanova et al., 2011; Park et al., 2014; Canpolat et al., 2014; Micozkadioglu et al., 2010; Tiberio et al., 2011), and in the context of LAM can lead to reduction in the size of rAMLs, provide stabilization of lung function, and a significant improvement in quality of life measures (McCormack et al., 2011). With such promising results, rapamycin was approved by the U.S. Food and Drug Administration (FDA) for the treatment of TSC tumors in 2012, and was subsequently FDA-approved in 2015 for the treatment of LAM.

A major caveat to the use of rapamycin to treat TSC and LAM, however, is that disease progression quickly resumes once rapamycin is withdrawn; thus, it is likely that patients must remain on the drug permanently to provide sustained treatment. Long-term rapamycin treatment is also not without potential challenges, as there is concern that LAM tumors, as well as other TSC lesions, may become unresponsive to rapamycin over an extended period of time. Additionally, while rapamycin can reduce aberrant mTORC1 signaling, it may also have the undesirable effect of promoting the survival of *TSC1*- or *TSC2*-null cells (reviewed in (Henske and McCormack, 2012)). This surprising phenomenon is attributed to the inherent inhibition of autophagy by activated mTORC1 signaling; inhibition of autophagy is a typical consequence of TSC1- or TSC2-deficiency (Crino, Nathanson et al. 2006, Parkhitko, Myachina et al. 2011, Henske and McCormack 2012, Saxton and Sabatini 2017, Valvezan and Manning 2019). Thus, while rapamycin appears to generally inhibit the growth of TSC1- or TSC2-deficient cells, it may

concurrently promote their survival by allowing pro-survival autophagy signaling programs to proceed.

Rapamycin has also been shown to induce expression of pro-survival micro-RNAs (Trindade et al., 2013), and a number of factors thought to help drive LAM pathogenesis are unaffected by rapamycin treatment, including increased expression of MMP2 (Lee et al., 2010b). These signaling mechanisms may therefore result in a precarious situation whereby the growth and proliferation of TSC1- or TSC2-deficient cells is halted with rapamycin treatment, but the cells remain viable and dormant, allowing them to expand once again once treatment is stopped. As long-term rapamycin treatment carries a significant risk of adverse side-effects (McCormack et al., 2011), and the cells that comprise TSC lesions may become resistant with prolonged treatment, additional therapeutic options are needed to provide effective and long-term treatment options to TSC and LAM patients. Furthermore, due to the evidence suggesting rapamycin treatment may promote the survival of tumor cells, and a number of mTORC1 independent pathogenic signaling pathways likely to contribute to TSC, there is a clear need for the development of alternative or combination therapies. Unfortunately, current models of LAM are limited in their ability to accurately model the disease, hindering the advancement of more innovative and targeted therapeutics. Thus, the development of new therapeutic approaches is currently of the highest priority within the LAM and TSC fields; in concert with this, the development of effective models to serve as the foundation for the development of potentially effective therapeutic interventions must be prioritized.

1.2 The Cells of Origin for TSC and LAM

Identification of the cell of origin for LAM is imperative for the development of more effective, long-lasting treatment strategies. For instance, mTOR activation can lead

to different primary phenotypes in distinct cell types. For example: precocious neuronal differentiation in the CNS (Hartman et al., 2013), increased cycling of hematopoietic stem cells (Gan et al., 2008), and exit of satellite cells from quiescence upon injury (Rodgers et al., 2014). Therefore, it stands to reason that the multisystem TSC and LAM-associated lesions may require unique tissue specific therapeutic approaches. Furthermore, the downstream targets of mTOR are diverse and affect multiple cellular signaling pathways, with both mTORC1 and mTORC2 participating in a number of feed-back signaling mechanisms (Laplante and Sabatini, 2012). Due to this complexity, truly effective treatment approaches are likely to require combination therapies in which multiple signaling nodes are targeted, and the most promising approaches may well be different for distinct tumor types. Only by identifying the cell of origin for distinct types of lesions will we be able to experimentally investigate the molecular mechanisms that lead to the induction of each type of tumor, and subsequent tumor progression (including growth, metastasis, behavioral and morphological changes), and to determine which vulnerable nodes within dysregulated pathways need to be targeted to inhibit each step of the process.

The cell(s) of origin for TSC and LAM lesions are largely unknown, however clinical observations and recent experimental evidence have offered some key clues. The extensive multi-system involvement in these diseases is remarkable, with evidence for both common and independent ‘first-‘ and ‘second-hit’ TSC1 or TSC2 mutations across multiple tumors within a given individual adding to the complexity of disease pathogensis (Tyburczy et al., 2014; Henske et al., 1996; Smolarek et al., 1998; Carsillo et al., 2000; Karbowniczek et al., 2003). While embryonic NSC and NPCs appear to function as a cell of origin for the CNS manifestations in TSC, the mesenchymal neural crest lineage has been postulated to give rise to LAM lesions. With the potential involvement of both NSCs/NPCs and the neural crest lineage in disease heterogeneity,

the influence of the developmental time-point at which TSC1 or TSC2 mutations occur on disease severity has also been called into question.

A clear distinction between individuals with TSC gene mutations who acquire multisystem TSC versus S-LAM is that the somatic mutations in TSC1 or TSC2 are more widespread in those with TSC, and are typically also present in the germline (Dabora et al., 2001; Strizheva et al., 2001). This was a substantial discovery toward our understanding of how S-LAM may develop in the absence of other TSC manifestations, pushing forth the concept that TSC and LAM lesions may develop from different founding cell types. This suggests TSC gene mutations are restricted to a specific lineage or cell type in S-LAM patients. The fact that there is considerable heterogeneity in the clinical presentation and severity of the disease spectrum among both LAM and TSC patients (Curatolo and Maria, 2013; Henske and McCormack, 2012), along with the evidence for gonadal and/or somatic mosaicism in some TSC patients that correlates with phenotypic variability (Verhoef et al., 1999; Boronat et al., 2014b; 2014a; Qin et al., 2010b; Rose et al., 1999), lends further support to the idea that disease spectrum is significantly affected by the proportion of cells. The findings from the CNS-related TSC mouse models discussed below provide strong experimental support for this concept. Although these studies are limited to the CNS manifestations, it is likely that this theme persists throughout the full spectrum of the disease and that, in general, a more restricted mutational burden will lead to the development of fewer types of lesions and fewer numbers of lesions. With this in mind, one could postulate that while TSC gene mutations in NPCs lead to the CNS lesions, mutations within the neural crest lineage are responsible for the development of LAM lesions. Thus, a mutational burden present in the embryonic ectoderm, which give rise to both NSC/NPCs and neural crest cells (NCCs), would likely lead to the greatest heterogeneity and disease penetrance in TSC patients.

1.2.1 The Cell of Origin for Neurological TSC Manifestations

Experimental approaches to identify the cell of origin in TSC have primarily focused almost exclusively on validating the hypothesis that the CNS tumors and behavioral phenotypes are driven by TSC1 or TSC2 mutations in the NSC lineage. Since the CNS manifestations cause significant morbidity and are apparent at such a young age, this focus is not surprising. Mouse models of homozygous TSC1- or TSC2-knockout lead to early embryonic lethality, and mice heterozygous for either TSC gene do not develop TSC-related CNS pathologies, likely due to the lack of a second-hit mutation during embryonic development (Kobayashi et al., 1999; 2001; Onda et al., 1999; Kwiatkowski et al., 2002). More sophisticated models have recently emerged to assess the effects of homozygous TSC gene mutation in select populations of NPCs and differentiating or differentiated neuronal cells (Uhlmann, Apicelli et al. 2002, Meikle, Talos et al. 2007, Ehninger, Han et al. 2008, Way, McKenna et al. 2009, Feliciano, Su et al. 2011, Goto, Talos et al. 2011, Magri, Cambiaghi et al. 2011, Zeng, Rensing et al. 2011, Zhou, Shrikhande et al. 2011, Carson, Van Nielen et al. 2012, Magri, Cominelli et al. 2013, Normand, Crandall et al. 2013, Prabhakar, Goto et al. 2013, Blair, Hockemeyer et al. 2018). These models have included a variety of drug inducible and non-inducible conditional knockouts, as well as adenoviral-mediated approaches or in utero electroporation to induce gene knockout stochastically. These have allowed for targeted induction of TSC1- or TSC2-deficiency in distinct neural cell populations and regional locations, as well as the proportion of the affected cell population, and the developmental time-point of induction.

Arising from these efforts, mouse models of TSC1- or TSC2-deficiency now exist that closely model the CNS manifestations of TSC that occur in human patients, including neuronal network dysfunction and seizure activity, sub-ependymal nodules that

lead to the development of SEGAs and elements of cortical tubers, accompanied by abnormal neuronal migration, enhanced astrogliosis, enlarged cells and cortical lamination defects (Magri et al., 2011; Goto et al., 2011; Normand et al., 2013; Prabhakar et al., 2013; Magri and Galli, 2013; Carson et al., 2012). Importantly, hyper-activation of mTORC1 signaling has indeed been confirmed as causative in the majority of TSC-like phenotypes in these models, confirmed by extensive phenotypic rescue following post-natal rapamycin treatment in many of these studies. Interestingly, these models have revealed that while abnormal, enlarged cells and nodule-like formations can be induced to some degree by TSC gene deletion in virtually all neuronal populations (progenitors and post-mitotic cells) and at different developmental stages (throughout embryogenesis and postnatally), neurological features such as seizure activity are only clearly reproduced by targeting NPCs and neurons prenatally, during peak stages of neurogenesis. Furthermore, the overall severity of CNS manifestations following TSC gene deletion at different stages occurs on a gradient scale, with the most severe and extensive phenotypes associated with mutations in NPC populations at the earliest stages of neurogenesis (in neuroepithelial cells and radial glia at E9.5 and E12.5, respectively). Furthermore, a recent *in vitro* study utilizing targeted genome engineering of the TSC genes in human embryonic stem cell (hESC)-derived cortical spheroids elegantly demonstrated that second hit mutations precipitate tumor formation during neural development (Blair, Hockemeyer et al. 2018). As appearance of the full spectrum of TSC-associated CNS lesions seems to require TSC gene mutation in early NPCs, these studies together provide solid evidence to support the hypothesis that a neural stem or progenitor cell is the cell of origin for the CNS manifestations in TSC.

1.2.2 The neural crest as a putative cell of origin for mesenchymal TSC and LAM

The neural crest is a transient population of migratory progenitor cells that emerge at the interface between the dorsal region of the neural plate and the non-neural ectoderm in embryonic development during neurulation. Although the migratory patterns of the neural crest can differ slightly across species, studies performed in model organisms, such as *Xenopus*, mouse, quail and chick embryos, have offered great insight into the contributions of the neural crest population to various tissues in the developing embryo. Although exact migratory patterning in humans is unknown, lineage tracing has revealed enough commonality between these model species to establish a paradigm for neural NCC migration and differentiation during human development. Through contact mediated interactions, NCCs emerge, undergo epithelial-to-mesenchymal transition (EMT), and migrate in specific succession and order in an anterior to posterior sequence (Theveneau and Mayor, 2012). Of note, both the neural plate and the surface ectoderm contribute cells to the neural crest population (Moury and Jacobson 1990, Selleck and Bronner-Fraser 1995). Once NCCs have emerged and delaminated, they follow distinct migratory patterns depending on their eventual fate (summarized in Table 1, Figure 1.3).

As NCCs emerge and begin migration, they can be categorized into four major subgroups based on their migratory cohort: cranial, cardiac, vagal and trunk. Cranial NCCs contribute to the tissues of the craniofacial region, differentiating into the widest array of cell types of the neural crest subgroups, including vascular smooth muscle cells and pericytes, chondrocytes, adipocytes, osteocytes, odontoblasts, melanocytes, connective tissue, and sensory and parasympathetic ganglia (Billon et al., 2007; D'Amico-Martel and Noden, 1983; Etchevers et al., 2001; Grenier et al., 2009; Köntges and Lumsden, 1996). Cardiac NCCs differentiate into parasympathetic cardiac ganglia, as well as smooth muscle of the branchial arches and the cardiac outflow tract, and form the aorticopulmonary septum (Kirby et al., 1983; Kirby and Stewart, 1983). Vagal NCCs

NC Subtype	Tissues	Cell types
Cranial	Craniofacial skeleton Skin Cornea Connective tissue	Fibroblasts Melanocytes Adipocytes Osteocytes Odontoblasts Chondrocytes Neurons Glia Mesenchymal cells Myocytes Pericytes
Cardiac	Branchial arches Cardiac septum Parasypathetic cardiac ganglia	Myocytes Pericytes Neurons Glia
Vagal	Enteric nervous system	Neurons Glia
Trunk	Peripheral nervous system Skin Adrenal medulla	Neurons Glia Melanocytes Chromafinn cells

Table 1.1: Neural crest subgroups and their respective cell lineage contributions.

Model organisms paired with lineage tracing have identified four major subgroups of NCCs, based on their respective migratory pattern and the tissues and they contribute to. It should be noted that individual NCC multipotency varies between subgroups, as well as within subgroups themselves. Reprint from Delaney et al. 2014. Front Cell Dev Biol. 2:69 (Delaney, Julian et al. 2019).

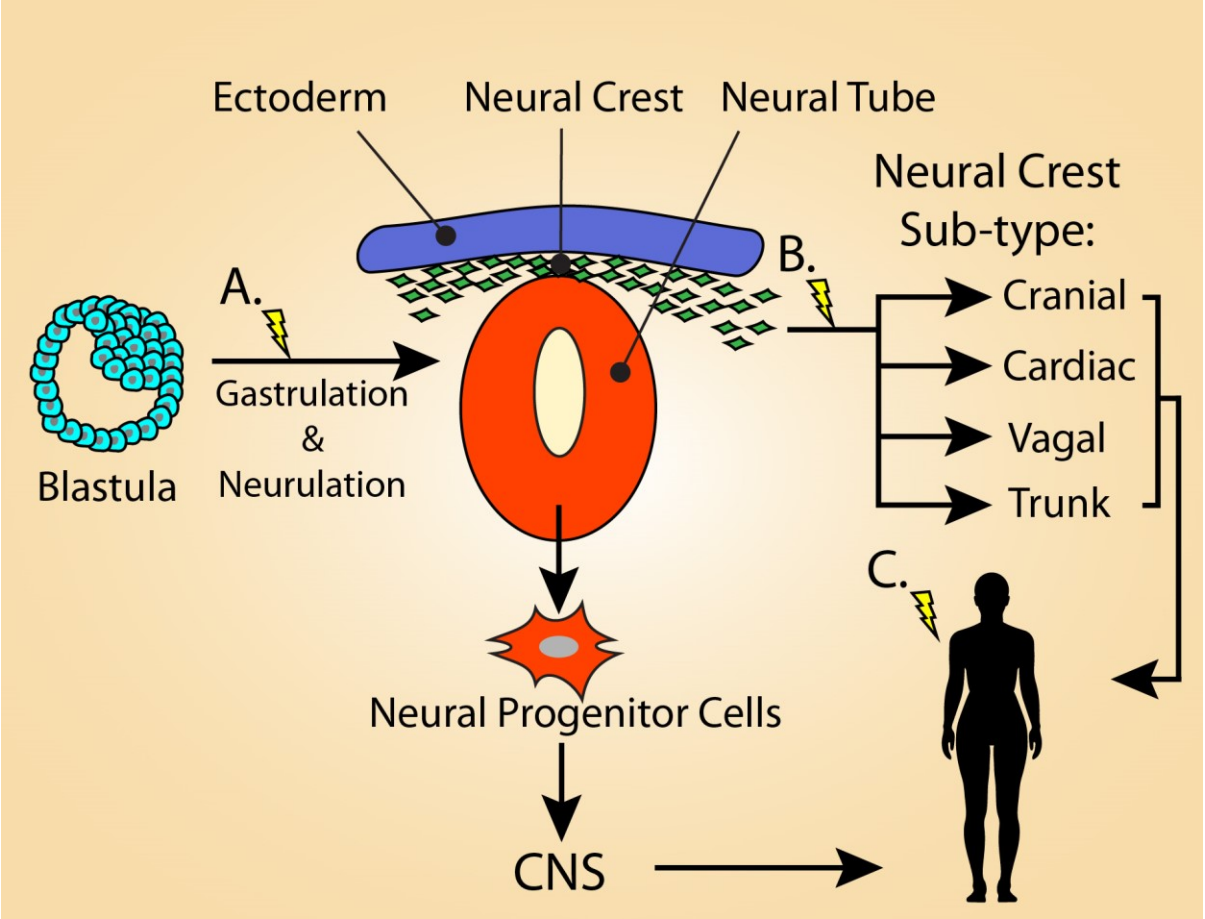

Figure 1.3: Developmental model of mutation acquisition and its potential contribution to TSC/LAM.
Tumor heterogeneity in TSC could be related to spatial/temporal factors during embryogenesis, dependent on when the first hit mutation in TSC1 or TSC2 occurs, or second hit mutation if germline heterozygous. A) Mutations acquired during early stages of development, such as gastrulation or neurulation, would result in a larger proportion of cells carrying the mutation, leading to a more severe and multisystem TSC/LAM phenotype. The affected cells could, theoretically, contribute not only to the neural crest population, but also the neural progenitor population of the neural tube, resulting in the CNS manifestations of TSC. B) Mutations occurring in the emerging neural crest population likely result in LAM and non-CNS symptoms of TSC. Disease severity would then be linked to the respective mutated cell's position along the anterior-posterior axis during development, thereby dictating the neural crest subtype, and, ultimately, the tissues affected. C) Frist and second hit mutations acquired later in development (such as in adult NCSCs) may result in S-LAM. Reprint from Delaney et al. 2014. Front Cell Dev Biol. 2:69 (Delaney, Julian et al. 2019).

primarily give rise to the neurons and glia of the enteric nervous system (Le Douarin and Teillet, 1973; Yntema and Hammond, 1954). Finally, trunk NCCs give rise to melanocytes and the neurons and glia of the peripheral nervous system (Raible and Ungos, 2006).

1.2.3 The embryonic neural crest cell of origin theory

NCCs are able to differentiate into a wide array of cell types that contribute to many of the tissues associated with non-neurological TSC tumors. Theoretically, distinct neural crest subtypes could be specifically associated with some of the multi-systemic tumors observed in TSC. For instance, the cranial neural crest may be implicated in the development of facial angiofibromas, dental pits, and retinal tumors. Indeed, cases of retinal lesions have been reported in connection with neurofibromatosis, a disease also thought to be of neural crest origin (Ishiko et al., 2006; Sachdeva et al., 2010). Extending this theory, TSC1- or TSC2-deficient cardiac neural crest may be the cell of origin for cardiac rhabdomyomas and even pulmonary LAM lesions (due to the involvement in aorticopulmonary septum development), and dysfunctional trunk neural crest may be responsible for ‘confetti’ skin lesions and hypomelanotic macules. From this developmental perspective, the determining factor in which tumor types ultimately form is perhaps both spatial and temporal (Figure 1.3). If the first-hit mutation occurs early on during embryogenesis within a cell of the developing neural plate or surface ectoderm before neurulation, the number of potential affected progeny with the potential to acquire a second-hit mutation would be much greater and could potentially affect all neural crest subgroups, leading to a more severe TSC phenotype affecting multiple tissues. If the first-hit mutation occurs later in development, perhaps in an emerging neural crest subtype, the affected cell may only have influence on the specific subtype emerging from its respective anterior/posterior position along the developing neural tube. Such a

scenario could explain the extreme variability in TSC disease spectrum that are observed in severely affected TSC patients versus individuals with S-LAM.

1.2.4 The adult neural crest cell of origin theory

The integration of migrating NCCs to tissue throughout the body is a fundamental process during embryonic development, however, NCCs with stem cell-like properties (NCSCs) are now known to persist in a number of adult tissues. Just as tissues that are innervated by embryonic NCCs during development theoretically have the potential to give rise to LAM-like cells or cells that comprise other TSC mesenchymal lesions, these adult NCSCs are a particularly promising population as a potential cell of origin for LAM. The tissues in which NCSCs reside in the adult are diverse, and include the gut, bone marrow, heart, dental mesenchyme, dorsal root ganglia, and cornea (reviewed in (Dupin and Sommer, 2012)). Intriguingly, a number of distinct multipotent stem cells with neural and/or neural crest differentiation potential have also been identified in the skin (Dupin and Sommer, 2012). As NCSCs possess inherent migratory and transdifferentiation potential and exhibit extensive interactions with their surrounding microenvironments that can instruct migratory, differentiation and invasiveness behaviors, many of these cell types could potentially serve as the cell of origin for mesenchymal TSC and LAM lesions in later development (Takahashi et al., 2013).

The susceptibility of the skin to ultraviolet (UV) radiation highlights NCSCs resident in the skin as particularly promising candidates as a cell of origin, as UV-induced damage could easily lead to second-hit mutations. Speaking to the likelihood of this potential, skin-derived precursors (SKPs), multipotent NCSCs found in the dermal sheath and papillae of hair follicles in both rodents and humans (Biernaskie et al., 2009; Jinno et al., 2010; Toma et al., 2005; Fernandes et al., 2004; Toma et al., 2001), have been heavily implicated as the cell of origin for the dermal tumors associated with the

neurocristopathic disorder Neurofibromatosis type I (Le et al., 2009). There is also compelling evidence that precursor cells found within the skin may serve as the cell of origin for facial angiofibromas in TSC patients, following the acquisition of UV-induced second-hit TSC2 mutations (Tyburczy et al., 2014). Given this potential, it is a distinct possibility that SKPs may similarly serve as the cell of origin for LAM and other TSC-associated lesions, if indeed SKPs possessing TSC gene mutations are able to invade the lymphatic and/or cardiovascular circulation.

1.3 Clinical and experimental evidence of a neural crest cell of origin

Sequencing of tissue from LAM nodules, disseminated LAM cells from body fluids, and rAMLs has indicated that germline *TSC1* or *TSC2* mutations are not prevalent in S-LAM patients (Astrinidis et al., 2000; Carsillo et al., 2000). Thus, the first-hit mutation that drives LAM must typically arise *de novo* in a somatic cell. The lack of CNS involvement in the pathology of S-LAM provides strong clinical evidence that the neural stem cell lineage is not affected in S-LAM patients. The molecular markers present in cells within mesenchymal lesions (alpha-smooth muscle actin (SMA), HMB-45, TRP-1), as well as the tissue types affected in the majority of TSC-associated tumors, do however present significant clues to the potential cell(s) of origin. The tissues in which lesions/abnormalities are observed in TSC patients are diverse, but all of them share the common feature that they are wholly or in part comprised of neural crest progeny (Figure 1.1, Table 1.1) (Dupin and Sommer, 2012). These tissues include the heart (cardiac rhabdomyomas), the skin (angiofibromas, most predominant in the facial region), dental enamel, eyes (retinal astrocytic hamartomas), and the innervation of the kidneys (rAMLs), uterus and lungs (Curatolo and Maria, 2013). Additionally, the abnormal cells observed LAM lesions express molecular markers of cells that are generated by the neural crest: smooth muscle, melanocytes, and adipocytes.

In addition to key molecular markers, there is also compelling evidence that LAM cells are able to migrate between different tissue sites (Karbowniczek et al., 2003; Smolarek et al., 1998), reminiscent of the highly migratory behavior of NCCs. Furthermore, LAM lung lesions contain a heterogeneous population of cells, with both highly proliferative spindle shaped cells and large epithelial cells making up LAM clusters. Moreover, both of these cell types express molecular markers of mesenchymal neural crest cells *in vivo* (e.g., smooth muscle actin in the spindle shaped cells, and PMEL (HMB45) in the epithelial cells). This suggests the intriguing possibility that, if indeed mesenchymal TSC and LAM cells originate from the neural crest, they may possess the ability to undergo EMT or even mesenchymal-to-epithelial transition (MET) within the lesion itself, accounting for the presence of these distinct cell types within single lesions.

1.3.1 Metastatic LAM cells and their similarities to migratory NCCs

Just as neural crest cells represent a highly migratory cell population, a striking characteristic of LAM cells is their ability to travel from one tissue site to another, leading to multi-tissue tumor formation. For example, mutation analysis has revealed that the same mutations are present in LAM cells of both pulmonary LAM nodules and rAMLs, indicating that the tumors originated from a common progenitor cell that was able to migrate or metastasize to and/or from either of these tissues (Sato, Seyama et al. 2002). Although identical *TSC1* or *TSC2* mutations among tumor cells are not always observed in TSC-LAM and S-LAM patients, it is clear that LAM cells are mobile; markedly, LAM cells are able to infiltrate and repopulate healthy donor lungs following transplantation (Bittmann, Rolf et al. 2003, Karbowniczek, Astrinidis et al. 2003). They are also are able to metastasize between the lungs, kidneys, lymphatics, and uterus using mechanisms that do not fit the classic cancer metastasis paradigm. LAM cells can be found

throughout the lymphatics in LAM patients, and their expression of vascular endothelial growth factor (VEGF)-C and VEGF-D along with VEGF receptor-3 indicates their lymphangiogenic potential (Glasgow et al., 2012), indicating that the extensive network of lymphatics may serve as the primary niche for LAM cells and facilitates their spread.

LAM cells are resistant to anoikis and can be found in the chylous fluid, bronchoalveolar fluid, urine, and blood of LAM patients, a phenomenon that may be directly related to estrogen signaling (Crooks et al., 2004; Gu et al., 2013; Yu et al., 2009). Although these cells do not present themselves as malignant and highly proliferative compared to most cancer cells, their apparent robustness and infiltrative ability is certainly not benign. A complete mechanistic model for LAM cell 'metastasis' has yet to be confirmed; however, numerous studies have shown that LAM cells display increased motility and invasive properties *in vitro*. This invasive phenotype can be directly linked to loss of function (LOF) mutations in either *TSC1* or *TSC2*, leading to pro-migratory cytoskeletal rearrangement and changes in focal adhesions. Primary LAM cells with TSC2 LOF mutations display increased invasive and migratory properties as a result of RhoA GTPase-mediated cytoskeletal rearrangement and modulation of focal adhesions. RhoA GTPase is normally regulated by TSC1 when complexed with TSC2, and this invasive phenotype is mitigated upon TSC2 re-expression or TSC1 knockdown (Goncharova et al., 2006; Lamb et al., 2000). Perhaps contributing to the robustness of migratory LAM cells, dysfunctional TSC2 leads to a loss in membrane bound E-cadherin via a rapamycin sensitive pathway. This, in turn, leads to reduced cell-cell adhesion, EMT, cell detachment, and resistance to anoikis (Barnes et al., 2010).

1.3.2 Phenotypic parallels between LAM cells and NCCs

Clearly, dysfunction of either TSC1 or TSC2 will result in a cell that is primed to undergo EMT and migrate, a scenario that is reminiscent of neural crest delamination

and migration during embryonic development. RhoA is critical in regulating the directionality of migrating neural crest cells, greatly affecting spatial-temporal patterning upon its loss (Matthews et al., 2008; Rupp and Kulesa, 2007). Cadherins play a crucial role during neurulation and help define the non-neural ectoderm and the neural plate (Dady et al., 2012; Taneyhill, 2008), the tissues whose interface from which neural crest cells delaminate and from which they migrate. Specifically, the transition from E-cadherin expression to N-cadherin plays a critical role in this process, and interestingly, a similar phenomenon is observed in LAM cells. As mentioned above, TSC2-deficiency results in internalization of E-cadherin leading to EMT; moreover, when LAM patient-derived cells are exposed to estrogen, E-cadherin expression is decreased and N-cadherin is upregulated, similar to the segregation of the germ layers during neurulation (Gu et al., 2013). Pairing well with the decrease in E-cadherin expression in TSC2-deficient cells, there is an upregulation in the expression of Snail, an important transcription factor involved in initiating EMT, migration, and neural crest specification (Aybar et al., 2003; Barnes et al., 2010; Cano et al., 2000). A second hit mutation in *TSC2* therefore causes a change in the expression profile in LAM cells that resembles a neural crest progenitor undergoing migration and fate specification.

Adding fuel to the fire, LAM cells have been shown to excrete matrix metalloproteinases (MMPs), particularly MMP-2 and MMP-9, that likely contribute to their invasiveness and lead to the slow destruction of the lung parenchyma (Hayashi et al., 1997; Lee et al., 2010a). MMP2 and MMP9 are required in neural crest cells for their initial delamination and migration, and inhibition of these MMPs during development results in the complete halt of NC migration and differentiation (Monsonego-Ornan et al., 2012).

Extending this comparative train of thought, changes in TGF-ß signaling in LAM cells also relates directly to the NC and its lineages. Histopathological analysis of LAM

cells, along with TSC2-null cell lines, show increased levels of transforming growth factor beta (TGF-ß) and alpha-SMA (Barnes et al., 2010; Lee et al., 2010a; Zhe and Schuger, 2004). Although expression of TGF-ß and alpha-SMA is common to the EMT process, TGF-ß signaling is involved in NC-derived smooth muscle specification *in vivo* and is a common element of smooth muscle differentiation protocols of neural crest cells *in vitro* (Curchoe et al., 2010; Shah et al., 1996; Xie et al., 2013). The initiation of signaling cascades resulting in a smooth muscle-like cell fate may help explain the presence of spindle-like alpha-SMA+ proliferative cells in LAM nodules and angiomyolipomas. A loss of TSC2 function could destabilize a NC-derived cell, causing it to dedifferentiate and undergo EMT. This cell could then potentially migrate to a favorable niche, (e.g. lung, kidney, lymphatics) and, due to increased TGF-ß signaling, differentiate into the smooth muscle cells and form the characteristic tumors associated with LAM.

The molecular signaling events that occur upon a second hit mutation in TSC1 or TSC2 may act in some capacity to recapitulate the developmental processes of neural crest migration and specification. Such an orchestration may be enough to perhaps destabilize a dormant NCSC or a fully differentiated NC cell, whose epigenetic memory is already prone to EMT, migration, and cell motility. Indeed, with the proper stimulus, fully differentiated NC progeny display the ability to dedifferentiate and migrate *in vivo*, as well as return to a multipotent state when isolated and cultured *in vitro* (Dupin and Sommer, 2012; Nagoshi et al., 2011; Real et al., 2006; 2005).

The neural crest have already been implicated in the reactivation of EMT in fully differentiated and mature cells in the form of the metastatic cancers melanoma and neuroblastoma (Grimmer and Weiss, 2006; Shakhova, 2014). Furthermore, dedifferentiation and redifferentiation (EMT-mesenchymal to epithelial switch) is a proposed mechanism of metastatic cancer supported by experimental evidence (Ocaña et al., 2012; Tsai et al., 2012). Neural crest cells have the unique ability to

transdifferentiate during embryonic development from a neural ectodermal lineage to specialized cells that are ultimately considered to be mesodermal. This phenotypic plasticity is a unique quality of the neural crest, which clearly requires precise signaling and environmental cues during development for precise specification. Similar to the notion that a machine with many small moving parts is more likely to malfunction, neural crest-derived cells may be more prone to undergo EMT, migrate, and differentiate based on their inherent plasticity if given the proper cues.

1.3.3 Current models of mesenchymal TSC and LAM

Most available experimental models of LAM include *Tsc1* and *Tsc2*-deficient murine strains, fibroblasts derived from these animals, or transformed patient rAML-derived cell lines (Howe, Gottardis et al. 1995, Zhang, Cicchetti et al. 2003, Yu, Astrinidis et al. 2004, Darling, Pacheco-Rodriguez et al. 2010, Kwiatkowski 2010, Goncharova, Goncharov et al. 2012, Prizant, Sen et al. 2013). Perhaps the oldest existing model of TSC and LAM is the Eker rat model and its derivative ELT3 cell line (Howe, Gottardis et al. 1995). The *Tsc2* heterozygous knockout Eker rats were used to confirm Knudson's two-hit hypothesis of tumor formation, as these rats spontaneously form renal tumors upon loss of heterozygosity at the *Tsc2* locus with near 100% penetrance (Knudson 1971, Yeung, Xiao et al. 1994). However, these renal tumors are epithelial neoplasms and bear no resemblance to LAM-associated rAMLs. Numerous mouse models of LAM have emerged over the years, however, each lack critical characteristics of LAM tumors themselves. *Tsc1* or *Tsc2* homozygous knockout results in embryonic lethality (Kobayashi, Minowa et al. 1999, Kobayashi, Minowa et al. 2001), and *Tsc1* or *Tsc2* heterozygous knockout mouse models exhibit renal cystadenomas much like the Eker rat, and exhibit tumors unrelated to LAM, such as liver and spleen hemangiomas.

In efforts to generate more accurate mouse models of LAM, strategies such as orthotopic injections and tissue restricted knockout of *Tsc* genes have been investigated. One interesting model utilizing uterine specific *Tsc*2 knockout has recapitulated some of the metastatic aspects of LAM (Prizant, Sen et al. 2013). This model generates estrogen-dependent progressive uterine enlargement and myometrial overgrowth, resulting in metastasis of myometrial tumors into the lungs. Although promising, these tumors do not result in cystic lesions and LAM-specific markers, such as HMB45 and VEGFD, are not reported. Another advanced orthotopic model of LAM makes use of tail vein injection of 'enhanced'-*Tsc2*$^{-/-}$ mouse tumor cells. These 'enhanced'-*Tsc2*$^{-/-}$ cells are selected for their increased invasive properties following subcutaneous *in vivo* culture of Tsc2$^{-/-}$ renal epithelial cells originally derived from *Tsc2*$^{+/-}$ mice. The resulting mouse model is promising, with injected mice display progressive growth of multiple lung tumors. These tumors feature multiple LAM-associated markers, such as VEGFD, multiple MMPs, and alpha-SMA, with mice also exhibiting destruction of lung parenchyma and lymphatic involvement (Goncharova, Goncharov et al. 2012). This is perhaps the most accurate mouse model of LAM available, but still does not recapitulate pathological manifestations observed in human, and, furthermore, utilizes thoroughly manipulated cells that display a selectively enhanced-invasiveness phenotype. This results in animal models that present with more aggressive malignancies that do not reflect the slow growing, neoplastic growths characteristic of LAM. Although the above-mentioned mouse models display some features LAM, they simply do not recapitulate LAM pathogenesis accurately enough and may not be reliable for to identify therapeutically effective drugs. The shortcomings of many of these animals are likely a consequence of their inability to model the cells of origin for LAM.

LAM models utilizing cells of human origin have also been generated; an attractive strategy to overcome many of the disadvantages of murine-based models.

One such model, known as the 621-101 cell line, were derived from a LAM patient associated rAML, followed by immortalization through introduction of HPV E6/E7 and human telomerase genes. Although undergoing immortalization, which introduce confounding variables when investigating neoplastic mechanisms, these cells have become a workhorse cell line for LAM-related research, including investigating the role of hormone signaling and autophagy in LAM (Yu, Astrinidis et al. 2004, Li, Lee et al. 2014, Li, Li et al. 2016). Efforts to generate xenotransplant mouse models using primary rAML cells have also been initiated. Through orthotopic intratracheal injections, this strategy yields systemic tumor formation, including the lung, in which some cystic lesions were observed (Liu, Lunsford et al. 2012). These observations were inconsistent, however, and the limitation of the availability of patient samples impedes implementation of this model as a platform for LAM research. Our laboratory has also generated a promising tissue-specific model of the proliferative component of LAM nodules and rAMLs, using in TSC patient-derived induced pluripotent stem cell (iPSC)-derived SMCs (Julian, Delaney et al. 2017). Using an *in vivo* differentiation strategy, $TSC2^{+/-}$ iPSCs were injected into the tibialis anterior of NOD/SCID mice to allow the formation of teratomas after approximately 2 months. These teratomas were then excised and cultured in smooth muscle growth media, which enriched for smooth muscle cells that display multiple phenotypic characteristics of LAM cells. These non-transformed cell lines illustrated that cells displaying *TSC2* haploinsufficiency may contribute to LAM pathogenesis. However, although a strong leap forward, these cells do not model homozygous loss of either *TSC1* or *TSC2*, a limitation that this thesis project is designed to overcome.

Shortcomings aside, taken together, both the human and murine animal models available to date have been extremely informative and have led to the establishment of rapamycin and its analogs as a first line treatment for LAM. However, a significant

limitation still persists that they do not represent the cell lineages that are implicated in driving tumor development in TSC and LAM. Very few studies have directly investigated the hypothesis that *TSC1* or *TSC2* mutations in NCCs drive the development of LAM tumors. Mice containing a conditional *TSC1* knockout allele crossed with mice expressing Cre driven by the *Wnt1* (homolog for human SOX10, a NCC-specific transcription factors) promoter die prenatally for unknown reasons, with no indication of renal or lung pathology (Kwiatkowski, 2010). A more recent neural crest sub-lineage-specific P0-Cre conditional *TSC1* knockout mouse model recapitulated TSC-like sclerotic craniofacial bone lesions, but did not exhibit other LAM-like phenotypes (rAML, lung nodules). As the authors noted, this is likely due to the limited proportion of *TSC1* knockout NCCs generated (Fang, Sun et al. 2015). No additional mouse or cell culture-based models of TSC1 or TSC2-deficiency in the neural crest lineage have been reported to date. However, a potential mechanism of origin implicating the loss of TSC2 in maintaining a multipotent, neural crest-like state through notch signaling was suggested using commonly used *TSC2* null LAM models, such as the transformed human rAML cell line, 621-101, and the ELT3 cell line (Howe, Gottardis et al. 1995, Yu, Astrinidis et al. 2004, Cho, Patel et al. 2017). However, the lack of clarity that current models provide regarding the development and progression of LAM in humans heavily underscores the need for improved models that more closely recapitulate human pathology.

1.4 CRISPR/Cas9 genome engineering in stem cells: potential to model LAM

Primary TSC1- or TSC2-deficient cells derived from patient explants do not grow well in culture. Furthermore, explants themselves are highly heterogeneous as LAM tumors themselves often have a mixture heterozygous and homozygous mutant *TSC1* or *TSC2* cells. When taken out of the *in vivo* environment and placed in culture,

heterozygous cells take over explant cultures such that homozygous mutant cells are outcompeted following the initial few passages. Further frustrating efforts to isolate pure populations of LAM cells, when fluorescent activated cell sorting (FACS) is utilized, the cell surface antigen used to reliably isolate these cells, CD44v6, induces cell death (Pacheco-Rodriguez, Steagall et al. 2007). Thus, the use of iPSCs derived from LAM or TSC patients is an attractive strategy to overcome this limitation. In pursuing this approach to modeling LAM, I and others in our research group have generated multiple iPSC lines with TSC2 deficiency from a number of TSC patients. However, we have shown that generating homozygous TSC2 null iPSCs is not possible using current methodology, as hyperactivation of the mTOR pathway inhibits reprogramming (Wang, Xia et al. 2013, Julian, Delaney et al. 2017). Therefore, the use of the highly effective CRISPR/Cas9 genome editing system to modify the TSC2 locus in well-characterized human embryonic stem cell (hESC) and iPSC lines is the most direct approach to accomplishing this objective. A significant advantage to this approach is that the parental human pluripotent stem cell (hPSCs) lines act as isogeneic controls for all experimentation. Importantly, the use of hPSCs allows researchers to investigate diseases in cell types with high relevance to the tissues affected in the disease in question. Thus, using genetically engineered hPSCs to specifically model LAM using *in vitro* differentiated NCCs is an attractive approach to model the likely cell type of origin for the disease (Delaney, Julian et al. 2014).

1.4.1 The emergence of the CRISPR/Cas system

The RNA-guided Cas9 nuclease from the microbial clustered regularly interspaced short palindromic repeats (CRISPR) adaptive immune system, has provided researchers the opportunity to investigate disease etiology by correcting or introducing genetic mutations into the genomes of a variety of cell types, including hESCs and

iPSCs (Gaj, Gersbach et al. 2013, Yang, Yang et al. 2014, Cong and Zhang 2015, Li, Li et al. 2018, Yumlu, Bashir et al. 2019). The CRISPR/Cas9 genome editing system exploits the microbial CRISPR/Cas adaptive immune system used to defend bacteria and archaea against viral infection and pathogenic plasmid DNA. In the natural world, this system functions though the integration of short DNA sequences originating from the pathogen into CRISPR loci, which are then used as a reference to identify future infection from the same pathogen. Future infection results in transcription of CRISPR RNA that effectively guides Cas nucleases with high specificity to the foreign viral/plasmid DNA for degradation via double stranded DNA (dsDNA) cleavage. In the laboratory setting, this system has been adapted for use in a wide variety of organisms and cell types to target highly specific DNA sequences with great precision, forever changing the course of scientific research.

For targeted binding and cleaving of double stranded DNA, spCas9 is required to complex with an RNA scaffold. This RNA scaffold is composed of two parts: a short CRISPR RNA (crRNA) molecule and a transactivating crRNA (tracrRNA) molecule. The mature crRNA serves to endow specificity to the Cas9 nuclease, which when complexed with the tracrRNA allows the shuttling of Cas9 to the specified target sequence. This crRNA/tracrRNA system has been simplified for experimental use by fusing these two components into one single-guide RNA (sgRNA) molecule. CRISPR systems cannot target any genomic sequence, however, and require short DNA motifs, protospacer-adjacent motifs (PAMs), for binding of the Cas/RNA guidance complex. One Cas nuclease, Cas9 from *Streptococcus pyogenes* (spCas9), has emerged as the workhorse nuclease for genome editing due to its flexibility of use and ability to target nearly any region of the genome due to its simplistic NGG PAM sequence (Cong, Ran et al. 2013, Jinek, East et al. 2013, Mali, Yang et al. 2013). Thus, any PAM adjacent DNA sequence can be targeted by spCas9 for the desired genome modifications allowing research

initiatives to be realized that were previously limited by the low efficiency and limited precision of previous genome editing techniques.

1.4.2 Mechanisms of DNA repair

To maintain genome stability within a given cell, the efficient and rapid repair of damaged DNA is paramount to maintaining the overall health of a given cell, its tissue, system, and ultimately, the organism as a whole. DNA damage is incurred through a number of factors, both endogenous and exogenous, causing either single strand or double strand breaks (DSBs); DSBs are particularly harmful to cell health. Endogenous factors inducing DNA damage are resultant of routine metabolic processes, which can generate reactive oxygen species (ROS), lipid peroxidation products, alkylating agents, and reactive carbonyl species, among others (De Bont and van Larebeke 2004). These endogenous factors result in an estimated 1×10^4 single strand breaks (SSBs) per cell per day, and although DSBs occurs at far less frequencies, SSBs themselves can precipitate DSBs through DNA replication stress and repair processes (Lieber and Karanjawala 2004, Hoeijmakers 2009). Furthermore, exogenous factors contribute to the formation of DSBs through exposure to factors such as ionizing radiation, ultraviolet radiation, chemical agents, and in the case of genome editing, the Cas9 nuclease.

Upon double strand cleavage of the targeted DNA sequence, DNA is repaired via two distinct pathways, homologous recombination (HR) and canonical nonhomologous end joining (NHEJ). The exact determinants of which pathway is utilized have not been fully elucidated, however, factors such as the complexity of DNA-lesion inflicted, genetic interactions/regulation, phase of the cell cycle, and kinetics of molecular recruitment to the site of damage play various roles in which repair pathway is utilized (Brandsma and Gent 2012). The two more influential factors appear to be cell cycle phase and binding kinetics of repair machinery. Whereas NHEJ can occur at any phase of the cell cycle,

HR is generally restricted to the S and G2 phases of the cell cycle by cyclin dependent kinases (CDKs) (Falck, Forment et al. 2012). These cell cycle phases intrinsically facilitate HR as sister chromatids are present during preparations for cell division to serve as homologous templates for repair (Brandsma and Gent 2012). Regarding the speed of repair mechanisms, NHEJ is initiated rapidly after identification of the DSB by the Ku70-Ku80 heterodimer (Ku), where it then binds to the free ends of DSBs. Depending on the nature of the DSB, several repair mechanisms are then quickly initiated to repair the break, the majority of which involve the nuclease, Artemis, and the DNA-PK catalytic subunit (DNA-PKcs) to modify the free ends for compatibility for subsequent ligation (Chang, Pannunzio et al. 2017). In contrast, the initial steps of HR are slow and more complex. Briefly, HR requires the binding of the Mre11-Rad50-Nbs1 (MRN) complex and CtBP-interacting protein (CtIP) to the DSB free ends for resection and generation of a 3'-single stranded DNA (ssDNA) tail. This is followed by the binding of replication protein A (RPA) to remove potential secondary structure, followed by the BRCA2-mediated replacement of RPA with RAD51, initiating a 'search' for homologous DNA on the sister chromatid to serve as a repair template. Thus, mere binding kinetics most likely serves as a primary determinate of which path is selected (Brandsma and Gent 2012).

1.4.3 CRISPR-mediated genome modifications

Depending on the desired genome modification, gene editing approaches take advantage of either the two intrinsic DNA-repair mechanisms, NHEJ and HR. In mammals, the more prevalent mechanism for DNA repair following a double strand break is NHEJ, however, this pathway is classically though to be more prone to error (Shibata, Conrad et al. 2011). However, this assumption may be an overstatement; NHEJ is utilized at far higher frequencies than HR in humans, repairs a wide range of

DSBs using multiple mechanisms, and error-free repair often remains undetected using current assay methods (Rodgers and McVey 2016). Nonetheless, with the high prevalence of NHEJ in the human system, sufficient levels of deleterious mutations resulting from base insertions and deletions facilitate the use of this pathway to knockout genes using CRISPR/Cas9.

Whereas NHEJ can result in random mutagenesis at a prescribed site, HR allows for the insertion of specific genetic modifications using a repair template. Under normal circumstance, sister chromatids serve as the repair template, however, the introduction of DNA sequences in the form of either ssDNA or dsDNA with homology to the target cut site allows for prescribed genome modification: single base substitutions and deletions, large insertions and deletions, complete transgene integration, and other genome modifications requiring high precision (Adli 2018). Thus, both NHEJ and HR allow a highly flexible system for the generation of a wide variety of genome modifications, the approach to which is determined by the end-user and customizable to their experimental aims.

1.5 Synthetic lethality

Synthetic lethality is the phenomenon in which the combined loss of normal functionality of two non-essential genes leads to cell death. Most commonly associated with synthetic lethality is loss-of-function mutations such as by gene knockout; however, alterations in gene expression levels/pharmacological inhibition (synthetic dosage lethal) (Reid, Du et al. 2016) and environmental changes can contribute to synthetic lethality (Chan, Pires et al. 2010). For example, in 2005, poly(ADP ribose) polymerase (PARP) was identified as a synthetic dosage lethal target for BRCA1/BRCA2 deficient tumors (Bryant, Schultz et al. 2005, Farmer, McCabe et al. 2005), leading to successful clinical application of PARP inhibitors. Although being a rather intuitive and rational approach to

identifying new cancer therapies, synthetic lethality has not advanced at a rapid pace until recently. Indeed, it was over 20 years ago that synthetic lethality was proposed as a strategy to identify drug targets (Hartwell, Szankasi et al. 1997). The slow pace is perhaps understandable as lethal genetic interactions are expectedly rare; genetic robustness is a necessary evolutionary principle (Hartman, Garvik et al. 2001, Masel and Siegal 2009). Genetic robustness is realized through the ability of cells and organisms to "buffer" mutational loads. To maintain homeostasis in the face of mutational burden, genetic redundancy in both gene function within distinct pathways and gene copy number itself stabilizes normal cellular function. Buffering mechanisms also exist in the form of phenotypic capacitors, such as hsp90 and its ability to maintain proper protein folding across multiple species, thereby masking potentially deleterious mutations (Bergman and Siegal 2003). Thus, until recently, efficiently detecting robust synthetic lethal interactions has proven difficult.

With the advent of next generation sequencing technologies combined with the advancements in genome-wide screening technologies in human cells, initiatives to identify synthetic lethal interactions in cancer cells are quickly gaining traction. The emergence of pooled RNA interference (RNAi) screens in human cells accelerated the discovery of essential genes in multiple cancer cell lines (Ngo, Davis et al. 2006, Silva, Marran et al. 2008). More recently, CRISPR-based pooled screens have overtaken the already ground-breaking RNAi-based screens due to their heightened sensitivity and greatly reduced off-target effects (Shalem, Sanjana et al. 2014, Smith, Greenside et al. 2017). Over the years since the adoption of these platforms, the technology has continued to improve in sensitivity and specificity and has uncovered lists of robust synthetic lethal interactions in multiple cancers and oncogenic pathways (Toledo, Ding et al. 2015, Wang, Yu et al. 2017).

Exploring synthetic lethality in the context of LAM presents a unique and exciting development in the field. With LAM being a monogenic disease, the confounding complexity of genetic interactions usually observed within cancers containing a high mutation load will be minimized; a potential shortfall of translating synthetic lethal targets found in genetically unstable cancer cells to the clinic. For instance, BRCA1/BRCA2 deficient tumors lacking functional TP53BP1 are rendered synthetically viable (Bunting, Callen et al. 2010), regardless of PARP inhibition. In contrast, the identification of a robust synthetic lethal target in LAM may apply widely to most LAM patients resulting in a high response rate to treatment. Furthermore, targets identified exhibiting synthetic lethal interactions may exhibit synthetic dosage lethality, thus, being more amenable to current strategies to quickly translate new treatments to the clinic.

While more than 95% of small molecule drugs are inhibitors of enzymes, this represents only a fraction of the protein-coding genes in the human genome. It has been estimated that of the approximately 20,000 protein coding genes within the human genome, only 600-1500 are ‘druggable’ using molecular inhibitors (Hopkins and Groom 2002, Griffith, Griffith et al. 2013). Thus, the vast majority of protein coding genes that potentially contribute to disease progression cannot be targeted using traditional pharmacological intervention strategies. Furthermore, although approximately 70% of the human genome is transcribed, only 2% encode protein-coding genes (Djebali, Davis et al. 2012). The expansive discrepancy between coding/non-coding transcripts suggests important physiological roles of non-coding RNA (ncRNA). Indeed, ncRNA has been shown to be highly influential in the regulation of gene expression, taking multiple forms to exact regulatory function; most prominently long non-coding RNA (lncRNA), small interfering RNA (siRNA), and micro RNA (miRNA) (Patil, Zhou et al. 2014). lncRNAs are generally over 200 nucleotides in length and are similar to mRNA as they feature 5’ caps and 3’ poly-adenosine tails. These ncRNA species have been implicated

in a wide range of physiological functions, such as regulating transcription, translation, mRNA processing, epigenetic regulation, and intracellular trafficking among other functions (Yao, Wang et al. 2019). In contrast, the range of direct regulatory functions of siRNA and miRNA is not as broad in scope; these ncRNA species are primarily have RNAi/gene silencing effects. As their names imply, siRNA and miRNA are far smaller RNA molecules than lncRNAs and, thus, may be easier to exploit pharmacologically than lncRNAs. siRNA and miRNA are similar in their function and share common molecular processing machinery; however, whereas siRNA typically target a specific mRNA molecule for silencing, miRNAs target multiple mRNAs (Lam, Chow et al. 2015). For instance, a single miRNA sequence can target multiple genes and have widespread affects within a specific pathway (Bartel 2009), can be expressed in a tissue-specific fashion (Ludwig, Leidinger et al. 2016), and regulate more than 60% of human protein-coding genes (Friedman, Farh et al. 2009). This makes miRNAs particularly interesting targets for therapeutic development. There are over 2000 unique miRNAs identified in the human genome, and many miRNAs have been characterized and exhibit diverse regulatory functions influencing many biological processes including cancer (Esquela-Kerscher and Slack 2006), viral pathology (Jopling, Yi et al. 2005), and metabolic disease (Fernandez-Hernando, Ramirez et al. 2013) among many others. However, the vast majority of miRNAs have not yet been characterized, presenting a vast frontier of potentially therapeutic targets for investigation.

The ability to regulate miRNA expression *in vivo* for therapeutic benefit is currently being investigated, leading to the initiation of a handful of clinical trials (phase I & II) (Rupaimoole and Slack 2017). Although multiple strategies have been investigated to modulate miRNA activity *in vivo*, the use of chemically modified oligonucleotides has come to the forefront to both enhance and inhibit miRNA activity: miRNA mimics and antimiRs, respectively. miRNA mimics are synthetic double stranded miRNA molecules

designed to imitate mature miRNA molecules and have proven useful in replacing tumor suppressive miRNAs in murine models of cancer, including lung cancer (Trang, Wiggins et al. 2011, Cortez, Valdecanas et al. 2014). In contrast, suppressing miRNA function is achieved using modified antisense RNA oligonucleotides known as antimiRs. AntimiRs function by directly binding to the mature strand of the target miRNA. Multiple chemical modifications can be added to antimiRs to protect them from nuclease degradation and increase their stability. One such chemical addition, 2′-O-methoxyethyl modification, results in a highly stable antisense oligonucleotide with strong binding affinity, known as antagomiRs (Krutzfeldt, Rajewsky et al. 2005).

A significant challenge that is faced in the development of RNA-based therapeutics (antisense oligonucleotides, miRNA mimics, and synthetic siRNAs) is efficient delivery. In the absence of a proper vehicle to deliver antimiRs, tissue dispersion is limited, and the oligonucleotides are quickly sequestered to the liver and kidneys for excretion. Furthermore, large doses of antimiRs (roughly 80mg/kg for antagomiRs) are required for adequate inhibition of target miRNAs (Li and Rana 2014). Thus, multiple strategies have been developed to aid in the delivery of antimiRs for therapeutic purposes. In particular, lipid nanoparticles have been designed to robustly generate encapsulated nanovectors of antimiRs of a uniform size while maximizing interactions *in vivo* (Campani, Salzano et al. 2016); these have proved most effective for *in vivo* delivery of antimiRs (Yung, Li et al. 2016), miRNA mimics (Beg, Brenner et al. 2017), and siRNAs (Sato, Matsui et al. 2018), with several multiphase clinical trials having been initiated. Excitingly, one such lipid-nanoparticle encapsulated siRNA therapeutic agent, patisiran, showed great promise throughout clinical trials and was FDA-approved on August 10th, 2018 for the treatment of hereditary transthyretin amyloidosis (Adams, Gonzalez-Duarte et al. 2018). Thus, with the successful implementation of this therapeutic strategy, it stands to reason that previously ‘non-

druggable' gene-products can now potentially be targeted using RNA-based therapeutics. This radically changes the approach modern medicine will take in the future, which is poised to provide highly specific and selective therapeutic regimes to treat a vast range of diseases.

1.6 Objectives, hypotheses, and summary of results

The CRISPR/Cas9 system has proven to be both the most effective and most accessible genome editing technology while generating minimal off-target mutations, and has been rapidly embraced by the research community (Veres, Gosis et al. 2014, Kim, Bae et al. 2015). Using CRISPR/Cas9 to modify the TSC2 locus in hPSC lines provides a unique opportunity to tease apart the function of TSC2. There is a wide array of pathogenic mutations in both *TSC1* and *TSC2* (over 680 and 1500 unique variants, respectively (Fokkema, Taschner et al. 2011)) with no mutational 'hot-spot' within coding regions or tendency toward a particular mutation type (e.g. small deletion, nonsense mutation) (Cheadle, Reeve et al. 2000, Crino, Nathanson et al. 2006, Au, Williams et al. 2007). Thus, I was afforded the freedom to generate isogenic disease models in hPSCs with high specificity to my objectives. Using this strategy (summarized in Figure 1.4), I explored TSC2 deficiency and its role in the pathogenesis of LAM and TSC by carrying out the following objectives: (i) generating TSC2 modified hPSC lines that display constitutive mTOR activation to model LAM, (ii) model TSC and LAM pathogenesis through transcriptomic profiling of differentiating the genome engineered hPSCs into the putative cells of origin believed to drive TSC (NPCs) and LAM (NCCs), and (iii) identify synthetic lethal genes in the context of TSC2 deficiency to more accurately target LAM cells using a genome-wide CRISPR knockout sgRNA screen.

In Chapter 3, I tested the hypothesis that *LAM can be accurately modeled through CRISPR/Cas9-mediated loss of functional TSC2 in NCCs*. In this chapter I detail

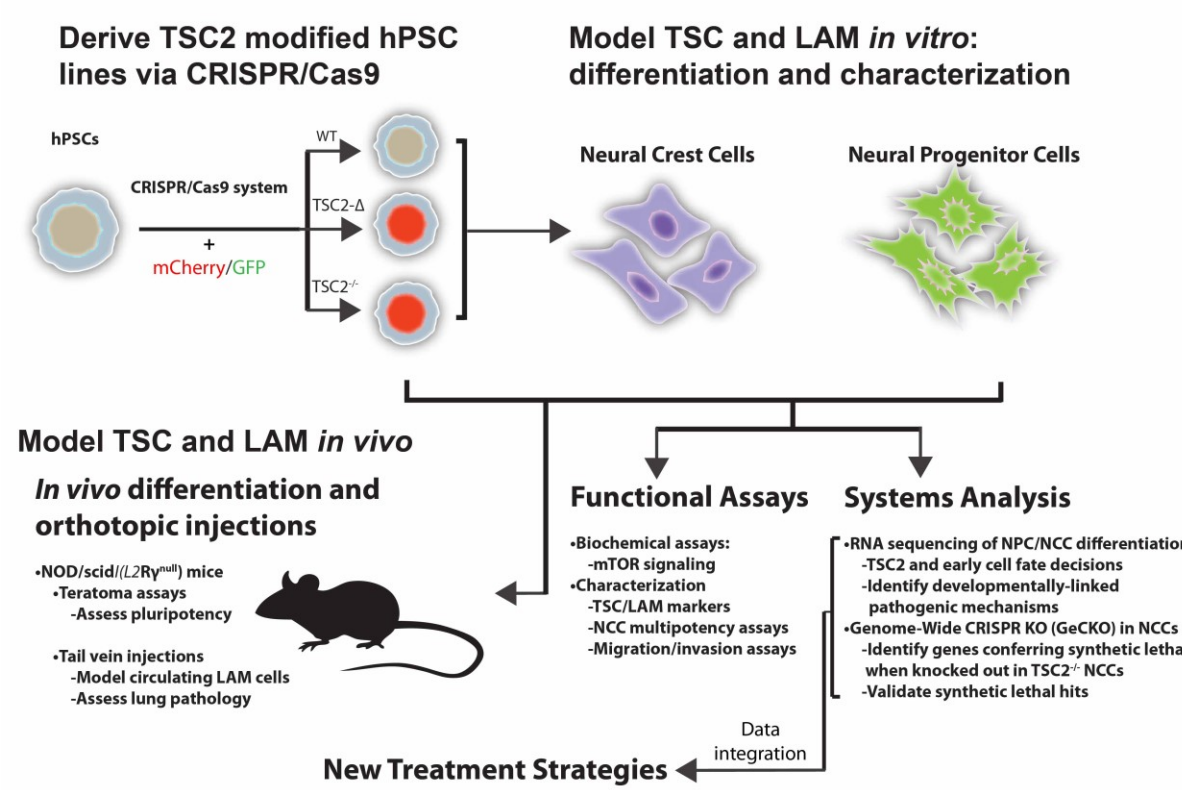

Figure 1.4: Overview of approaches utilized to model TSC and LAM.
To model TSC and LAM three major initiateves were empoyed. First, CRISPR-mediated genome editing of the TSC2 locus was performed to generate mutant alleles of TSC2 in 4 unique pluripotent stem cell lines. These cells were then used to model TSC and LAM by differentiating them to the putative cells of origin for neurological TSC and mesenchymal TSC and LAM, NPCs and NCCs, respectively. These differentiated cells were characterized and their ability to model TSC/LAM associated phenotypes was evaluated. The transcriptional landscape of NPC/NCC differentiation was then captured to identify TSC2-associated effects on early cell fate decisions and any potential pathogenic mechanisms at play. NCC cells were also subjected to a genome-wide CRISPR knockout screen to identify genes that are synthetic lethal in $TSC2^{-/-}$ cells. By integrating the RNA-seq datasets with the synthetic lethal CRISPR knockout screen, new therapeutic strategies can now be explored in depth. Furthermore, to develop a robust preclincal model of LAM, proof of principle experiments were performed through orthotopic tail vein injections of NCCs into NOD/SCID mice were performed to model circulating LAM cells and assess any pulmonary LAM-like disease manifestations.

the results of genomic engineering of hPSCs and subsequent modeling of LAM. Within this chapter, I tested the I employed a CRISPR/Cas9 genomic engineering approach to introduce inactivating mutations in the *TSC2* locus in four well-characterized hPSC lines; this allowed me to establish a robust modeling system permitting the analysis of phenotypes driven by *TSC2*-deficiency among multiple genetic backgrounds. In consideration of the sex-specificity of LAM, two male and two female hPSC lines were utilized in this study: WA01 (H1, male), WA07 (H7, female), and WA09 (H9, female) embryonic stem cells, as well as 168 1d2 induced hPSCs (168; male, healthy control derived, characterized in (Chen, Chang et al. 2017)). Using CRISPR/Cas9, I generated two unique *TSC2* mutant alleles utilizing both HR and NHEJ approaches. The first TSC2 mutant allele utilizes an in-frame deletion of *TSC2* exon 11 (Δ), a critical exon coding for the TSC1 binding domain. The second TSC2 mutant allele, targeting *TSC2* exon 3, is a knockout allele resulting in a complete ablation of TSC2. Both of these alleles result in constitutive activation mTORC1 signaling. I show that homozygous TSC2 null hPSCs (*TSC2*$^{-/-}$) maintain pluripotency, can be differentiated to multipotent NCCs, and accurately model multiple aspects of LAM, both *in vitro* and *in vivo*.

In Chapter 4, I investigate the hypothesis that *transcriptomic profiling of NCC and NPC differentiation will reveal novel insights into LAM and neurological TSC pathogenesis*. The resource of genome edited isogenic stem cells I generated underwent two parallel neural lineage induction protocols to favor the generation of either NPCs or NCCs. I, along with a postdoctoral fellow working closely on this project, Dr. Lisa Julian, show that in addition to the capability of *TSC2*$^{-/-}$ NCCs to model LAM, we show that *TSC2*$^{-/-}$ NPCs and neuronal/glial derivatives accurately model critical features of neurological TSC. We provide a comprehensive resource of RNA-sequencing (RNA-seq) datasets capturing the transcriptional landscape over a developmental time course of NPC and NCC induction using all four paired *WT* and *TSC2*$^{-/-}$ hPSC lines. Analysis

revealed wide-spread, developmental stage specific, transcriptional alterations in differentiating *TSC2*$^{-/-}$ cells, and a large-scale neuralization-induced cellular signaling response to proteostatic stress was detected. We demonstrated that this phenomenon is resolved in *TSC2*$^{-/-}$ NCCs, but is maintained in *TSC2*$^{-/-}$ NPCs. This resulted in long-term alterations in endosomal signaling, proteostasis and metabolic profiles that are characteristic of neurological TSC tumor cells. We further went on to show that *TSC2*$^{-/-}$ NPCs are selectively sensitized to proteasome inhibition with clinically relevant compounds irrespective of mTORC1 inhibition with rapamycin. This suggests this therapeutic approach holds promise as a stand-alone therapy or complimentary treatment to existing regimens for the neurological, but not mesenchymal, features of TSC.

In Chapter 5, I test the hypothesis that *a genome-wide CRISPR knockout screen in TSC2*$^{-/-}$ *NCCs will identify novel targets to specifically sensitize TSC2 deficient cells to death. WT* and *TSC2*$^{-/-}$ cell lines were differentiated to NCCs and the genome-wide CRISPR knockout (GeCKOv2) screen was performed to identify synthetic lethal genes in TSC2-null NCCs. Analysis of essential genes specific of *TSC2*$^{-/-}$ NCCs reveals pathways that have been previously investigated, with limited success, to target LAM. This assay, however, provides gene-level resolution to the vulnerable nodes within these pathways, allowing more precise targeting strategies to be developed in the future. Importantly, additional genes were identified that are synthetic lethal to TSC2-null cells with high specificity, providing a new frontier to explore previously unconsidered treatment strategies for LAM. Integration of the RNA-seq data from Chapter 4 with the synthetic lethal gene list will undoubtedly steer future experimental avenues for the treatment of LAM and TSC.

CHAPTER 2:

Materials and Methods

Chapter 2 contains methods described and adapted from:

Delaney, S.P., Julian, L.M., Pietrobon, A., Yockell-Lelièvre, J., Doré, C., Wang, T.T., Doyon, V.C., Raymond, A., Patten, D.A., Harper, M.-E., Sun, H., Stanford, W.L. (2019). “TSC2-deficiency potentiates a catabolic signaling switch that differentiates neural and neural crest lineage development and progressive disease manifestations”. bioRxiv, 683359. (Delaney, Julian et al. 2019)

Cell Culture

hESC lines H9 (WiCell WA-09), H7 (WiCell WA-07), H1 (WiCell WA-01) and induced pluripotent stem cell line 168 (Chen, Chang et al. 2017) were maintained on diluted Matrigel (BD Biosciences #354230) in Essential 8 (E8) media: DMEM/F-12 (Life Technologies #11330), 0.064µg/ml Ascorbic Acid 2 Phosphate Mg (Sigma #A8960), 14µg/ml sodium selenium (Sigma #S526), 0.1µg/ml FGF2 (Life Technologies #PHG0263), 19.4µg/ml human Insulin (Wisent #511-016-CM), 10.7µg/ml transferrin (Sigma #T0665), 0.002µg/ml TGF-β1 (Life Technologies #PHG9202), 543µg/ml NaHCO3 (Sigma #5761) (Chen, Gulbranson et al. 2011). Media was replaced daily, and PSCs were passaged every 4-5 days using 0.5mM EDTA.

NCCs were maintained on poly-L-ornithine (PLO; 0.0015%)/fibronectin (10µg/ml) coated growth surface in neural induction media (NIM): 1:1 DMEM/F-12: Neural Basal Media (Life Technologies #21103-049), 0.5x N2 Supplement (Life Technologies #17502-048), 0.5x B27 Supplement (Life technologies #17504-044), 5µg/ml human Insulin, 0.02µg/ml FGF2, 0.02µg/ml hEGF (Sigma #E9644), 0.5x GlutaMax (Life Technologies #35050061). Media was replenished every second day. For passaging, 90% confluent NCCs were dissociated with Accutase and plated at a density of 20,000-25,000 cells/cm^2, approximately every 4-6 days, until a maximum of 10 passages. NPCs were maintained on diluted Matrigel in NIM (Matrigel diluted 1/18 in DMEM-F12 for coating). For passaging, cells were dissociated with Accutase and plated at a density of 100,000-150,000 cells/cm^2, at the highest end of this range for the first 2 passages. Cells were supplemented with 10µM y-27632 (ROCKi; Tocris #1254) for the first passage 2h prior to harvest and for 48h post-plating. A half-media change was performed every 2-3 days with 75% of media replenished weekly. Cells were passaged when confluent, typically 2-3 weeks for the first 2 passages, and 1-1.5 weeks thereafter for a maximum of 10

passages, when growth of *TSC2*$^{-/-}$ NPCs markedly slows. All cells were maintained at 37°C, 5% O_2, 10% CO_2.

CRISPR/Cas9 Genome Editing

At 80% confluence, hPSCs were dissociated with Accutase (STEMCELL Technologies #07920). Cells were rinsed off of the growth surface and gently triturated. Accutase was then diluted 1:4 in PBS$^{-/-}$ (Life Technologies #14190-250) and then pelleted (250g, 5 min). Cells were resuspended in PBS$^{-/-}$ for counting. For each CRISPR/Cas9 transfection sample, 1 x 10^6 cells were aliquoted into microcentrifuge tubes and pelleted (250g, 5 min). Pellets were resuspended in 100µl electrolyte buffer E2 (Thermo Fisher #MPK10096) with either 1) 3µg of each *TSC2* exon 11 Cas9/sgRNA plasmid (Addgene #48139) (Ran, Hsu et al. 2013) for TSC2Δ modification, 2) 3µg of *TSC2* exon 3 Cas9/sgRNA plasmid with 1.75µg of TSC2 exon 3 ssODN donor sequence (Integrated DNA Technologies), or 3) 3µg AAVS1 Cas9/sgRNA with 3µg *AAVS1:mCherry* donor plasmid (Table S1, Appendix I: Supplemental Information). Samples were electroporated using the Neon Transfection System (Thermo Fisher MPK5000) using 100µl tips (Thermo Fisher #MPK10096) at 2 pulses of 1050v, 30ms pulse width. Electroporated cells were then plated onto diluted Matrigel at low density in E8 media containing 10µM ROCKi. Electroporated cultures were left to grow until individual colonies formed. Expanding colonies were picked into Matrigel coated 96-well cluster plates for PCR/restriction enzyme-based screening for edited cells. Karyotypic analysis revealed no chromosomal abnormalities in 7 of the 8 CRISPR/Cas9 edited cell lines utilized in this study (data not shown). Trisomy 12, a common chromosomal abnormality in hPSC cultures (Mayshar, Ben-David et al. 2010), was detected in a subpopulation of H1 *TSC2*$^{-/-}$ cells (35%) and is, thus, not related to CRISPR/Cas9 editing. sgRNA sequences utilized to modify the *TSC2* and *AAVS1* loci (Table S1) were

identified and high scoring (98 and 80, respectively) (Hsu, Scott et al. 2013) sgRNA sequences were selected to minimize potential off target cleavage events. To identify potential CRISPR/Cas9-induced off-target mutations in *TSC2*$^{-/-}$ hPSCs, the highest scoring predicted sgRNA off-target sites were identified using the CRISPOR algorithm (Haeussler, Schönig et al. 2016). Sequencing of these regions revealed no off-target cleavage induced mutations in any of the *TSC2*$^{-/-}$ hPSC lines (Table S2).

PCR Screening/Genotyping of CRISPR/Cas9 Edited Cells

Genomic DNA (gDNA) was harvested using QuickExtract solution (screening of CRISPR/Cas9 clones; Epicentre EPI-QE0905T) or NucleoSpin Tissue kit (routine genotyping; Macherey-Nagel #740952.25). OneTaq DNA polymerase (New England BioLabs #M0480) was utilized using primers flanking the genome editing target site of exon 3 of *TSC2*. Cycling parameters are as follows: Exon 3 - 94°C initial denaturation for 30s, 25x [94°C 20s, 56.5°C 30s, 68°C 30s], 68°C 5m, 4°C ∞, *TSC2*∆ - 94°C initial denaturation for 30s, 25x [94°C 20s, 55°C 30s, 68°C 1:30s], 68°C 5m 4°C ∞. PCR amplicons of *TSC2* exon 3 were then digested with PmeI restriction enzyme (New England BioLabs #R0560S) in OneTaq buffer for 1h at 37°C. Agarose gel electrophoresis was utilized to resolve digested amplicons indicating successful integration of 'stop codon' donor sequence or deletion of *TSC2* exon 11.

EB-NCC Differentiation

Day 0: Aggrewell plates (STEMCELL Technologies #34425, #34415) were prepared using pluronic solution (2% pluronic w/v in sterile H_2O), centrifuging at 1,300g for 5min, followed by 2 washes with prewarmed DMEM/F-12. Half differentiation culture volume of NIM +10μM ROCKi was added to each well and placed at 37°C until ready for use. One day prior to routine passaging, 10μM ROCKi was added to pristine

undifferentiated hPSCs 2h before dissociation with Accutase. Cells were incubated in Accutase for 10-20min, until cells were easily washed off of the growth surface. Cell suspension was diluted 1:4 in DMEM/F-12 and pelleted at 250g for 5min. Cells were resuspended in NIM +10μM ROCKi and counted. Appropriate volumes of cell suspension were added to Aggrewells to generate 750cell EBs, and wells were topped up to 5ml (6 well format) or 2ml (24 well format) with NIM+ROCKi. Aggrewell plates were centrifuged at 100g for 3min and placed at 37°C, 5% O_2, 10% CO_2. Day 1: 24h later, all media was carefully removed from each well to minimize disturbing newly formed EBs in microwells. NIM +10μM SB431542 (Tocris: 1614) and 500nM LDN-193189 (Stemgent: 04-0074) (NIM+SB/LDN) was carefully added to each well and Aggrewell plates were returned to 37°C, 5% O_2, 10% CO_2. Days 2-4: Half media changes with NIM+SB/LDN. Day 5: EBs were dislodged from microwells using a P1000 and transferred to 15ml conical tubes to allow EBs to gravity settle. Media was refreshed with NIM+SB/LDN, and EBs were plated onto PLO/fibronectin coated plates at a density of 40 EBs/cm^2. EBs were placed at 37°C, 5% O_2, 10% CO_2 and dispersed evenly over the growth surface. Days 6-11: Media was replaced every other day with NIM+SB/LDN. Day 12: Neuralized adherent EB clusters were carefully washed off of the growth surface using a P1000, and media was aspirated. Cells were dissociated with Accutase and passed through a 40μM mesh filter to remove any remaining cell clumps. Accutase was diluted 1:4 with DMEM/F-12, and enriched NCCs were pelleted (250g, 5min), resuspended in NIM, and seeded onto PLO/fibronectin coated culture ware at a density of 25,000-30,000 cells/cm^2.

NCC Neural/Glial/Mesenchymal Differentiation

At routine passaging, maintenance NCCs were seeded at a density of 20,000-25,000 cells/cm^2 onto PLO/fibronectin coated tissue culture ware in NIM. Differentiation

towards neural, glial, and mesenchymal fates was initiated 24h later. Neural: NIM was replaced with basal NIM (bNIM; NIM without insulin, hEGF, and FGF2) supplemented with 50ng/µl BMP2 (STEMCELL Technologies #78135). Glial: NIM was replaced with bNIM supplemented with 20ng/ml Heregulin-β1 (STEMCELL Technologies #78071) for 5 days. Media was then changed to bNIM supplemented with 5µM Forskolin (STEMCELL Technologies #72112) and 10% FBS (Life Tech #12483-020). Mesenchymal: Adipocyte differentiation was carried out using the MesenCult Human Adipogenic Differentiation kit (STEMCELL Technologies #05412) according to the manufacturer's instructions. Smooth muscle cell (SMC) differentiation was carried out by replacing NIM with bNIM supplemented with 10ng/ml TGF-β3 (Sigma #SRP3171). After 72h, media was replaced with 1:1 blend of bNIM and Media 231 (Life Technologies #M-231-500) supplemented with smooth muscle growth supplement (SMGS; Life Technologies #S00725) and 10ng/ml TGF-β3. After a total of 7 days, media was replaced with Media 231 supplemented with SMGS and 10ng/ml TGF-β3. Differentiating SMCs were passaged at 90-95% confluence when needed. All differentiations were carried out for 14 days, with media replacement every other day. Cultures were fixed with 3.7% paraformaldehyde (PFA) at endpoint for analysis. Oil red staining of adipocytes was carried out as previously described (Mehlem, Hagberg et al. 2013).

Monolayer-NPC Differentiation

hPSCs were passaged as intact colonies, maintained on Matrigel, and neural lineage differentiation was initiated when the cultures were 90%+ confluent to promote neuroepithelial induction (Tchieu, Zimmer et al. 2017), typically 3-5 days post-passage. Neuroectoderm differentiation was initiated by replacing E8 with KSR media containing 10µM SB and 500nM LDN. KSR media (for 500mL) contains 414mL of Knockout-DMEM (Life Tech, #10829-018) with 15% Knockout-serum replacement (Life Tech, #10828-

028), 5mL of 100X Glutamax (Thermo Fisher, #35050061), 5mL of 100X MEM-NEAA (Gibco, #11140-050), 500uL β-ME (Thermo Fisher, #21985023), and 500µL Gentimicin (Wisent, #450-135). Media was changed daily as KSR+ SB & LDN from days 0-3. At day 4, N2 media was added in increasing amounts in the following ratios: days 0-3 100% KSR, days 4-5 75:25 KSR:N2, days 6-7 50:50 KSR:N2, days 8-9 25:75 KSR:N2, days 10-11 100% N2, harvest at day 12. LDN supplementation was maintained at all days, while SB was included only on days 0-3. N2 media composition is as follows (for 500mL): 486.5mL of DMEM-F12, 15% glucose, 5mL N2 supplement, 20µg/mL human insulin, 2.5mL Hepes (Life Tech, #15630080), and 500µL Gentimicin. Cells were maintained at 37°C, 5% O_2, 10% CO_2 during differentiation.

NPC-neuronal Differentiation

hPSC-derived NPCs at passage 0-2 were harvested with Accutase and plated on PLO/Laminin-coated glass coverslips (Thermo Fisher, #12-545-101) at a density of 10,000-20,000 cells/cm^2. For substrate coating, coverslips were first sterilized in EtOH and washed extensively in sterile 1X $PBS^{-/-}$, then placed in plastic wells and submerged in PLO (Sigma, P4957) solution (15% of 0.01% stock in sterile H_20) for 2h at room temperature or overnight at 4°C. PLO was aspirated and immediately replaced with 25µg/mL laminin in 1X $PBS^{-/-}$, incubated at 37°C for 2h and stored at 4°C for up to 1 week or at -20°C for long-term storage. Differentiation to neuronal cultures was performed as described (Costa, Aigner et al. 2016) with some modifications. Briefly, differentiation was induced when cells were ~70% confluent, typically 2-3 days post-plating, by replacing media with Neuronal differentiation media, containing 50:50 DMEM-F12: Neurobasal, 2.5mL N2 supplement and 5mL B27 supplement per 500mL, and 20ng/mL each of BDNF (Peprotech, 450-02) and GDNF (Peprotech, 450-10), 500µg/mL Dibutyryl cAMP (Sigma, #D0627), and 200nM L-ascorbic acid (Sigma). Cells were also

transferred to normoxic conditions at the time of differentiation induction (37°C, 5% CO_2). Cells were fed twice weekly by replacing 75% of spent with fresh media. Cells were differentiated for 4-6 weeks prior to collection for functional assays or fixation for immunohistochemistry (IHC). Cell fixation was performed by removing all but 250µL of cell media from each well (24-well format) and adding 250µL of 8% PFA, to limit loss of fragile neurite networks. Cells were fixed on ice for 1h, and then at room temperature for 30 minutes before carefully removing PFA, washing gently once in 1X $PBS^{-/-}$ and stored at 4°C in 1X $PBS^{-/-}$.

Whole-cell Patch Clamp Recording

Cells were collected from glass coverslips in 24-well culture plates. Before transfer to the recording chamber in an upright Nikon Eclipse E600FN microscope, culture medium was gradually changed to oxygenated artificial cerebral spinal fluid (ACSF) containing (mM): 124 NaCl, 5 KCl, 1.25 NaH2PO4, 1.2 MgSO4, 26 NaHCO3, 2 CaCl2, and 10 glucose, in 30 mins at room temperature (Gunhanlar, Shpak et al. 2018). Whole-cell patch clamp recordings were obtained from differentiated neurons at 4-6 weeks following the initiation of the differentiation procedure (Sun, Takesian et al. 2018). Patch electrodes with a resistance of 5-10 M were prepared from borosilicate glass capillaries with a Narishige micropipette puller (Model PC-100, Tokyo, Japan). Pipette intracellular solution contains (mM): 130 K-Gluconate, 2 MgCl2, 0.6 EGTA, 10 HEPES, 5 KCl, 2 ATP-Mg(Na2), pH 7.3. Data were collected using MultiClamp 700B amplifier. Signals were filtered at 2kHz, digitized at 20kHz by a Digidata 1500 interface, acquired by the pClamp 10.7 software, and analyzed with the Clampfit 10.7 program (Molecular Devices). To characterize the intrinsic membrane properties of cells, hyper- and depolarizing rectangular pulses of 500-1000ms duration were applied. Spontaneous EPSCs (sEPSCs) were recorded at a -60mV holding potential for at least 10 mins to

isolate AMPAR mediated currents from NMDAR mediated currents. Additionally, picrotoxin (PTX) (100M), a GABAA blocker, was administered to further pharmacologically isolate AMPAR mediated currents. sEPSC events were detected automatically using Clampfit 10.7, and frequency and amplitude histograms were constructed using this program. All events were confirmed visually on the basis of the rise and decay times. All electrophysiology data were expressed as mean ± SEM. Data was first tested for normality using the Shapiro-Wilk normality test. Then, statistical significance was assessed using a one-way ANOVA test followed by post hoc Bonferroni test, and a Mann-Whitney rank test for comparisons of data that were not normally distributed. Statistical significance differences are established as $p<0.05$.

Teratoma Assays and derivation of tSMC lines

Teratoma assays were performed as previously described (Chang, Lavoie et al. 2013). Briefly, hPSCs were harvested using Accutase 1 day prior to routine passaging, diluted 1:4 in DMEM/F-12, and pelleted (250g, 5min). Cells were resuspended in E8 media and counted. 1 x 10^6 cells were aliquoted, pelleted, and resuspended in 100µl ice cold Matrigel for each planned injection. Matrigel embedded cells were injected intramuscularly into the tibialis anterior of *NOD/SCID* mice. Once large visible leg tumors were observed (8-12 weeks), mice were sacrificed and teratomas were excised and fixed in 10% formalin. Teratomas were then processed for paraffin embedding, sectioned, and stained with hematoxylin and eosin for analysis. To generate tSMC lines, following excision, teratomas were dissociated with dispase (Thermo Fisher # 17105041; 2U/ml in $PBS^{-/-}$) for 1h at 37°C. Dissociated cells were plated and maintained on Matrigel coated tissue culture ware with Media 231 (Thermo Fisher # M231500) supplemented with smooth muscle growth supplement (Thermo Fisher #S00725).

Imaging Flow Cytometry

hPSCs were dissociated with Accutase, diluted 1:4 in $PBS^{-/-}$, and then pelleted (250g, 5min). Cell pellets were resuspended in 3.7% PFA and fixed for 15min at room temperature. Fixed cells were washed twice with excess $PBS^{-/-}$, followed by permeabilization in ice-cold 90% methanol for 30min on ice, followed by 2 washes in staining buffer: 1% BSA (Wisent # 800-095-EG), 0.1% Triton-X (BioShop #TRX777) in $PBS^{-/-}$. Samples of 5 x 10^5 cell were aliquoted into 5ml round bottom tubes and blocked in excess staining buffer for 30min on ice. Cells were pelleted and resuspended in 100µl of 1:100 TSC2 or Cas9 antibody (Table S3) diluted in staining buffer and incubated at room temperature for 1h. Cells were washed in excess blocking/staining buffer, and resuspended in 100µl of 1:1000 secondary antibody diluted in staining buffer and incubated for 30min at room temperature, shielded from light. Cells were washed once with excess staining buffer and resuspended in 200µl containing 2µg/ml Hoechst 33342 (Invitrogen #H3570) diluted in $PBS^{-/-}$. Single stain and no stain controls were prepared in parallel. Cells were passed through a 40µm cell strainer (Falcon #352340) prior to imaging on the Amnis ImageStreamX Imaging Flow Cytometer.

Flow Cytometry

EB-NCC cultures were rinsed with media to remove neuralized adherent EB-clusters using a P1000, prior to harvesting with Accutase. Cas9/mCherry knockout assays (Chapter 5) were carried out as follows: cells were passed through a 40µm filter, prior to staining with1:2000 diluted Sytox Blue nucleic acid stain (Thermo Fisher #S11348). Samples were placed on ice until measured. For p75 measurements in Chapter 4, matching undifferentiated hPSC lines were harvested in parallel with Accutase. Cells were gently lifted via trituration, diluted 1:4 in DMEM/F-12, and passed through a 40µm cell strainer. Cells were pelleted, resuspended in NIM, counted, and 5 x

10^5 cells were aliquoted into round bottom tubes for staining. Cells were blocked in excess FACs buffer (4% FBS [Life Tech #12483-020], 100μM EDTA in $PBS^{-/-}$) for 15min on ice. Cells were pelleted and resuspended in 100μl 1:20 diluted p75-Alexa Fluor 647 conjugated antibody (BD Biosciences: #560326) in FACS buffer. Cells were incubated for 30min on ice, shielded from light. Cells were washed once with excess FACS buffer and resuspended in 500μl of 1:2000 diluted Sytox Blue nucleic acid stain in FACS buffer. Mouse IgG_1-Alexa Fluor 647 isotype controls (BD Biosciences #557783) and no stain controls were prepared in parallel. Cells were passed through a 40μm filter and immediately measured using the BD Biosciences LSR-Fortessa flow cytometer and analyzed with FloJo (version 10.5.3).

Western Blotting

Cell lysates were collected after washing cells with ice cold $PBS^{-/-}$, followed by brief incubation on ice with RIPA cell lysis buffer: 150mM NaCl, 1% Triton-X, 0.1% SDS, 50mM Tris, 1x PhosSTOP phosphatase inhibitor mix (Sigma # 4906845001), 1x complete protease inhibitor mix (Sigma 11873580001). Cells were scraped and transferred to microcentrifuge tubes and rotated at 4°C for 30min, followed by centrifugation at 16,000g at 4°C for 20min to generate cleared lysates. Lysates were stored at -80°C. After thawing for analysis, protein concentrations were normalized and probed via western blot, imaged using the Odyssey Classic Infrared System (LI-COR Biosciences), and analyzed using standard densitometry techniques using FIJI (Schindelin, Arganda-Carreras et al. 2012). Antibodies utilized for western blot can be seen in Table S3.

RT-qPCR

RNA was harvested from cultures using the Nucleospin RNA kit (Machery Nagel #740955) and RNA was reverse transcribed using Superscript II the kit (Thermo Fisher #18064-014). Samples were then amplified using SYBR Green mastermix (Roche #4707516001) and gene-specific primers using the LightCycler 480 Platform (Roche). Log2FC was calculated using the Pfaffl method (Pfaffl 2001) with GAPDH as the housekeeping reference gene.

Live Cell Staining

NPC or NCCs were dissociated on day of routine passaging and seeded into 96-well cluster plates for live high content imaging assays. NPCs were seeded at a density of 20,000 cells per well and NCCs were seeded at a density of 7,500 cells per well. 24h after plating media was replenished and, if applicable, cells were administered treatments of rapamycin or chloroquine. After 24h incubation (or 72h for post-rapamycin Lysosensor staining of NPCs), cells were prepared for live imaging by washing with media, followed by the addition of live cell dyes in NIM with 2µg/ml Hoechst 33342: 1:1000 Lysosensor Green DND-189 (Thermo Fisher #7535), 1:2000 Cyto-ID Autophagy Detection dye (ENZO # ENZ-51031), 20nM Mitotracker Deep Red FM (Thermo Fisher #M22426), or 25µM carboxy-H2DCFDA (Thermo Fisher #I36007). Cells were incubated with live cell dyes for 30min under maintenance conditions. Cultures were then carefully washed three times for 5min with NIM, and media was replenished with appropriate treatments for imaging. Imaging for high content quantification was performed using the Thermo Fisher ArrayScan VTI High Content Screening (HCS) platform, utilizing the live cell chamber at 37°C, 5% CO_2. Image analysis was facilitated by HCS Studio software (version 6.5.0).

Cytotoxicity Assays

Cells were seeded and grown following maintenance conditions for 24 hours. For cytoxicity assays described in Chapter 4, cells were treated with 100nM Rapamycin (Calbiochem #553211) and/or 10μM Chloroquine (Sigma, C6628) and/or various concentrations of Bortezomib (Adooq Bioscience #A10160) or Carfilzomib (Adooq Bioscience #A11278) as well as 0.1% DMSO for 24 or 48 hours. For cytotoxicity screening described in Chapter 5, cells were treated with various concentrations of FIIN2, NVP-BGJ398, ACTB-1003, BMS-345541, Nintedanib esylate, LOXO-101 (Adooq #s A12357-5, A15194-5, A14431-5, A11318-5, A16197-10, A15974-5, respectively) or 0.1% DMSO for 72h. In all cytoxicity assays, cells were then stained with 2μg/mL Hoechst and 10nM Sytox Green (Thermo Fisher #S7020) for 30 minutes. Imaging was performed using the Thermo Fisher ArrayScan VTI HCS platform, utilizing the live cell chamber at 37°C, 5% CO2. Image analysis was facilitated by HCS Studio software, in which cell death was assessed using the percentage of Sytox Green positive cells in a given population.

mTOR Stress Tests

Hypoxia: hPSCs were treated as follows to assess mTOR dysregulation. 2 days prior to normal passaging, hPSC cultures were incubated either at 37°C, 1% O_2, 10% CO_2 (stress condition) or at 37°C, 5% O_2, 10% CO_2 with and without the addition of 100nM rapamycin. After 6h of incubation, cell lysates were collected on ice in the presence of protease and phosphatase inhibitors for analysis via western blot. Starvation: NCCs were treated as follows to assess mTOR dysregulation. NCCs were seeded into 96 well tissue culture plates at maintenance seeding densities in triplicate. 24h after seeding, cultures were rinsed once with $PBS^{-/-}$ and media was replaced with NIM, NIM +100nM rapamycin, or $PBS^{+/+}$ (Thermo Fisher #14040133). Cells were

incubated under maintenance conditions for 24h, followed by 3.7% PFA fixation for 10min. Cells were then stained as detailed below with P-S6 antibody (Table S3) for analysis on the ArrayScan VTI HCS platform and Studio software.

Immunofluorescence

Unless specified for specific antibody targets, all immunostaining was performed as follows: Cells were fixed with 3.7% PFA for 15min at room temperature after removing media, followed by 3 washes with $PBS^{-/-}$. Cells were permeabilized and blocked in excess immunofluorescence staining buffer (IF-SB; 1% BSA, 0.1% Triton-X in $PBS^{-/-}$) for 1h at room temperature. IF-SB used for blocking was removed, and IF-SB containing diluted primary antibodies (Table S3) was added to each sample and incubated overnight at 4°C. Samples were then washed three times for 10min before the addition of secondary antibody diluted 1:1000 (Table S3) in IF-SB. Samples were incubated in secondary antibody solution for 1h at room temperature, followed by three washes with $PBS^{-/-}$, in which 2µg/ml Hoechst 33342 was included in the final wash step. Images were captured using the Zeiss Observer A1 or Observer Z1 fluorescence microscopes or captured for high content analysis using the ArrayScan VTI HCS platform and Studio software.

Alterations to the immunostaining protocol: HNK-1 cell surface staining was completed after PFA fixation, but prior to cell permeabilization. For HMB45 staining, samples were permeabilized using 100% ice-cold methanol for 10min on ice following PFA fixation. For LAMP1 and LC3ß immunostaining, cells were fixed in ice-cold 100% methanol prior to proceeding with blocking and staining.

Proteostat Staining

Cells were fixed with 3.7% PFA for 15min at room temperature, followed by three washes with $PBS^{-/-}$. Cells were then permeabilized with 0.1% Triton-X diluted in $PBS^{-/-}$ for 10min, followed by three washes with $PBS^{-/-}$. Proteostat aggresomes detection dye (ENZO #ENZ-51035-K100) was diluted 1:2000 in $PBS^{-/-}$ containing 2µg/ml Hoechst 33342. Samples were incubated for 30min at room temperature, followed by three washes, 10min each, with $PBS^{-/-}$. Images were captured using the Zeiss Observer A1 or Observer Z1 fluorescence microscopes, or captured for high content analysis using the ArrayScan VTI HCS platform and Studio software.

Intratrachael/Tail Vein Injections and Immunohistochemistry

For each injection, 2.5×10^5 *in vitro* differentiated NCCs were injected intratracheally or into the tail vein of *NOD/SCID* mice. At time of sacrifice, mice were anesthetized with euthanyl and lungs were inflated and fixed under constant pressure using 3.7% PFA as previously described (Ionescu, Alphonse et al. 2012). Lungs were excised maintaining internal lung pressure and incubated at room temperature overnight in 3.7% PFA. Lungs were then transferred to a 20% sucrose solution for 24h before OCT media embedding and storage at -80°C. Frozen lungs were sectioned at 10µm onto glass slides and processed for immunostaining. Lung sections were processed for IF as described above in “Immunofluorescence” section. IHC was performed as follows: sections were incubated in ice-cold acetone, followed by 3x washes in $PBS^{-/-}$ for 5min each, and incubation with 0.3% H_2O_2 for 15min. Sections were washed 3x n $PBS^{-/-}$ followed by 1h blocking in IF-SB. Sections were then incubated overnight in primary antibody diluted in IF-SB. Sections were then rinsed 3x in $PBS^{-/-}$ and stained with HRP polymer (Abcam #2891). Sections were rinsed 3x in $PBS^{-/-}$, prior to DAB and

hematoxylin staining, dehydration, and mounting. Antibodies used for IHC can be seen in Table S3.

Motility Assay

NCCs were dissociated for plating on day of routine passaging and seeded into 96-well cluster plates at increasing densities of 1,000 to 6,000 cells per well in NIM. 24h later, media was replenished and 100nM rapamycin or DMSO was added to appropriate samples. Time lapse imaging (15 minute intervals over 6h) of mCherry or CellTracker Deep Red (Thermo Fisher #C34565) signal was performed utilizing the Thermo Fisher ArrayScan VTI HCS platform, utilizing the live cell chamber at 37°C, 5% CO_2. CellTracker Deep Red staining was performed according to the manufacturers recommended protocol. Cell tracking image analysis was performed on wells displaying 30-60% confluence, using HCS Studio software.

RNA-Seq sample preparation and sequencing

Cells were dissociated using Accutase and diluted 1:4 in $PBS^{-/-}$ prior to pelleting (250g, 5min). Cells were resuspended in $PBS^{-/-}$ and total cell count was noted. Cells were pelleted (250g, 5min) and resuspended in TRIzol reagent (Thermo Fisher # 15596026). Samples were stored immediately at -80°C until processing for RNA extraction. RNA extraction was performed in batches including all differentiation time points within a *WT* and *TSC2*$^{-/-}$ cell line pairing. RNA extraction was performed according to the manufacturer's protocol followed by DNase digestion (Qiagen #79254) and ethanol precipitation of RNA. RNA concentration was estimated using NanoDrop 2000 spectrophotometer (Thermo Fisher ND-2000) and ERCC spike in (Thermo Fisher #4456740) was added, normalizing to cell number. Quality control of RNA integrity and total RNA concentration was then measured using the Bioanalyzer Eukaryote Total RNA

Pico kit (Agilent #5067-1513). Only samples with RIN values of 8.0 or greater were submitted for sequencing. Total RNA H9 *WT* and *TSC2*$^{-/-}$ NCC sample libraries were prepared with ribosome depletion (Illumina # 20020598), all other sample libraries were prepared using the TruSeq Stranded mRNA kit (Illumina #RS-122-2101). All samples were sequenced on the Illumina NextSeq500 or NovaSeq6000 platform (Illumina) generating at least 30 million reads per sample. Reads were assigned to transcripts from GENCODE release 27 using Salmon (Patro, Duggal et al. 2017) and differentially expressed genes were identified using DESeq2 v1.20.0 (Love, Huber et al. 2014). DESeq2 analysis modelled fold change between time points using the cell line as an independent factor (using the model '*~cell_line + condition*'), and fold changes were calculated using lfcShrink function, applying the apeglm method (v 1.2.1) (Zhu, Ibrahim et al. 2018). Gene ontology enrichment analysis was performed using clusterProfiler R package (Yu, Wang et al. 2012). Time course gene expression clustering was performed using Dirichlet process Gaussian process mixture model using the DP_GP_Cluster Python package (McDowell, Manandhar et al. 2018) to cluster TPM values for genes that show a significant expression difference (using a 5% FDR threshold) between sequential timepoints. Separate gene lists were calculated for NPC and NCC time courses, and expression patterns were clustered separately for *WT* and *TSC2*$^{-/-}$ cells within each protocol. Datasets are available on GEO, accession #GSE137614.

Statistical analysis

Sample data acquired from H9, H7, H1 and 168 hPSCs and their derivatives were considered biological replicates within a given assay or experiment. Multiple biological replicates from each cell line were utilized within a given experiment whenever possible. When data were normalized to *WT* samples, test sample data were normalized to their respective isogenic *WT* control before determining mean values, etc., of

biological replicates. Unless otherwise indicated, statistical significance was assessed using a one-way ANOVA test followed by Bonferroni post hoc analysis for multiple comparisons to determine statistical significance between experimental groups. When only 2 groups were compared a student's t-test was used.

GeCKOv2 Lentiviral Library Preparation

The human GeCKOv2 libraries A & B (Addgene #1000000049) (Sanjana, Shalem et al. 2014) were diluted to 5ng/µl in sterile ddH2O for electroporation. 2µl of Library A or B were added to 25µl of 5-alpha electrocompetent cells (New England Biolabs #C2989K) were added to a prechilled 1mm electroporation cuvette, and cells were electroporated (4 per GeCKOv2 library) using the GenePulser electroporator (Bio-Rad) using the following parameters: 1.7 kV, 200 Omega, and 25 µF. 1ml of SOC outgrowth media (New England Biolabs #B9020S) was added immediately following electroporation, and cells were transferred to 17mm x 100mm round-bottom culture tubes for recovery in a bacterial shaker 250rpm at 37°C for 1h. Each respective library was then combined. 10µl of recovered bacteria from each library was diluted into 1ml of SOC. 20µl of or diluted cells were spread onto pre-warmed ampicillin LB-agar plates. Plates were incubated overnight at 32°C. 1ml of LB was added to each plate and bacterial colonies were scraped, combined, and pelleted at 6,000g for 5min, and then weighed. One maxiprep (Thermo Fisher # K210016) column per 500mg bacteria was utilized to isolate plasmid DNA.

Lentivirus production and determination of functional titer

HEK 293T cells were seeded in 150mm tissue culture dishes (Corning # 353025) for transfection. Cells were cotransfected with second-generation lentiviral pachaing plasmids pMD2G, pPAX2, and the GeCKOv2 libraries A&B, lentiCas9-Blast (Addgene

#52962), or lentiGuide-Puro (Addgene #52963) in the presence of polyethylenimine (4.1 µmol/L) and NaCl (2.25×10^{-4} mol/L). GeCKOv2 and lentiCas9-Blast virus was produced using 40x15-cm dishes for each virus construct, and lentiGuide-Puro virus with 1x15cm dish. Supernatant containing the virus was collected at 48h after transfection and immediately aliquoted and stored at -80°C. Functional titers were established as follows: Virus supernatant were thawed in warm rapidly in warm water. *WT* or *TSC2*$^{-/-}$ NCCs were plated into 6x PLO/Fn coated 100mm dishes at 1.2×10^6 cells per dish including 500, 250, 125, or 62.5µl of virus supernatant, leaving 1 dish as selection control and 1 dish as a no treatment control. 24h post transduction, transduced cells and one not treatment control were administered selection (1µg/ml puromycin (Thermo Fisher # A1113803) or 5µg/ml blasticidin (InvivoGen #ant-bl-1)) for 48h. Cells were then harvested and counted, comparing no treatment control to transduced samples to establish the number of functional virus particles per µl of virus supernatant.

Synthetic Lethal Screen

NCC were differentiated on a massive scale in the same manner as described above. For optimal GeCKOv2 transduction at 700x representation, 2.9×10^8 NCCs were combined with enough virus supernatant to allow 8.7×10^7 NCCs to be transduced (30% of seeded), and seeded into PLO/Fn coated 150mm dishes (7.595×10^6 NCCs in 16.5ml NIM media per dish). 2x100mm dishes were seeded in addition to determine experimental MOI for representation calculations (# cells/123,411 gRNAs). 24h post transduction, media was changed to NIM with 1µg/ml puromycin (1x100mm dish was not selected with puromycin) and NCCs were selected for 72h. NCC within the 100mm dishes were counted to determine transduction efficiency (30-50% ideal, at least 700x representation). For d0 baseline time points at least 61.7×10^6 NCCs were collected and pelleted at 500g for 5min, and then placed at -80°C for storage. Media was replenished

in remaining cultures, which were maintained per usual in 150mm dishes, ensuring at least 1000x representation for 14 days. At endpoint, cells were harvested using Accutase, counted, and pelleted at 500g for 5min, and stored at -80°C for downstream processing for deep sequencing of genomic integrations.

Genomic DNA isolation: Synthetic Lethal Screen

Frozen samples were divided into 30-50 x10^6 per 15ml centrifuge tubes. For each tube, 6 ml of NK Lysis Buffer (50 mM Tris, 50 mM EDTA, 1% SDS, pH 8) and 30 µl of 20 mg/ml Proteinase K (Qiagen #19131) were added to the cell sample and incubated at 55 °C overnight in a water bath. The following day, 30 µl of 10 mg/ml RNAse A (Qiagen #19101, diluted in NK Lysis Buffer to 10 mg/ml) was added to the lysed sample. Tubes were then inverted at least 25 times and incubated at 37 °C for 30 minutes. Samples were then immediately cooled on ice before addition of 2 ml of pre-chilled 7.5M ammonium acetate (Sigma #A1542) to precipitate proteins. Stock solutions of 7.5M ammonium acetate were made in sterile ddH2O and kept at 4 °C until use. Samples were then vortexed at high speed for 20 seconds and followed by centrifugation at ≥ 4,000 x g for 10 minutes. Supernatant was then carefully decanted into a new 15ml centrifuge tube. 6 ml of 100% isopropanol was then added and inverted at least 50 times before centrifugation at ≥4,000 x g for 10 minutes. The supernatant was then discarded and pelleted DNA was washed twice with 70% ethanol (≥4,000 x g for 1 minute for each wash). Ethanol was carefully removed and DNA pellets were air dried for 10-20min. DNA was resuspended in 1x TE buffer (Sigma #9285) and incubated at 65°C for 1h and left at room temperature overnight to fully dissolve. The gDNA concentration was measured using the Nanodrop Microvolume Spectrophotometer (Thermo Scientific).

Library Preparation and Sequencing Parameters: Synthetic Lethal Screen

PCR1: To maintain proper representation for deep sequencing of lentiviral integrations, 450µg of gDNA per time point was used as a template and split into 50µl reactions using the NEBNext® Ultra II Q5 Master Mix (New England Biolabs #M0544), using the GeCKOv2 Adaptor_F and GecKOv2 Adaptor_R primers (Table S1), using the manufacturers recommended reaction composition and thermocycling parameters. Cycling parameters were as follows: 98°C initial denaturation for 30s, 13x [98°C 10s, 65°C 75s,], 65°C 5m, 4°C ∞. For each time point, PCR reactions were combined into a single 15ml centrifuge tube and mixed well, to serve as a template for PCR2 reactions to generate Illumina adaptors to PCR1 amplicons. PCR2: For each time point, 13x 50µl reactions of NEBNext® Ultra II Q5 Master Mix were prepared using 2µl/50µl reaction of PCR1. All time points used the reactions used the GeCKO_Master_F forward primer combined with unique reverse primers for each samples to barcode each time point separately for multiplexing (GeCKO R01-R08, Table S1). The thermocycling parameters were identical to PCR1. PCR2 reactions from each time point were pooled and then gel purified to attain the desired ~360 base pair amplicons using the QIAquick Gel Extraction Kit (Qiagen #28704) following the manufacturers protocol except gels were dissolved at 30°C. Library concentrations were then estimated using the Nanodrop (Thermo Scientific). Samples were stored at -20°C until further processed. Sample were sequenced with 15% Phi-X spike in on the NextSeq500 platform (Illumina) using High Output chemistry using 30 dark cycles, followed by 20 imaging cycles, and 8 index read cycles. Minimum 60 millions for day 0 samples, and minimum 25 million reads for day 14 samples. Data analysis, including ontology enrichment analyses, was carried out using MAGeCK-VISPR and MAGeCKFlute (Li, Köster et al. 2015, Wang, Wang et al. 2019) software packages. Ontology Network analysis was performed with Cytoscape running the ClueGo plugin (Shannon, Markiel et al. 2003, Bindea, Mlecnik et al. 2009).

CHAPTER 3:

CRISPR/Cas9 genome engineering and modeling of LAM

Portions of Chapter 3, sections 3.1-3.3, have been adapted from:

Delaney, S. P., L. M. Julian, A. Pietrobon, J. Yockell-Lelièvre, C. Doré, T. T. Wang, V. C. Doyon, A. Raymond, D. A. Patten, M.-E. Harper, H. Sun and W. L. Stanford (2019). "Stem cell models identify lineage-specific catabolic signaling, neoplastic mechanisms and therapeutic vulnerabilities in tuberous sclerosis." bioRxiv: 683359.

Original Manuscript:
Conceptualization, **S.P.D.**, L.M.J., and W.L.S.
Methodology, **S.P.D.** and L.M.J.
Investigation, **S.P.D.**, L.M.J., A.P., J.Y-L., C.D., T.T.W., V.C.D., A.R., D.A.P., M.E.H., and H.S.
Formal Analysis, **S.P.D.**, L.M.J., A.P., J.Y-L, T.T.W., and S.H.
Writing – Original Draft, **S.P.D.** and L.M.J.
Writing – Review & Editing, **S.P.D.**, L.M.J., A.P., J.Y-L., D.A.P., M.E.H., H.S., and W.L.S.
Funding Acquisition, **S.P.D.**, L.M.J., and W.L.S
Resources, W.L.S.
Visualization, **S.P.D.**, L.M.J., J.Y-L.
Supervision, W.L.S.

Contributions to this chapter:
All experiments were conceptualized and performed by **SPD**, with guidance from WLS, except for the experiments in which data is presented in Figures 3.3.1, 3.3.2. Figures 3.3.1, 3.3.2A-D were performed and conceptualized by LMJ, and experiments for Figure 3.3.2E-G were performed by TTW and HS. *In vivo* experimentation was performed with assistance from CD. Figure 3.1.4 was generated with assistance from JY-L.

3.1 Generation of an hPSC library to model LAM using CRISPR/Cas9

To reflect the genetic diversity of patients affected by TSC and permit robust validation of disease-relevant phenotypes, I utilized multiple, well-characterized hPSC lines within this study. As TSC affects both men and women, with LAM affecting exclusively females, two male (H1 & 168 hPSCs) and two female (H7 & H9 hPSCs) lines were selected (Figure 1A). To aid in live cell assays, co-culture experimentation, and in vivo studies, these parental lines were modified at the AAVS1 locus with CRISPR/Cas9 to express green (emGFP) or red (mCherry) fluorescent reporters along with a Zeocin resistance gene (Figure 3.1.1A-C). Due to the higher prevalence and more severe disease phenotypes associated with mutations in *TSC2* compared to *TSC1* (Dabora, Jozwiak et al. 2001), the *TSC2* locus was targeted for genetic modification via CRISPR/Cas9. As mentioned previously, there is a wide array of documented pathogenic mutations in *TSC2* (over 2600 unique variants) with no mutational 'hotspot' within coding regions or tendency towards a particular mutation (Au, Williams et al. 2007, Fokkema, Taschner et al. 2011, Martin, Zhou et al. 2017). Thus, I was afforded the freedom to generate two unique iterations of TSC2 mutant LAM disease models in hPSCs.

3.1.1 Iteration 1: TSC2-∆ allele

The translated product of *TSC2* exon 11 coincides with the coiled-coil domain of TSC2 that interacts and dimerizes with TSC1, allowing the TSC1/2 complex to carry out its canonical physiological function to negatively regulate mTORC1 signaling. A previous report detailing a TSC patient with a large deletion in exon 11 has shown two near full length splice variants were produced: one in which exon 11 is skipped, and another where exons 10 and 11 are skipped leaving the rest of the transcript intact (van Bakel, Sepp et al. 1997). To generate the TSC2∆-allele in hPSCs, two CRISPR/Cas9 constructs targeting intronic sequences flanking exon 11 were co-transfected to generate an in-frame deletion of exon 11 through after NHEJ-mediated

repair of the large chromosome lesion (Figure 3.1.2A). Successful excision of exon 11 results in a roughly 1.1kb decrease in the *TSC2* locus, which is easily visualized via standard agarose gel electrophoresis utilizing primers flanking the targeted region (Figure 3.1.1B). Using this approach, I generated both heterozygous-*TSC2*Δ (*TSC2*$^{+/\Delta}$) and homozygous-*TSC2*Δ (*TSC2*$^{\Delta/\Delta}$) cell lines derived from all four parental hPSC lines utilized in this study (Figure 3.1.2B). In culture, both *TSC2*$^{+/\Delta}$ and *TSC2*$^{\Delta/\Delta}$ hPSCs display characteristic undifferentiated colony morphology and can be maintained indefinitely (data not shown). As expected, the TSC2Δ modification indeed results in the translation of a near full length protein (Fig. 3.1.2C); a phenomenon documented in a subset of TSC patients (van Bakel, Sepp et al. 1997, Fokkema, Taschner et al. 2011).

A defining characteristic of both neurological TSC and LAM lesions is their inability to properly regulate mTORC1 signaling, attributed to loss of function of the inhibitory TSC1/2 complex. Under maintenance conditions, both undifferentiated *WT* and *TSC2*Δ hPSCs exhibited active mTORC1 signaling as indicated by the phosphorylation of mTOR (Ser2448) and the downstream effectors of the mTORC1 complex, p70 S6K (S6K; Thr389) and S6 ribosomal protein (S6; Ser235/236). However, when exposed to stress conditions (6h at 1% O_2), *TSC2*$^{\Delta/\Delta}$ hPSCs maintain constitutive phosphorylation of the mTORC1 axis as indicated by constitutive mTOR and S6 phosphorylation; *WT* cells can repress this pathway, and to a lesser extent, TSC2$^{+/\Delta}$ cells (Figure 3.1.2D). The absence of TSC1 following immunoprecipitation of TSC2 from *TSC2*$^{\Delta/\Delta}$ cells (Figure 3.1.2E) is indicative that mTORC1 dysregulation is the consequence of the lack of a functional TSC1/2 complex.

Interestingly, immunofluorescent (IF) staining probing for TSC2 indicates that the intracellular localization of TSC2 is not discernably altered in *TSC2*$^{\Delta/\Delta}$ cells (Figure

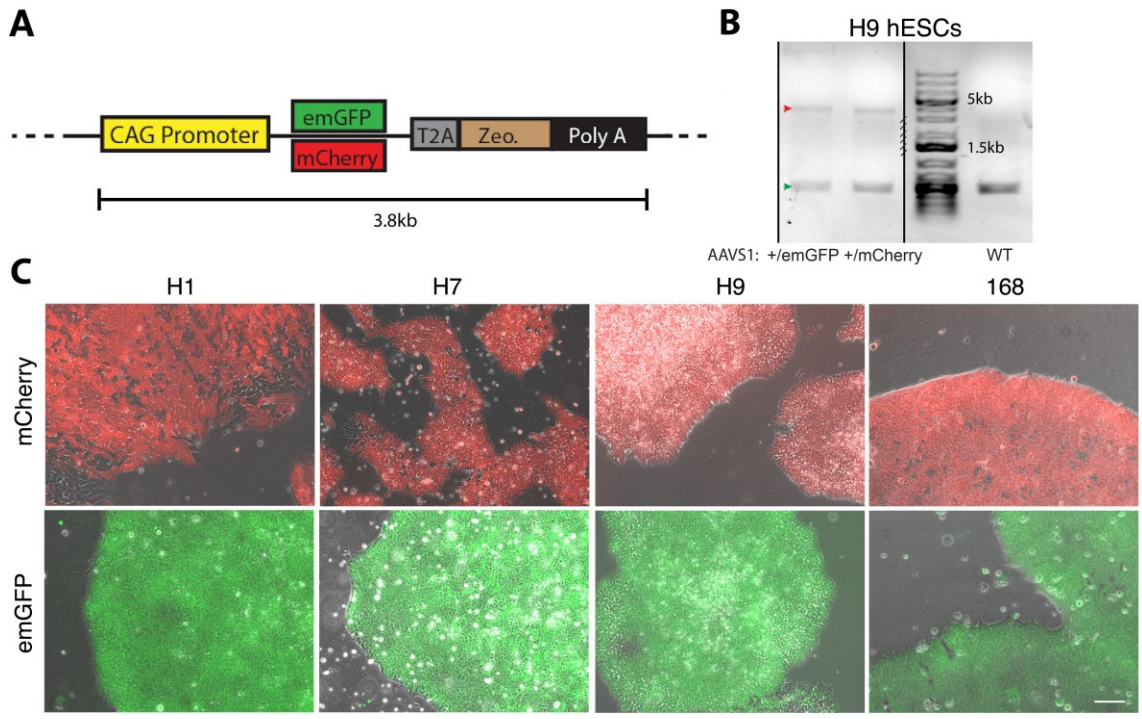

Figure 3.1.1: Integration of selection markers in to the AAVS1 locus in hPSCs
(A) Schematic of the selection marker transgene. Driven by the CAG promoter, leads to emGFP or mCherry expression along with zeocin resistance utilizing the T2A self-cleaving peptide sequence. (B) Representative PCR genotype of H9 hPSCs revealing heterozygous integration of selection marker transgenes in the AAVS1 locus. Red arrowhead indicates transgene amplicon, green arrow is *WT* AAVS1 amplicon. (C) Phase contrast/fluorescence image overlay of hPSC lines with selection marker integrations. Scale bar, 100μm.

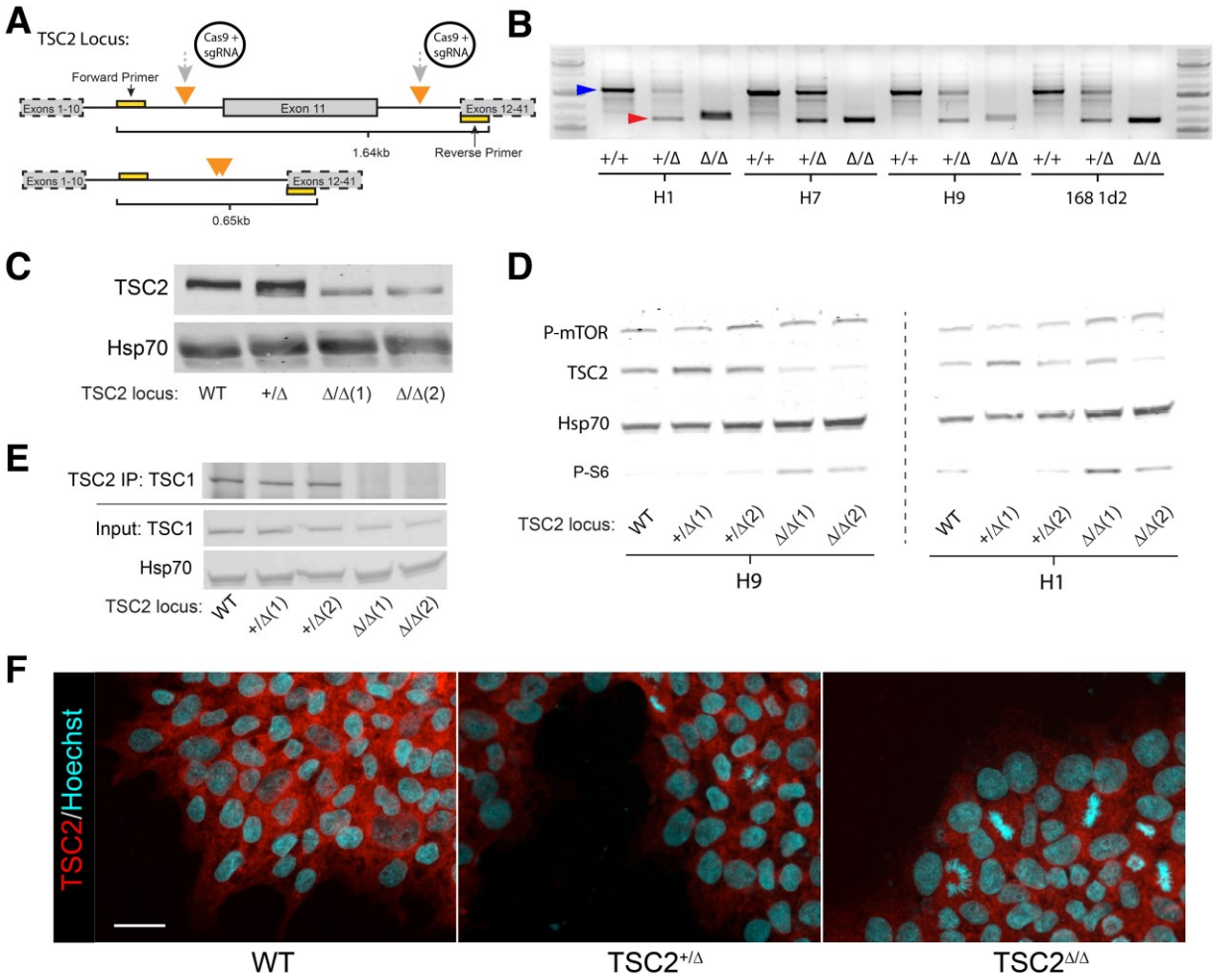

Figure 3.1.2: The TSC2Δ mutation results in a unique TSC2 mutant isoform and mTOR dysregulation

(A) Schematic of the TSC2-Δ-exon11 modification. Two CRISPR/Cas9 vectors targeting intronic regions flanking TSC2 exon 11 results in an in-frame excision of the exon 11 genomic region. (B) PCR genotyping of TSC2Δ H1, H7, H9, and 168 hPSCs shows heterozygous and homozygous *TSC2*Δ alleles. Blue arrowhead indicates WT amplicons, red arrowhead indicates TSC2Δ mutant amplicons. (C) Western blot of H9 hPSC *TSC2*Δ cell lines probing for TSC2 resolves a near full length TSC2 protein resulting from Δ modification. (D) Western blot of multiple H9 and H1 *TSC2*Δ clones probing for mTORC1 dysregulation. Exposing *WT*, $TSC2^{+/\Delta}$, and $TSC2^{\Delta/\Delta}$ to hypoxia (1% O_2) for 6h results in mTORC1 pathway inhibition in *WT* cells, as indicated by dephosphorylation of mTOR and S6. $TSC2^{\Delta/\Delta}$ cells, and to a lesser extent $TSC2^{+/\Delta}$ cells, display constitutive mTORC1 pathway activation under these stress conditions. (E) Immunoprecipitation was performed using TSC2 baiting for TSC1. No detectable TSC1 is present in $TSC2^{\Delta/\Delta}$ samples, indicating that the TSC1/2 complex can no longer form as a result of the *TSC2*Δ genome modification. (F) IF probing for TSC2 in WT, $TSC2^{+/\Delta}$, and $TSC2^{\Delta/\Delta}$. Scale bar, 50μm.

3.1.2F). This suggests that the TSC2Δ isoform may still perform noncanonical functions unrelated to the regulation of mTORC1, however this has yet to be determined and is the subject of a related project currently in development. Thus, although much preliminary work was performed in the *TSC2*Δ cell lines, to avoid potential confounding factors related to noncanonical TSC2 interactions, a *TSC2* knockout allele was generated. The majority of the characterization and modeling data presented in this thesis utilized homozygous *TSC2* knockout (*TSC2*$^{-/-}$) cell lines.

3.1.2 Iteration 2: The TSC2 knockout allele

To effectively knockout TSC2 expression, *TSC2* exon 3 was selected for targeting due to its ubiquity across all documented variants and its proximity to the N-terminus of TSC2. To minimize any potential variation in gene knockout across CRISPR/Cas9 edited cell lines, a HR strategy was employed to achieve the highest possible editing precision. Using a single stranded oligonucleotide (ssODN) containing a 35-base 'stop-codon' donor sequence (Gagnon, Valen et al. 2014), a frame shift-inducing insertion containing stop codons in all frames was introduced into *TSC2* exon 3. Integration of the donor sequence was confirmed through genotyping utilizing PmeI digestion of PCR amplicons of the *TSC2* exon 3 target site (Figure 3.1.3A).

Homozygous integration of the stop-codon sequence (*TSC2*$^{-/-}$) resulted in complete ablation of TSC2 expression, with no detectable TSC2 by IF or western blot (Figure 3.1.3B&C). Much like their *WT* counterparts and the TSC2-Δ hPSCs, the *TSC2*$^{-/-}$ hPSCs maintain characteristic undifferentiated colony morphology and can be maintained in an undifferentiated state indefinitely and exhibit normal expression levels of hallmark pluripotency markers OCT4, SOX2, and NANOG (Figure 3.1.3D), demonstrating that the pluripotency regulatory network functions unperturbed in

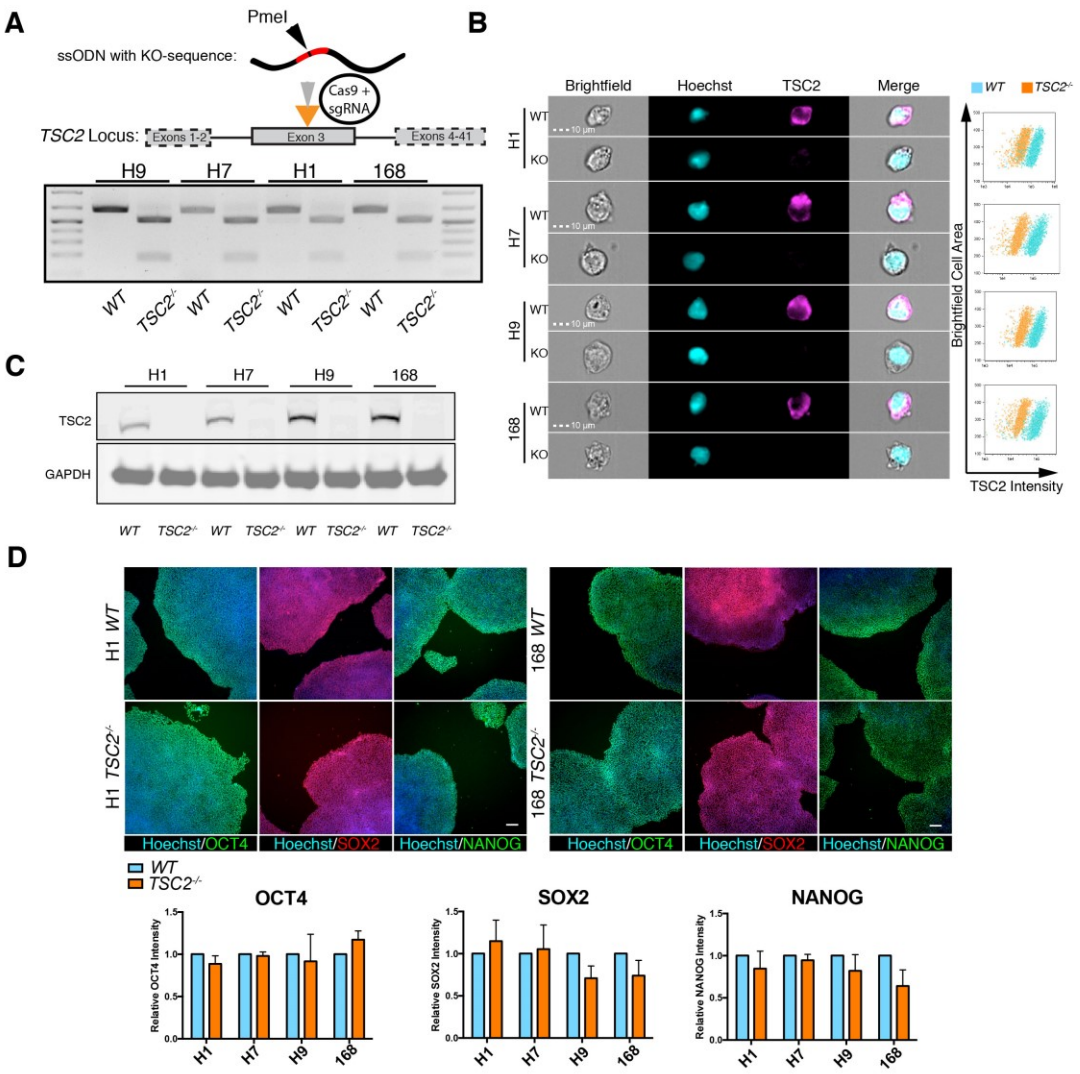

Figure 3.1.3: The TSC2 knockout genome modification results in ablation of TSC2 protein expression and does not affect pluripotency

(A) Homologous recombination strategy to knockout *TSC2* utilized an ssODN containing a 'STOP-codon' donor sequence containing the unique restriction site, PmeI. PmeI digestion of PCR amplicons containing the target cut site reveals homozygous integration of the donor sequence in *TSC2*$^{-/-}$ hPSC lines. (B) Imaging flow cytometry image capture following staining with TSC2 antibody revealing clonal populations of *TSC2*$^{-/-}$ cells. (C) Western blot of *WT* and *TSC2*$^{-/-}$ hPSCs probing for TSC2. (D) Representative IF images and quantification of fluorescence intensity of pluripotency markers OCT4, SOX2, and NANOG in each hPSC line under maintenance conditions, normalized to respective parental *WT* hPSC lines. Values are the mean ± SEM (n = 12; 3x for each cell line), no statistical significance between WT and TSC2$^{-/-}$ samples was observed. Scale bars, 100µm. Adapted from Delaney et al. 2019, bioRxiv, 683359 (Delaney, Julian et al. 2019).

complete absence of TSC2. Furthermore, *TSC2* deficiency does not overtly affect pluripotency, as all *TSC2*$^{-/-}$ hPSCs were able to form tissues of ectodermal, mesodermal, and endodermal origin during *in vivo* teratoma assays (Figure 3.1.4).

As expected, complete ablation of TSC2 resulted in constitutive activation of the mTORC1 signaling axis, recapitulating this hallmark LAM molecular signaling abnormality. *TSC2*$^{-/-}$ hPSCs were exposed to stress conditions (1% O2 for 6h) and were unable to suppress phosphorylation of mTOR, S6K, and S6, in contrast to *WT* hPSCs (Figure 3.1.5A-C). Thus, all four *TSC2*$^{-/-}$ hPSC lines are able to successfully recapitulate the mTORC1 molecular signaling abnormalities observed in TSC and LAM-associated lesions.

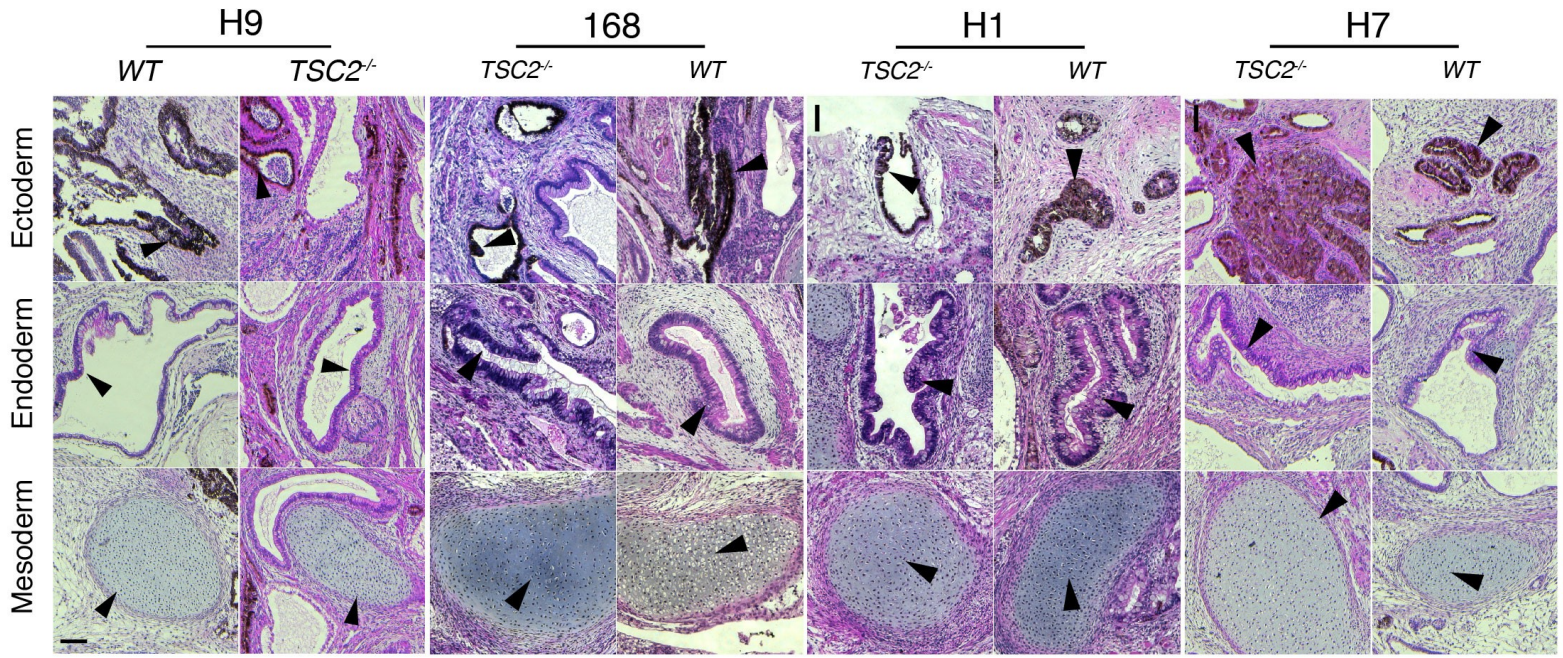

Figure 3.1.4: *TSC2*$^{-/-}$ hPSCs are able to differentiate into all three germ layers *in vivo*.
Haematoxylin and eosin staining of H9 *WT* and *TSC2*$^{-/-}$ teratoma explants. Arrows indicate examples of immature tissues of ectodermal, endodermal, and mesodermal origin. Scale bar, 100μm. Adapted from Delaney et al. 2019, bioRxiv, 683359 (Delaney, Julian et al. 2019).

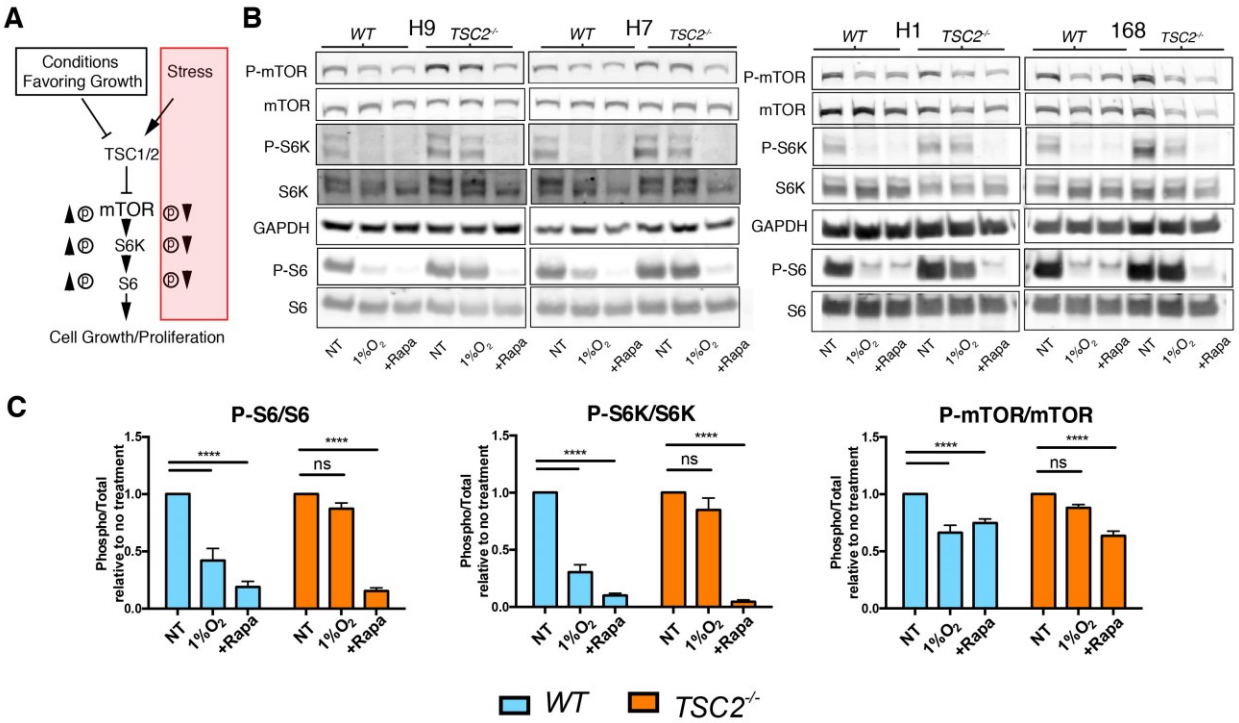

Figure 3.1.5: *TSC2*$^{-/-}$ hPSCs display constitutive mTORC1 activation under stress conditions.

(A) Schematic of expected phosphorylation status of mTORC1 effectors under supportive and stress conditions. (B) Western blots probing for total and phosphorylated mTOR (P-mTOR), S6K (P-S6K), and S6 (P-S6) of samples treated for 6h under no treatment, 1% O_2, and +100nM rapamycin conditions. (C) Densitometry quantification of western blots displaying the ratio of phosphorylated to total protein of mTOR, S6K, and S6 (n = 8; 2x for each cell line). Statistical significance was determined using two-way ANOVA and Tukey's post hoc analysis Adapted from Delaney et al. 2019, bioRxiv, 683359 (Delaney, Julian et al. 2019).

3.2 TSC2 deficiency alters, but does not inhibit neuroectoderm differentiation

To model both neurological TSC and mesenchymal LAM manifestations, a parallel lineage induction approach was developed utilizing the small molecules, SB431542 (SB) and LDN193189 (LDN), for dual inhibition of SMAD signaling (dSMADi) of hPSCs (Figure 3.2.1). The dSMADi approach is a well-established method for efficient neuralization of hPSC cultures and promotes rapid exit from pluripotency and induction of a predominant dorsal neuroectoderm (NE) fate. This allows the enrichment of NE-derived NPCs or NCCs in defined culture conditions (Chambers, Fasano et al. 2009, Tchieu, Zimmer et al. 2017). Applying dSMADi to differentiating hPSC cultures at high density (monolayer-NPC protocol; Figure 3.2.1A) efficiently generates NPC populations, whereas neuralizing diffuse hPSC cultures favors the enrichment of the migratory NCC population (Lee, Chambers et al. 2010).

3.2.1 TSC2 deficiency does not impede NCC differentiation

To model the putative cell of origin for LAM, NCCs, a 12-day embryoid body (EB)-based differentiation (EB-NCC) protocol was developed (Figure 3.2.1B). Considering that differentiating low density hPSC cultures biases enrichment toward NCCs differentiation in dSMADi protocols, the EB-NCC protocol was designed to spatially enrich for NCCs; at day 5 of differentiation, plating of neuralized EBs onto a fibronectin substrate at an optimal density allows maximum expansion of NCCs after their subsequent migration away from neuralized adherent EB clusters. The EB-NCC protocol also recapitulates aspects of natural development of vertebrates, with the neuralized EBs being reminiscent of the developing neural tube. At the interface of neuralized EBs and the fibronectin coated growth surface, NCCs emerge and migrate away before expanding. Importantly, this protocol also allows concurrent observations to be made of both NPC and NCC populations throughout differentiation.

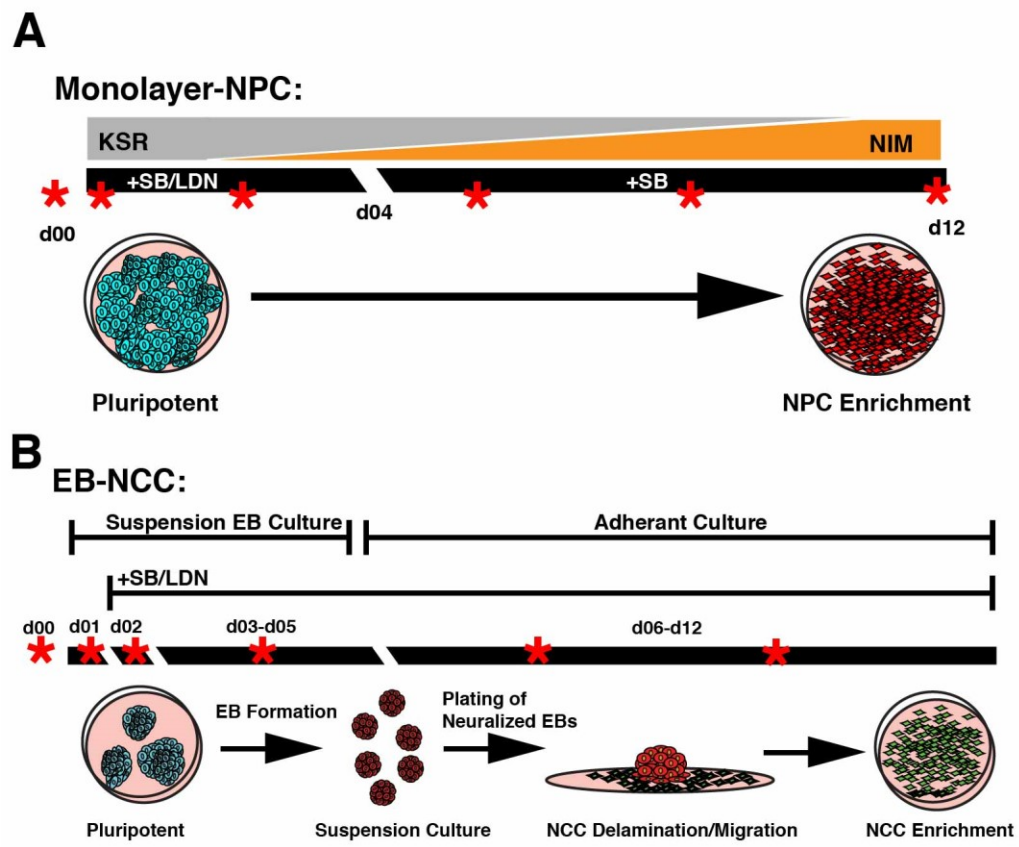

Figure 3.2.1: Schematic representation of monolayer-NPC and EB-NCC differentiation protocols.
Red asterisks indicate time points harvested for RNA extraction for RT-qPCR and RNA-seq. Time points were samples throughout the monolayer-NPC differentiation time course (days 0, 1, 3, 5, 8, 12). EB-NCC RNA-seq time points were sampled at key points of transition: pluripotency (day 0), EB formation (day 1), addition of neutralizing factors SB and LDN (day 2), neuralization of EBs (day 4), delamination of NCCs (day 7), and NCC enrichment (day 10). KSR: knockout serum replacement media; NIM: neural induction media; SB: SB431542 ALK inhibitor; LDN: LDN193189 ALK inhibitor. Adapted from Delaney et al. 2019, bioRxiv, 683359 (Delaney, Julian et al. 2019).

To ensure robustness of the differentiation protocol, EBs were generated using AggreWell technology (STEMCELL technologies), which utilizes a centrifugal forced-aggregation strategy to efficiently generate a high number of EBs of a defined size (Ungrin, Joshi et al. 2008). Confirming the generation of NCCs, by day 10 of differentiation, migratory cells expressing the neural crest markers SOX9 and HNK-1 can be observed migrating away from $PAX6^+$ neural clusters (Figure 3.2.2A). Selective dissociation of migratory outgrowths at day 12 efficiently enriched for cells expressing the NCC-associated marker, p75, in all cell lines, regardless of TSC2 genotype (Figure 3.2.2B&C). This resulted in highly enriched maintenance populations of $SOX9^+$ NCCs co-expressing the NCC-migratory marker, HNK-1, with minimal contamination of PAX6 expressing NPC populations (Figure 3.2.2D). Irrespective of *TSC2*-deficiency, the generated NCCs are multipotent and can be differentiated to both ectodermal and mesodermal lineages, including smooth muscle cells and adipocytes which are characteristic of LAM tumors (Figure 3.2.2E).

3.2.2 Loss of TSC2 alters NE gene expression during EB-NCC differentiation

Early observations of EB-NCC differentiation using $TSC2^{+/\Delta}$ and $TSC2^{\Delta/\Delta}$ hPSCs revealed distinct morphological differences when compared to *WT* cells. $TSC2^{\Delta/\Delta}$ neuralized adherent EB clusters displayed disorganized neural rosette morphology. In addition, NCC outgrowths displayed spindle-like morphology and enhanced migratory phenotype (Figure 3.2.3A). These morphological phenotypes were also observed in $TSC2^{-/-}$ cells (Figure 3.2.3B). Furthermore, through the use of competitive growth and differentiation assays using genotype-specific fluorescence tagging (WT=emGFP, TSC2 *Δ*=mCherry) (Figure 3.1.1A-C), we observed that $TSC2^{\Delta/\Delta}$ cells do not have a distinct growth advantage *in vitro* until they are differentiated, where they proceed to dominate the culture (Figure 3.2.3C). Although $TSC2^{\Delta/\Delta}$ cells do not outcompete *WT* and $TSC2^{+/\Delta}$

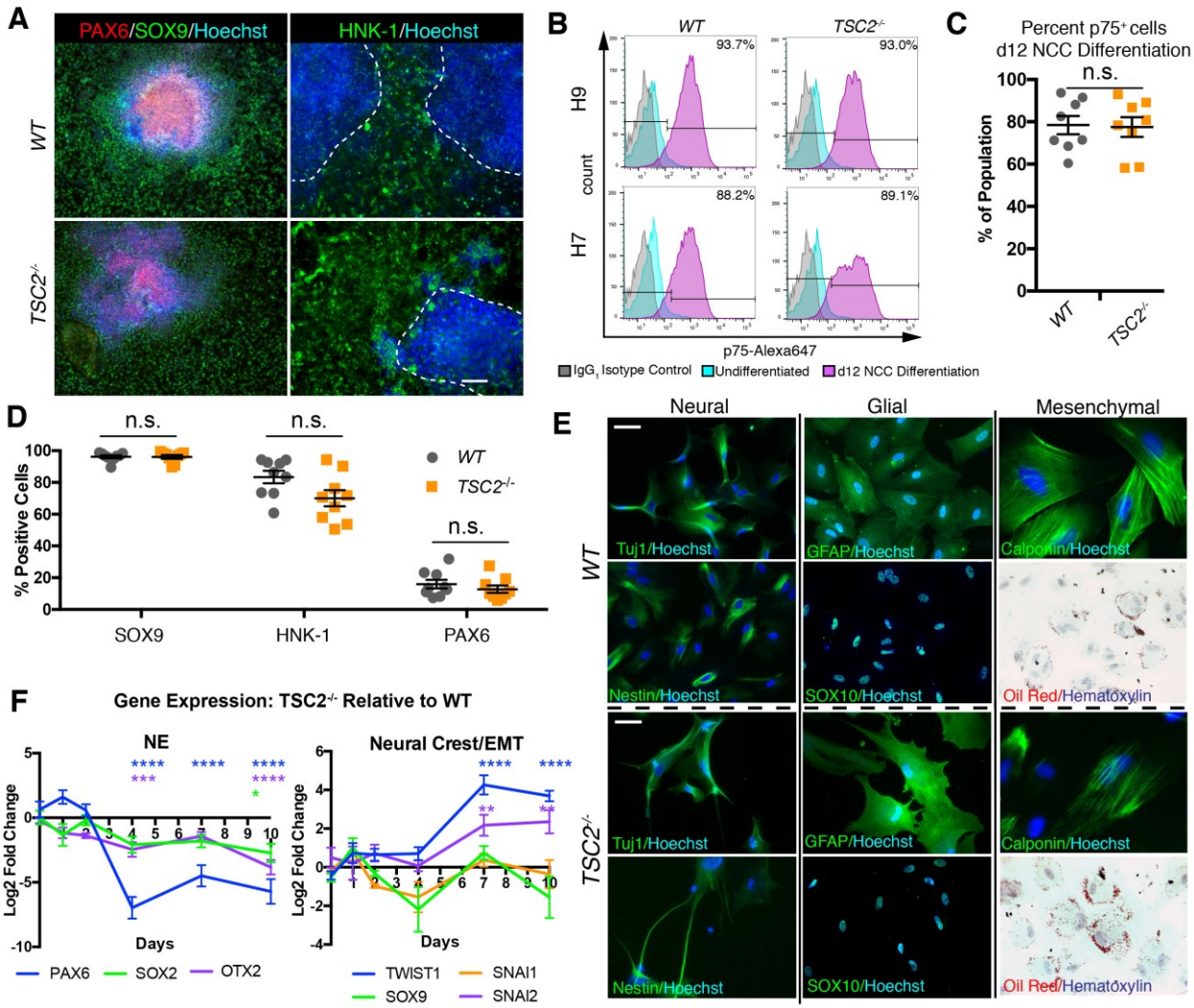

Figure 3.2.2: Loss of TSC2 does not affect NCC specification
(A) Representative IF staining of lineage specific markers PAX6 (neural ectoderm), SOX9 and HNK-1 (neural crest) in *WT* and *TSC2*$^{-/-}$ cultures at d12 EB-NCC differentiation. Scale bar, 100µm. (B) Representative flow cytometry analysis of p75 expression in *WT* and *TSC2*$^{-/-}$ cultures at d12 EB-NCC differentiation prior establishing maintenance populations. (C) Percent p75^{+} cells at d12 of EB-NCC differentiation. Error values are the mean ± SEM (total n = 8; 2x for each cell line). (D) Percentage of maintenance NCC populations expressing NCC specific lineage markers SOX9 and HNK-1, and NPC specific marker PAX6. Values are mean ± SEM (n = 9; ≥ 2x for each cell line) (E) Representative IF staining of *WT* and *TSC2*$^{-/-}$ 168 NCCs differentiated towards neural (neuronal markers: Tuj1, Nestin), glial (Schwann cells: GFAP, maintaining SOX10 expression at endpoint) and mesenchymal lineages (smooth muscle cells: Calponin; adipocytes: oil red staining). Scale bars, 50µm. (F) Gene expression profiles of early neural (NE) and neural crest markers as measured through RT-qPCR of *TSC2*$^{-/-}$ cells throughout EB-NCC differentiation relative to *WT* cells. Values are the mean ± SEM (total n = 7; 3x H9, 2x H7&168). Adapted from Delaney et al. 2019, bioRxiv, 683359 (Delaney, Julian et al. 2019).

-

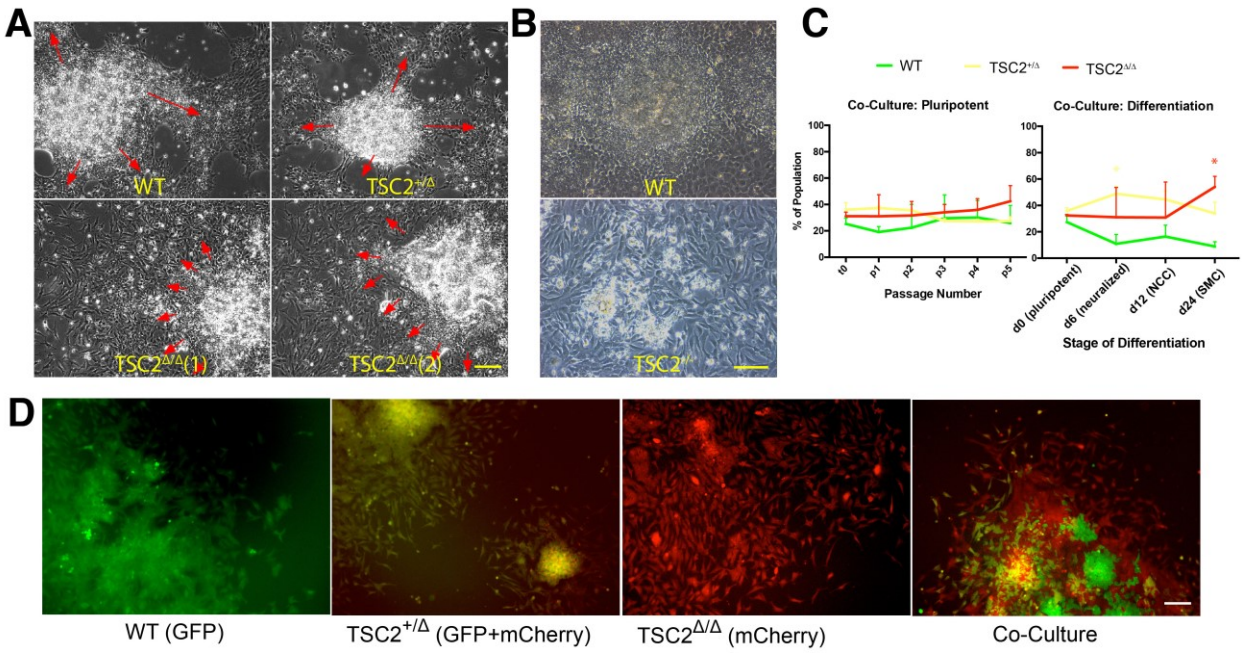

Figure 3.2.3: *TSC2* mutant cultures display altered morphological and migratory features during EB-NCC differentiation.

(A) Phase images of *WT* and *TSC2*Δ mutant cultures undergoing EB-NCC differentiation. Red arrows indicate paths of migration. $TSC^{\Delta/\Delta}$ NCCs migrate in a radial and disorganized fashion. Scale bar, 100μm. (B) Phase images of *WT* and $TSC2^{-/-}$ cultures undergoing EB-NCC differentiation. Scale bar, 100μm. (C&D) Genotype-specific fluorescent tagging effectively identifies genotypes in mixed co-cultures. (C) Co-culture of *WT,* $TSC2^{+/\Delta}$, $TSC2^{\Delta/\Delta}$ H9 hPSCs shows no evidence of genotype-specific competitive growth over multiple passages. Upon differentiation, a genotype dependent growth advantage is observed. Values are mean ± SEM (n = 2). Statistical significance was calculated using 2-way ANOVA with Tukey's multiple comparisons. Significant findings are observed comparing to WT cultures. (D) NCC differentiation displays a genotype specific enhanced migratory phenotype of TSC2ΔEx11 mutant NCCs from neuralized clusters. Scale bar, 100μm.

cells at the pluripotent and neural crest stages, it is clear *TSC2*$^{\Delta/\Delta}$ NCCs exhibit an enhanced migratory phenotype in co-culture (Figure 3.2.3D), confirming previous qualitative observations.

Considering these observations, and although TSC2 does not inhibit NCC differentiation, it was clear that TSC2-dependent phenotypes were emerging during EB-NCC differentiation. To evaluate gene expression contributing to this phenomenon, RNA was harvested at key timepoints to emphasize phases of transition during differentiation: pluripotency (day 0), EB-formation (day 1), neuralization (days 2&4), NCC specification (day 7) and enrichment (day 10) (Figure 3.2.1B, red asterisks). Interestingly, reverse transcription quantitative PCR (RT-qPCR) revealed that loss of TSC2 results in a marked decrease in gene expression of early key neural genes markers SOX2, OTX2, and PAX6 (Figure 3.2.2F). These are unexpected results, considering the well characterized dSMADi differentiation protocols describe the emergence of NCCs from PAX6^{+} neural rosette clusters (Chambers, Fasano et al. 2009). However, this data fits well within the context of the CNS tumors of TSC, namely, cortical tubers and subependymal giant cell astrocytomas. These tumors are characterized by disorganized glial cells and dysmorphic neurons, the result of aberrant neural differentiation (Magri et al., 2011; Goto et al., 2011; Normand et al., 2013; Prabhakar et al., 2013; Magri and Galli, 2013; Carson et al., 2012).

Interestingly, key NCC specification genes display irregular expression profiles compared to *WT* cells over the course of the differentiation (Figure 3.2.2F). For instance, comparing *TSC2*$^{-/-}$ gene expression relative to *WT* cultures, both SOX9 and SNAI1 expression is comparable between *WT* and *TSC2*$^{-/-}$ cells. However, TWIST1 and SNAI2 TWIST1 are highly upregulated. In addition to being neural crest specifier genes, SNAI1, SNAI2, and TWIST1 are all associated with EMT, cell migration, and invasiveness. This expression profile aligns with the phenotypic observations of increased migration,

motility, and invasion of TS2 null cells in culture. Of note, TWIST1 is markedly upregulated compared to other NCC genes, and has been associated with the repression of pro-neural factors, perhaps influencing the down regulation of early NE genes (Das and Crump 2012, Vincentz, Firulli et al. 2013).

3.3 TSC2$^{-/-}$ NPCs NCCs accurately model TSC and LAM

Multiple cell and animal models have been generated to model the neurological features of TSC, resulting in the generally accepted notion that CNS TSC tumors originate from aberrant proliferation, migration, and differentiation of NSC/NPC populations. Surprisingly, however, human NPC TSC cell models are lacking that can directly evaluate the proliferative progenitor cell populations contributing to the formation of neurological TSC tumors. In parallel, the origin of the deleterious mesenchymal manifestations of TSC and LAM is still unknown, and no known human cell model exists to investigate the progenitor cell lineage most likely to contribute to tumor growth. Thus, to fill this significant gap in TSC/LAM cell models, this study utilized dSMADi-based differentiation protocols to generate the presumed cells of origin for neurological TSC and LAM, NPC and NCCs, respectively.

3.3.1 TSC2$^{-/-}$ NPCs accurately model multiple features of neurological TSC tumors

TSC2-deficiency results in cognitive abnormalities and the growth of low-grade tumors in the developing brain, specifically cortical tubers, subependymal nodules (SENs) and SEGAs, that contain molecular features indicative of aberrant neural lineage differentiation, maturation, and organelle dysfunction (Goto, Talos et al. 2011). In addition to dysplastic neurons and astrocytes, which to date have been the predominant focus within the field in understanding TSC brain tumors, enlarged cells that

demonstrate atypical neural progenitor identity are primary constituents of these tumors (Zhou, Shrikhande et al. 2011, Martin, Zhou et al. 2017). To ultimately model both progenitor-like and mature TSC brain tumor cell types, we induced hPSC cultures into NPCs using the high-density monolayer-NPC protocol (Figure 3.2.1A). Within 96 hours, we observed that *TSC2*$^{-/-}$ cells were visibly enlarged and had accumulated an abundance of globular structures which persisted throughout the differentiation time course (Figure 3.3.1A). This struck us as being highly reminiscent of vesicle accumulation observed in mTORC1 hyperactive cells in patient tumors (Goto, Talos et al. 2011). *WT* and *TSC2*$^{-/-}$ cultures were harvested 12 days following initiation of NPC induction and maintained in neural progenitor expansion medium for multiple passages to examine long-term progenitor phenotypes. *TSC2*$^{-/-}$ cultures exhibited increased phosphorylation of S6 (P-S6) under fully supplemented media conditions, indicative of mTORC1 hyperactivation (Figure 3.3.1B&C), and were larger than their *WT* counterparts (Figure 3.3.1A&D). Both *WT* and *TSC2*$^{-/-}$ cells expressed the NPC lineage markers SOX2, NESTIN and PAX6, demonstrating a progressive increase in expression of NPC determinants and the glial marker GFAP in *TSC2*$^{-/-}$ cells with time in culture (Figure 3.3.1B, E-H). Mitochondrial content was also progressively increased in *TSC2*$^{-/-}$ NPCs (Figure 3.3.1I). These phenotypes reflect the aberrant organelle and lineage development observed in patient tumors and imply a dynamic regulation of cell fate and mitochondrial content in NPCs lacking *TSC2*. Additionally, putative vesicle accumulation observed during lineage induction was visibly reduced over the first passage in maintenance cultures but re-emerged progressively over subsequent passages. Altogether these data reveal that *TSC2*$^{-/-}$ NPC cultures reflect multiple phenotypes reflective of patient brain tumors in TSC and can be exploited to model both disease initiation and progression.

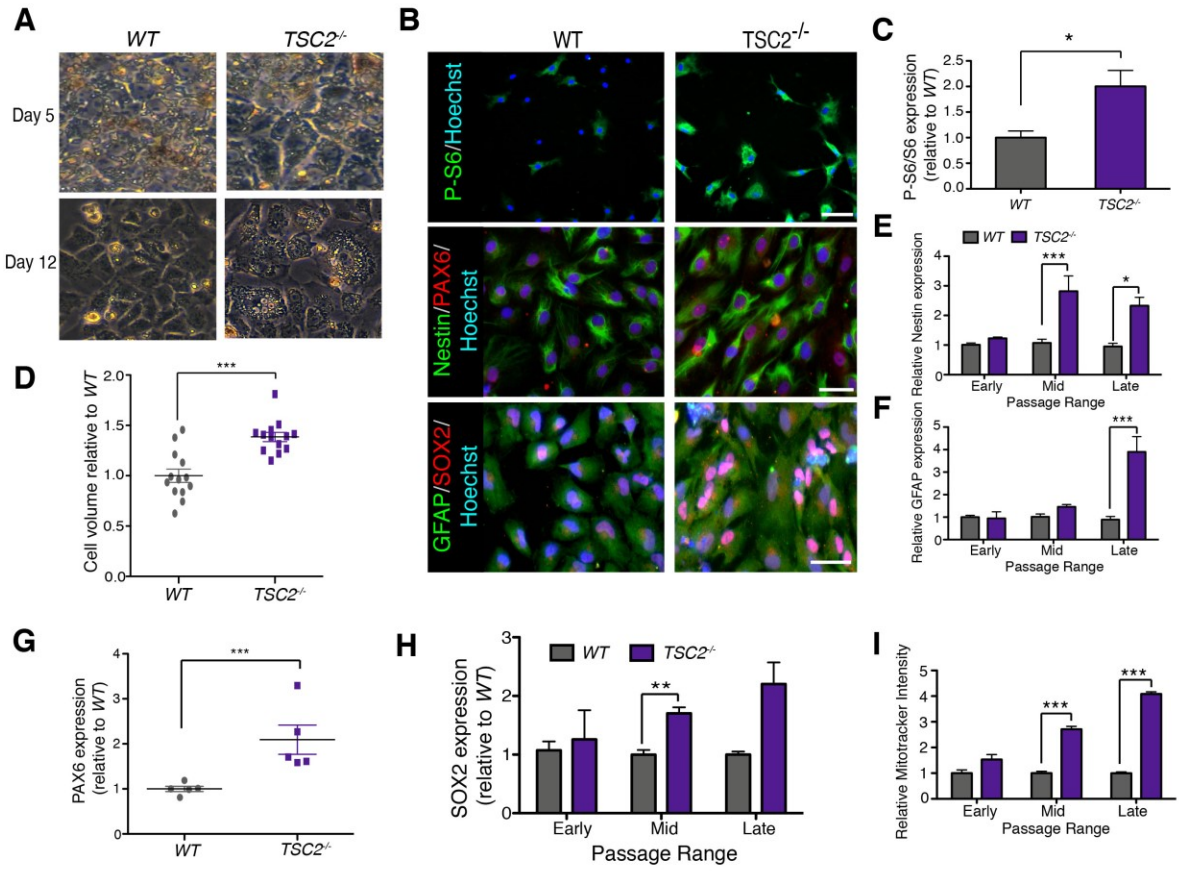

Figure 3.3.1: *TSC2*$^{-/-}$ NPCs model neurological TSC tumors
(A) Phase images of *WT* and *TSC2*$^{-/-}$ cells during monolayer-NPC induction at differentiation days 5 and 12, displaying increased cell size and vesicle accumulation in *TSC2*$^{-/-}$ cultures. Scale bar, 50µm. (B) Immunofluorescence images of *WT* and *TSC2*$^{-/-}$ NPC maintenance cultures, displaying phenotypic markers of neurological TSC tumors: P-S6, Nestin/PAX6, and GFAP/SOX2. Scale bar, 50µm. (C) Ratio of P-S6 to total S6 fluorescence intensity in maintenance NPCs, relative to *WT* levels. Values are ± SEM (n=3; 1x H9, 2x 168 between passages 2-5). (D) Quantification of NPC volume, relative to *WT* by Cellomics ArrayScan imaging analysis. Values are the mean ± SEM (n=13, including all cell lines). (E&F) Quantification of fluorescence intensity of the lineage markers (E) Nestin (neural) and (F) GFAP (glial) over early, mid, and late passage ranges in culture, relative to *WT* NPCs. For all relevant figures, passage (p) ranges are defined as: early (p0-2), mid (3-5), late (p6-8). Values are the mean ± SEM (For Nestin: [n=3 early (1 each H7, H9, 168), n=5 mid (2x H1, 1 each H7, H9, 168), n=3 late (1x H1, 2x H7)]; for GFAP: [n=5 early (2x H1, 2x H7, 1x 168), n=4 mid (1x H9, 3x 168), n=3 late (1x H1, 2x H7)]). (G) Quantification of PAX6 fluorescence intensity in NPCs, relative to *WT* NPCs. Values are mean ± SEM (n = 5; 1x H7, 2x for H1 and 168 at p0-3). (H) Quantification of SOX2 fluorescence intensity in NPCs over early, mid, and late passage ranges, normalized to *WT* NPCs. Values are mean ± SEM (n = 6 early, n = 5 mid, n = 3 late) (I) Relative intensity of Mitotracker deep red staining in NPCs over early, mid, and late passage ranges, normalized to *WT* NPCs. Values are the mean ± SEM (n=5 early (1x H1, 2x each H9 and 168), n=3 mid (1x H9, 2x 168), n=4 late (2x 168, 1 each H1 and H9). Adapted from Delaney et al. 2019, bioRxiv, 683359 (Delaney, Julian et al. 2019).

Neuronal differentiation produced *TSC2*$^{-/-}$ cultures with enlarged soma and an expanded neurite network (Figure 3.3.2A&B) and an increased capacity for gliogenesis in mature cultures (Figure 3.3.2C&D), modeling neuronal structure, network and neural and glial cell fate phenotypes observed in TSC brain lesions. To determine whether *TSC2*$^{-/-}$ cultures exhibited functional hyperactivation typical of TSC epileptic and cognitive phenotypes, we isolated AMPA receptor (R)-mediated spontaneous excitatory post-synaptic currents (sEPSCs) and measured the amplitude and frequency (Figure 3.3.2E-G) of these events via whole-cell patch clamp technique. Indeed, *TSC2*$^{-/-}$ cells showed significant increases in the amplitude of AMPAR-mediated sEPSCs compared to untreated *WT* cells. Additionally, this could be rescued by rapamycin during differentiation (Figure 3.3.2E), revealing that the neuronal hyperexcitability in *TSC2*$^{-/-}$ cells is mTORC1-dependent (Figure 3.3.2E-G). Collectively, our analyses of *WT* and *TSC2*$^{-/-}$ progenitor and differentiated neuronal cultures demonstrated that our modelling approach permits the recapitulation of all major cell types observed in TSC brain tumors, reflecting both molecular and functional aspects of these aberrant cells.

3.3.2 TSC2$^{-/-}$ *NCCs accurately model multiple features of LAM*

The most significant clinical features affecting the quality of life of TSC and LAM patients include renal angiomyolipomas and pulmonary LAM nodules, the latter being associated with high morbidity and mortality (Oprescu, McCormack et al. 2013). As detailed in Chapter 1, these lesions are composed of potential neural crest progeny: angiomyolipomas and LAM nodules consist of proliferative spindle-shaped cells that express smooth muscle markers (e.g., α-SMA) and larger epithelioid cells that react with HMB45 (a monoclonal antibody that recognizes the melanoma-associated protein gp100), with adipocytes contributing to angiomyolipomas only. Other melanocyte

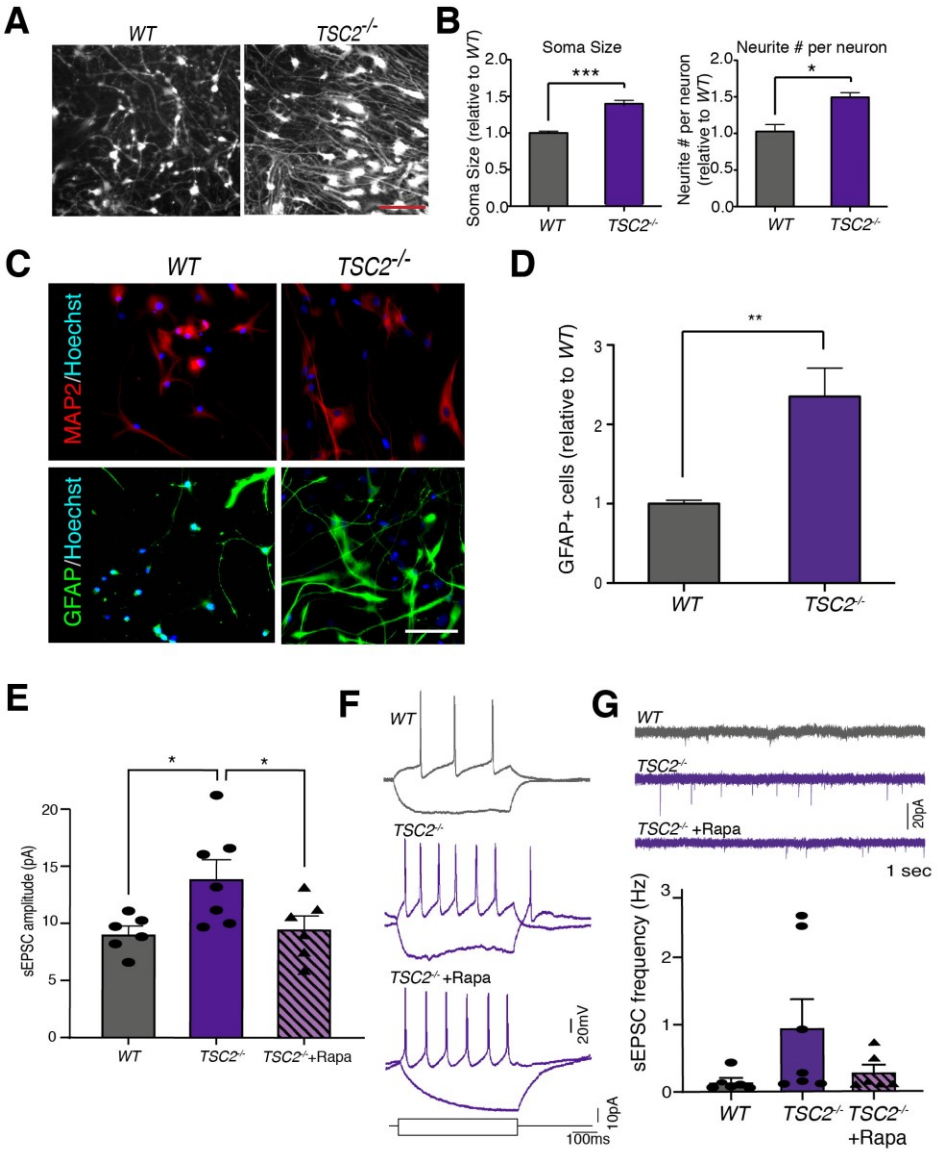

Figure 3.3.2: NPCs model multiple CNS TSC tumor phenotypes
(A) Representative images of *WT* and *TSC2*$^{-/-}$ neurons. (B) Quantification of the morphological features soma size (left) and neurite outgrowths per cell (right) imaged by endogenous mCherry expression, relative to *WT*. Values are mean ± SEM (n=3 H9). Scale bar, 50µm. (C) Representative immunostaining for neuronal marker MAP2 (top image) and glial marker GFAP (bottom image). Scale bar, 50µm. (D) Percentage of cells in neuronal cultures expressing high levels of GFAP relative to *WT*. (n = 4; 2x each H7 and H9). (E) Quantification of the amplitude of AMPA receptor-mediated spontaneous excitatory post-synaptic currents (sEPSCs) measured in H7 and H9 *WT* (n=6 cells), *TSC2*$^{-/-}$ (n=7 cells) and *TSC2*$^{-/-}$ +rapamycin (n=6 cells) neurons in culture. Values are mean ± SEM. (F) Representative traces of current clamp recordings of action potentials. (G) Voltage clamp recordings of AMPA receptor-mediated sEPCs (top) in *WT, TSC2*$^{-/-}$, and *TSC2*$^{-/-}$ +rapamycin neurons; quantification of sEPSC frequency (bottom). Values are mean ± SEM. Adapted from Delaney et al. 2019, bioRxiv, 683359 (Delaney, Julian et al. 2019).

markers are also expressed within angiomyolipomas and LAM nodules (e.g., TRYP1, MART1, GD3) (Klarquist, Barfuss et al. 2009, Gilbert, Eby et al. 2013, Grzegorek, Lenze et al. 2015). These data suggest that the cell-type of origin for LAM is a mesenchymal, neural crest-like cell. Thus, both WT and *TSC2*$^{-/-}$ NCCs were investigated for potential LAM-like disease phenotypes.

As constitutive activation of the mTORC1 signaling axis is the hallmark phenotype of LAM cells, maintenance *WT* and *TSC2*$^{-/-}$ NCCs were exposed to stress conditions and evaluated via IF probing for the mTORC1 downstream effector, P-S6. As expected, after 24h of nutrient and growth factor starvation, sustained P-S6 staining in T*SC2*$^{-/-}$ NCCs confirms these cells are unable to negatively regulate mTORC1 signaling (Figure 3.3.3A). In addition, NCCs also displayed classic mesenchymal stem cell phenotypes. As described in section 3.2.2, *TSC2*$^{-/-}$ cells displayed increased expression of select EMT related genes during differentiation (Figure 3.2.2F); indeed, *TSC2*$^{-/-}$ cells showed a significant functional increase in migratory potential compared to *WT* cells assayed via live cell tracking over a 6h time period (Figure 3.3.3B). In both *WT* and *TSC2*$^{-/-}$ NCCs, rapamycin only partially reduced migratory potential of *TSC2*$^{-/-}$ NCCs.

Common histological markers for mesenchymal TSC tumors include HMB45, α-SMA, ERα, PR, and elevated P-S6 indicative of mTORC1 hyperactivation. In addition, PDGFRß expression is elevated in TSC lesions (Arbiser, Govindarajan et al. 2002, Liang, Zhang et al. 2014, Siroky, Yin et al. 2014), and increased serum VEGFD levels are present in TSC patients with angiomyolipomas and LAM (Seyama, Kumasaka et al. 2006, Dabora, Franz et al. 2011). To determine whether *TSC2*$^{-/-}$ NCCs express these hallmark mesenchymal TSC markers, passage 1 NCCs were fixed 24h after completion of the differentiation protocol. Interestingly, both *WT* and *TSC2*$^{-/-}$ NCCs stained positive for P-S6 and α-SMA at comparable levels (Figure 3.3.3C-E). Importantly, reminiscent of LAM patient tumor explants, HMB45 staining revealed a significant subpopulation of

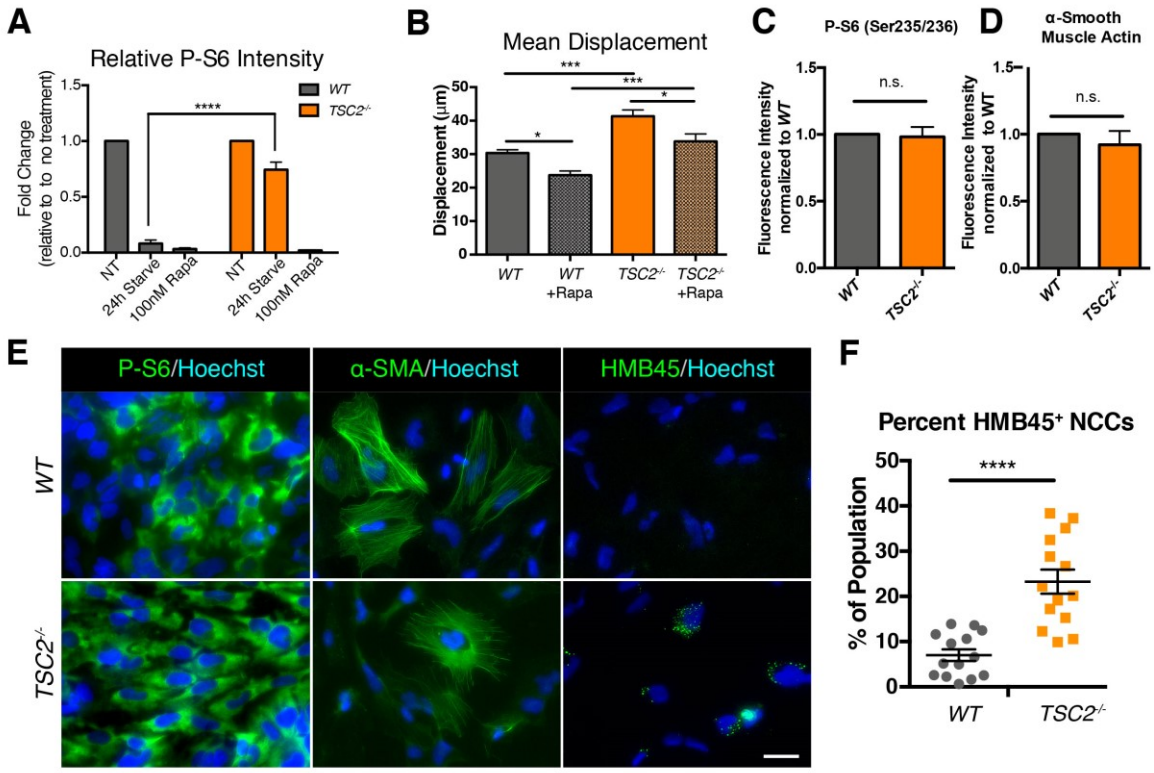

Figure 3.3.3: *TSC2*$^{-/-}$ NCCs recapitulate LAM-associated phenotypes
(A) Quantification of P-S6 immunofluorescence intensity of NCC maintenance cultures exposed to 24h of no treatment, media starvation, and +100nM rapamycin. Values are normalized to no treatment samples within each cell lineage, displaying the mean ± SEM (n = 10; ≥ 2x for each cell line). Statistical significance was determined using two-way ANOVA and Sidak's post hoc analysis. (B) Mean displacement over 6h of NCC cultures under maintenance conditions evaluated through time lapse imaging (see also supplemental multimedia). Values are the mean ± SEM. Statistical significance was determined using one-way ANOVA and Tukey's post hoc analysis. (C&D) Quantification of immunofluorescence intensity of mesenchymal TSC markers, (C) P-S6 (n = 10; 3x for H1, H7, 168, 1x for H9) and (D) α-smooth muscle actin (n = 12; 3x for each line), in maintenance NCCs. (E) Representative immunofluorescence LAM marker staining of *WT* and *TSCS2*$^{-/-}$ NCCs. Scale bar, 50μm. (F) Percentage of NCCs reactive to HMB45 immunofluorescence staining. Values are the mean ± SEM (n = 14, ≥ 3x for each cell line). Statistical significance was determined using unpaired t-test. Adapted from Delaney et al. 2019, bioRxiv, 683359 (Delaney, Julian et al. 2019).

TSC2$^{-/-}$ cells reactive with this antibody and displayed similar staining patterns to that seen in primary LAM cells (Figure 3.3.3E&F) (Pacheco-Rodriguez, Steagall et al. 2007). Additionally, both WT and *TSC2*$^{-/-}$ NCCs stain positive for ERα and PR at comparable levels (Figure 3.3.4A). In addition, immunoblotting of NCC maintenance cultures revealed expression of the TSC biomarker VEGFD in both WT and *TSC2*$^{-/-}$ NCCs, with increased PDGFRß protein levels in *TSC2*$^{-/-}$ NCCs (Figure 3.3.4B&C). The expression of multiple hallmark TSC tumor markers in both *WT* and *TSC2*$^{-/-}$ cells suggests that NCCs are inherently well suited to model mesenchymal TSC. However, elevated HMB45 reactivity and PDGFRß expression, together with the enhanced migratory mesenchymal phenotype of *TSC2*$^{-/-}$ NCCs, strongly support the use of these cells as an accurate model of the mesenchymal manifestations of TSC and LAM.

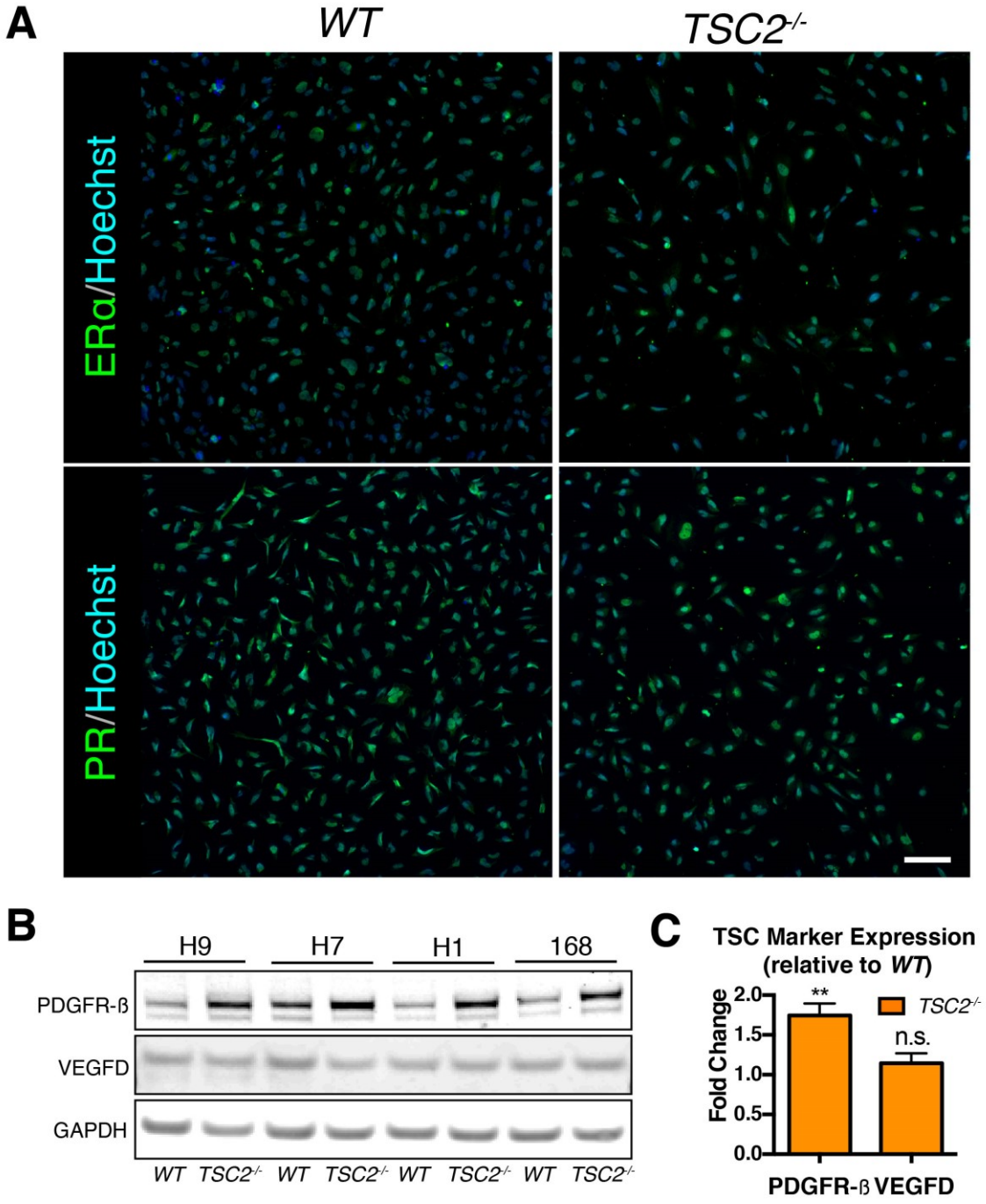

Figure 3.3.4: *TSC2*$^{-/-}$ NCCs express hallmark markers of LAM.
(A) Representative immunofluorescence staining of the LAM markers ERα and PR in *WT* and *TSCS2*$^{-/-}$ NCCs. Scale bar, 100μm. (B) Western blot of maintenance NCCs probing for VEGFD and PDGFRß, (C) quantified via densitometry and normalized to *WT* protein levels using GAPDH, reveals PDGFRß expression is significantly upregulated. Values are mean ± SEM (n = 8; 2x for each cell line), statistical significance was calculated using student's t-test. Adapted from Delaney et al. 2019, bioRxiv, 683359 (Delaney, Julian et al. 2019).

3.4 TSC2 mutant NCCs show promise for use in a preclinical model of LAM

As detailed in Chapter 1, section 1.3.3, no animal model exists to specifically investigate the neural crest cell of origin theory. Furthermore, no preclinical model exists that accurately recapitulates LAM disease pathogenesis. Furthermore, section 3.3 clearly establishes that *TSC2*$^{-/-}$ NCCs accurately models multiple LAM cell phenotypes *in vitro*. Thus, using these cells to develop a preclinical model of LAM through orthotopic xenotransplantation is a rational next step to advance the LAM research field.

Early preliminary data using tdTomato labeled *TSC2*$^{\Delta/\Delta}$ teratoma-derived explant SMC (tSMCs) cultures provided insight on this front. 2 months following intratracheal injection of *TSC2*$^{\Delta/\Delta}$ tSMCs into immunocompromised NOD/SCID mice, lungs were harvested for both explant culture and sectioning for immunohistochemistry (IHC). Multiple tumors were clearly visible via tdTomato fluorescence immediately following lung excision for explant culture (Figure 3.4.1A&B). IHC analysis of lung sections furthermore revealed micro-foci of cells reactive to RFP antibody (tdTomato^{+}) and human specific Calponin antibody (Figure 3.4.1C&D) Although promising, these micro-foci were sparse and did not appear to be forming cystic lesions. In addition, this modeling approach is cumbersome, as both specialized surgical skills are required to perform intratracheal injections and throughput is limited due to the complexity and time required to perform these injections.

With the preliminary *TSC2*$^{\Delta/\Delta}$ xenotransplantation data in consideration, a more accessible *in vivo* modeling approach was designed (Figure 3.4.2A). Tail vein injection of NCCs into immunodeficient mice was postulated to better model the circulating LAM cells observed in LAM patients while concurrently modeling the cell of origin. Furthermore, endpoint was extended to 10 months to allow pathological mechanisms to more fully progress as LAM tumors are slow growing neoplasms. Thus, *WT*, *TSC2*$^{\Delta/\Delta}$, and *TSC2*$^{-/-}$ NCCs were injected via tail vein into NOD-SCID mice and were monitored

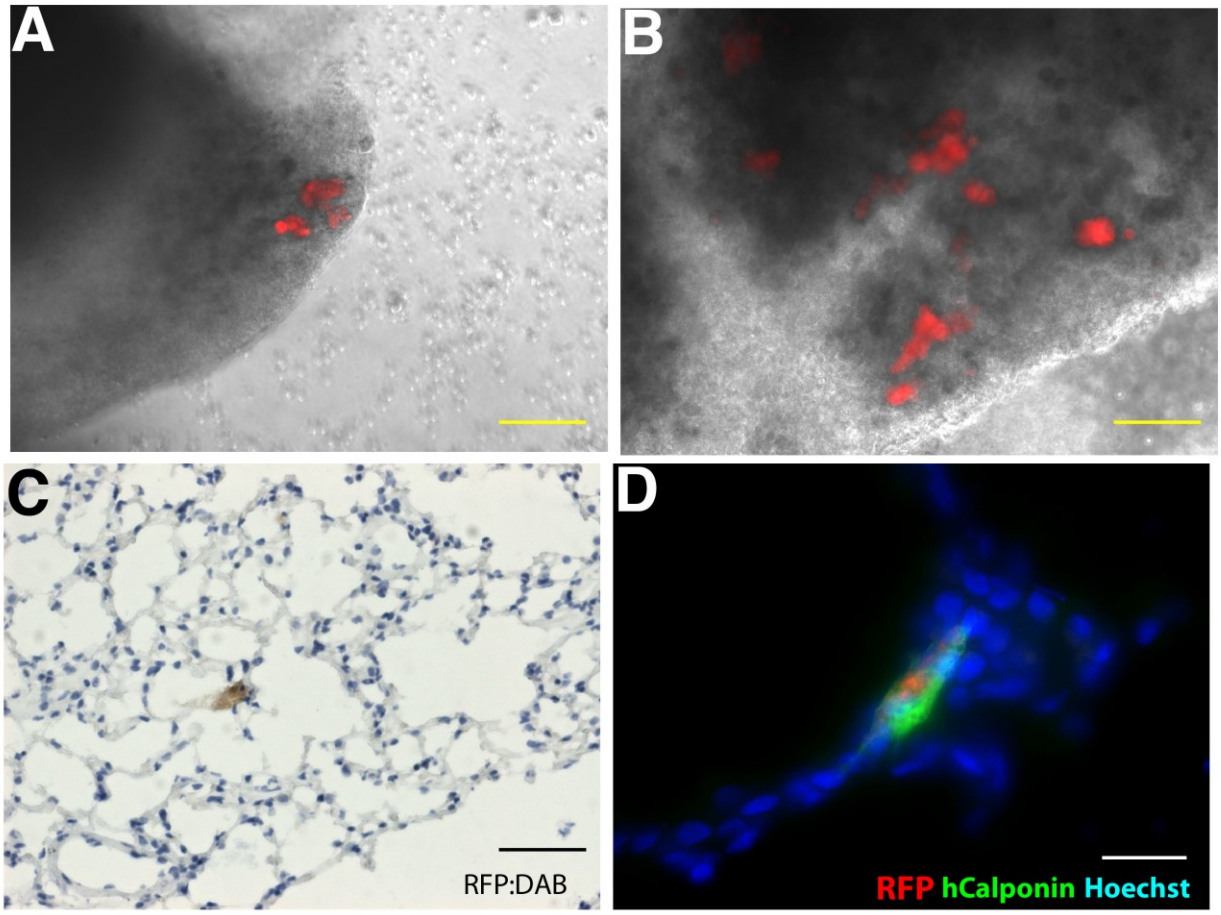

Figure 3.4.1: Preliminary *in vivo* modeling data utilizing *TSC2*$^{\Delta/\Delta}$ tSMCs
(A&B) Phase contrast/tdTomato fluorescence overlay of lung explants from NOD/SCID mice injected intratracheally with *TSC2*$^{\Delta/\Delta}$ tSMCs. tdTomato^{+} growths can clearly be observed embedded within the lungs. Scale bars, 100μm. (C) IHC probing with RFP antibody reactive to tdTomato. DAB staining (brown) shows a small cluster of tSMCs. Scale bar, 100μm. (D) IF of mouse lungs probing for both tdTomato and calponin using a human-specific calponin antibody. Fluorescence image overlay reveals a small cluster of tSMCs within the lungs. Scale bar, 50μm.

over 10-month period. No obvious distress or behavioral changes were noted in any treatment group. After 10 months, mice were sacrificed, and lungs were harvested and sectioned for IHC analysis. Upon inspection of lung tissue explants, multiple mCherry^{+} growths were observed in all mice injected with NCCs (Figure 3.4.2B). The formation of tumors in *WT* samples was not unexpected, as the injection of proliferative progenitor cells are likely to result in tumor formation in most any context. Tissue explant cultures could not be established. However, supporting the use of TSC2 deficiency NCCs to model LAM, IHC probing for the LAM marker, P-S6, revealed the accumulation of P-S6^{+} cells within the bronchioles of mice injected with *TSC2*$^{\Delta/\Delta}$ and *TSC2*$^{-/-}$ NCCs (Figure 3.4.2C), highly reminiscent of pathological findings in LAM patients; mice injected with *WT* NCCs displayed limited P-S6 staining. Although limited (n = 2 for each treatment group), these are promising proof of concept data and are supportive of continued investigation and development of a humanized NCC-based preclinical model of LAM.

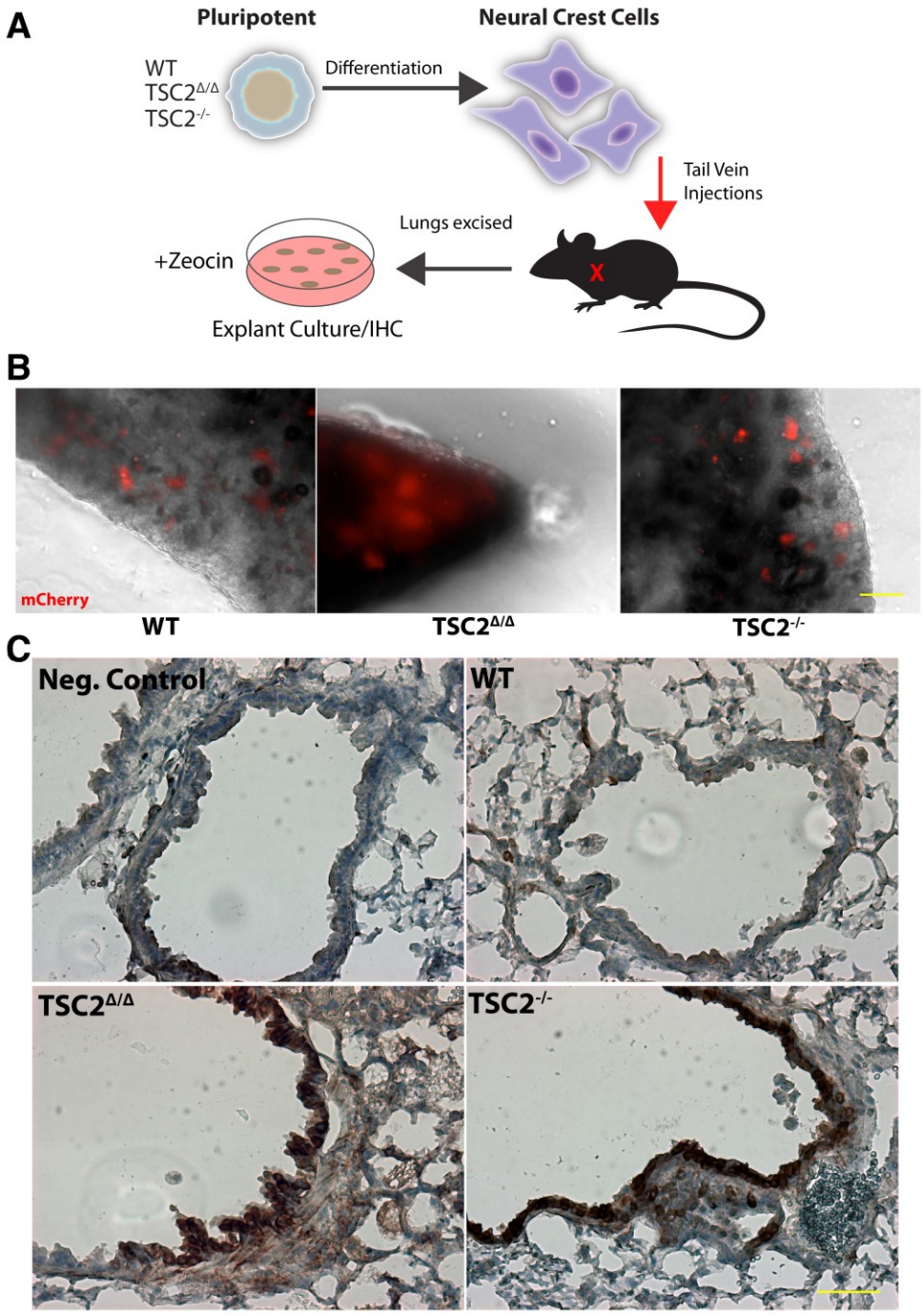

Figure 3.4.2: Xenotransplantation of *TSC2* mutant NCCs results in LAM nodule-like pathology

(A) Schematic representation of xenotransplantation NCC-LAM model. (B) Lung tissue explants of NSG mice injected via tail vein with WT, *TSC2*$^{\Delta/\Delta}$, and *TSC2*$^{-/-}$ NCCs indicate the presence of multiple mCherry^{+} positive growths. Scale bar, 100μm. (C) IHC of mouse lung tissue sections probing for P-S6. Mice injected with *TSC2* mutant NCCs display clusters of P-S6^{+} cells within the bronchioles, reminiscent of LAM lung pathology. Scale bar, 100μm.

CHAPTER 4:

Transcriptomic profiling of NPC/NCC lineage induction in TSC2 deficient cells

Chapter 4 has been adapted from:

Delaney, S. P., L. M. Julian, A. Pietrobon, J. Yockell-Lelièvre, C. Doré, T. T. Wang, V. C. Doyon, A. Raymond, D. A. Patten, M.-E. Harper, H. Sun and W. L. Stanford (2019). "Stem cell models identify lineage-specific catabolic signaling, neoplastic mechanisms and therapeutic vulnerabilities in tuberous sclerosis." bioRxiv: 683359.

Original Manuscript:
Conceptualization, **S.P.D.**, L.M.J., and W.L.S.
Methodology, **S.P.D.** and L.M.J.
Investigation, **S.P.D.**, L.M.J., A.P., J.Y-L., C.D., T.T.W., V.C.D., A.R., D.A.P., M.E.H., and H.S.
Formal Analysis, **S.P.D.**, L.M.J., A.P., J.Y-L, T.T.W., and S.H.
Writing – Original Draft, **S.P.D.** and L.M.J.
Writing – Review & Editing, **S.P.D.**, L.M.J., A.P., J.Y-L., D.A.P., M.E.H., H.S., and W.L.S.
Funding Acquisition, **S.P.D.**, L.M.J., and W.L.S
Resources, W.L.S.
Visualization, **S.P.D.**, L.M.J., J.Y-L.
Supervision, W.L.S.

Contributions to this chapter:
All experiments were conceptualized by **SPD** and LMJ, with guidance from WLS. Data presented in Figures 4.1.1D, 4.1.2, 4.1.4D-F, 4.1.5, 4.2.1A&D, 4.2.2C,E&F were generated by LMJ. Data presented in Figures 4.2.1E-I, 4.2.2A&B were generated by AP. Data presented in Figure 4.3.1 was generated with assistance from JY-L. All other data presented in this chapter was generated by **SPD**.

4.1 Transcriptome analysis of NPC & NCC lineage specification in TSC2 deficient cells

Chapter 3 described the generation and validation of the stem cell-based model of LAM and neurological TSC using NCCs and NPCs, respectively. These progenitor cell lineages faithfully recapitulate multiple aspects of LAM and TSC pathophysiology, validating their use as cell models for these diseases. As described in section 3.2.2, both qualitative and quantitative observations indicated TSC2-dependent phenotypes emerge upon differentiation towards NPC/NCC lineages. These observations included altered morphology and migratory phenotypes in *TSC2*$^{-/-}$ cultures, and RT-qPCR-based analysis of key genes involved in early neural and neural crest differentiation suggested differential transcriptome profiles emerge in TSC2 deficient cultures. As the differentiation protocols utilized in this study model early neural/neural crest lineage specification during embryonic development, we reasoned that in-depth transcriptomic profiling of both NPC and NCC differentiation could reveal valuable insight into the developmental pathogenesis of TSC and LAM.

Thus, genome-wide RNA-seq was performed along a developmental time course of *TSC2*$^{-/-}$ and *WT* hPSCs as they were induced to differentiate through the NPC and NCC lineages using the parallel dSMADi strategies (Figure 3.2.1). RNA-seq timepoints were selected to monitor global gene expression throughout the high-density monolayer NPC-differentiation protocol corresponding to states of pluripotency (day 0), early neural induction (day 1), neuralization (days 3&5), and neural precursor specification and maturation (days 8&12) (Figure 3.2.1A, red asterisks). As mentioned previously, to identify transcriptional changes at various stages of the EB-based NCC protocol, RNA-seq time points were similarly selected to emphasize phases of transition during differentiation: EB-formation (day 1), dSMADi-induced neuralization (days 2&4), NCC specification (day 7) and enrichment (day 10) (Figure 3.2.1B, red asterisks). RNA-seq was performed on all four isogenic paired lines, serving as biological replicates for

analysis of expression patterns within each respective differentiation time course for a total of 96 sequenced libraries.

4.1.1 TSC2-deficiency drives large-scale cell type-specific transcriptional dysregulation upon NPC and NCC lineage induction

Initial analysis of the RNA-seq data structure through principal component analysis (PCA) revealed distinct trajectories between *WT* and *TSC2*$^{-/-}$ samples within each differentiation time course, indicating dynamic transcriptional changes between genotypes from pluripotency to target cell lineage (Figure 4.1.1A). Clear separation between *WT* and *TSC2*$^{-/-}$ samples was attributed to principal component (PC) 2 during NPC differentiation and to PC4 during NCC induction, implying that TSC2-deficiency is more impactful to transcriptional variance in NPC differentiation.

Confirming our findings that TSC2-deficiency does not affect maintenance and pluripotency of hPSCs (Figure 3.1.3D, Figure 3.1.4), the number of differentially expressed genes (DEGs) between *WT* an d *TSC2*$^{-/-}$ cells at day 0 (pluripotent state) was negligible (6 and 19 genes identified respectively in NPC and NCC data sets) (Figure 4.1.1B). Likewise, very few DEGs were detected at day 1 of NCC induction (59 genes), a time-point representing a change in cell substrate interactions (switch from Matrigel adherence to suspension EB formation) but prior to the initiation of neuralization using dSMADi. Strikingly, *TSC2*$^{-/-}$ cells in both differentiation paradigms demonstrated a substantial number of DEGs compared to *WT* within 24 hours of neural induction (day 1 NPCs, 621 genes; day 2 NCCs, 189 genes), which expanded to thousands of DEGs at 3 days post-induction (day 3 NPCs, 3626 genes; day 4 NCCs, 2830 genes) (Figure 4.1.1B). While the TSC2-mTORC1 signaling axis has been implicated in transcriptional regulation in various biological settings this has not been previously evaluated in the context of lineage induction during embryonic development. The magnitude of DEGs

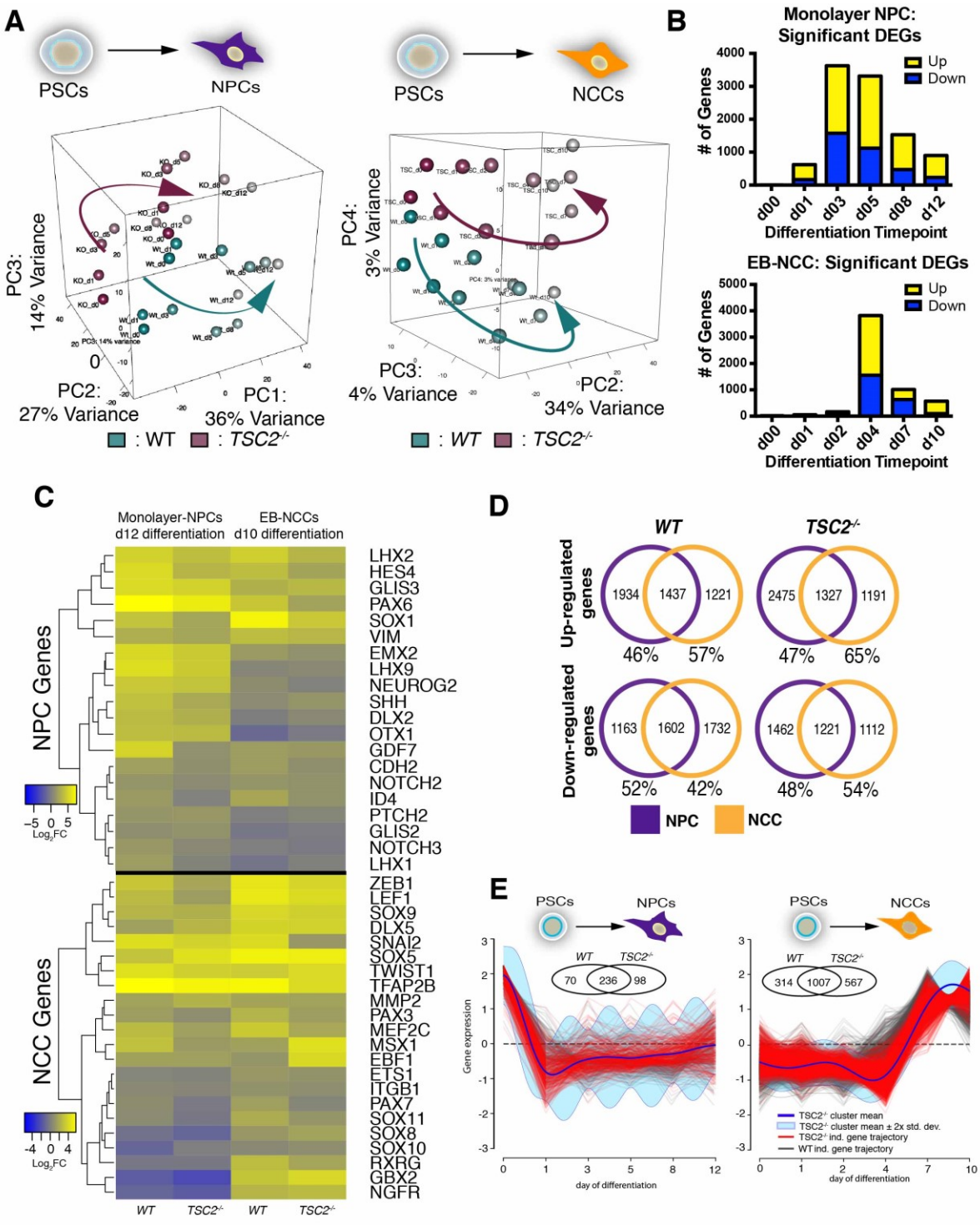
A
PSCs
NPCs
PC3: 14% Variance
PC2: 27% Variance
PC1: 36% Variance
: WT : TSC2-/-
PSCs
NCCs
PC4: 3% Variance
PC3: 4% Variance
PC2: 34% Variance
: WT : TSC2-/-
B
Monolayer NPC: Significant DEGs
# of Genes
Up
Down
d00 d01 d03 d05 d08 d12
Differentiation Timepoint
EB-NCC: Significant DEGs
# of Genes
Up
Down
d00 d01 d02 d04 d07 d10
Differentiation Timepoint
C
Monolayer-NPCs d12 differentiation
EB-NCCs d10 differentiation
NPC Genes
NCC Genes
Log2FC
LHX2
HES4
GLIS3
PAX6
SOX1
VIM
EMX2
LHX9
NEUROG2
SHH
DLX2
OTX1
GDF7
CDH2
NOTCH2
ID4
PTCH2
GLIS2
NOTCH3
LHX1
ZEB1
LEF1
SOX9
DLX5
SNAI2
SOX5
TWIST1
TFAP2B
MMP2
PAX3
MEF2C
MSX1
EBF1
ETS1
ITGB1
PAX7
SOX11
SOX8
SOX10
RXRG
GBX2
NGFR
WT TSC2-/- WT TSC2-/-
D
WT
TSC2-/-
Up-regulated genes
1934 1437 1221
46% 57%
2475 1327 1191
47% 65%
Down-regulated genes
1163 1602 1732
52% 42%
1462 1221 1112
48% 54%
NPC
NCC
E
PSCs
NPCs
WT TSC2-/-
70 236 98
Gene expression
day of differentiation
PSCs
NCCs
WT TSC2-/-
314 1007 567
TSC2-/- cluster mean
TSC2-/- cluster mean ± 2x std. dev.
TSC2-/- ind. gene trajectory
WT ind. gene trajectory
day of differentiation

Figure 4.1.1: RNA-seq time-course analysis reveals differential gene expression during NPC and NCC differentiation
(A) Representative three-dimensional plotting of PCA of monolayer-NPC (H1 & 168) and EB-NCC (H7 & H9) differentiations. (B) Number of total DEGs identified (FDR < 5%) over the RNA-seq differentiation time-course in monolayer-NPC and EB-NCC RNA-seq datasets. (C) Heatmap displaying log_2 fold change of select hallmark NPC and NCC genes at RNA-seq endpoint for monolayer-NPC and EB-NCC differentiations. (D) Venn diagrams featuring the intersections of significantly up/down regulated genes of *WT* and *TSC2*$^{-/-}$ cultures at differentiation endpoint. Genes included were those with FDR<0.05, and a log2FC of >1.0 (up-regulated) or >-1.0 (down-regulated) at end-point compared to day0 of the given cell type. (E) Representative gene clusters displaying similar expression trajectories in *WT* and *TSC2*$^{-/-}$ cultures throughout monolayer-NPC and EB-NCC differentiations. Adapted from Delaney et al. 2019, bioRxiv, 683359 (Delaney, Julian et al. 2019).

that we observed within 24-72 hours of neural induction was highly unexpected and indicates that TSC2 is a potent regulator of genome-wide transcriptional programs during NE fate determination, potentially affecting NPC and NCC specification.

During both induction protocols, the number of *WT* versus *TSC2*$^{-/-}$ DEGs peaked 3 days following the addition of neuralization cues and remained substantially elevated at each respective end-point (day 12 NPCs, 898 genes; day 10 NCCs, 609 genes) (Figure 4.1.1B). Notably, NPC cultures exhibited larger gene expression differences across all differentiation time-points compared to NCCs. Confirming that our parallel differentiation strategies generate distinct cell populations, NPC/NCC lineage-specific gene expression is distinct between differentiation protocols at endpoint (Figure 4.1.1C).

Furthermore, 42-57% of DEGs at end-point compared to day 0 in *WT* cultures are unique to their target cell type (Figure 4.1.1D). In *TSC2*$^{-/-}$ cultures, cell-type specific DEGs at endpoint increased up to 65% (Figure 4.1.1D). Together, this reveals that while there is a large degree of overlapping DEGs between NPC and NCC-induced cultures, as is expected given their similar developmental origins, NPC and NCC-induced cultures also display distinct transcriptional profiles reflecting their unique cell lineages. This is reminiscent of the distinct disease phenotypes in patient neurological versus mesenchymal lesions.

To evaluate the influence of TSC2-deficiency on specific gene expression profiles, differential gene expression was evaluated between adjacent differentiation time points of NPC and NCC differentiation. Genes displaying significant fold-change in at least one set of adjacent time points were selected and grouped by similarity of expression trajectories into multiple clusters using DP_GP_cluster (McDowell, Manandhar et al. 2018). The largest gene clusters within *WT* and *TSC2*$^{-/-}$ datasets of respective NPC and NCC analyses were selected and found to display similar trajectories with a high degree of overlap in DEG membership (Figure 4.1.1E). Of note,

the EB-NCC differentiation trajectory displays a sharp increase in gene expression at day 7. This represents the shift in gene expression coinciding with NCC specification and enrichment in adherent culture, whereas the monolayer-NPC trajectory shows stable expression of dSMADi induced genes from day 1 to endpoint. These trajectories illustrate that TSC2-deficiency does not overtly perturb dSMADi-induced expression profiles during differentiation. Indeed, at differentiation end-point, *TSC2*$^{-/-}$ cells did not display significantly altered expression of NE and NCC genes in NPC and NCC cultures, respectively, compared to WT samples (Figure 4.1.1C). Upon further investigation of gene sets relevant to NE and NCC formation, reflecting gene expression analysis in section 3.2.2, a reduction in NE gene expression (Figure 4.1.2A) in *TSC2*$^{-/-}$ cells during NPC differentiation was observed, most prominently during mid-stages of differentiation. No change in NCC gene signatures was observed during NCC differentiation (Figure 4.1.2B). Corroborating these findings, expression of NE determinant genes in both *WT* and *TSC*$^{-/-}$ cultures was largely induced at days 3 and 5 in monolayer-NPC cultures, further increasing or remaining high through day 12 (Figure 4.1.2C). These same genes were induced to a similar degree at day 4 (and some at day 7) in EB-based NCC cultures but did not increase further or were completely lost at later time points. In contrast, expression of neural crest lineage genes was much higher in EB-based NCC cultures, initiating at day 4 and further increasing through day 10, revealing the progressive emergence of a dominant NCC fate in these cultures following initial neuralization (Figure 4.1.2D). Thus, while TSC2-deficiency delays NPC fate induction, it does not overtly impede differentiation towards either the NPC or NCC lineage.

To assess the biological context of TSC2-deficiency on differential gene expression across NPC and NCC differentiation, gene ontology (GO) enrichment analysis was performed on significant DEGs between *TSC2*$^{-/-}$ and *WT* samples at each time point. The most dominant GO biological process terms resulting from this analysis

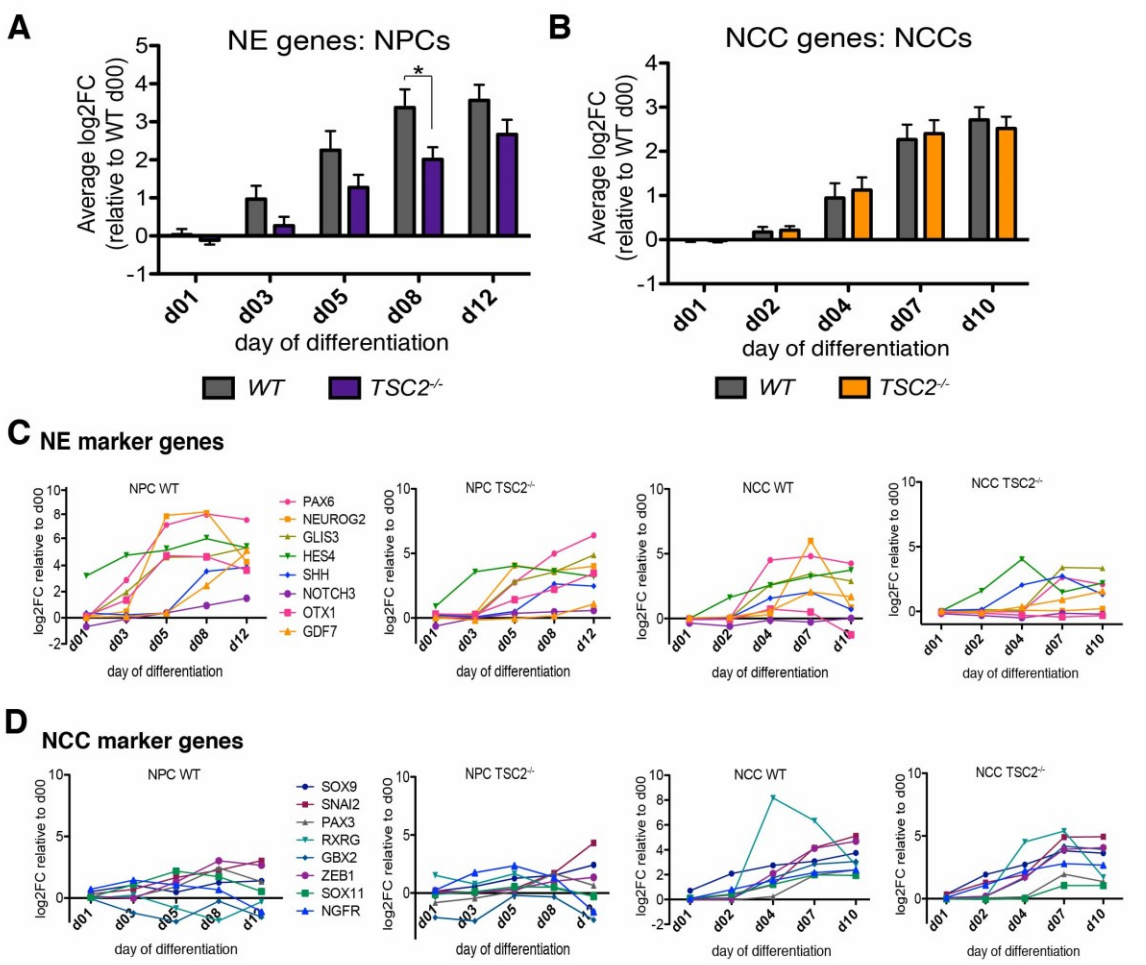

Figure 4.1.2: RNA-seq analysis reveals lineage-specific transcriptomic profiles
(A) Log_2 fold change (Log_2FC) of hallmark neuroectodermal (NE) genes over the monolayer-NPC RNA-seq time-course. (B) Log_2FC of hallmark NCC specification genes over the EB-NCC RNA-seq time-course. No statistical significance was observed between WT and $TSC2^{-/-}$ samples at any time point. (C) Expression profiles of neuroepithelial (NE) genes throughout NPC and NCC differentiation, with the gene set analyzed indicated at the top of each graph. (D) Expression profiles of neural crest specification genes throughout NPC and NCC differentiation, with the gene set analyzed indicated at the top of each graph. Adapted from Delaney et al. 2019, bioRxiv, 683359 (Delaney, Julian et al. 2019).

were related to endoplasmic reticulum (ER)/proteostatic-stress, response to unfolded protein, and autophagy (Figure 4.1.3A, red box). During *TSC2*$^{-/-}$ NPC differentiation these GO term groupings were over-represented consistently across most timepoints, all of which were significantly enriched until day 5, with autophagy-related terms being maintained until day 8. In contrast, these terms were only over-represented at days 2 and 4 of *TSC2*$^{-/-}$ NCC differentiation. This temporal enrichment pattern is consistent with KEGG pathway analysis, which revealed enrichment for “protein processing in the ER”, “lysosome”, and “phagosome”, in *TSC2*$^{-/-}$ cultures compared to *WT* (Figure 4.1.3B). Similar to GO enrichment analysis (Figure 4.1.3A), the KEGG pathway terms associated with ER/proteostatic stress response and catabolic vesicular signaling are enriched only transiently during *TSC2*$^{-/-}$ NCC differentiation, specifically at days 4 and 7. Of note, these time points are associated with the neuralization stages of differentiation (days 2 and 4) and precede NCC enrichment (day 7) when adherent neuralized clusters predominate the differentiating cultures. This implies that the activation and stability of an ER/proteostatic stress and catabolic signaling response in *TSC2*$^{-/-}$ cells is associated with neuralization of the differentiating cultures and maintenance of an NPC fate.

4.1.2 TSC2$^{-/-}$ *NPCs and NCCs exhibit unique catabolic signalling profiles during development*

RNA-seq analyses of NPC and NCC differentiation revealed significant enrichment of genes involved in lysosomal and autophagy signaling in differentiating *TSC2*$^{-/-}$ populations. These genes were differentially expressed throughout the entire monolayer-NPC differentiation protocol, whereas during EB-based NCC induction, these enrichment terms were transient. To investigate this further, hierarchical clustering was performed on all RNA-seq samples comparing *TSC2*$^{-/-}$ to *WT* gene expression at each

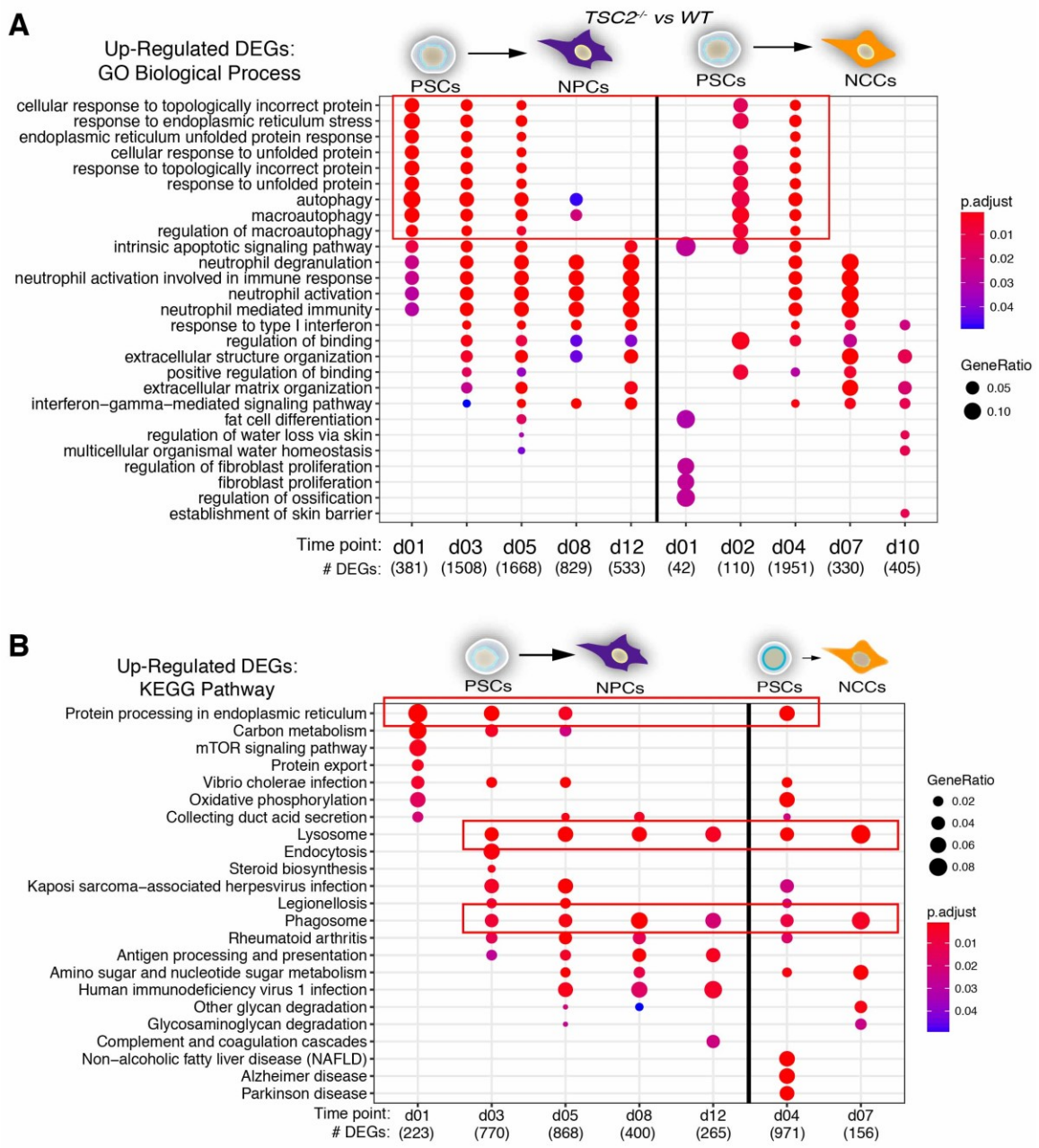

Figure 4.1.3: A cell stress response underlies neuroepithelial induction of *TSC2*-deficient cells

(A) Comparative gene ontology (GO)-Biological Function enrichment analysis of upregulated DEGs (padj < 0.05) between matched *TSC2*$^{-/-}$ and WT samples at each respective time point of monolayer-NPC and EB-NCC differentiations. Red box highlights enrichment of stress response GO terms. (B) Comparative KEGG pathway enrichment analysis of upregulated DEGs (padj < 0.05) in *TSC2*$^{-/-}$ samples compared to *WT* at each respective time point of monolayer-NPC and EB-NCC differentiations. Red boxes highlight enrichment of stress response pathways. Enrichment data is available in Tables S4 and S5. Adapted from Delaney et al. 2019, bioRxiv, 683359 (Delaney, Julian et al. 2019).

time point, focusing on genes associated with lysosome signaling and formation, along with positive and negative regulation of autophagy (Figure 4.1.4A-C). As expected, NCC differentiation sample day 4, the height of EB neuralization, clusters with NPC differentiation days 3 and 5, showing distinctive upregulation of lysosome-associated genes (Figure 4.1.4A, red box). In contrast, early NPC time points cluster well with both early and late NCC differentiation time points and display limited differential gene expression from *WT* cells (Figure 4.1.4A, green box). Interestingly, NCC day 4 and NPC days 3 and 5 display similar expression patterns of genes associated with negative regulation of autophagy (Figure 4.1.4B, red box); however, NPC days 3 and 5 cluster separately from NCC day 4 when profiled with genes positively regulating autophagy (Figure 4.1.4C, red box). In the latter case, NCC day 4 continues to cluster with NPC time points, separate from all other NCC samples (Figure 4.1.4C, yellow box). Thus, gene-set specific hierarchical clustering of DEGs between *WT* and *TSC2*$^{-/-}$ cells in both NPC and NCC datasets reveals that lysosome/autophagy gene expression dysregulation reaches its peak at differentiation time points associated with neuralization of the respective cell populations, and that this catabolic signaling phenotype persists uniquely within the NPC lineage. Lysosome staining of differentiating NPC cultures with both a LAMP1 antibody and Lysosensor live cell dye confirmed that lysosomal content is significantly increased in *TSC2*$^{-/-}$ cells throughout the differentiation time course post-neuralization (Figure 4.1.4D-F). This phenotype is rescued when the mTORC1 inhibitor rapamycin is included in culture medium starting 6 hours prior to dSMADi, revealing the dependency of *TSC2* on mTORC1 for lysosomal regulation during early neural lineage induction. As this is counter-intuitive, considering how mTORC1 activation is typically thought to repress catabolic signaling, we investigated the sub-cellular localization of the lysosomal transcription factor TFE3, which is typically excluded from the nucleus upon mTORC1 activation resulting in inhibition of lysosomal biogenesis. Corroborating our

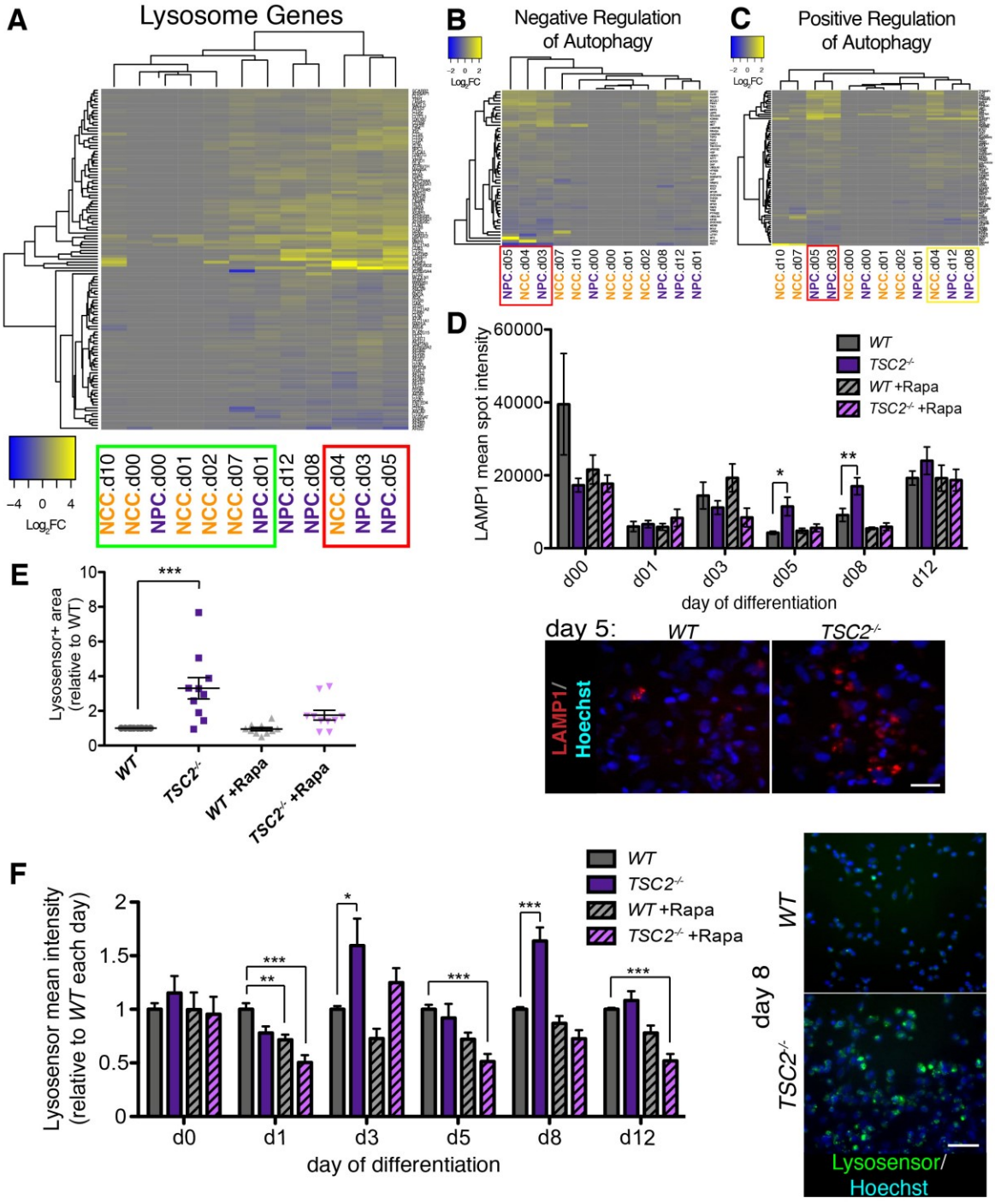
A
Lysosome Genes
−4 0 4
Log2FC
NCC.d10
NCC.d00
NPC.d00
NCC.d01
NCC.d02
NCC.d07
NPC.d01
NPC.d12
NPC.d08
NCC.d04
NPC.d03
NPC.d05
B
Negative Regulation of Autophagy
C
Positive Regulation of Autophagy
D
LAMP1 mean spot intensity
60000
40000
20000
0
WT
TSC2-/-
WT +Rapa
TSC2-/- +Rapa
d00
d01
d03
d05
d08
d12
day of differentiation
day 5:
WT
TSC2-/-
LAMP1/
Hoechst
E
Lysosensor+ area (relative to WT)
10
8
6
4
2
0
***
WT
TSC2-/-
WT +Rapa
TSC2-/- +Rapa
F
Lysosensor mean intensity (relative to WT each day)
2
1.5
1
0.5
0
WT
TSC2-/-
WT +Rapa
TSC2-/- +Rapa
d0
d1
d3
d5
d8
d12
day of differentiation
day 8
WT
TSC2-/-
Lysosensor/
Hoechst

Figure 4.1.4: NPCs and NCCs exhibit distinct catabolic signalling profiles during development, which are exacerbated by TSC2-deficiency
(A) Heatmap featuring hallmark lysosome genes displaying Log_2FC of *TSC2*$^{-/-}$ compared to *WT* samples at each respective timepoint of monolayer-NPC and EB-NCC RNA-seq datasets. Red box highlights time points associated with increased lysosome gene expression. Green box highlights time points of minimal differential lysosome gene expression. (B&C) Heatmaps of genes involved in negative and positive regulation of autophagy, displaying Log_2FC of *TSC2*$^{-/-}$ compared to *WT* samples at each respective time point of monolayer-NPC and EB-NCC RNA-seq datasets. Red boxes highlight timepoints associated with increased differential gene expression. Yellow box highlights clustering of NCC d04 time point with late NPC timepoints featuring moderate differential gene expression. (D) Representative images (at differentiation day 5) and quantification of LAMP1 immunofluorescence intensity (mean spot analysis) in the presence and absence of rapamycin throughout monolayer-NPC differentiation. Values are mean ± SEM (n = 10; 1x H9, 3x H1, 2x H7, 4x 168). Scale bar, 50μm. (E) Quantification of the cytoplasmic area of Lysosensor staining relative to *WT* at day 5 of monolayer-NPC differentiation. Values are mean ± SEM (n = 10; 1x H9, 3x H1, 2x H7, 4x 168). (F) Quantification of fluorescence intensity of Lysosensor live cell stain in *WT* and *TSC2*$^{-/-}$ cultures during monolayer-NPC differentiation, ± 20nM rapamycin. Values are mean ± SEM (n=10; 1x H9, 3x H1, 2x H7, 4x 168); representative images of Lysosensor staining of differentiating NPCs at day 8 of differentiation. Scale bar, 50μm. Adapted from Delaney et al. 2019, bioRxiv, 683359 (Delaney, Julian et al. 2019).

findings, TFE3 nuclear localization was increased in *TSC2*$^{-/-}$ NPCs, in a rapamycin-dependent manner, with the largest changes occurring during days 3 and 5 of differentiation (Figure 4.1.5A&B), when catabolic gene expression was most highly dysregulated in these cultures in our RNA-seq data sets.

Our findings suggest that NCCs resolve this developmental catabolic response as they are specified and acquire migratory capacity. To investigate this, day 7 EB differentiation cultures were fixed and probed for lysosome and autophagosome indicators (LAMP1 and LC3β, respectively) via IF and coincide with lineage specific markers for NCCs (SOX9) and NPCs (PAX6) (Figure 4.1.6A&B). As expected, neuralized rosette clusters stain positive for PAX6, while migrating NCCs are SOX9^{+}. Neuralized rosette clusters, however, display a clear increase in lysosomal content compared to SOX9^{+} cells, as indicated by LAMP1 expression and Lysosensor staining (Figure 4.1.6A,C). Furthermore, autophagosome content was also increased in neural clusters as indicated by LC3β staining and autophagosome staining with Cyto-ID live cell dye (Figure 4.1.6A,D). Of note, lysosomal and autophagosome content appeared increased in *TSC2*$^{-/-}$ neuralized EB clusters compared to *WT* cells. Both LAMP1 and LC3β were detected in migrating SOX9^{+} cells; however, their expression is visibly diminished compared to NPC-rich clusters. Mirroring hierarchical clustering observations of 'positive' and 'negative' regulators of autophagy (Figure 4.1.4B&C), *TSC2*$^{-/-}$ monolayer cultures demonstrated reduced autophagosome staining compared to isogenic *WT* cultures during early induction. This is an expected consequence of *TSC2* loss, however, an atypical increase in autophagosome content was observed at late differentiation (Figure 4.1.5C). This suggests a dynamic regulation of autophagy signaling in *TSC2*$^{-/-}$ cells particularly as they differentiate through the neural lineage, with a lineage-dependent induction of autophagy signaling which, together with their

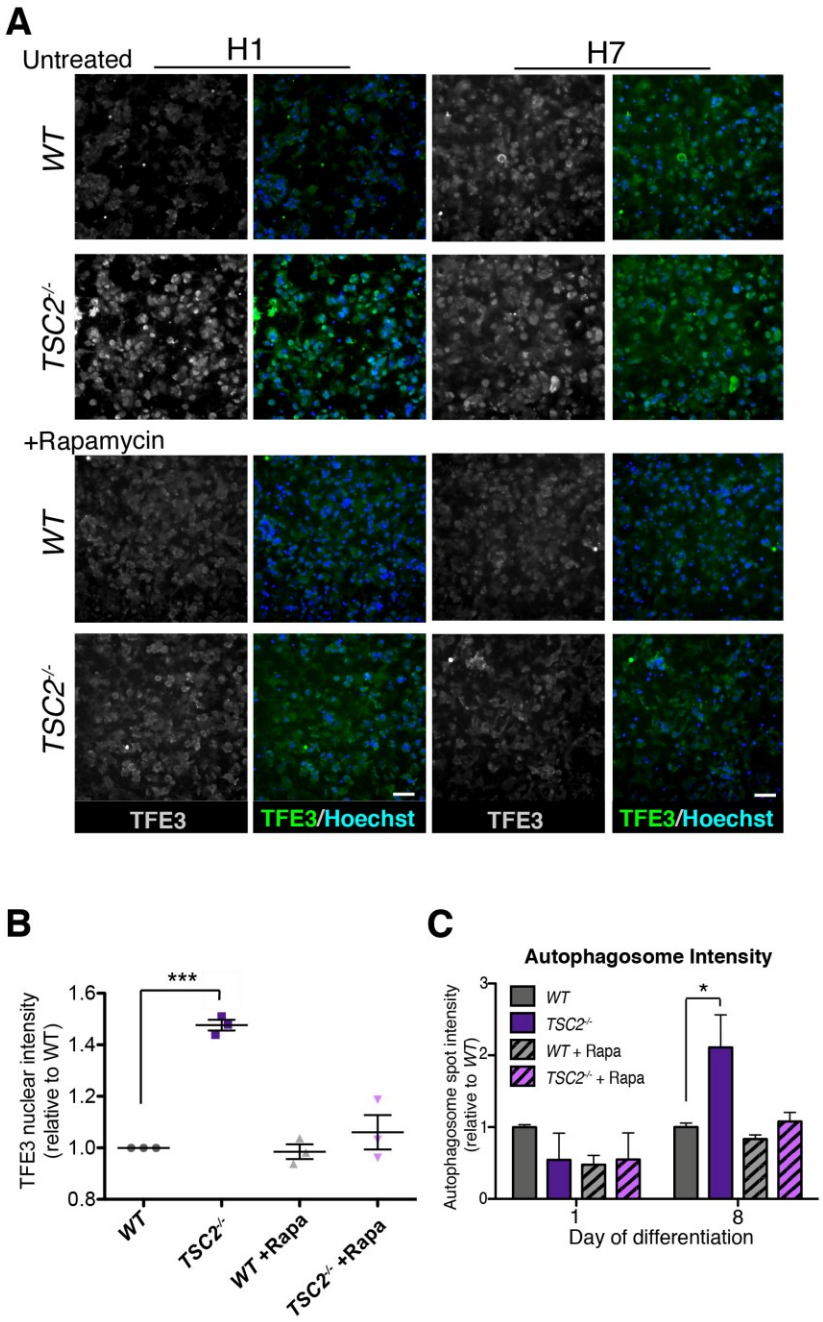

Figure 4.1.5: Aberrant catabolic signaling in *TSC2*$^{-/-}$ NPCs
(A&B) Representative images (A) and quantification (B) of fluorescence intensity relative to *WT* of nuclear TFE3 signal at day 5 of monolayer-NPC differentiation in J1 and J7 hPSCs. Values are mean ± SEM (n = 10; 1x H9, 3x H1, 2x H7, 4x 168). Scale bar, 50μm. (C) Quantification of CytoID autophagosome intensity in monolayer-NPC cultures at day 1 and 8 of lineage induction, in the absence and presence of 20nM rapamycin. Values are mean ± SEM (n=10; 1x H9, 3x H1, 2x H7, 4x 168). Adapted from Delaney et al. 2019, bioRxiv, 683359 (Delaney, Julian et al. 2019).

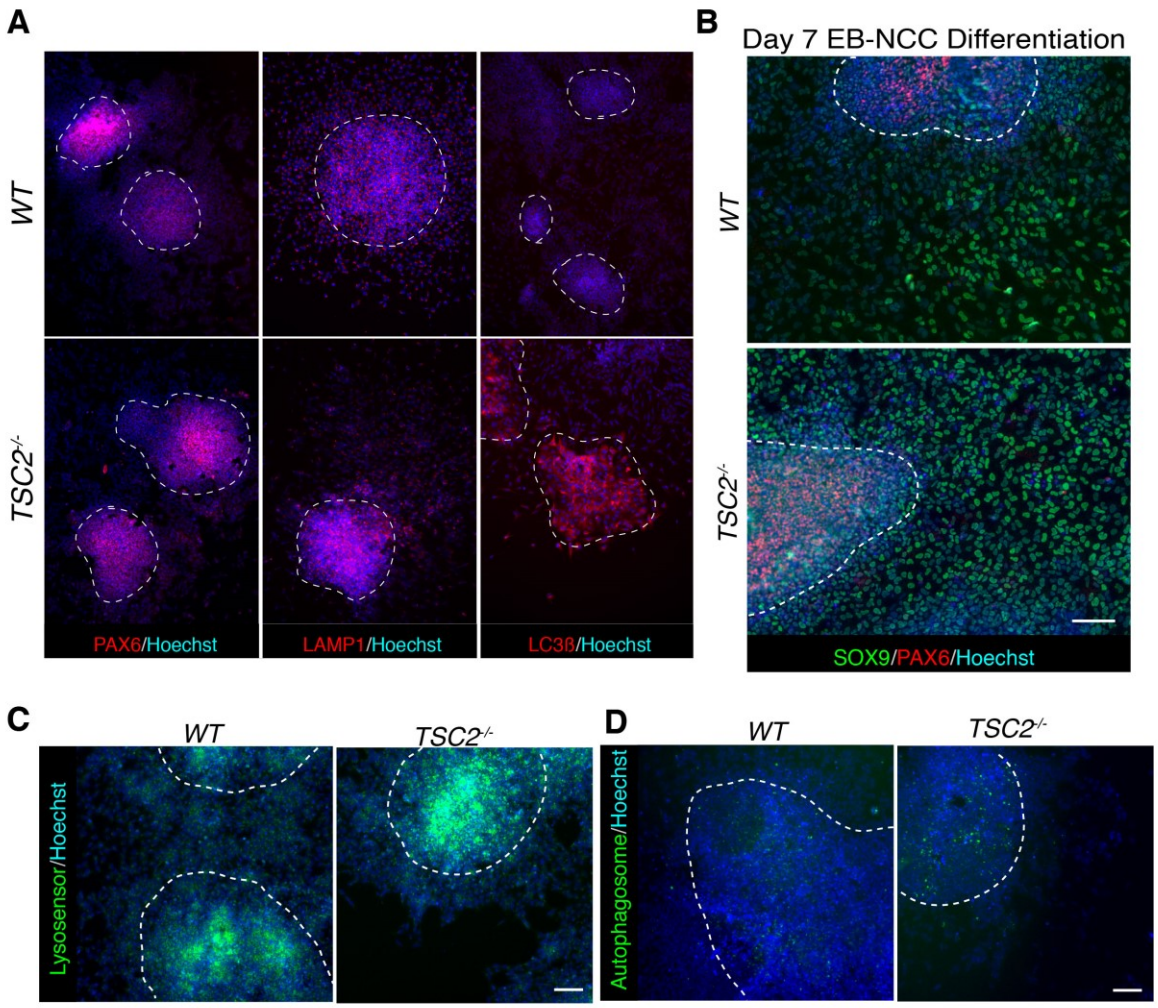

Figure 4.1.6: *TSC2*$^{-/-}$ NPCs uniquely display aberrant lysosome and autophagosome biogenesis.
(A) Immunofluorescent staining of attached neuralized EB clusters and migratory NCC outgrowths at day 7 EB-NCC differentiation. Dotted lines delineate the boundary of attached neuralized EB clusters. Scale bar, 100μm. (B) Example immunofluorescence staining of neuralized EB clusters (PAX6^{+}) and migratory NCCs (SOX9^{+}) at day 7 of EB-NCC differentiation. Dashed lines delineate borders of attached neuralized EB clusters. Scale bar, 100μm. (C&D) Example Lysosensor (C) and Autophagosome (D) live cell staining at day 7 EB-NCC differentiation. Dashed lines define the borders of adherent neuralized EB clusters. Scale bars, 100μm. Adapted from Delaney et al. 2019, bioRxiv, 683359 (Delaney, Julian et al. 2019).

increased lysosomal content, reflects the accumulation of vesicular structures observed in these cultures (Figure 3.3.1A) as well as in TSC tumors specifically within the brain (Goto, Talos et al. 2011, Di Nardo, Wertz et al. 2014).

4.2 TSC2-deficiency drives long-term catabolic and proteostatic dysregulation in NPCs but not NCCs

To determine whether the observed developmental cell stress responses we observed led to long-term lineage-specific differences in catabolic signaling mechanisms, we measured levels of endosomal vesicles in NCCs and monolayer culture-induced NPCs after multiple passages in maintenance culture. Reflecting developmental phenotypes, lysosomal content was highly increased in *TSC2*$^{-/-}$ NPCs (Figure 4.2.1A) compared to *WT* counterparts, but only slightly elevated in NCCs (1.4-fold versus 6-fold in NPCs) (Figure 4.2.1B&C). Rapamycin treatment had no effect on Lysosensor levels in either cell type; thus, unlike during lineage development, normal lysosomal content can no longer be restored with short-term mTORC1 inhibition. Furthermore, autophagosome content was unchanged between *WT* and *TSC2*$^{-/-}$ NCCs (Figure 4.2.1C) as measured by CytoID live cell dye; however, we observed a 7-fold increase in autophagosome intensity in *TSC2*$^{-/-}$ NPCs compared to *WT*s (Figure 4.2.1D). Autophagosome intensity was further increased following chloroquine treatment, demonstrating that both *WT* and *TSC2*$^{-/-}$ NPCs undergo autophagic flux (Figure 4.2.1D). This indicates that increased autophagosome content in *TSC2*$^{-/-}$ NPCs is primarily a consequence of increased biogenesis of these vesicles and not flux inhibition, contrary to the current paradigm of how mTORC1 hyperactivation is presumed to direct autophagy signaling. This unexpected observation was corroborated by a progressive increase in LC3β and autophagosome levels during *TSC2*$^{-/-}$ NPC induction (Figure

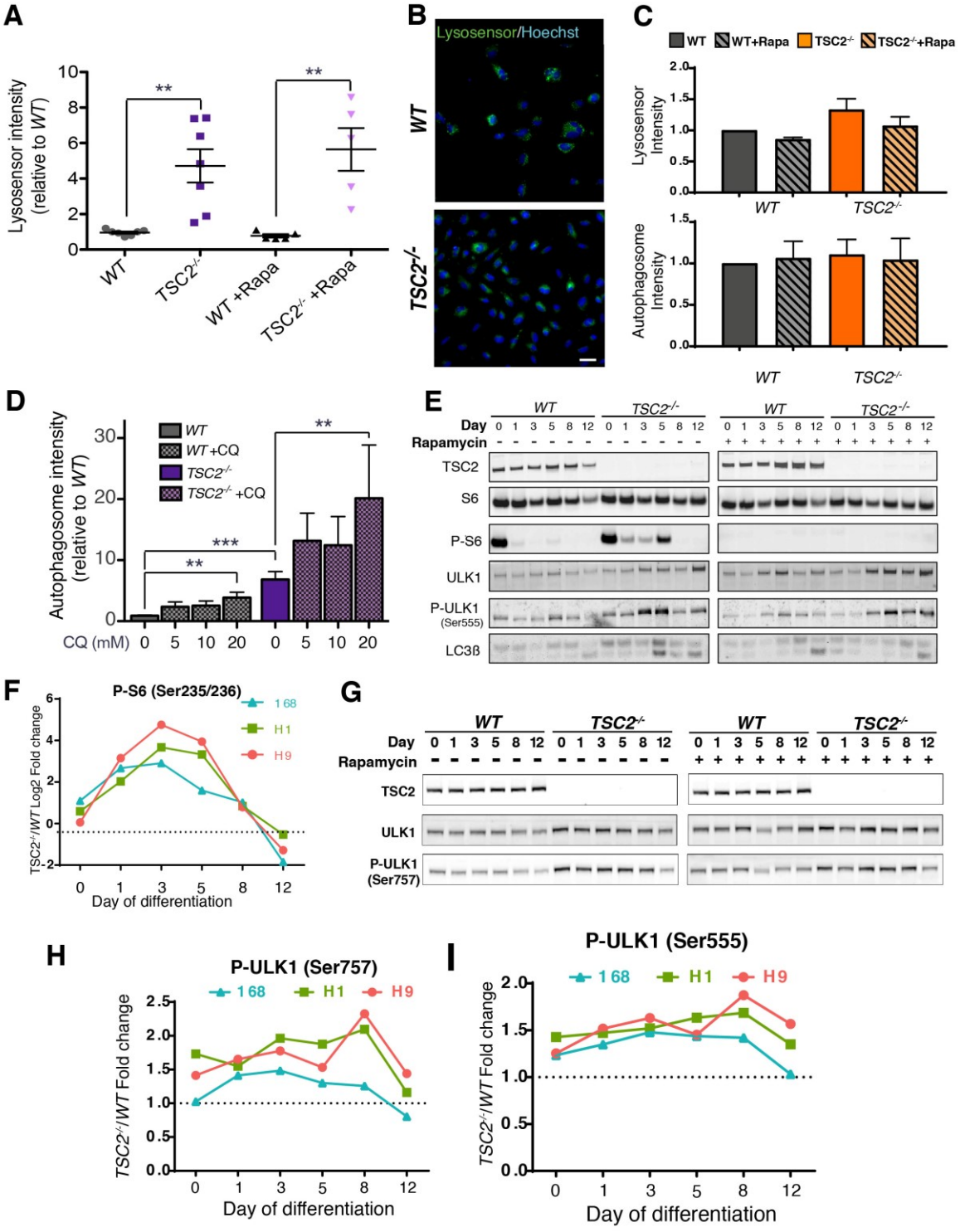
A
Lysosensor intensity (relative to WT)
WT
TSC2-/-
WT +Rapa
TSC2-/- +Rapa
B
Lysosensor/Hoechst
WT
TSC2-/-
C
WT
WT+Rapa
TSC2-/-
TSC2-/-+Rapa
Lysosensor Intensity
Autophagosome Intensity
D
Autophagosome intensity (relative to WT)
WT
WT +CQ
TSC2-/-
TSC2-/- +CQ
CQ (mM)
E
Day
Rapamycin
TSC2
S6
P-S6
ULK1
P-ULK1 (Ser555)
LC3β
F
P-S6 (Ser235/236)
168
H1
H9
TSC2-/-/WT Log2 Fold change
Day of differentiation
G
Day
Rapamycin
TSC2
ULK1
P-ULK1 (Ser757)
H
P-ULK1 (Ser757)
168
H1
H9
TSC2-/-/WT Fold change
Day of differentiation
I
P-ULK1 (Ser555)
168
H1
H9
TSC2-/-/WT Fold change
Day of differentiation

Figure 4.2.1: TSC2-deficiency drives long-term lineage-specific endosomal signaling adaptations
(A) Quantification of Lysosensor intensity in *WT* and *TSC2*$^{-/-}$ maintenance NPCs with and without 100nM rapamycin, relative to *WT* NPCs. Values are mean ± SEM (n = 7, representing all cell lines). Scale bar, 50μm. (B) Representative fluorescence images of maintenance *WT* and *TSC2*$^{-/-}$ NCCs. Scale bar, 50μm. (C) Quantification of Lysosensor (top) and autophagosome (Cyto-ID staining; bottom) fluorescence intensity signal in maintenance NCCs relative to *WT* NCCs. Values are mean ± SEM (n = 9; ≥ 2x for each line). No statistical significance was observed between treatment groups. (D) Quantification of autophagosome fluorescence intensity in maintenance NPCs, relative to *WT* NPCs, with and without 5-20nM chloroquine (CQ). Values are mean ± SEM (n = 13 for basal analysis, n = 7 (*WT*) and 8 (*TSC2*$^{-/-}$) for +CQ samples, representing all cell lines). (E) Representative Western blot in *WT* and *TSC2*$^{-/-}$ cultures during monolayer-NPC differentiation with and without 20nM rapamycin initiating 6h prior to differentiation. Proteins assessed are TSC2, ribosomal protein S6 and P-S6 at Ser-235/246, ULK1 and P-ULK1 at Serine-555 (AMPK-dependent), and LC3β. (F) Quantification of P-S6 by densitometry of 1 representative Western blot, as shown in panel E per cell line (H1, H9, 168). Results displayed are log2FC of *TSC2*$^{-/-}$ compared to *WT*. (G) Representative Western blot in *WT* and *TSC2*$^{-/-}$ cultures at days 0, 1, 3, 5, 8, and 12 of monolayer-NPC differentiation in the absence (left panel) and presence (right panel) of 20nM rapamycin initiating 6h prior to differentiation. Proteins assessed are TSC2, ULK1, and P-ULK1 at Serine-757 (mTORC1). (H) Quantification by densitometry of 1 representative Western blot (panel G) per cell line (H1, H9, 168), displayed as *TSC2*$^{-/-}$ over *WT* fold-change, for P-ULK1 at Serine-757. (D) Quantification as in panel F for P-ULK1 at Serine-555. Adapted from Delaney et al. 2019, bioRxiv, 683359 (Delaney, Julian et al. 2019).

4.2.1E, 4.1.5C), revealing an early establishment of this altered autophagy mechanism during lineage development.

To investigate likely mechanisms by which *TSC2*$^{-/-}$ NPCs are capable of promoting autophagy in the presence of hyperactive mTORC1 activity, we examined the phosphorylation status of ULK1, a kinase with essential roles in the early stages of pre-autophagosome formation. Phosphorylation of ULK1 at serine-757 is a critical event through which mTORC1 inhibits autophagy signaling. We confirmed both mTORC1 hyperactivation, based on increased P-S6 (serine-235/236) (Figure 4.2.1E&F), and increased phosphorylation of ULK1 serine-757 in *TSC2*$^{-/-}$ cells during NPC induction (Figure 4.2.1G&H). AMPK is a secondary kinase with ULK1-dependent activity, with its phosphorylation of serine-555 driving autophagy. We observed an increase in ULK1 serine-555 phosphorylation in differentiating *TSC2*$^{-/-}$ NPCs (Figure 4.2.1E&I) while AMPK levels were similar across genotypes (Figure 4.2.2A), revealing activation of this alternative autophagy-promoting pathway in these cells. Corroborating pro-autophagy signaling in *TSC2*$^{-/-}$ NPCs, total, unprocessed and lipidated forms of LC3β were increased in *TSC2*$^{-/-}$ cultures during monolayer-NPC induction, indicating increased autophagosome content (Figure 4.2.1E, Figure 4.2.2B). An increased LC3β-II/ LC3β-I ratio was also observed, demonstrating that autophagic flux is also elevated in *TSC2*$^{-/-}$ cells during NPC induction (Figure 4.2.2B).

Comparative gene ontology (GO) enrichment analysis of our RNA-seq data (Figure 4.1.3) illustrated an early activation of the misfolded protein response, which may function as a driving event for catabolic signaling activation in *TSC2*$^{-/-}$ cells during differentiation. We confirmed an increase in protein aggregate accumulation in *TSC2*$^{-/-}$ cells during neural differentiation using Proteostat aggresome indicator dye (Figure 4.2.2C-E). This phenotype was transient, however, with aggregate levels peaking at day

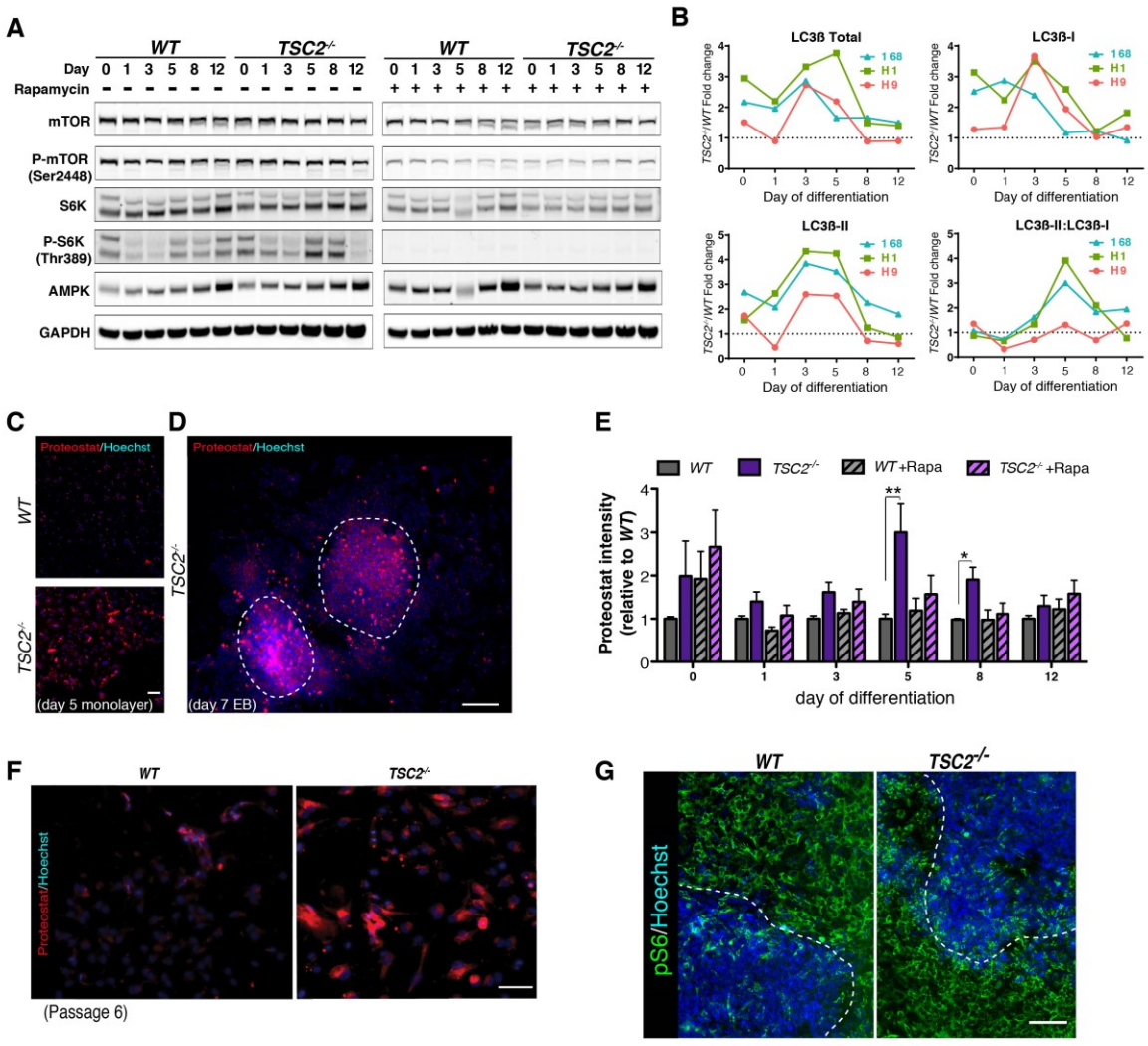

Figure 4.2.2: Aberrant autophagy activation and proteostasis dysregulation during *TSC2*$^{-/-}$ NPC differentiation.

(A) Western blot image as described in panel S8B during monolayer-NPC differentiation. Proteins assessed are mTOR, P-mTOR at Serine-2448, S6K, P-S6K at Threonine-389, AMPK, and GAPDH. (B) Quantification of western blot in Figure 4.2.1E for total LC3ß signal, LC3ß-I, LC3ß-II, and the LC3ß-II/ LC3ß-I ratio. (C) Representative images of Proteostat aggresome staining in *WT* at day 5 monolayer-NPC differentiation. Scale bar, 50µm. (D) Representative image of Proteostat aggresome staining at day 7 of EB-NCC differentiation. Scale bar, 100µm. (E) Quantification of Proteostat staining during monolayer-NPC differentiation with and without 100nM rapamycin. Values are mean ± SEM (n=10; 1x H9, 3x H1, 2x H7, 4x 168). (F) Representative image of Proteostat staining in *WT* and *TSC2*$^{-/-}$ NPC maintenance cultures at passage 6. Scale bar, 50µm. (I) Representative P-S6 immunofluorescence staining at day 7 of EB-NCC differentiation cultures. Dashed lines delineate borders of attached neuralized EB clusters. Scale bar, 100µm. Adapted from Delaney et al. 2019, bioRxiv, 683359 (Delaney, Julian et al. 2019).

8 of differentiation and reducing to normal levels in end-point *TSC2*$^{-/-}$ NPC cultures. Reflecting endosomal phenotypes and lineage specificity in proteostasis regulation, Proteostat intensity was more predominant in differentiating neural clusters than in migratory NCCs (Figure 4.2.2D). Accordingly, we observed low levels of aggregates during early stages of maintenance culture, but by late passages reflecting extensive aging they had accumulated selectively in *TSC2*$^{-/-}$ NPCs (Figure 4.2.2F). Together these data demonstrate that *TSC2*$^{-/-}$ cells mount an early developmental response to increased protein production and suggest that *TSC2*$^{-/-}$ NPCs maintain selective reliance on lysosome-autophagy signaling to limit protein aggregate accumulation over time.

Underscoring the concept of an early protein stress response in *TSC2*$^{-/-}$ cells, levels of the mTORC1 effector P-S6K and especially its target P-S6, a mark of active protein translation, were strongly reduced within the first 24 hours of dual SMAD inhibition in *WT* cultures, but this inhibition was incomplete at early time points in *TSC2*$^{-/-}$ cells (Figure 4.2.1E&F, Figure 4.2.2A). Interestingly, P-S6 is undetectable by day 8 of NPC differentiation in spite of mTORC1 hyperactivation in *TSC2*$^{-/-}$ cells (Figure 4.2.1E&F). P-S6 staining of day 7 NCC differentiations reveal P-S6^{+} migratory NCCs delaminating from largely P-S6 negative neural clusters (Figure 4.2.2G), revealing that NPCs specifically down-regulate S6 phosphorylation during lineage induction. Demonstrating the dependence of this signaling axis on mTORC1 regulation, P-S6 levels were strongly reduced by rapamycin treatment (Figure 4.2.1E); partial restoration of P-ULK1 serine-555, LC3β and autophagosome levels by rapamycin reflects a mechanistic connection between proteostasis and endosomal regulation in *TSC2*$^{-/-}$ NPCs (Figure 4.2.1E, 4.1.5C).

4.3 Clinically-relevant proteasome inhibitors permit selective, lineage-specific cytotoxicity of TSC2$^{-/-}$ cells

The accumulation of lysosomes and autophagosomes, paired with the abundance of aggresomes within NPC populations as they both differentiate and self-renew is indicative of the importance of functional proteolytic machinery in the maintenance of cell homeostasis in this cell lineage. TSC2-deficiency exacerbates these phenomena, offering a potential vulnerability of *TSC2*$^{-/-}$ cells that could be exploited for therapeutic benefit if protein degradation pathways are rendered inoperative pharmacologically. To test this, both NPCs and NCCs were exposed to the FDA-approved proteasome inhibitors bortezomib and carfilzomib, as well as the lysosomal inhibitor chloroquine, both alone and in combination. To investigate the compatibility and/or potential synergistic effects of these treatments with mTOR inhibitors, these drugs were administered both in the presence and absence of rapamycin. After 48h exposure to proteasome inhibitors, selective toxicity to *TSC2*$^{-/-}$ NPCs was observed at 40nM, with minimal effect on WT NPCs (Figure 4.3.1A&B). At 200nM of bortezomib or carfilzomib, *TSC2*$^{-/-}$ NPC samples continued to display increased sensitivity to proteasome inhibition, although *WT* cells began to show low level toxicity. These trends were observed following 24h exposure to proteasome inhibitors, though less pronounced (data not shown). In contrast, both *WT* and *TSC2*$^{-/-}$ NCCs showed nearly identical toxicity profiles with increasing concentrations of proteasome inhibitors at 48h (Figure 4.3.1A&B). Interestingly, treatment with the mTORC1 inhibitor rapamycin or targeting the lysosomal/autophagy pathway with chloroquine did not affect the viability of either NPCs or NCCs (Figure 4.3.1C), nor did chloroquine or rapamycin display any synergistic cytotoxic effects when combined with bortezomib or carfilzomib (Figure 4.3.1D). Taken together, these data demonstrate that *TSC2*$^{-/-}$ NPCs, but not *WT* NPCs, are specifically

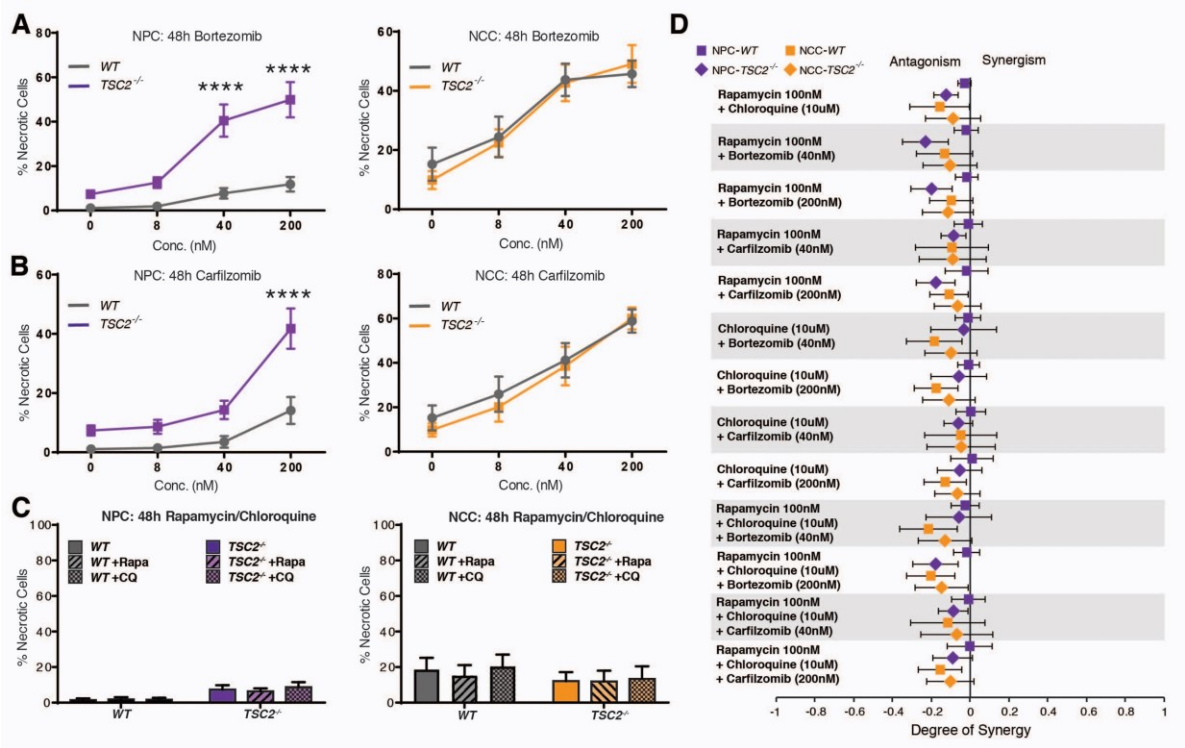

Figure 4.3.1: *TSC2*$^{-/-}$ NPCs but not NCCs are selectively sensitive to proteasome inhibition.

(A-C) Toxicity observed in NPCs (left) and NCCs (right) 48 hours after treatments with Bortezomib (A), Carfilzomib (B) and Rapamycin or Chloroquine (C). Values are the mean ± SEM. (A-B) n=7 for NPCs; 1x for H7, 4x for H9 and 2x for 168. n=11 for NCCs; 2x for H1, 2x for H7, 3x for H9 and 4x for 168. (C) n=4 for NPCs; 1x for H7and 168, 2x for H9. n=6 for NCCs; 1x for H7 and H9, 2x for H1 and 168. Statistical significance ($p < 0.05$) was established by Two-way ANOVA and Tukey's post hoc analysis. C) Bliss independence analysis of interactions between the proteasome inhibitors (Bortezomib and Carfilzomib), Rapamycin and Chloroquine after 48h of exposure. Values are the mean degree of synergy (difference between theoretical and observed toxicities) ± SE. n=4 for NPCs; 1x for H7 and 168, 2x for H9. n=6 for NCCs; 1x for H7 and H9, 2x for H1 and 168)). Statistical significance ($p < 0.05$) was determined by the Holm-Sidak method. Adapted from Delaney et al. 2019, bioRxiv, 683359 (Delaney, Julian et al. 2019).

sensitized to proteasome inhibition. Furthermore, these effects are cell-lineage dependent, as both *WT* and *TSC2*$^{-/-}$ NCCs are not able to tolerate low levels of proteasome inhibition. These lineage-specific vulnerabilities are a likely result of the catabolic and proteostatic adaptations that are acquired following neuralization, a phenomenon that clearly will have impact in the development of future therapeutics for TSC and LAM (Figure 4.3.2).

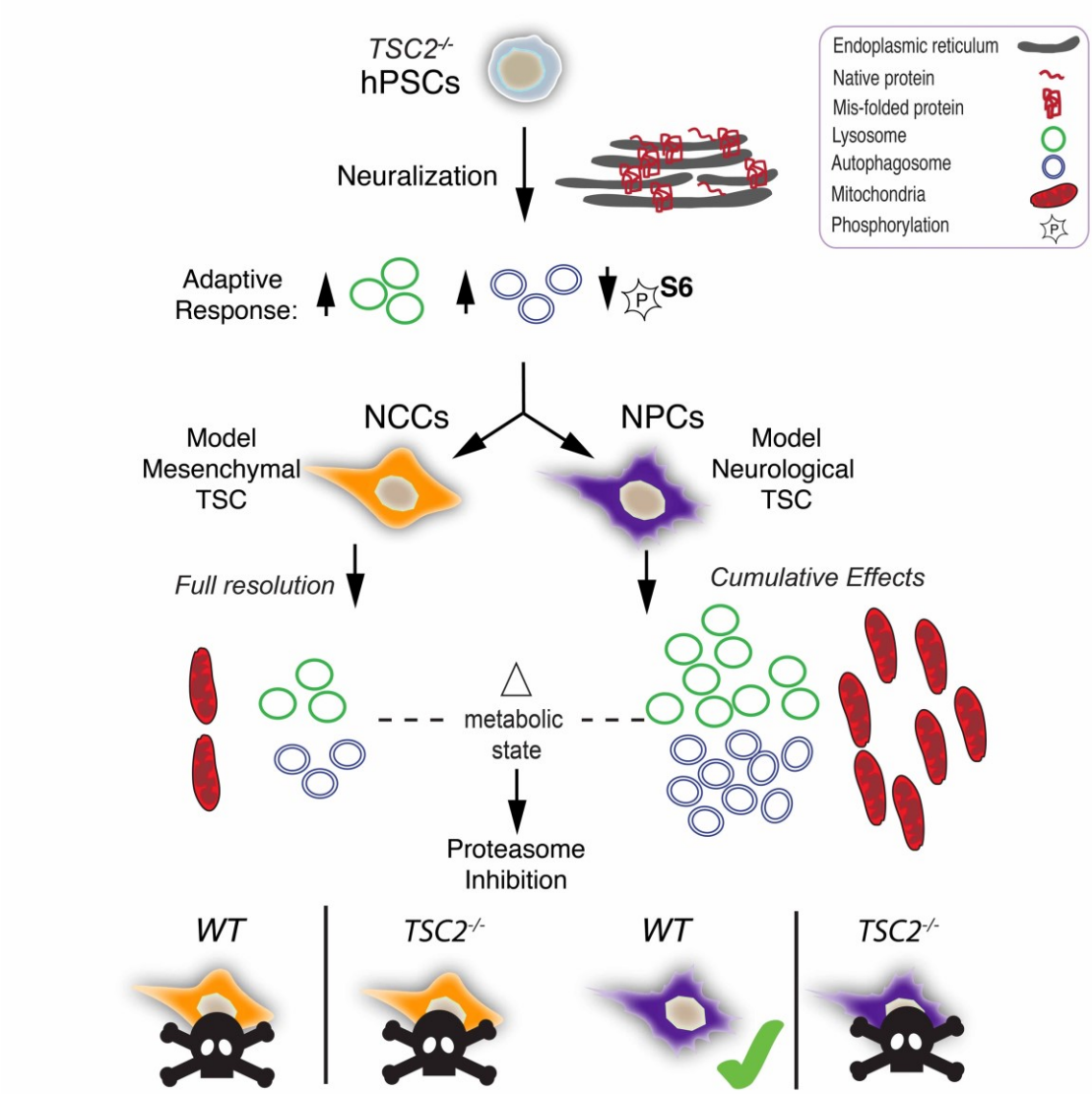

Figure 4.3.2: Schematic summary of the findings presented in Chapter 4. Upon induction of neuralization from the pluripotent state, neutralizing cells immediately downregulate global protein translation. *TSC2*$^{-/-}$ cells initiate a proteostatic stress response, which is selectively maintained in NPCs, but ameliorated upon NCC specification. This results in cell-lineage specific catabolic and proteostatic adaptations, leading to a differential response to proteasome inhibitors. Adapted from Delaney et al. 2019, bioRxiv, 683359 (Delaney, Julian et al. 2019).

CHAPTER 5:

Synthetic Lethal Genome-Wide CRISPR Knockout Screen

In Chapters 3 and 4, I established that *TSC2*$^{-/-}$ hPSC are able to differentiate into the putative cells of origin for neurological TSC and LAM, NPCs and NCCs, respectively, and both of these cell lineages recapitulate key phenotypes associated with the tissue-specific lesions that they are intended to model. Of note, *TSC2*$^{-/-}$ NCCs display several hallmark phenotypes of the mesenchymal lesions associated with LAM. *TSC2*$^{-/-}$ NPCs and NCCs display unique catabolic signaling adaptations; these lineage-specific signaling adaptations render only *TSC2*$^{-/-}$ NPCs susceptible to selective targeting via proteasome inhibition. This suggests proteasome inhibition may be a therapeutic route suitable for the treatment of the neurological manifestations of TSC, but not LAM-associated mesenchymal tumors. In order to quickly and efficiently identify new therapeutic avenues for the treatment of LAM and mesenchymal TSC, a genome wide CRISPR knockout screen was performed in both *WT* and *TSC2*$^{-/-}$ NCCs to identify genes that are essential for cell survival. Essential genes that are unique to *TSC2*$^{-/-}$ NCCs would be considered synthetic lethal genes which may act as therapeutic targets for the treatment of LAM and mesenchymal TSC.

5.1 Synthetic Lethal Screen

The sgRNA library selected for this assay was the human genome-wide CRISPR knockout version 2 (GeCKOv2) library, containing 123,411 unique sgRNA sequences targeting 19,050 genes (6 sgRNAs per gene), 1,864 miRNAs (4 sgRNAs per miRNA), and utilizes 2,000 negative control sgRNAs (Sanjana et al., 2014; Shalem et al., 2014). When this sgRNA library is applied to cell lines previously transduced to express Cas9, successful lentiviral-mediated genomic integration of a unique sgRNA expression cassette results in sgRNA-associated gene knockout. When cells are cultured under maintenance conditions in the absence of selective pressure, viral integrations of sgRNA

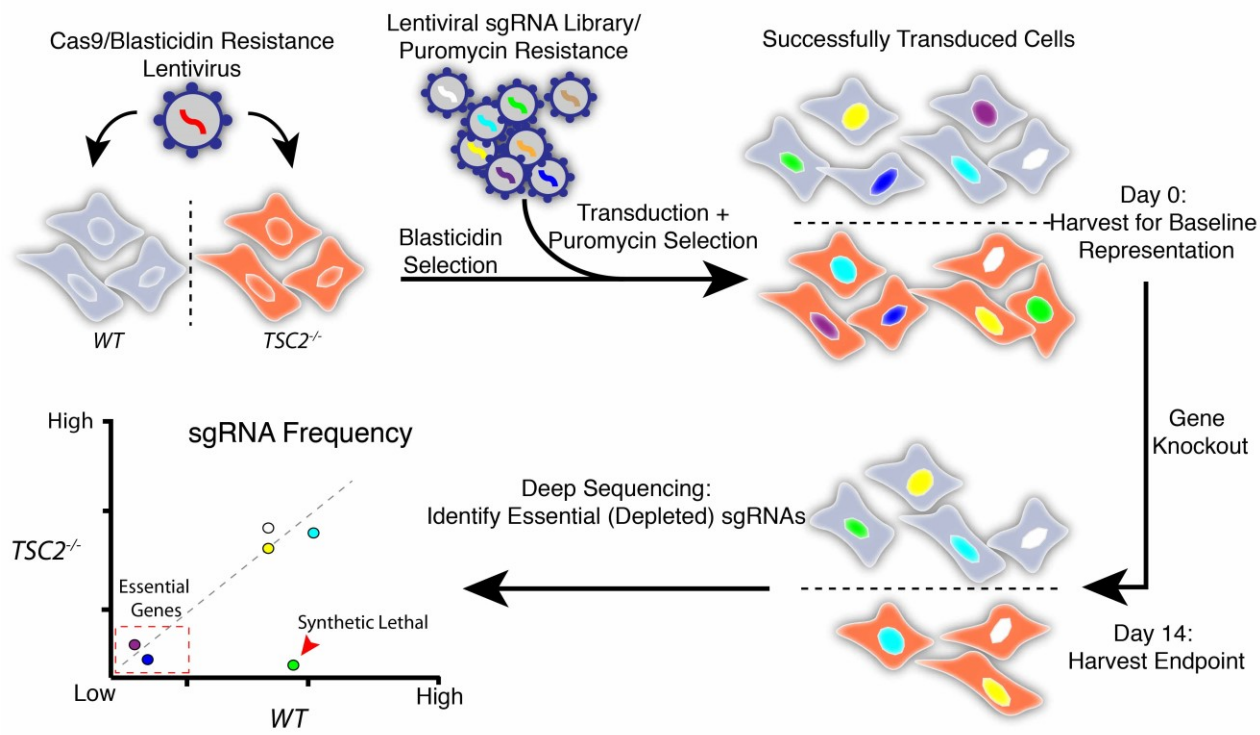

Figure 5.1.1: Schematic of the genome-wide CRISPR knockout synthetic lethal screen.
Cas9 expressing wild-type and *TSC2*$^{-/-}$ cells were generated and differentiated to NCCs, then the human GeCKOv2 sgRNA library was transduced at a low MOI (0.3). Cells underwent antibiotic selection for successfully transduced cells, and gDNA was harvested to establish baseline gRNA representation at day 0. NCCs were cultured for 14 days in maintenance conditions to allow synthetic lethal gRNA viral integrations to "drop out" of the population before gDNA was harvested. Samples were deep sequenced and analyzed to identify synthetic lethal genes based on sgRNA representation in each respective cell population.

sequences that target genes essential to cell survival lose representation within the population over time through negative selection. To identify genes that are synthetic lethal in the context of TSC2 deficiency, the GeCKOv2 library was applied to both *WT* and *TSC2*$^{-/-}$ NCCs to identify genes that are negatively selected specifically in *TSC2*$^{-/-}$ cultures. This assay principle is summarized in (Figure 5.1.1).

To generate Cas9 expressing cell cultures, *WT* and *TSC2*$^{-/-}$ H9 hPSCs were transduced with the lentiCas9-Blast lentiviral vector (Sanjana et al., 2014). Transduced cells then underwent blasticidin selection to enrich for transduced cells before subcloning to establish uniform populations of Cas9 expressing cells (Figure 5.1.2A&B). To assess the functionality of the assay, these cell lines were transduced with an sgRNA vector targeting mCherry. As both of these cell lines constitutively express mCherry, knockout of this transgene would confirm the expression of functional Cas9. After 14 days of maintenance, both *WT* and *TSC2*$^{-/-}$ hPSC lines displayed knockout of mCherry expression; knockout efficiencies of *WT* and *TSC2*$^{-/-}$ were at predicted rates based on the efficacy score of the mCherry sgRNA sequence (Figure 5.1.2C&D; Broad Institute CIRSPRko algorithm). Cas9 expressing cell lines were then expanded in the undifferentiated state before initiation of NCC differentiation and subsequent GeCKOv2 sgRNA library transduction. To ensure that only one lentiviral integration occurred per cell, a low multiplicity of infection (MOI; 0.3) was used at time of transfection. To achieve adequate coverage of the 123,411 sgRNAs (700X), a target population size of 288 million NCCs were transduced with the GeCKOv2 sgRNA library. Two biological replicates were performed for both *WT* and *TSC2*$^{-/-}$ NCCs. 24 hours post-transduction, puromycin selection was applied to the cells for 3 days to enrich for successfully transduced cells, establishing the day 0 timepoint and gDNA was harvested for baseline sgRNA representation. Cultures were grown for an additional 2 weeks (endpoint day 14) before harvesting gDNA to allow sgRNA lentiviral integrations targeting synthetic lethal

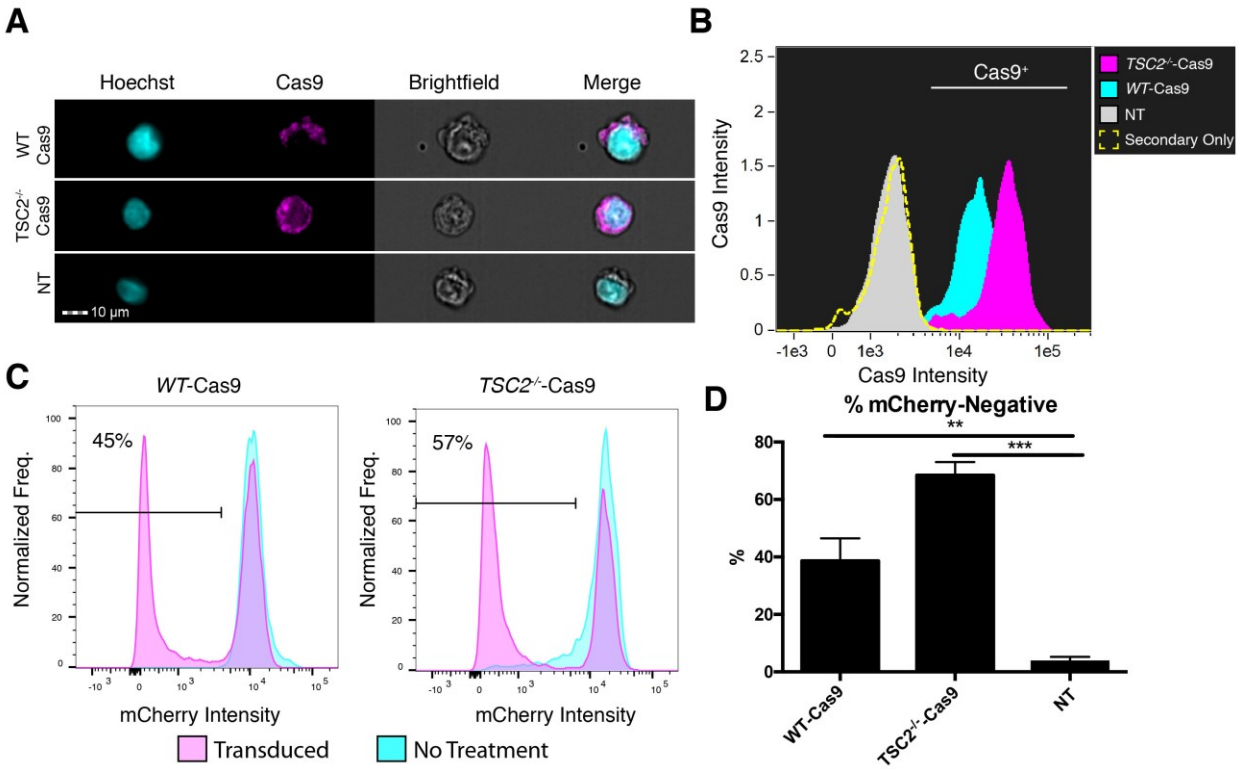

Figure 5.1.2: Functional validation of the GeCKO assay system.
(A) Imaging flow cytometry image capture of Cas9 expressing WT and *TSC2*$^{-/-}$ cell lines. Scale bar = 10µm. (B) Histogram of imaging flow cytometry analysis displaying enriched population of Cas9 expressing cells in WT-Cas9 and *TSC2*$^{-/-}$ Cas9 cell lines. (C&D) Representative histograms of flow cytometry analysis (C) and quantifications (D) of WT-Cas9 and *TSC2*$^{-/-}$-Cas9 cell lines transduced with mCherry sgRNA lentivirus showing significant levels of mCherry knockout. Values are mean ± SEM. n = 2 (*WT-Cas9*) and 3 (*TSC2*$^{-/-}$-Cas9).

genes to lose representation within the population, as well as allow for sgRNA sequences that are associated with selective advantage to increase proportionally in the pool. Lentiviral integrations containing the unique sgRNA sequences were PCR amplified and underwent deep sequencing to determine representation at each time point, targeting minimum 500X depth for day 0 samples and 200X for day 14.

5.1.1 Quality Control

sgRNA counts were analyzed and scored using the MAGeCK-VISPR software package (Li et al., 2015) and initial quality assessments were performed. To ensure proper representation across the entire GeCKOv2 library, the pool was sequenced prior to lentiviral preparation (Figure 5.1.3A). Sequencing revealed a pristine library in which 100% of sgRNAs have at least one read. Furthermore, a ratio of 4.78 between the 90th and 10th percentile of reads indicates unbiased amplification during preparation of sequencing libraries. PCA of the synthetic lethal screen datasets (Figure 5.1.3B) showed clustering of day 0 samples is observed as expected, with day 14 *WT* samples clustering together as well. However, the *TSC2*$^{-/-}$ day 14 samples are separated across PC1-3, indicating significant variability between these replicates. It is clear when plotting normalized read counts that the distribution of day 14 *TSC2*$^{-/-}$ replicate 2 read counts is greater than that of d14 *TSC2*$^{-/-}$ replicate 1 (Figure 5.1.3C). This is reflected in the Gini index values of samples, a measure of read evenness (Figure 5.1.3D). The Gini index would be expected to increase in day 14 samples due to the enrichment and depletion of sgRNAs within the population over time, however, *TSC2*$^{-/-}$ day14 replicate 2 value is nearly double that of replicate 1. Furthermore, the number of sgRNA zero counts is over five-fold higher in the *TSC2*$^{-/-}$ day 14 replicate 2 sample compared to replicate 1 (Figure 5.1.3E). These inconsistencies were likely due to unforeseen factors introducing

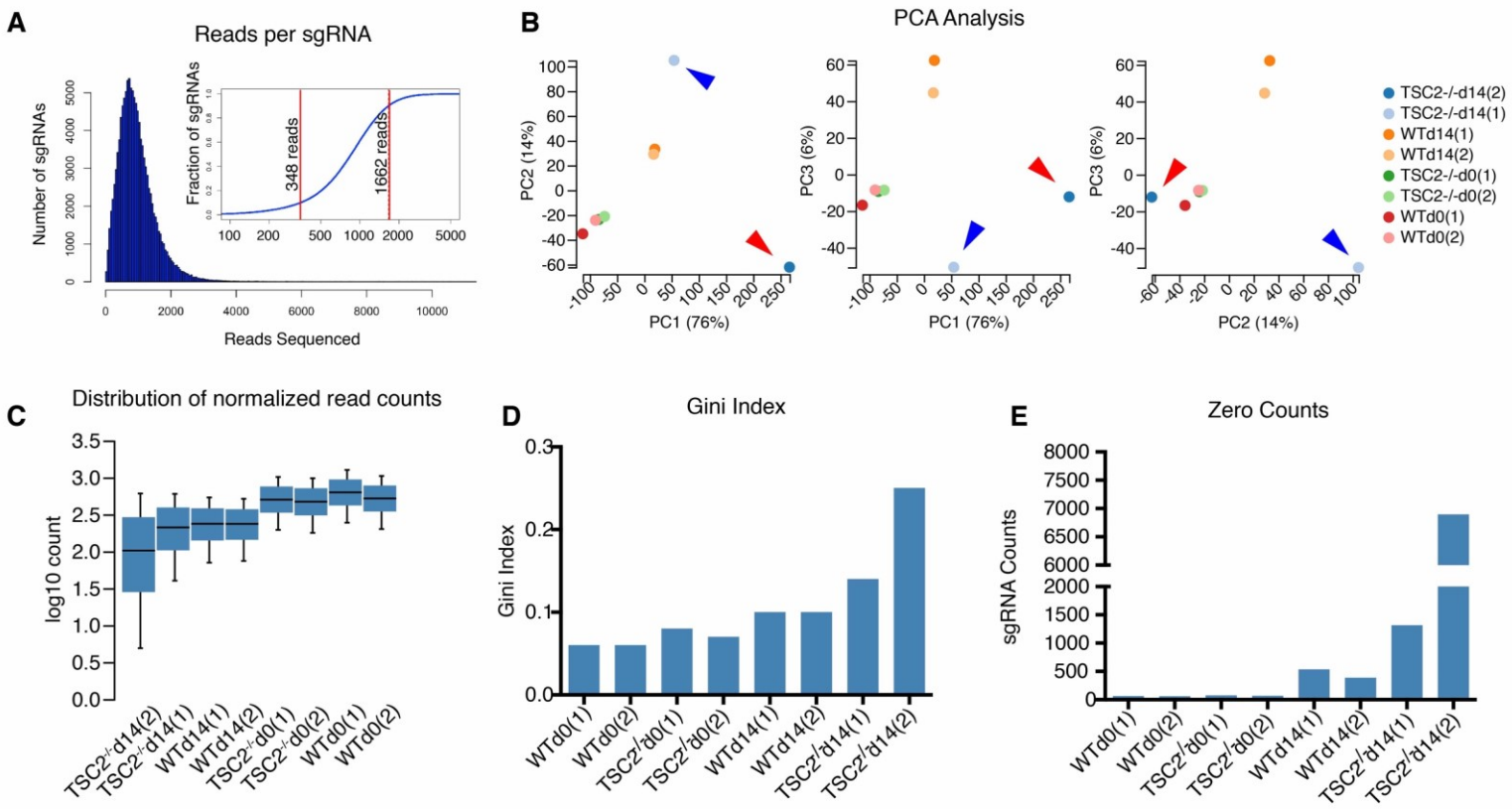

Figure 5.1.3: Quality control of synthetic lethal screen dataset.
(A) Sequencing of the GeCKOv2 plasmid library used for lentiviral preparation prior to lentiviral preparation. (B) PCA of the sequenced samples reveals expected clustering of all day 0 samples and *WT* day 14 samples. Day 14 *TSC2*$^{-/-}$ replicate samples display variability between replicates. Blue arrowheads indicate *TSC2*$^{-/-}$ day 14 replicate 1, red arrowheads indicate *TSC2*$^{-/-}$ day 14 replicate 2. (C) Normalized read counts across all samples. (D) Gini index values of all replicates. (E) Zero counts within each replicate.

selective pressure during the maintenance period during the second replicate of *TSC2*$^{-/-}$ cultures. Therefore, the *TSC2*$^{-/-}$ day 14 replicate 2 was removed from further downstream analysis.

5.1.2 Ontology-based analysis of negatively selected genes

Significantly depleted/enriched sgRNAs were identified by conversion of the sgRNA counts into gene essentiality rankings (beta scores) using the MLE module of MAGeCK-VISPR. Negative beta scores indicate a negatively selected gene, and positive beta scores indicate genes that were positively selected. Using the MAGeCKFlute analysis pipeline (Wang et al., 2019), beta scores were normalized between WT and *TSC2*$^{-/-}$ samples using the beta scores of cell-cycle-associated genes to account for potential differences in proliferation rates between genotypes. KEGG pathway analysis of overrepresented negatively selected genes common between *WT* and *TSC2*$^{-/-}$ NCCs showed enrichment for multiple terms relating pathways essential for cell homeostasis (Figure 5.1.4A). These include “Ribosome”/’Ribosome biogenesis in eukaryotes’, “Proteasome”, “Cell cycle”, and “Oxidative phosphorylation” among others.
The depletion of sgRNAs targeting genes that are essential to basic cellular processes and metabolism is indicative that the assay system was indeed functional.

Through plotting the beta scores of *WT* and *TSC2*$^{-/-}$ samples, genes that were negatively or positively selected for in *TSC2*$^{-/-}$ cells that do not endow selective advantage/disadvantage in *WT* cultures were identified (Figure 5.1.4B). As shown in Figure 5.1.4B, data points in group IV (purple) represent genetic elements that were specifically depleted by day 14 in *TSC2*$^{-/-}$ NCCs and are considered a synthetic lethal gene set. KEGG pathway gene set enrichment analysis (GSEA) of group IV genes enriched for pathways terms relating to signaling pathways related to LAM that have

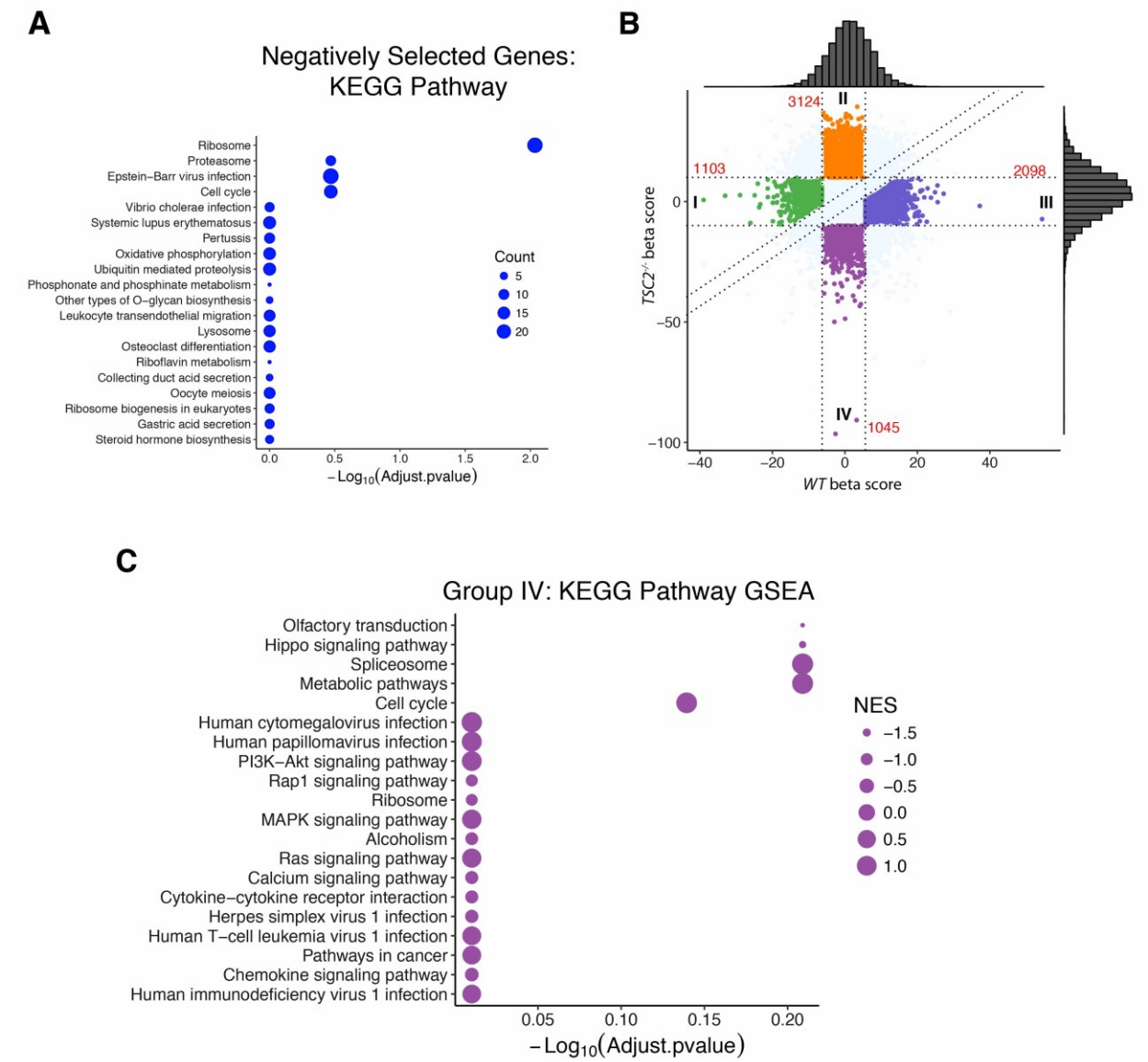

Figure 5.1.4: Ontology-based verification of negatively selected genes.
(A) KEGG pathway enrichment analysis of negatively selected genes common to both *WT* and *TSC2*$^{-/-}$ populations. (B) Plot of *WT* vs. *TSC2*$^{-/-}$ beta scores, highlighting treatment-associated genes. Positive beta scores indicate genes conferring growth advantage when knocked out, whereas negative beta scores indicate genes essential to cell survival. (C) KEGG pathway GSEA of genes identified as synthetic lethal (group IV in panel (B)) NES: normalized enrichment score.

either been previously targeted or suspected to be vulnerable to therapeutic targeting (Figure 5.1.4C). These include “PI3-Akt signaling pathway”, “MAPK signaling pathway”, “Ras signaling pathway”, “Metabolic pathways” and “Cell cycle”. Interestingly, three of the identified synthetic lethal pathways are upstream of and converge through the TSC1/2 complex and mTOR. The identification of these LAM-related pathways suggests that the synthetic lethal screen was able to accurately determine genes that are essential to TSC2 deficient cells.

5.1.3 Small molecule mediated validation synthetic lethal genes

Among the most significantly synthetic lethal genes identified in this screen, few are known to be able to be targeted directly via small molecule inhibition. The most significant (FDR ≤ 0.5) synthetic lethal genes within group IV are summarized in Table 5.1. Three of these genes are ‘druggable’ using small molecules and were selected for initial validation as synthetic lethal interactors: *NTF3, IKBKE, and FGFR1*. A concise panel of small molecules was selected to test for selective lethal targeting of *TSC2*$^{-/-}$ deficient cells and is summarized in Table 5.2. These small molecules were applied to both *WT* and *TSC2*$^{-/-}$ NCCs over a wide dilution range using a high content-based cell viability assay to establish a dose-response curve for each compound (Figure 5.1.5). Small molecules BMS-345541 and LOXO-101 targeting IKBKE and NTF3 interactions, respectively, showed limited therapeutic potential. Although NTF3 has been shown to be critical for sensory neurons (Usui et al., 2012), this may be a cell type specific role. BMS-345541 did, however, show selective toxicity in *TSC2*$^{-/-}$ NCCs at the highest concentration of 10μM, though this is likely not a clinically relevant effective concentration (Smith and Houghton, 2013). Three of the four compounds targeting FGFR1, NVP-BGJ398, FIIN-2, and Nintedanib esylate, showed similar dose related

Gene	*TSC2*$^{-/-}$ beta	WT beta	*TSC2*$^{-/-}$ pValue	*TSC2*$^{-/-}$ FDR
hsa-mir-6127	-91.349223	3.57711862	0	0
NAGPA	-41.41373	3.0656345	4.61E-05	0.16667
PGC	-42.883819	4.74346593	4.61E-05	0.16667
RPS11	-40.239017	-0.5002223	4.61E-05	0.16667
BTF3L4	-38.843621	-1.7908076	9.22E-05	0.22222
FABP3	-38.436206	-5.386168	9.22E-05	0.22222
hsa-mir-1199	-48.984858	0.39644874	0.00023045	0.35714
hsa-mir-3135a	-50.295376	-2.5654429	0.00023045	0.35714
CCDC63	-34.151558	-0.8386602	0.00032263	0.36842
TFPT	-33.738032	4.978207	0.00036871	0.3913
hsa-mir-6510	-43.678278	4.44745919	0.00055307	0.42857
ABHD15	-31.675834	4.07623719	0.00069134	0.48148
FGFR1	-30.036328	5.04897678	0.0010601	0.48148
JKAMP	-29.801725	-2.9602718	0.0011522	0.48148
LRRC57	-30.683099	5.90838251	0.00092179	0.48148
IKBKE	-29.712433	2.2664214	0.0012444	0.49091
NTF3	-29.404495	-1.2825937	0.0014288	0.5
THAP8	-29.227949	1.16782913	0.0014288	0.5

Table 5.1: Beta score readouts of the top scoring synthetic lethal genes.
Processing genome-wide synthetic lethal sequencing results with MAGeCK-MLE generates Beta scores which represent gene essentiality. Positive Beta scores indicate a gene that confers a growth advantage when knocked out, and negative Beta scores indicate genes that is more essential to cell survival when knocked out.

Compound	Target
LOXO-101	NTF3 receptors TRKB&C
BMS-345541 HCl	IKBKE(IKK)
ACTB-1003	FGFR1/KDR/TIE2
Nintedanib esylate	FGFR1/PDGF/TGFβ
FIIN-2	FGFR 1-4
NVP-BGJ398	FGFR 1-3

Table 5.2: Panel of small molecule inhibitors for validation of "druggable" synthetic lethal targets.

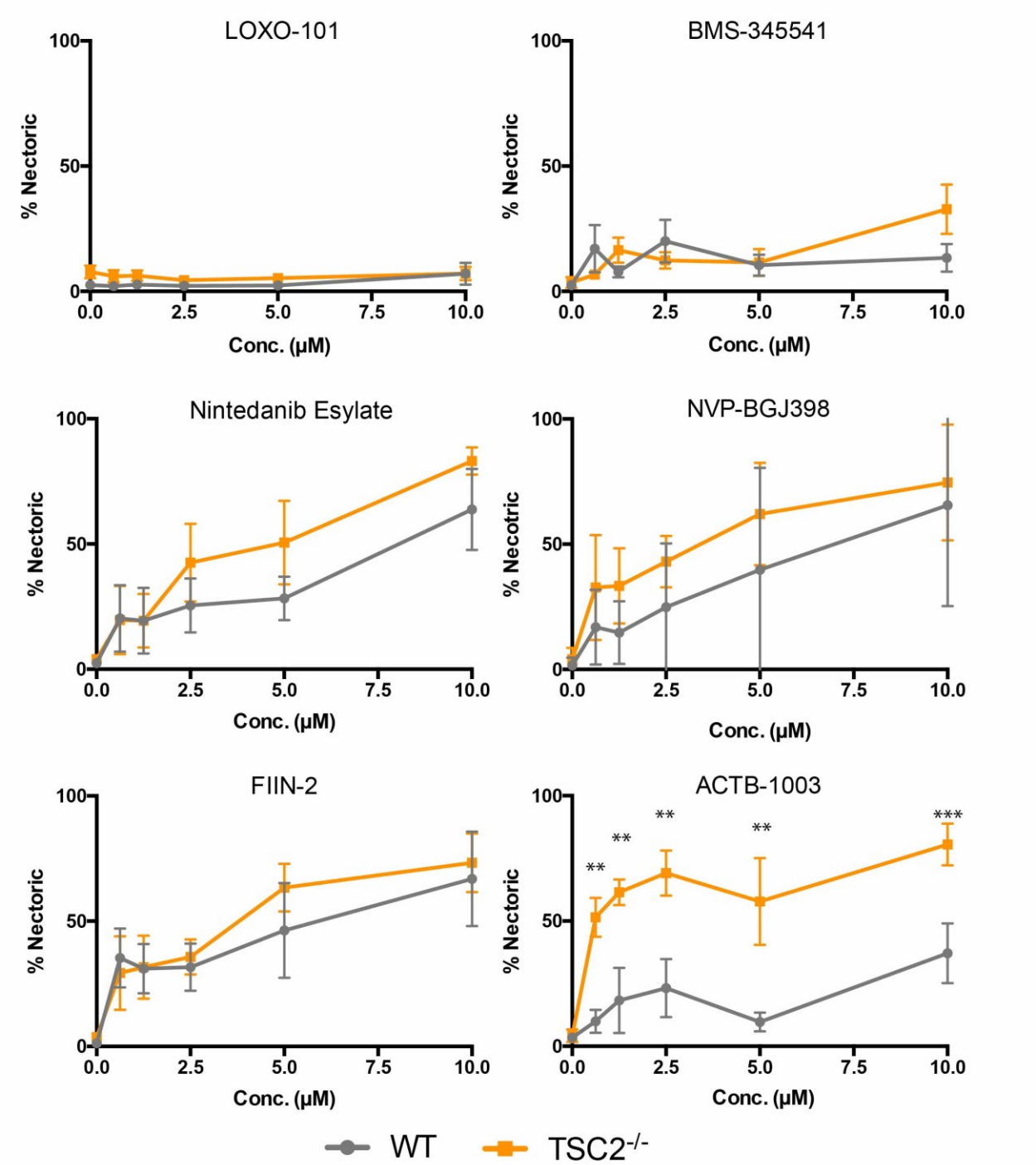

Figure 5.1.5: Dose response of small molecule panel.
WT and *TSC2*$^{-/-}$ NCCs were exposed small molecule inhibitors of NTF3 (LOXO-101), IKBKE (BMS-345541), and FGFR (Nintedanib esylate, NVP-BGJ398, FIIN-2, and ACTB-1003), and cell viability was assessed at varying concentrations. ACTB-1003 displays selective toxicity towards *TSC2*$^{-/-}$ NCCs. Values are mean ± SEM. n = 4; 2x for H7 and H9 NCCs. Statistical significance was determined using multiple student's t-tests.

toxicity across both *TSC2* genotypes. The selective FGFR1 inhibitor, ACTB-1003, however, clearly elicited a selectively lethal effect in *TSC2*$^{-/-}$ NCCs. This is observed at the lowest concentration used in this assay (0.625μM). *WT* NCCs show increased toxicity with increasing concentration of ACTB-1003, however, a wide therapeutic window is apparent across the entire range tested. ACTB-1003 also elicits inhibitory interaction towards KDR (VEGFR2) and TIE2 in addition to FGFR1 and may have contributed to the effectiveness of this drug. Taken together, this data is supportive of FGFR1 as a bonafide synthetic lethal interactor in TSC2 deficient NCCs and may have potential as a therapeutic target in LAM and TSC.

Although this a limited data set for validating the gene targets identified in this screen, initial results are promising; one of three 'druggable' synthetic lethal hits has been identified as a true positive. However, these three genes still require further validation using additional small molecules. This is underscored by that fact that only one of four compounds targeting FGFR1 selectively sensitized *TSC2*$^{-/-}$ NCCs to cell death. Thus, both *NTF3* and *IKBKE* require additional verification before being classified as false positive hits. This can be perhaps most efficiently accomplished through the use of RNAi or CRISPR-based approaches. Indeed, the majority of the synthetic lethal genes identified in this screen will require gene knockdown or knockout approaches to validate their status as synthetic lethal to TSC2 deficient cells. These experiments are to be carried out in continuation of this study, as well as further investigation into the mechanism of cell death resultant of gene knockdown/knockout in TSC2 deficient NCCs.

5.2 Analysis of the synthetic lethal dataset

The list of potential synthetic lethal genes identified in this screen is vast. Furthermore, at the present moment, the lack of a second replicate sample of *TSC2*$^{-/-}$

day 14 limits the statistical power of the MAGeCK readout, resulting in a short list of high confidence synthetic lethal genes. Until an additional replicate is added to this dataset, likely true positive genes may be prioritized for validation through data exploration and logical reasoning. This could be accomplished through integration of the synthetic lethal dataset with the RNA-seq dataset profiling the transcriptome of day 10 differentiated NCCs as detailed in Chapter 4. Using these strategies, synthetic lethal genes may be enriched *in silico* and prioritized for validation.

5.2.1 Targeting signaling pathways upstream of TSC2 and mTOR

As detailed in section 5.1.2, ontology-based analysis of the synthetic lethal gene set revealed enrichment for genes relating to multiple signaling pathways known to be dysregulated in LAM, namely PI3-AKT, MAPK, and RAS signaling. Closer investigation of the gene lists associated with these pathways revealed a concise overlapping gene set shared between PI3-AKT, MAPK, and RAS signaling pathways (Figure 5.2.1A). These genes include *KDR, NTF3, PDGFRA, and FGF22*. Of note, all four of these genes encode for receptor tyrosine kinases (RTKs) or their ligands. Interestingly, the LAM diagnostic marker VEGFD is a ligand for the protein product of *KDR* and VEGFR2; furthermore, inhibition of VEGF signaling has previously been proposed as a treatment strategy for LAM (Radzikowska, 2015). Furthermore, the small molecule inhibitor of FGFR1, ACTB-1003, which exhibited selective toxicity to *TSC2*$^{-/-}$ NCCs (Figure 5.1.5), also targets VEGFR2; targeting both FGFR1 and VEGFR2 may explain its effectiveness in targeting *TSC2*$^{-/-}$ NCCs. An additional noteworthy hit within this overlapping gene set is *PDGFRA,* which encodes the RTK PDGFRα. Aberrant PDGFRα expression has not been documented in LAM or TSC, however, this gene's transcripts are significantly upregulated in differentiating NCCs by day 10 (Table 5.3). Furthermore, its counterpart,

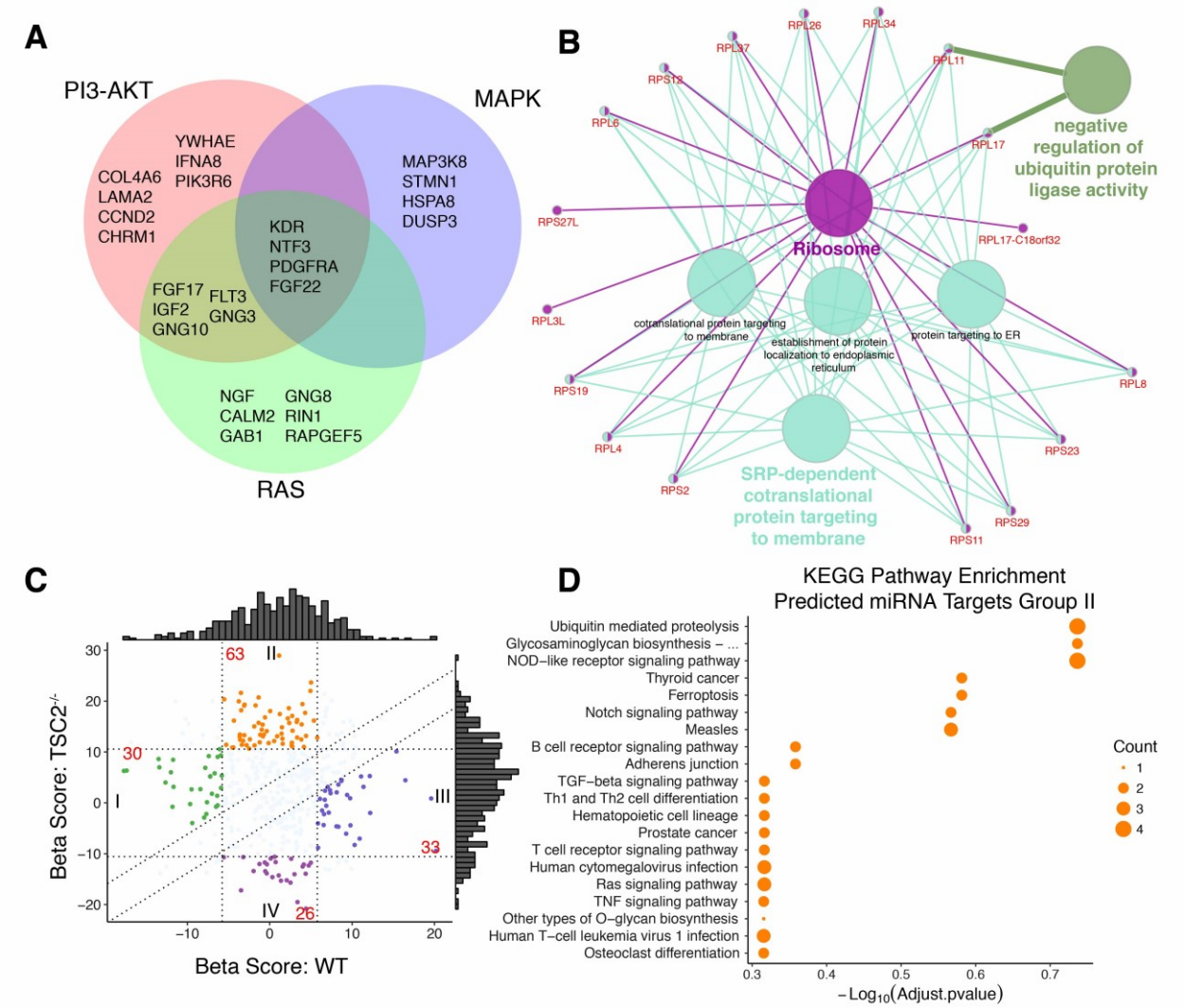

Figure 5.2.1: Analysis of synthetic lethal hits allows the prioritization of hits. (A) Overlap of synthetic lethal gene sets enriching for the PI3-AKT, MAPK, and RAS signaling pathways suggests genes common to all pathways may be most effective in exerting synthetic lethal interations in TSC2 deficient cells. (B) KEGG pathway network of ribosome-associated synthetic lethal genes reveals non-canonical roles of *RPL11* and *RPL17* may be exploited. Color of nodes corresponds to enrichment term. (C) Plot of WT and *TSC2*$^{-/-}$ beta scores corresponding to high scoring predicted targets of the top 8 synthetic lethal miRNAs. (D) KEGG pathway enrichment of the predicted targets of the top scoring synthetic lethal miRNAs falling within group II.

PDGFRβ, is overexpressed in LAM-associated rAMLs (Arbiser et al., 2002; Liang et al., 2014; Siroky et al., 2014), and is overexpressed in *TSC2*$^{-/-}$ NCCs (3.3.4C&C). Both PDGFRα and PDGFRβ function independently as homodimers, but they also exert function as heterodimers (Chen et al., 2013), suggesting that PDGFRα may indeed influence the activity of PDGFRβ signaling; this pathway is currently under investigation as a therapeutic avenue for LAM within a phase II clinical trial (IRCCs). Therefore, inhibition or knockdown of PDGFRα may prove to be an effective approach to target TSC2 deficient cells.

5.2.2 Ribosomal subunits as potential therapeutic targets

Although ribosomal genes are generally considered essential to the maintenance of cellular function, numerous ribosomal genes were enriched in the synthetic lethal gene set of group IV. This enrichment may be the result of the reliance of *TSC2*$^{-/-}$ cells on translational machinery under mTORC1 hyperactivation and subsequent increase in global translation, a potential vulnerability of TSC2 deficient cells. Gene ontology analysis of these ribosomal genes (Figure 5.2.1B) resulted in the expected enrichment of terms relating to canonical ribosome function in protein translation and processing. However, the two ribosomal genes, *RPL11* and *RPL17*, are associated with the negative regulation of ubiquitin protein ligase activity. RPL11 acts to inhibit the ubiquitin ligase, MDM2, and thereby influence the activation of p53 signaling (Mahata et al., 2012; Zhang et al., 2003). In turn, RPL17 has been shown to influence cell proliferation in vascular smooth muscle cells (Smolock et al., 2012). Clearly, both of these genes have physiological roles outside of their canonical function as ribosomal subunits. Thus, targeting these ribosomal genes may result in more widespread physiological imbalances in TSC2 deficient cells and exhibit synthetic lethal effects.

5.2.3 Synthetic lethal miRNAs are predicted to target key growth and survival genes

Four of the top sixteen high confidence synthetic lethal genetic elements were miRNAs (hsa-mir-6127, hsa-mir-1199, hsa-mir-3135a, and hsa-mir-6510). This is perhaps not surprising in *TSC2*$^{-/-}$ cells; with constitutive mTORC1 activation leading to increased global transcription and translation, the loss of an essential negative regulator of specific genes in this scenario could indeed prove lethal. Such synthetic lethal miRNAs are intriguing therapeutic targets due to the tolerability of their loss in *WT* cells that are able to better maintain optimal levels of miRNA target gene expression; this suggests minimal toxicity to LAM patients. To investigate the potential of these synthetic lethal miRNAs further, the 8 highest scoring synthetic lethal miRNAs were selected and predicted target genes were identified using the miRDB miRNA target prediction algorithm (Wong and Wang, 2015). Selecting only predicted miRNA gene targets with high quality targets scores above 90, these genes were plotted by their respective WT and *TSC2*$^{-/-}$ beta scores. Nearly two-fold more of these predicted targets fell into group II than the other treatment-specific groups (Figure 5.2.1C). Group II is associated with genes that confer selective advantage to *TSC2*$^{-/-}$ NCCs when knocked out, suggesting these predicted targets affect physiological processes affecting cell growth and survival. KEGG pathway enrichment analysis of these 63 potential miRNA target genes revealed pathways associated with cell growth (TGF-beta and RAS signaling), cancer (thyroid and prostate cancer), and cell homeostasis (ubiquitin mediated proteolysis) (Figure 5.2.1D). Thus, the top scoring miRNAs are likely to influence the expression of a wide array of physiologically impactful genes, which suggests these genetic elements be further investigated for their therapeutic potential.

5.2.4 Transcriptomic and synthetic lethal datasets offer functional insight into synthetic lethal hits

The rich transcriptomic dataset generated while investigating the role of *TSC2* in LAM and TSC disease pathogenesis through neural/neural crest development offers a unique opportunity to delve deeper into the synthetic lethal dataset. Integration of these two datasets may offer physiological context to the genes and pathways enriched as synthetic lethal. Table 5.3 summarizes the synthetic lethal genes in group IV that are also significantly differentially expressed in *TSC2*$^{-/-}$ NCCs compared to their WT counterparts. Theoretically, synthetic lethal genes that exhibit significant differential gene expression or are involved in differentially regulated pathways may be more readily exploitable as therapeutic targets.

Overlapping the gene sets of significant DEGs (FDR < 0.05) at day 10 EB-NCC differentiation of *WT* and *TSC2*$^{-/-}$ cultures relative to day 0 with the synthetic lethal gene set revealed 243 genes that are common to all three datasets (Figure 5.2.2A). Selecting the synthetic lethal genes that are unique to *TSC2*$^{-/-}$ NCCs may enrich for genes that can selectively target TSC2 deficient cells. Gene ontology network analysis of this set of 51 genes revealed enrichment for terms relating to SRP-dependent protein targeting to the ER membrane, response to gamma irradiation, and the proteasome (Figure 5.2.2A). Of the 23 significantly upregulated genes in this gene list, only two show pathway enrichment, *CCDN2* and *MMAB*. These genes enrich for the “cellular response to gamma irradiation” pathway. Interestingly, the protein product of *CCDN2*, cyclin D2, is involved in cell cycle regulation and is implicated in a cancer progression (Evron et al., 2001; Granados-Aparici et al., 2019; Koyama-Nasu et al., 2013; Sicinski et al., 1996). Targeting this gene may prove beneficial; previous studies have shown that knockdown of cyclin D2 in neural lineages results in cell cycle arrest (Koyama-Nasu et al., 2013), a

Gene	Log_2FC	FDR
IGSF1	-1.6503937	6.62E-05
CDNF	-0.9386921	0.00332038
C20orf194	-0.8669886	1.34E-05
ZNF397	-0.6877137	0.0257782
ATP6AP1L	-0.6757851	0.0386901
POU5F1	0.02706397	0.02151401
S100A14	0.03308485	0.03209142
GJB2	0.04528399	0.00057183
C1orf116	0.0635003	0.00658407
LAD1	0.06417781	0.01762738
LLGL2	0.06616793	0.03162603
EPHA1	0.08193764	0.00721548
YARS	0.5583485	0.03627297
CTH	0.69695404	0.00978807
PROM1	0.86272502	0.01930545
NID2	1.01082349	0.01311229
CHST15	1.19091417	0.02808905
PDLIM1	1.21410446	0.01082108
UPP1	1.28457013	0.03880447
PDZRN3	1.33755614	0.0014878
PDGFRA	1.62354369	0.01163702
GRID2	1.74997668	0.00673406
ACP5	1.78765827	6.83E-05
ANPEP	1.8865766	0.00351622
FOXB1	2.43358852	9.56E-05
SGCD	2.733431	0.00971036
TWIST1	2.85715764	0.00096143

Table 5.3: Synthetic lethal genes identified as significantly differentially expressed DEGs (FDR < 0.05) in *TSC2*$^{-/-}$ NCCs relative to *WT* NCCs at day 10 of EB-NCC differentiation.

promising finding suggesting a similar response may observed TSC2$^{-/-}$ NCCs, and potentially other TSC2 deficient cell lineages as well.

Noteworthy is the emergence of enriched pathways related to proteostasis in these overlapping datasets (Figure 5.2.2A). This is reminiscent of the proteostatic stress response initiated upon dSMADi induced neuralization of *TSC2*$^{-/-}$ cultures characterized in Chapter 4. The majority of the terms enriched in this analysis are involved with protein processing in the ER and proteolytic processes, including the proteasome itself. Although catabolic signaling phenotypes were less pronounced in NCCs compared to NPCs, these processes may nonetheless offer vulnerabilities that can be exploited for therapeutic benefit. Further investigation into proteasome-associated gene expression by comparing *TSC2*$^{-/-}$ cultures relative to *WT* cultures during EB-NCC differentiation reveals two key genes involved in the immunoproteasome (i-proteasome), PSMB8 and PSMB9 (Basler et al., 2013), to be significantly upregulated as cells specify and enrich as NCCs (Figure 5.2.2B). Interestingly, none of the proteasome-associated genes in the synthetic lethal dataset (Figure 5.2.2B, red font) display marked differential gene expression, nor do they hierarchically cluster. However, the apparent upregulation of immunoproteasome genes in *TSC2*$^{-/-}$ NCCs suggests an important role for these proteolytic process in the maintenance of cell homeostasis. Thus, further investigation into the interplay between the constitutive proteasome and the i-proteasome through gene-level targeted inhibition of these pathways in TSC2 deficient NCCs is warranted.

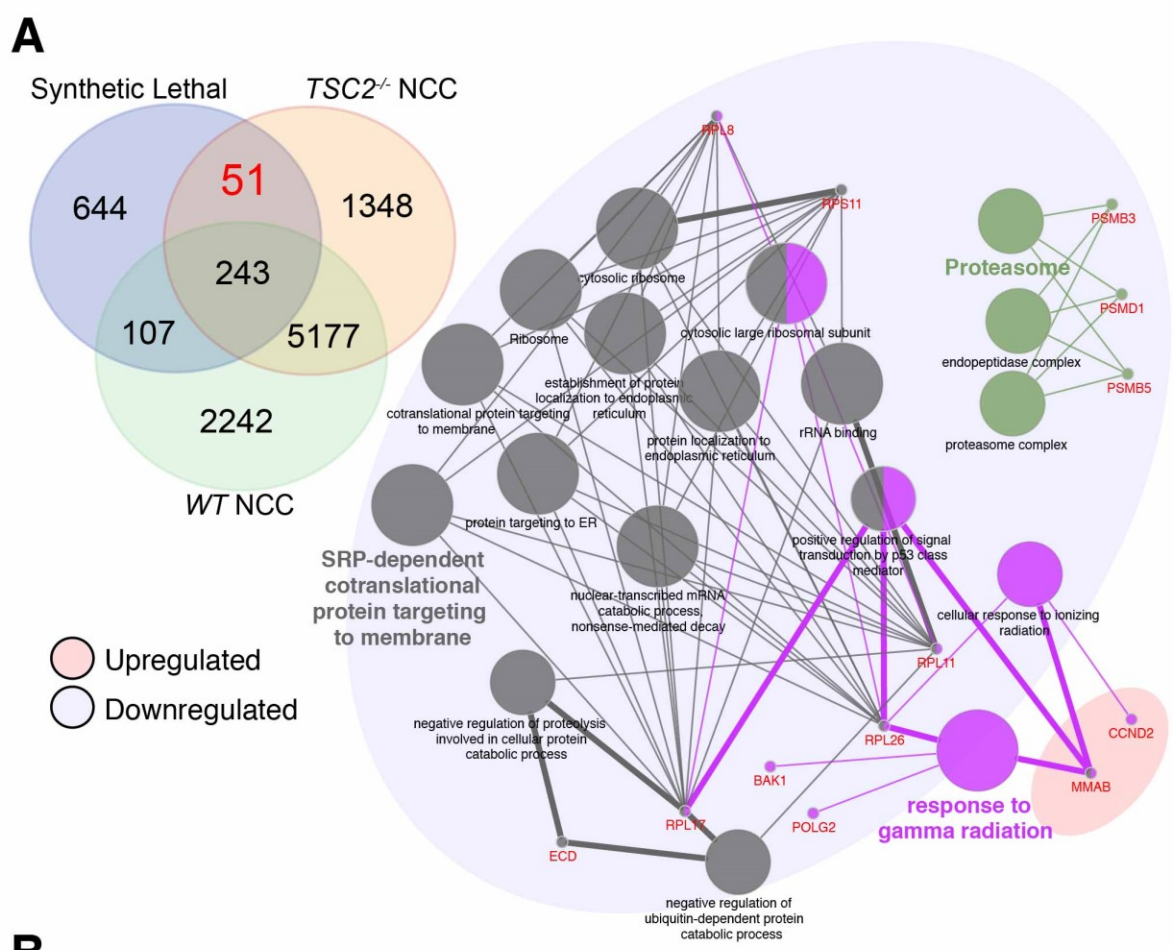
A
Synthetic Lethal
TSC2-/- NCC
644
51
1348
243
107
5177
2242
WT NCC
Upregulated
Downregulated
RPL8
RPS11
cytosolic ribosome
Ribosome
cytosolic large ribosomal subunit
establishment of protein localization to endoplasmic reticulum
cotranslational protein targeting to membrane
protein localization to endoplasmic reticulum
rRNA binding
protein targeting to ER
SRP-dependent cotranslational protein targeting to membrane
nuclear-transcribed mRNA catabolic process, nonsense-mediated decay
positive regulation of signal transduction by p53 class mediator
cellular response to ionizing radiation
RPL11
negative regulation of proteolysis involved in cellular protein catabolic process
RPL26
CCND2
BAK1
MMAB
response to gamma radiation
RPL17
POLG2
ECD
negative regulation of ubiquitin-dependent protein catabolic process
Proteasome
PSMB3
PSMD1
endopeptidase complex
PSMB5
proteasome complex

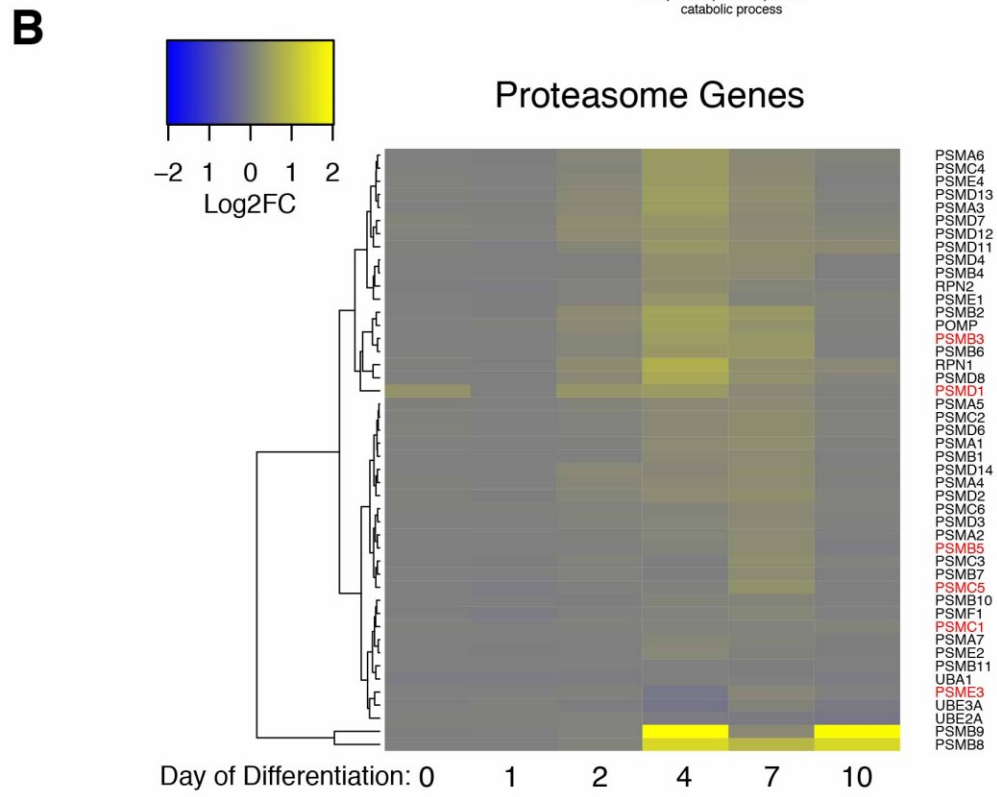
B
Proteasome Genes
−2 1 0 1 2
Log2FC
PSMA6
PSMC4
PSME4
PSMD13
PSMA3
PSMD7
PSMD12
PSMD11
PSMD4
PSMB4
RPN2
PSME1
PSMB2
POMP
PSMB3
PSMB6
RPN1
PSMD8
PSMD1
PSMA5
PSMC2
PSMD6
PSMA1
PSMB1
PSMD14
PSMA4
PSMD2
PSMC6
PSMD3
PSMA2
PSMB5
PSMC3
PSMB7
PSMC5
PSMB10
PSMF1
PSMC1
PSMA7
PSME2
PSMB11
UBA1
PSME3
UBE3A
UBE2A
PSMB9
PSMB8
Day of Differentiation: 0 1 2 4 7 10

Figure 5.2.2: KEGG pathway network analysis identifies potential vulnerabilities in proteasome components.
(A) KEGG pathway network analysis of synthetic lethal genes overlapping with genes that are uniquely expressing in *TSC2*$^{-/-}$ NCCs at day 10 of EB-NCC differentiation (51 genes). Color of nodes correspond to enrichment term. (B) Heatmap of gene expression of proteasome genes throughout EB-NCC differentiation. Genes identified as synthetic lethal are highlighted in red.

CHAPTER 6:

General Discussion

Portions of section 6.1 have been adapted from:

Delaney, S. P., L. M. Julian, A. Pietrobon, J. Yockell-Lelièvre, C. Doré, T. T. Wang, V. C. Doyon, A. Raymond, D. A. Patten, M.-E. Harper, H. Sun and W. L. Stanford (2019*).* "TSC2-deficiency potentiates a catabolic signaling switch that differentiates neural and neural crest lineage development and progressive disease manifestations." bioRxiv: 683359.

Original Manuscript:
Writing – Original Draft, **S.P.D.** and L.M.J.
Writing – Review & Editing, **S.P.D.**, L.M.J., and W.L.S.

To identify the most effective therapies for the various tissue specific manifestations of TSC, robust and authentic tissue-relevant disease models of human origin are required. Up until now, the workhorse cell models of LAM are either heavily manipulated, of murine origin, are derived from irrelevant tissue sources, or some combination of these shortcomings. Furthermore, although some animal models have shown promise and have led to important breakthroughs in understanding TSC and LAM, the disease phenotypes do not recapitulate the pathological manifestations seen in human patients and are generally more severe. It should be noted, however, that the advancements that have been made using the presently available models have resulted in but one FDA-approved treatment for LAM, rapamycin. Although beneficial, the inability of rapamycin to serve as a curative therapy has led the LAM and TSC fields to continue to develop new and more advanced and accurate models for these diseases. Indeed, with the advent of the groundbreaking technologies, CRISPR/Cas9 and iPSC reprogramming, the potential to generate such models has grown immensely. Taking advantage of these advancements, our group moved quickly to pursue epigenetic reprogramming of TSC patient tumor cells to generate the first iPSC models of TSC and LAM. However, it was quickly realized that the loss of TSC2 inhibited reprogramming, a consequence of hyperactive mTORC1 signaling (Wang, Xia et al. 2013, Armstrong, Westlake et al. 2017, Julian, Delaney et al. 2017). To the best of my knowledge at the time of writing, no *TSC1* or *TSC2* null iPSC lines have been generated using reprogramming technology alone to model either TSC or LAM. Therefore, a genome engineering approach is required to establish homozygous TSC1 or TSC2 knockout/loss of function hPSC lines to generate next generation models of TSC and LAM, an initiative undertaken and described in this thesis.

6.1 Summary of findings and contributions to the field

In this thesis, I present a pluripotent stem cell library of TSC2 deficient cells, which we utilized to model cells of origin of both neurological TSC and LAM. This model has multiple important implications, one of the foremost being the flexibility of this system to model tissue-specific manifestations of TSC and LAM. Indeed, this study presents the first multi-lineage model of both TSC and LAM, and strongly emphasizes the importance of using cell types of high relevance to the tissues affected in both of these diseases. This hPSC-based modeling platform permits analyses of the initiation and progression of multiple disease cell types and aberrant phenotypes relevant to TSC and LAM, including neuro-cognitive dysfunction and neural and mesenchymal tumorigenesis, importantly using a human stem cell model.

Recently reported TSC stem cell models have predominantly focused on investigating aberrant glial and neuronal cells (Li, Cao et al. 2017, Nadadhur, Alsaqati et al. 2019), however, these models employ TSC2 heterozygous iPSC lines. In addition, recent work utilizing CRISPR edited hPSCs has confirmed biallelic loss of *TSC1* or *TSC2* genes in cortical spheroids precipitates TSC brain tumor (Blair, Hockemeyer et al. 2018). Although informative, these studies investigate the non-proliferative components of neural TSC lesions and are often limited to one genetically engineered hPSC line. Thus, well validated mechanistic insight into actual TSC neurological tumor development is lacking. These previous studies overlooked the consequences of *TSC2*-deficiency in the progenitor pools that drive tumorigenesis and the associated mechanisms that give rise to cellular dysfunction. Furthermore, although some murine models have emerged that investigate *TSC* gene deficiency in mesenchymal progenitors (Klover, Thangapazham et al. 2017, Wu, Wu et al. 2017), to the best of my knowledge at the time of writing there is currently no known human progenitor stem cell model of mesenchymal

TSC or LAM. This lack of a foundational human mesenchymal TSC and LAM model contributes to the gap in knowledge in the origin of these lineage-specific tumors.

The model system I have developed allows the investigation of the progenitor cell types presumed to drive tumorigenesis in LAM and TSC. In the past, efforts on this front have generally been hampered by the limitation that *TSC1*$^{-/-}$ and *TSC2*$^{-/-}$ mouse models die embryonically with failed neural tube closure (Kobayashi, Minowa et al. 1999, Onda, Lueck et al. 1999, Kobayashi, Minowa et al. 2001), requiring lineage-specific knockout of the *TSC* genes; an approach that has yielded insight into only the CNS manifestations of TSC. As proliferative neural and mesenchymal progenitor cells have been presumed to be the cells of origin for TSC tumors (Delaney, Julian et al. 2014), we hypothesized that loss of TSC2 in NPCs and mesenchymal-like NCCs would have substantial biological consequences that are reflective of disease etiology. The model system presented in this project offers an unprecedented opportunity to investigate the development and maturation of both *TSC2*$^{-/-}$ NPCs and NCCs, which I now show broadly reflect the mesenchymal tumors that develop in multiple tissue systems such as the kidneys (rAML) and lungs (LAM nodules) in TSC patients.

Across all four hPSC lines utilized in this study, I confirm that the loss of TSC2 does not affect the pluripotency regulatory network, nor does it affect the ability of these cell lines to be differentiated into the three germ layers. We, furthermore, establish that TSC2 deficient cells are able to differentiate into the progenitor cell populations presumed to drive tumor progression in both neurological TSC and LAM, NPCs and NCCs, respectively. We demonstrate that *TSC2*$^{-/-}$ NPCs and their neural derivatives exhibit multiple TSC brain tumor characteristics, including aberrations in organelle biogenesis and lineage development, enhanced gliogenesis, and electrophysiological hyperactivity reminiscent of TSC patient epileptic phenotypes. Similarly, I show that NCCs are innately reflective of mesenchymal TSC tumors, supporting long standing

suppositions of the neural crest origin of these tissue specific manifestations (Henske 2003, Crooks, Pacheco-Rodriguez et al. 2004, Goncharova, Goncharov et al. 2008, Delaney, Julian et al. 2014). Interestingly, both *WT* and *TS2*$^{-/-}$ NCCs express common markers of TSC and LAM mesenchymal tumors, such as P-S6, α-SMA, ERα, PR, and VEGFD. This is supportive evidence that the neural crest lineage itself is a representative cell type for LAM. However, *TSC2*$^{-/-}$ NCCs specifically display increased reactivity to the TSC/LAM markers, HMB45 and PDGFRβ, while exhibiting classic oncogenic phenotypes of mTORC1 hyperactivation and increased migratory potential.

Few human cell models have been generated that express the multitude of LAM markers exhibited by *TSC2*$^{-/-}$ NCCs. Cells isolated from patient tumor samples clearly express LAM markers but suffer the caveats of being difficult to maintain in culture, are rare, and are often mixed populations of cells. Although some studies have isolated pure populations of TSC2 null cells from rAMLs that express nearly all of the hallmark markers of LAM, these cells are not able to be maintained indefinitely and are intrinsically limited in supply (Lesma, Sirchia et al. 2009). Immortalized cell lines, such as the LAM patient rAML-derived cell line, 621-101, do display characteristic constitutive mTORC1 activation but express only a subset of LAM markers, such as ERα, PR, and α-SMA (Yu, Astrinidis et al. 2004, Julian, Delaney et al. 2017). Thus, not only do *TSC2*$^{-/-}$ NCCs model LAM with high accuracy across 4 genetic backgrounds, these non-transduced model cells are easily generated at high number and purity and can be made readily available to the entire TSC/LAM research community.

The characterization data both NPC and NCC populations presented in this thesis clearly demonstrate that both of these progenitor cell models accurately reflect neurological TSC and LAM, respectively. As described in both Chapters 3 and 4, no overt effects on lineage specification towards these progenitor cells are observed. However, it is clearly evident that as progenitor populations are established, TSC2-

associated phenotypes quickly surface, suggesting a role of TSC2 in disease pathogenesis at the establishment of these progenitor populations. To shed light on the consequences of *TSC2*$^{-/-}$ deficiency during development and its contribution to disease pathogenesis, a comprehensive developmental RNA-seq experiment was performed, compiling the transcriptomic profiles of both NPC and NCC differentiation.

Analysis of the RNA-seq dataset quickly revealed the immediate initiation of stress response signaling to protein misfolding and ER stress upon neuralization in *TSC2*$^{-/-}$ cells. The resulting protein aggregation phenotype is transient in *TSC*$^{-/-}$ cells during differentiation, being likely due to the simultaneous activation of lysosomal and autophagy pathways contributing to a proteolytic response. Interestingly, whereas protein aggregation is transient in differentiating *TSC*$^{-/-}$ cells, lysosome and autophagosome content is sustained in both WT and *TSC*$^{-/-}$ cells undergoing NPC selective differentiation. This phenomenon is significantly more pronounced in *TSC*$^{-/-}$ cells and we demonstrate that this is cell lineage dependent. By monitoring the NPC and NCC populations during the EB-NCC differentiation protocol, cell-lineage specific phenotypes are clearly visualized. Cells that have specified to the NCC lineage and migrate from neuralized EB clusters have resolved the proteostatic stress response and display reduced lysosome/autophagosome content, with no significant difference observed between *WT* and *TSC*$^{-/-}$ NCCs. We validate this phenomenon within our EB-NCC differentiation protocol, revealing that cells expressing NPC lineage marker, PAX6, maintain elevated lysosome/autophagosome content, which is exacerbated in *TSC*$^{-/-}$ cultures.

These findings have important implications for understanding the initiation of neoplastic tumor development in TSC and LAM, as well as for future development of targeted treatments for system-specific disease manifestations. Several biological mechanisms have been proposed to contribute to tumorigenesis in TSC and LAM, many

of which have undergone investigation as potential therapeutic targets. Dysregulation of autophagy has been clearly established as a component to tumor formation (Parkhitko, Myachina et al. 2011); however, lysosome and autophagosome accumulation has been reported only in TSC brain tumors and in neural-lineage specific murine and cell models of TSC (Goto, Talos et al. 2011, Di Nardo, Wertz et al. 2014). Our data confirm these previous observations by revealing that *TSC2*$^{-/-}$ NPCs, but not NCCs or hPSCs, uniquely develop elevated endosomal signaling mechanisms. Furthermore, these signaling abnormalities are established during early stages of neural lineage specification before generating the well-studied aberrant neural and glial cell types characteristic of TSC brain lesions. Furthermore, mitochondrial and metabolic defects, as well as proteasome dysfunction, have also been identified as potential therapeutic targets for both neurological TSC and LAM (Siroky, Yin et al. 2012, Parkhitko, Priolo et al. 2014, Ebrahimi-Fakhari, Saffari et al. 2016, Van Scheppingen, Broekaart et al. 2016, McKenna III, Kapfhamer et al. 2018, Abdelwahab, Pal et al. 2019). These previous studies did not, however, permit analysis of the mechanistic origin of these phenotypes, let alone during lineage specification; until now, it has been entirely unclear which biological mechanisms drive the induction of disease phenotypes, and which are secondary adaptations of *TSC2*$^{-/-}$ cells. This study reveals for the first time that proteostatic stress is a driving event in the developmental origin of TSC-relevant tumor cell types, and that lineage-specific signaling responses result in the unique metabolic and endosomal adaptations that define the long-term development and identity of each cell type.

Analysis and validation of the RNA-seq dataset in this study reveals a decisive role for the tight regulation of translation as well as catabolic signaling following neural lineage induction from pluripotency. Following the addition of neural induction cues, levels of P-S6, a marker of active protein translation, decrease sharply in both *WT* cells and *TSC2*$^{-/-}$ cells irrespective of hyperactive mTORC1 signaling in *TSC2*$^{-/-}$ cells. This

introduces a paradigm in which decreased global protein translation is favored under normal conditions during early neural cell fate commitment. Additionally, we establish that AMPK/ULK1-mediated pro-autophagy signaling is concurrently activated in differentiating *TSC2*$^{-/-}$ cells, corroborating previous observations of mTORC1-independent regulation of autophagy in patient CNS tumors and *TSC1/TSC2*-deficient cell lines (Di Nardo, Wertz et al. 2014). Thus, *TSC2*$^{-/-}$ NPCs, which cannot regulate mTORC1-mediated protein translation and degradation (Zhang, Nicholatos et al. 2014), potently activate catabolic signaling mechanisms as an adaptive response to promote proteolysis and restore homeostasis. Of note, this catabolic response is resolved upon NCC specification, revealing dynamic, lineage-specific regulation of metabolic and proteostasis signaling. We further demonstrate that although these lineage-specific metabolic adaptations are ameliorated by rapamycin treatment administered while inducing neuralization, they ultimately become rapamycin insensitive. This is consistent with a progressive reliance on mTORC1-independent signaling mechanisms to maintain endosomal signaling in these cells. Furthermore, mTORC1 independent adaptations are reflected in the lack of synergistic toxicity when rapamycin is combined with proteasome inhibitors to selectively target *TSC2*$^{-/-}$ cells. Although active lysosomal-autophagy signaling is observed in *WT* NPCs, this system is exacerbated and cumulative in *TSC2*$^{-/-}$ cells. While maintenance *TSC2*$^{-/-}$ NPC cultures exhibit intact autophagic flux at a level comparable to *WT* cells, we show that they exhibit an overall increase in the biogenesis of endosomal vesicles which display incomplete clearance and progressive accumulation over time. The fact that proteosome inhibitors, but not autophagic flux inhibition (chloroquine), are selectively toxic to *TSC2*$^{-/-}$ NPCs clearly demonstrates that these cells are ultimately dependent on proteolytic activity to maintain their survival.

It is apparent that tight regulation of proteostasis and catabolic signaling is integral in the development of neural lineages. Indeed, catabolic signaling is quickly

revealing itself to be an important pathway across multiple levels of neural development, with involvement in the exit from pluripotency, lineage specification, and the maintenance and activation of adult neural stem cell populations (Audesse and Webb 2018, Leeman, Hebestreit et al. 2018, Villegas, Lehalle et al. 2019). Here, we advance these previous observations to show that this phenomenon is highly specific to the neural lineage, with the developmentally related neural crest lineage adopting distinct mechanisms. Additionally, although several studies have investigated the metabolic consequences of *TSC2*-deficiency in neural and glial lineages, there is limited information regarding derivation of these phenotypes in the neural progenitor pools that gives rise to TSC brain tumors, and sparse knowledge of mesenchymal progenitor pools contributing to TSC. The comprehensive RNA-seq dataset presented here compiles the transcriptomic profiles of early NPC and NCC differentiation, shedding light on the developmental origin of TSC and LAM neoplasms while presenting insight into the role of TSC2-mTORC1 signaling in early cell fate decisions.

Emphasizing the importance of using tissue-relevant cell models to investigate potential therapies for multisystem diseases, this study highlights that lineage specific adaptations pose consequences in the therapeutic context. Bortezomib and carfilzomib are both FDA-approved proteasome inhibitors that have been considered for treatment of TSC manifestations. Proteasome inhibition has been applied predominantly toward mesenchymal tumors. Strikingly, we show that *TSC2*$^{-/-}$ NPCs can be selectively targeted for cell death using these agents, leaving *WT* NPCs unaffected. However, the same treatments display no genotype specific toxicity in NCCs. These latter findings are in contrast to previous studies demonstrating the potential therapeutic effectiveness of these treatments *in vitro*; however, we note that the *TSC2*-deficient cell types used in these studies were murine cell lines with limited tissue-specific relevance to TSC tumors or are immortalized human rAML cell lines (Zhou, Ikenoue et al. 2009, Siroky, Yin et al.

2012, Babcock, Nguyen et al. 2013, Johnson, Dunlop et al. 2018). Indeed, in a preclinical trial using a *Tsc2*$^{+/-}$ mouse model, bortezomib treatment was ineffective in targeting mesenchymal renal tumors (Auricchio, Malinowska et al. 2012). This thesis, which employs four unique human genetic backgrounds, explains the findings of this *Tsc2*$^{+/-}$ mouse model. Importantly, this thesis demonstrates that the utility of proteasome inhibition therapy for TSC/LAM tumors is limited to the neural lineage manifestations. These results underscore the importance of using stem cell-based models to generate relevant cell types when investigating mechanisms of disease using *in vitro* systems, particularly in the case of multisystem disorders.

To uncover previously unconsidered therapeutic avenues that could be used to specifically target the mesenchymal manifestations of LAM, and potentially all tumor manifestations of TSC, a genome-wide CRISPR knockout screen was performed to identify genes that confer synthetic lethality when knocked out in TSC2 deficient cells. One previous study has utilized a similar genome-wide approach to identify novel treatments for TSC (Housden, Valvezan et al. 2015); however, the authors combined CRISPR modified *TSC1* and *TSC2 Drosophila* cell lines with a genome-wide RNAi screen. Although many physiological processes and gene functions are conserved between fly and human, significant disparity is to be expected (Pandey and Nichols 2011). This aspect, combined with the use of RNAi, a less sensitive approach than gene knockout with higher rate of off-target effects, may limit the applicability of findings to treat tissue specific disease manifestations. Indeed, when identified targets in this screen were cross validated using mammalian orthologs in TSC2 deficient mouse embryonic fibroblasts and 621-101 cells, synthetic effects were mild and limited to growth inhibition. Thus, the work presented in this thesis offers the first genome-wide synthetic lethal gene knockout screen to identify novel treatment strategies for LAM and TSC using an accurate and tissue-relevant disease model.

Aligning with previously postulated vulnerabilities of TSC1 or TSC2 deficient cells, the synthetic lethal screen identified negatively selected genes specific to *TSC2*$^{-/-}$ NCCs that, following GSEA, are associated with pathways or biological processes that have been previously investigated or proposed as potential therapeutic targets. These pathway terms included “PI3K-Akt”, “MAPK” and “Ras” signaling, along with “cell cycle” and “metabolic pathways” (Figure 5.1.4C, Table S8) (Mi, Ma et al. 2009, McCormack, Inoue et al. 2011, Taveira-DaSilva and Moss 2012, Sun, Gu et al. 2014, Medvetz, Priolo et al. 2015, Tam, Yockell-Lelievre et al. 2019). Of note, although inhibition of autophagy in combination with mTORC1 inhibition has been investigated as a potential treatment for LAM (Parkhitko, Myachina et al. 2011, El-Chemaly, Taveira-Dasilva et al. 2017), pathways relating to autophagy were not enriched in this screen. Indeed, although larger phase II/III studies are required to thoroughly evaluate the efficacy of this treatment approach, a recent phase I clinical trial pairing hydroxychloroquine with rapamycin did not show a clear benefit to patient outcome (El-Chemaly, Taveira-Dasilva et al. 2017). Furthermore, this corroborates the results presented in Chapter 4 regarding the ineffective targeting of TSC2 deficient NCCs and NPCs with the autophagy inhibitor, chloroquine, in combination with rapamycin.

Although the synthetic lethal gene list enriched for pathways that may have been targeted with limited success in the past, this assay provides gene-level resolution within each of these pathways. Therefore, these therapeutic avenues could be revisited and targeted with high specificity for these newly identified genetic vulnerabilities. For instance, genes involved in PI3K-Akt-, MAPK-, and Ras-signaling pathways are all upstream and eventually converge to mTORC1 signaling; the “mTOR signaling” pathway term does not enrich following GSEA (Figure 5.1.4C). This suggests inhibition of mTOR signaling will not result in selective lethal targeting of TSC2 deficient cells; however, it is well established that the first line treatment strategy for LAM and TSC is mTORC1

inhibition, resulting in mere cytostatic effects. The synthetic lethal screen in this thesis provides evidence that targeting upstream of mTOR may yield more promising results in regard to selective lethal targeting of TSC2 deficient cells. This study already provides evidence supporting this approach. Targeting upstream of the above listed pathways, the receptor tyrosine kinase, FGFR1, the 13th highest ranked synthetic lethal gene and first directly 'druggable' target (Table 5.1, Table S6), yielded very promising results. The drug, ACTB-1003, showed highly selective synthetic lethal dosage interactions towards *TSC2*$^{-/-}$ NCCs, while leaving *WT* NCCs unaffected over a wide dosage range. Interestingly, this is in contrast with to the other FGFR1 inhibitors tested, which displayed adverse effects in both *WT* and *TSC2*$^{-/-}$ NCCs. This is likely due to the documented selectivity of ACTB-1003 for FGFR1, whereas the other molecular inhibitors showed broader inhibition of FGFRs 1-4 (NCATS 2018). This implies that specificity is critical when targeting protein products of synthetic lethal genes, a potential limitation of employing molecular inhibitors which often have adverse non-specific effects. As only a small portion of the genome is considered 'druggable' (≤7.5%) (Hopkins and Groom 2002, Griffith, Griffith et al. 2013), alternative approaches to target synthetic lethal genetic elements outside of traditional pharmacological inhibition, such as RNA-based or CRISPR-based technologies, may prove to be most effective at exerting synthetic lethal effects.

One caveat of using a pooled sgRNA screen to identify synthetic lethal genetic elements is that the mechanism of cell death, if indeed death, is not identified. As this assay is based on quantifying sgRNA sequence representation within the population, gene knockout may have influence on representation through factors that do not affect cell viability in the *in vitro* culture system. For instance, in the absence of TSC2, the knockout of a gene may confer synthetic interactions relating to inhibiting proliferation, causing senescence, or simply affect cell adherence to the growth surface resulting in

loss of representation during culture maintenance. As a consequence, some synthetic 'lethal' hits may be false positives or offer no more therapeutic benefit than rapalogs, i.e. inhibiting cell growth and proliferation. Hits falling into the latter category, however, may still prove beneficial to patients by potentially offering more targeted therapy with ideally more mild side effects than rapamycin and its analogs. Moving forward, any potential false positives can be quickly identified upon validation of the synthetic lethal gene hits, and true positives will be selected and developed for preclinical investigation. Following extensive validation of the synthetic lethal genetic elements identified in this screen, a clearer picture of the vulnerabilities of TSC2 deficient cells will assuredly emerge. Thus, the synthetic lethal dataset generated in this project may serve as a detailed road map for the further development of previously unconsidered and more effective treatments for both TSC and LAM.

6.2 Future Development

The strength of the cell model system I present in this thesis and its implications for TSC and LAM research is evident. Being a stem cell-based model, we are afforded the flexibility to test multiple cell lineages for tissue-specific phenotypes in a variety of contexts to advance both therapeutic development and our understanding of disease pathogenesis in TSC, LAM, and mTORopathies as a whole. This hPSC model system and the accompanying resource of transcriptomic and synthetic lethal data can serve as foundational infrastructure from which further research can be advanced. Of high priority for further development are research initiatives that are focused on advancing accurate preclinical models of LAM, understanding mTORC1 independent functions of both TSC1 and TSC2 and their contribution to disease, and identifying and developing new therapeutic avenues.

6.2.1 Development of accurate preclinical models for LAM

There is a great need for more advanced and accurate preclinical models for LAM. The currently available animal models of LAM do not sufficiently recapitulate disease pathology. On this front, the preliminary *in vivo* work presented in Chapter 3 of this thesis strongly supports further development of a xenotransplant preclinical model of LAM using *TSC2*$^{-/-}$ NCCs. Multiple parameters must be optimized, however. Within this study, mice were injected and monitored over a 10-month period to better simulate the slow growing, but progressive, nature of LAM. This is a considerable amount of time which limits throughput and the use of such an approach as a preclinical model to test treatment efficacy. Decreasing this time frame would greatly increase its practical use as an animal model, utilizing strategies such as increasing the number of cells injected from 2.5×10^5 (used in this study) by an order of magnitude. Furthermore, although not entirely understood, LAM is clearly hormone dependent; introducing exogenous estrogen or progesterone may promote the onset of LAM-like phenotypes in a time frame that is more practical to serve as a preclinical model. Disease progression could potentially be monitored using minimally-invasive techniques before endpoint, such as measuring serum levels of biomarkers that correlate with declining lung function and presence of rAMLs, such as VEGFD and/or Galectin 3 (Young, Lee et al. 2013, Klover, Thangapazham et al. 2017). If successful, this xenotransplant model could be potentially employed to investigate the validated synthetic lethal genetic elements identified during the synthetic lethal CRISPR knockout screen.

Extending this initiative, an exciting development in which the goal of generating a highly accurate *in vivo* model of LAM may be realized is the use of mouse-human neural crest chimeras. Recent work has established a method to investigate neural crest development and disease using human NCCs injected into mouse embryos. The injection of developmentally matched differentiated human NCCs to mouse embryonic-

day-8 embryos was shown to generate chimeras with functional integration of human neural crest derivatives (Cohen, Wert et al. 2016, Cohen, Markoulaki et al. 2018). Recently, this mouse-human neural crest chimera system was successfully used to generate neuroblastoma, a known neurocristopathy (Cohen, Zhang et al. 2019). Accordingly, utilizing this chimera system with TSC2 deficient NCCs could offer exciting and undoubtedly impactful insight into the NCC cell of origin theory for TSC and LAM. If TSC2 deficient human NCCs successfully integrate into the developing embryo and form lesions reminiscent of mesenchymal TSC and LAM, it would provide the most impactful evidence of a neural crest cell of origin for LAM and mesenchymal TSC. Furthermore, with faithful recapitulation of LAM lesions, promising therapeutic approaches may be investigated using this system. For instance, immune checkpoint blockade therapy is quickly gaining traction and has been successfully utilized to treat a number of different cancers (Page, Postow et al. 2014, Darvin, Toor et al. 2018). This has already been proposed as a viable approach to treat LAM and has undergone initial testing in a preclinical setting (Liu, Lizotte et al. 2018, Maisel, Merrilees et al. 2018, Pietrobon, Delaney et al. 2018). However, progress is limited by the inherent issues of utilizing xenotransplants in immunocompromised mice or solely relying on murine systems to perform immunotherapy studies. A human-mouse chimera system would offer an ideal modeling platform to investigate anti-tumor immune response in a fully immunocompetent mouse model (Cohen, Zhang et al. 2019). This human NCC-mouse chimera system is currently under development in the Stanford Lab, and we expect our efforts to yield highly impactful results for the LAM and TSC research community.

6.2.2 Exploring non-canonical roles of TSC1 and TSC2 in disease pathogenesis

An important aspect of TSC and LAM pathogenesis that is not well understood are the non-canonical roles of both *TSC1* and *TSC2*. Evidence suggests that such mTORC1 independent functions of these genes play an important role in disease progression and severity (Neuman and Henske 2011). In Chapter 3, the *TSC2*Δ genome modification was introduced, and although it shows great promise as a mutant allele to model TSC and LAM, its characterization in this study was limited. The persistence of a near full length TSC2 mutant isoform that maintained intracellular localization suggested that the TSC2Δ isoform may still retain functions that are independent from its canonical role within the TSC1/2 complex. Therefore, to minimize potentially confounding factors, in-depth characterization of TSC2 deficiency was reserved for the TSC2 knockout allele. However, the *TSC2*Δ modification will serve well in ongoing studies, specifically investigating the non-canonical roles of TSC2 in the pathogenesis of TSC and LAM. Indeed, as mentioned previously, loss of TSC2 results in more severe disease phenotypes which served as the rationale for targeting this gene for CRISPR/Cas9-mediated genome modifications (Dabora, Jozwiak et al. 2001, Muzykewicz, Sharma et al. 2009). If paired with both *TSC1* knockout and *TSC2* knockout hPSC lines, the *TSC2*Δ cell lines can help elucidate mTORC1-independent pathological mechanisms that contribute to the severity of disease. Such work would greatly contribute to the development of new strategies to treat LAM in particular, as strategies to inhibit the spread of LAM tumors would well complement the beneficial (albeit cytostatic) effects of rapamycin. Our group is currently advancing this approach towards therapeutic development by employing the *TSC2*Δ cell lines generated in this study, and effort that is expected to yield impactful results for the LAM and TSC research community.

6.2.3 Targeting synthetic lethal interactors in TSC2 deficient cells

A promising validated synthetic lethal candidate, FGFR1, has emerged from the results of the synthetic lethal screen. It should be noted, however, that this target, along with the other synthetic lethal hits in this screen, were identified using a single cell lineage; the *TSC2*$^{-/-}$ NCCs utilized in this screen act to model the cell of origin for LAM tumors. Although potentially offering substantial therapeutic benefit, the synthetic lethal genes identified here may only affect the cells of origin and not the aberrantly differentiated cells within neoplastic tumors themselves. As clearly indicated in Chapter 4, disease-associated phenotypes are highly cell type dependent, and thereby, may have important implications when targeting therapeutically. Therefore, the synthetic lethal genes identified in this screen may not offer broad targeting capabilities in all TSC tumors, or may be perhaps limited to cell sub-lineages, such as the proliferative smooth muscle-like, or melanocyte-like components of mesenchymal TSC and LAM tumors. Fortunately, the stem cell-based model presented in this study allows the specific investigation of multiple cell lineages with the same genetic background. Thus, testing and validating the identified hits across multiple cells lineages implicated in LAM and TSC will undoubtedly reveal targets that offer broad therapeutic effect for LAM and, ideally, the majority of TSC tumors.

This TSC2 deficient hPSC model system has already proven useful in identifying lineage specific susceptibility to therapeutic agents, specifically proteasome inhibitors in NPCs versus NCCs. Although the FDA-approved proteasome inhibitors utilized in this study did not selectively sensitize *TSC2*$^{-/-}$ NCCs to cell death, both bortezomib and carfilzomib are broad spectrum proteasome inhibitors. This is potentially consequential; following integration of the synthetic lethal dataset with the transcriptomic profile of differentiated NCCs reveal that the proteasome may still be a viable target pathway to

sensitize TSC2 deficient NCCs. Close inspection revealed differential expression of i-proteasome-specific genes which may be exploitable for selective targeting. Supporting this finding, recent work has identified dysregulation of the i-proteasome in human TSC cortical tubers (van Scheppingen, Broekaart et al. 2016). The i-proteasome is a specialized assembly within the ubiquitin-proteasome system and is involved in a number of processes outside of its canonical role in antigen processing, including differentiation, wound healing, and stress response (Seifert, Bialy et al. 2010, Ferrington, Roehrich et al. 2013, Cui, Hwang et al. 2014, Yun, Kim et al. 2016). The i-proteasome has been documented to be more rapid than the constitutive proteasome while displaying an increased proteolytic processing capacity (Seifert, Bialy et al. 2010), a potentially beneficial feature in the context of mTORC1 hyperactivation. Indeed, mTORC1 has been shown to interact with i-proteasome β subunits and cells exhibit dependency on the immunoproteasome for survival under constitutive mTORC1 activation (Yun, Kim et al. 2016). Therefore, the use of i-proteasome specific inhibitors, such as ONX-0914 or ML604440 (Yun, Kim et al. 2016), warrants further investigation as they may offer selective targeting of TSC2 deficient NCCs and their derivatives.

One family of genes that may be easily overlooked when processing synthetic lethal datasets are ribosomal genes. Genes involved in translation processes, such as genes coding for ribosomal subunits, may be generally considered essential to cell survival in all cell types. However, in the context of hyperactive mTORC1 signaling, where pathways attributed to transcription and translation are constitutively active, the translational machinery may be overloaded, leaving cells susceptible to treatments targeting these cellular constituents. Ribosome composition and function have recently been gaining more attention for their potential role in cancer (Goudarzi and Lindstrom 2016, Sulima, Hofman et al. 2017). Of note, the ribosomal gene, RPS11, was ranked as the 4th most synthetic lethal gene in this study (Table 5.1, Table S6) and has been

associated with poor prognosis in glioblastoma, suggesting a significant physiological role for this ribosomal subunit (Yong, Shabihkhani et al. 2015). Targeting this and other ribosome constituents in LAM and TSC may be an important new therapeutic strategy. Supporting the rationale of this approach, many ribosomal subunit genes have multiple paralogs, which ultimately endow cells with plasticity in the structure and function of the ribosome assemblies themselves (Komili, Farny et al. 2007, O'Leary, Schreiber et al. 2013, Palumbo, Fuchs et al. 2017, Segev and Gerst 2018). Accordingly, it stands to reason that what may be a tolerable loss of translational machinery in WT cells, may be highly detrimental to the survival of TSC2 deficient cells.

In order to most accurately investigate the synthetic lethal targets identified in this study, highly specific and advanced approaches must be taken. The use of molecular inhibitors is simply not applicable to the vast majority of the synthetic lethal hits, both due to their respective 'druggability' and the promiscuity of molecular inhibitors; utilizing RNAi technologies or CRISPR-based technologies to optimize specificity to therapeutic targets is necessary. Fortunately, these approaches are quickly gaining momentum in clinical applications. For instance, the FDA has recently approved at least 3 antisense oligonucleotide drugs (nusinersen to treat spinal muscular atrophy, fomivirsen to treat cytomegalovirus retinitis, and mipomersen to treat high blood cholesterol) and 1 siRNA drug (patisiran to treat hereditary transthyretin amyloidosis), with many more currently in development (Yin and Rogge 2019). This new class of drugs have demonstrated efficacy and safety for a variety of indications and opens the door to thousands of new drug targets to treat a variety of diseases including LAM. Thus, employing RNAi-based strategies to investigate synthetic lethal targets is a viable avenue towards developing clinically relevant treatments for LAM.

Alternatively, perhaps the most precise targeting strategy to employ when targeting synthetic lethal interactors would be through the use of CRISPR-based

technologies. Utilizing CRISPR for gene knockout in the clinical setting, however, may not be realized for many years to come until issues regarding Cas9 specificity, immunogenicity, and efficiency are resolved (Kleinstiver, Pattanayak et al. 2016, Slaymaker, Gao et al. 2016, You, Tong et al. 2019). With this in consideration, investigating tangential approaches to CRISPR/Cas9-mediated gene knockout, such as CRISPR/Cas9-mediated transcriptional interference (CRISPRi) may be more clinically relevant. Utilizing a catalytically inactive mutant Cas9 conjugated with Krüppel-associated box repression domain (dCas9-KRAB), gene expression can be efficiently inhibited with high precision in a reversable manner (Gilbert, Larson et al. 2013, Qi, Larson et al. 2013, Mandegar, Huebsch et al. 2016).

Both CRISPRi and RNAi offer highly selective approaches to inhibit gene expression at levels of transcription and translation, respectively, and will undoubtedly aid in the further investigation of synthetic lethal genes as therapeutic targets. With these advanced approaches, nearly the entire genome has become ‘druggable’, remarkably changing the landscape of modern therapeutics. Importantly, RNAi and CRISPRi approaches would facilitate the targeting of miRNAs, which, over the last 10 years, have emerged as important players across multiple diseases (Paul, Chakraborty et al. 2018). A single miRNA may act to influence the expression of multiple genes (Lam, Chow et al. 2015), effectively acting as a multipronged regulators of disease relevant pathways (Ben-Hamo and Efroni 2015). With this in consideration, it is of note that over 10% of the top 100 synthetic lethal genes identified in the synthetic lethal screen are miRNAs, whose predicted mRNA targets conferred a growth advantage when knocked out. This implies that their dysregulation is indeed consequential physiologically, supporting their further investigation for therapeutic targeting. Thus, with both RNAi and CRISPRi tools at our disposal, we expect to quickly and efficiently identify novel therapeutic targets for TSC and LAM.

6.3 Conclusion

Collectively, the results presented in this thesis exemplify the strength of using a hPSC-based approach to model TSC and LAM. Through pairing genome editing with stem cell biology, I have generated a useful resource to serve as a platform for continued study of the cells of origin and their derivatives to faithfully model both of these diseases. Additionally, the emergence of a neural crest-based model of the progenitor cell of origin for mesenchymal TSC and LAM is an advancement of the field. Evidence has suggested this cell to be of neural crest origin and this study is the first to specifically utilize human NCCs to investigate this hypothesis. In doing so, I have provided strong evidence that *TSC2*$^{-/-}$ NCCs serve as an accurate cell model for LAM. Through transcriptomic profiling of NCC and NPC differentiation, we also uncover previously unappreciated lineage-specific mechanisms and therapeutic vulnerabilities that require strong consideration when moving forward to develop tissue-specific treatments for TSC and LAM. Furthermore, combining both the rich transcriptomic dataset with the results of the genome-wide synthetic lethal CRISPR knockout screen, I have provided an expansive resource to advance LAM and TSC research (Figure 6.1). This resource and *in vitro* model system are together intended to serve as a platform to further investigate the mechanisms underlying TSC tumorigenesis that remain elusive, such as the sex-specific mesenchymal manifestations of LAM, and to identify previously unconsidered vulnerabilities that accompany TSC2 deficiency spanning multiple cell lineages. In summary, this non-transformed, stem cell-based model of LAM and TSC, paired with the genome-wide approaches to identify vulnerabilities of TSC2-null cells, provides a framework from which novel and efficient therapeutic strategies can identified and developed quickly and efficiently.

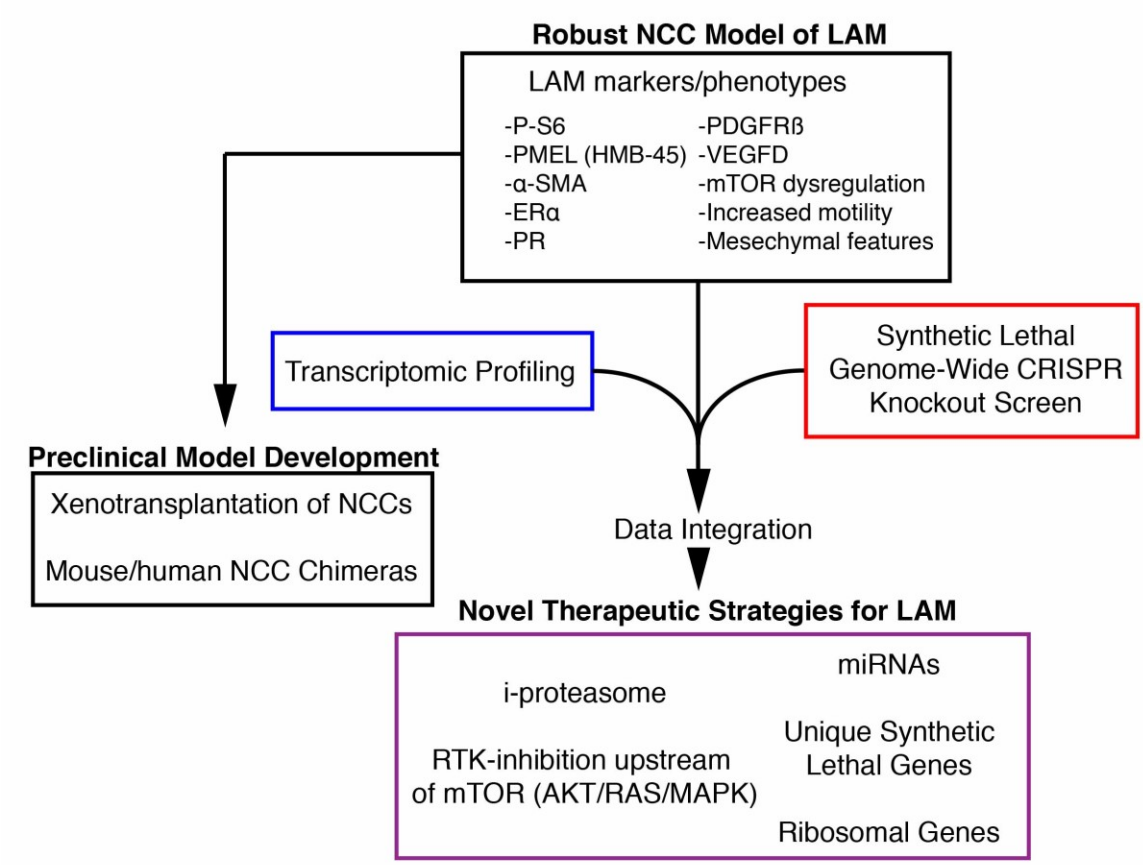

Figure 6.1: Summary of findings and future directions of therapeutic development for LAM.
The work presented in thesis provides a strong framework from which to further develop new and effective treatments for LAM. $TSC2^{-/-}$ NCCs model a multitude of LAM-associated phenotypes that is unmatched by any existing *in vitro* models of LAM. This highly accurate cell model underwent transcriptomic profiling and a genome-wide CRISPR knockout screen to identify genes that are synthetic lethal in $TSC2^{-/-}$ NCCs. Combining these rich datasets allows the identification of novel vulnerabilities within signaling pathways, unique genes, and gene families that have not yet been identified as therapeutic targets for LAM. To further facilitate the validation and development of these newly identified genetic weaknesses, these LAM-like $TSC2^{-/-}$ NCCs are ideal for developing advanced humanized preclinical models that faithfully recapitulate LAM disease manifestations.

References

Abdelwahab, E., S. Pal, K. Kvell, V. Sarosi, P. Bai, R. Rue, V. Krymskaya, D. McPhail, A. Porter and J. Pongracz (2019). "Mitochondrial dysfunction is a key determinant of the rare disease lymphangioleiomyomatosis and provides a novel therapeutic target." Oncogene **38**(16): 3093.

Adams, D., A. Gonzalez-Duarte, W. D. O'Riordan, C. C. Yang, M. Ueda, A. V. Kristen, I. Tournev, H. H. Schmidt, T. Coelho, J. L. Berk, K. P. Lin, G. Vita, S. Attarian, V. Plante-Bordeneuve, M. M. Mezei, J. M. Campistol, J. Buades, T. H. Brannagan, 3rd, B. J. Kim, J. Oh, Y. Parman, Y. Sekijima, P. N. Hawkins, S. D. Solomon, M. Polydefkis, P. J. Dyck, P. J. Gandhi, S. Goyal, J. Chen, A. L. Strahs, S. V. Nochur, M. T. Sweetser, P. P. Garg, A. K. Vaishnaw, J. A. Gollob and O. B. Suhr (2018). "Patisiran, an RNAi Therapeutic, for Hereditary Transthyretin Amyloidosis." N Engl J Med **379**(1): 11-21.

Adli, M. (2018). "The CRISPR tool kit for genome editing and beyond." Nat Commun **9**(1): 1911.

Ao, X., L. Zou and Y. Wu (2014). "Regulation of autophagy by the Rab GTPase network." Cell Death Differ **21**(3): 348-358.

Arbiser, J. L., B. Govindarajan, X. Bai, H. Onda, A. Kazlauskas, S. D. Lim, M. B. Amin and L. Claesson-Welsh (2002). "Functional tyrosine kinase inhibitor profiling: a generally applicable method points to a novel role of platelet-derived growth factor receptor-beta in tuberous sclerosis." Am J Pathol **161**(3): 781-786.

Armstrong, L. C., G. Westlake, J. P. Snow, B. Cawthon, E. Armour, A. B. Bowman and K. C. Ess (2017). "Heterozygous loss of TSC2 alters p53 signaling and human stem cell reprogramming." Hum Mol Genet **26**(23): 4629-4641.

Asha, H., N. D. de Ruiter, M. G. Wang and I. K. Hariharan (1999). "The Rap1 GTPase functions as a regulator of morphogenesis in vivo." EMBO J **18**(3): 605-615.

Astrinidis, A., W. Senapedis, T. R. Coleman and E. P. Henske (2003). "Cell cycle-regulated phosphorylation of hamartin, the product of the tuberous sclerosis complex 1 gene, by cyclin-dependent kinase 1/cyclin B." J Biol Chem **278**(51): 51372-51379.

Au, K. S., A. T. Williams, E. S. Roach, L. Batchelor, S. P. Sparagana, M. R. Delgado, J. W. Wheless, J. E. Baumgartner, B. B. Roa, C. M. Wilson, T. K. Smith-Knuppel, M.-Y. C. Cheung, V. H. Whittemore, T. M. King and H. Northrup (2007). "Genotype/phenotype correlation in 325 individuals referred for a diagnosis of tuberous sclerosis complex in the United States." Genetics in Medicine **9**(2): 88-100.

Audesse, A. J. and A. E. Webb (2018). "Enhancing Lysosomal Activation Restores Neural Stem Cell Function During Aging." Journal of experimental neuroscience **12**: 1179069518795874.

Auricchio, N., I. Malinowska, R. Shaw, B. D. Manning and D. J. Kwiatkowski (2012). "Therapeutic trial of metformin and bortezomib in a mouse model of tuberous sclerosis complex (TSC)." PLoS One **7**(2): e31900.

Babcock, J. T., H. B. Nguyen, Y. He, J. W. Hendricks, R. C. Wek and L. A. Quilliam (2013). "Mammalian target of rapamycin complex 1 (mTORC1) enhances bortezomib-induced death in tuberous sclerosis complex (TSC)-null cells by a c-MYC-dependent induction of the unfolded protein response." Journal of Biological Chemistry **288**(22): 15687-15698.

Bartel, D. P. (2009). "MicroRNAs: target recognition and regulatory functions." Cell **136**(2): 215-233.

Basler, M., Kirk, C.J., and Groettrup, M. (2013). The immunoproteasome in antigen processing and other immunological functions. Curr Opin Immunol *25*, 74-80.

Beg, M. S., A. J. Brenner, J. Sachdev, M. Borad, Y. K. Kang, J. Stoudemire, S. Smith, A. G. Bader, S. Kim and D. S. Hong (2017). "Phase I study of MRX34, a liposomal miR-34a mimic, administered twice weekly in patients with advanced solid tumors." Invest New Drugs **35**(2): 180-188.

Ben-Hamo, R. and S. Efroni (2015). "MicroRNA regulation of molecular pathways as a generic mechanism and as a core disease phenotype." Oncotarget **6**(3): 1594-1604.

Ben-Sahra, I., J. J. Howell, J. M. Asara and B. D. Manning (2013). "Stimulation of de novo pyrimidine synthesis by growth signaling through mTOR and S6K1." Science **339**(6125): 1323-1328.

Ben-Sahra, I., G. Hoxhaj, S. J. H. Ricoult, J. M. Asara and B. D. Manning (2016). "mTORC1 induces purine synthesis through control of the mitochondrial tetrahydrofolate cycle." Science **351**(6274): 728-733.

Bergman, A. and M. L. Siegal (2003). "Evolutionary capacitance as a general feature of complex gene networks." Nature **424**(6948): 549-552.

Bindea, G., B. Mlecnik, H. Hackl, P. Charoentong, M. Tosolini, A. Kirilovsky, W. H. Fridman, F. Pages, Z. Trajanoski and J. Galon (2009). "ClueGO: a Cytoscape plug-in to decipher functionally grouped gene ontology and pathway annotation networks." Bioinformatics **25**(8): 1091-1093.

Birchenall-Roberts, M. C., T. Fu, O. S. Bang, M. Dambach, J. H. Resau, C. L. Sadowski, D. C. Bertolette, H. J. Lee, S. J. Kim and F. W. Ruscetti (2004). "Tuberous sclerosis complex 2 gene product interacts with human SMAD proteins. A molecular link of two tumor suppressor pathways." J Biol Chem **279**(24): 25605-25613.

Bissler, J. J., J. C. Kingswood, E. Radzikowska, B. A. Zonnenberg, M. Frost, E. Belousova, M. Sauter, N. Nonomura, S. Brakemeier and P. J. De Vries (2013). "Everolimus for angiomyolipoma associated with tuberous sclerosis complex or sporadic lymphangioleiomyomatosis (EXIST-2): a multicentre, randomised, double-blind, placebo-controlled trial." The Lancet **381**(9869): 817-824.

Bittmann, I., B. Rolf, G. Amann and U. Lohrs (2003). "Recurrence of lymphangioleiomyomatosis after single lung transplantation: new insights into pathogenesis." Hum Pathol **34**(1): 95-98.

Blair, J. D., D. Hockemeyer and H. S. Bateup (2018). "Genetically engineered human cortical spheroid models of tuberous sclerosis." Nat Med **24**(10): 1568-1578.

Brandsma, I. and D. C. Gent (2012). "Pathway choice in DNA double strand break repair: observations of a balancing act." Genome Integr **3**(1): 9.

Bryant, H. E., N. Schultz, H. D. Thomas, K. M. Parker, D. Flower, E. Lopez, S. Kyle, M. Meuth, N. J. Curtin and T. Helleday (2005). "Specific killing of BRCA2-deficient tumours with inhibitors of poly(ADP-ribose) polymerase." Nature **434**(7035): 913-917.

Bunting, S. F., E. Callen, N. Wong, H. T. Chen, F. Polato, A. Gunn, A. Bothmer, N. Feldhahn, O. Fernandez-Capetillo, L. Cao, X. Xu, C. X. Deng, T. Finkel, M. Nussenzweig, J. M. Stark and A. Nussenzweig (2010). "53BP1 inhibits homologous recombination in Brca1-deficient cells by blocking resection of DNA breaks." Cell **141**(2): 243-254.

Caban, C., N. Khan, D. M. Hasbani and P. B. Crino (2017). "Genetics of tuberous sclerosis complex: implications for clinical practice." Appl Clin Genet **10**: 1-8.

Campani, V., G. Salzano, S. Lusa and G. De Rosa (2016). "Lipid Nanovectors to Deliver RNA Oligonucleotides in Cancer." Nanomaterials (Basel) **6**(7).

Canpolat, M., H. Per, H. Gumus, A. Yikilmaz, E. Unal, T. Patiroglu, L. Cinar, A. Kurtsoy and S. Kumandas (2014). "Rapamycin has a beneficial effect on controlling epilepsy in children with tuberous sclerosis complex: results of 7 children from a cohort of 86." Childs Nerv Syst **30**(2): 227-240.

Capo-Chichi, J. M., J. Tcherkezian, F. F. Hamdan, J. C. Decarie, S. Dobrzeniecka, L. Patry, M. A. Nadon, B. E. Mucha, P. Major, M. Shevell, B. O. Bencheikh, R. Joober, M. E. Samuels, G. A. Rouleau, P. P. Roux and J. L. Michaud (2013). "Disruption of TBC1D7, a subunit of the TSC1-TSC2 protein complex, in intellectual disability and megalencephaly." J Med Genet **50**(11): 740-744.

Carsillo, T., A. Astrinidis and E. P. Henske (2000). "Mutations in the tuberous sclerosis complex gene TSC2 are a cause of sporadic pulmonary lymphangioleiomyomatosis." Proc Natl Acad Sci U S A **97**(11): 6085-6090.

Carson, R. P., D. L. Van Nielen, P. A. Winzenburger and K. C. Ess (2012). "Neuronal and glia abnormalities in Tsc1-deficient forebrain and partial rescue by rapamycin." Neurobiology of disease **45**(1): 369-380.

Casanova, A., R. Maria Giron, O. Acosta, M. Barron, C. Valenzuela and J. Ancochea (2011). "Lymphangioleiomyomatosis treatment with sirolimus." Arch Bronconeumol **47**(9): 470-472.

Chambers, S. M., C. A. Fasano, E. P. Papapetrou, M. Tomishima, M. Sadelain and L. Studer (2009). "Highly efficient neural conversion of human ES and iPS cells by dual inhibition of SMAD signaling." Nature biotechnology **27**(3): 275.

Chan, N., I. M. Pires, Z. Bencokova, C. Coackley, K. R. Luoto, N. Bhogal, M. Lakshman, P. Gottipati, F. J. Oliver, T. Helleday, E. M. Hammond and R. G. Bristow (2010). "Contextual synthetic lethality of cancer cell kill based on the tumor microenvironment." Cancer Res **70**(20): 8045-8054.

Chang, H. H. Y., N. R. Pannunzio, N. Adachi and M. R. Lieber (2017). "Non-homologous DNA end joining and alternative pathways to double-strand break repair." Nat Rev Mol Cell Biol **18**(8): 495-506.

Chang, W. Y., J. R. Lavoie, S. Y. Kwon, Z. Chen, J. L. Manias, J. Behbahani, V. Ling, R. A. Kandel, D. J. Stewart and W. L. Stanford (2013). "Feeder-independent derivation of induced-pluripotent stem cells from peripheral blood endothelial progenitor cells." Stem Cell Res **10**(2): 195-202.

Cheadle, J. P., M. P. Reeve, J. R. Sampson and D. J. Kwiatkowski (2000). "Molecular genetic advances in tuberous sclerosis." Hum Genet **107**(2): 97-114.

Chen, G., D. R. Gulbranson, Z. Hou, J. M. Bolin, V. Ruotti, M. D. Probasco, K. Smuga-Otto, S. E. Howden, N. R. Diol and N. E. Propson (2011). "Chemically defined conditions for human iPSC derivation and culture." Nature methods **8**(5): 424.

Chen, P.H., Chen, X., and He, X. (2013). Platelet-derived growth factors and their receptors: structural and functional perspectives. Biochim Biophys Acta *1834*, 2176-2186.

Chen, Z., W. Y. Chang, A. Etheridge, H. Strickfaden, Z. Jin, G. Palidwor, J. H. Cho, K. Wang, S. Y. Kwon and C. Doré (2017). "Reprogramming progeria fibroblasts re-establishes a normal epigenetic landscape." Aging cell **16**(4): 870-887.

Cho, J. H., B. Patel, S. Bonala, S. Manne, Y. Zhou, S. K. Vadrevu, J. Patel, M. Peronaci, S. Ghouse, E. P. Henske, F. Roegiers, K. Giannikou, D. J. Kwiatkowski, H. Mansouri, M. M. Markiewski, B. White and M. Karbowniczek (2017). "Notch transactivates Rheb to maintain the multipotency of TSC-null cells." Nat Commun **8**(1): 1848.

Cohen, M. A., S. Markoulaki and R. Jaenisch (2018). "Matched Developmental Timing of Donor Cells with the Host Is Crucial for Chimera Formation." Stem Cell Reports **10**(5): 1445-1452.

Cohen, M. A., K. J. Wert, J. Goldmann, S. Markoulaki, Y. Buganim, D. Fu and R. Jaenisch (2016). "Human neural crest cells contribute to coat pigmentation in interspecies chimeras after in utero injection into mouse embryos." Proc Natl Acad Sci U S A **113**(6): 1570-1575.

Cohen, M. A., S. Zhang, S. Sengupta, H. Ma, B. Horton, G. W. Bell, R. E. George, S. Spranger and R. Jaenisch (2019). "Development of Human Neuroblastomas in Mouse-Human Neural Crest Chimeras." bioRxiv: 523795.

Cong, L., F. A. Ran, D. Cox, S. Lin, R. Barretto, N. Habib, P. D. Hsu, X. Wu, W. Jiang, L. A. Marraffini and F. Zhang (2013). "Multiplex genome engineering using CRISPR/Cas systems." Science **339**(6121): 819-823.

Cong, L. and F. Zhang (2015). "Genome engineering using CRISPR-Cas9 system." Methods Mol Biol **1239**: 197-217.

Cortez, M. A., D. Valdecanas, X. Zhang, Y. Zhan, V. Bhardwaj, G. A. Calin, R. Komaki, D. K. Giri, C. C. Quini, T. Wolfe, H. J. Peltier, A. G. Bader, J. V. Heymach, R. E. Meyn and J. W. Welsh (2014). "Therapeutic delivery of miR-200c enhances radiosensitivity in lung cancer." Mol Ther **22**(8): 1494-1503.

Costa, V., S. Aigner, M. Vukcevic, E. Sauter, K. Behr, M. Ebeling, T. Dunkley, A. Friedlein, S. Zoffmann, C. A. Meyer, F. Knoflach, S. Lugert, C. Patsch, F. Fjeldskaar, L. Chicha-Gaudimier, A. Kiialainen, P. Piraino, M. Bedoucha, M. Graf, S. Jessberger, A. Ghosh, J. Bischofberger and R. Jagasia (2016). "mTORC1 Inhibition Corrects Neurodevelopmental and Synaptic Alterations in a Human Stem Cell Model of Tuberous Sclerosis." Cell Rep **15**(1): 86-95.

Crino, P. B., E. Aronica, G. Baltuch and K. L. Nathanson (2010). "Biallelic TSC gene inactivation in tuberous sclerosis complex." Neurology **74**(21): 1716-1723.

Crino, P. B., K. L. Nathanson and E. P. Henske (2006). "The tuberous sclerosis complex." N Engl J Med **355**(13): 1345-1356.

Crooks, D. M., G. Pacheco-Rodriguez, R. M. DeCastro, J. P. McCoy, Jr., J. A. Wang, F. Kumaki, T. Darling and J. Moss (2004). "Molecular and genetic analysis of disseminated neoplastic cells in lymphangioleiomyomatosis." Proc Natl Acad Sci U S A **101**(50): 17462-17467.

Cui, Z., S. M. Hwang and A. V. Gomes (2014). "Identification of the immunoproteasome as a novel regulator of skeletal muscle differentiation." Mol Cell Biol **34**(1): 96-109.

Curatolo, P., R. Bombardieri and S. Jozwiak (2008). "Tuberous sclerosis." Lancet **372**(9639): 657-668.

Dabora, S. L., D. N. Franz, S. Ashwal, A. Sagalowsky, F. J. DiMario, Jr., D. Miles, D. Cutler, D. Krueger, R. N. Uppot, R. Rabenou, S. Camposano, J. Paolini, F. Fennessy, N. Lee, C. Woodrum, J. Manola, J. Garber and E. A. Thiele (2011). "Multicenter phase 2 trial of sirolimus for tuberous sclerosis: kidney angiomyolipomas and other tumors regress and VEGF- D levels decrease." PLoS One **6**(9): e23379.

Dabora, S. L., S. Jozwiak, D. N. Franz, P. S. Roberts, A. Nieto, J. Chung, Y.-S. Choy, M. P. Reeve, E. Thiele and J. C. Egelhoff (2001). "Mutational analysis in a cohort of 224 tuberous sclerosis patients indicates increased severity of TSC2, compared with TSC1, disease in multiple organs." The American Journal of Human Genetics **68**(1): 64-80.

Darling, T. N., G. Pacheco-Rodriguez, A. Gorio, E. Lesma, C. Walker and J. Moss (2010). "Lymphangioleiomyomatosis and TSC2-/- cells." Lymphat Res Biol **8**(1): 59-69.

Darvin, P., S. M. Toor, V. Sasidharan Nair and E. Elkord (2018). "Immune checkpoint inhibitors: recent progress and potential biomarkers." Exp Mol Med **50**(12): 165.

Das, A. and J. G. Crump (2012). "Bmps and id2a act upstream of Twist1 to restrict ectomesenchyme potential of the cranial neural crest." PLoS Genet **8**(5): e1002710.

De Bont, R. and N. van Larebeke (2004). "Endogenous DNA damage in humans: a review of quantitative data." Mutagenesis **19**(3): 169-185.

DeKlotz, C. M., A. E. Ogram, S. Singh, S. Dronavalli and J. L. MacGregor (2011). "Dramatic improvement of facial angiofibromas in tuberous sclerosis with topical rapamycin: optimizing a treatment protocol." Arch Dermatol **147**(9): 1116-1117.

Delaney, S. P., L. M. Julian, A. Pietrobon, J. Yockell-Lelièvre, C. Doré, T. T. Wang, V. C. Doyon, A. Raymond, D. A. Patten, M.-E. Harper, H. Sun and W. L. Stanford (2019). "Stem cell models identify lineage-specific catabolic signaling, neoplastic mechanisms and therapeutic vulnerabilities in tuberous sclerosis." bioRxiv: 683359.

Delaney, S. P., L. M. Julian and W. L. Stanford (2014). "The neural crest lineage as a driver of disease heterogeneity in Tuberous Sclerosis Complex and Lymphangioleiomyomatosis." Front Cell Dev Biol **2**: 69.

Demetriades, C., M. Plescher and A. A. Teleman (2016). "Lysosomal recruitment of TSC2 is a universal response to cellular stress." Nat Commun **7**: 10662.

Di Nardo, A., M. H. Wertz, E. Kwiatkowski, P. T. Tsai, J. D. Leech, E. Greene-Colozzi, J. Goto, P. Dilsiz, D. M. Talos and C. B. Clish (2014). "Neuronal Tsc1/2 complex controls autophagy through AMPK-dependent regulation of ULK1." Human molecular genetics **23**(14): 3865-3874.

Dibble, C. C., W. Elis, S. Menon, W. Qin, J. Klekota, J. M. Asara, P. M. Finan, D. J. Kwiatkowski, L. O. Murphy and B. D. Manning (2012). "TBC1D7 is a third subunit of the TSC1-TSC2 complex upstream of mTORC1." Mol Cell **47**(4): 535-546.

Djebali, S., C. A. Davis, A. Merkel, A. Dobin, T. Lassmann, A. Mortazavi, A. Tanzer, J. Lagarde, W. Lin, F. Schlesinger, C. Xue, G. K. Marinov, J. Khatun, B. A. Williams, C. Zaleski, J. Rozowsky, M. Roder, F. Kokocinski, R. F. Abdelhamid, T. Alioto, I. Antoshechkin, M. T. Baer, N. S. Bar, P. Batut, K. Bell, I. Bell, S. Chakrabortty, X. Chen, J. Chrast, J. Curado, T. Derrien, J. Drenkow, E. Dumais, J. Dumais, R. Duttagupta, E. Falconnet, M. Fastuca, K. Fejes-Toth, P. Ferreira, S. Foissac, M. J. Fullwood, H. Gao, D. Gonzalez, A. Gordon, H. Gunawardena, C. Howald, S. Jha, R. Johnson, P. Kapranov, B. King, C. Kingswood, O. J. Luo, E. Park, K. Persaud, J. B. Preall, P. Ribeca, B. Risk, D. Robyr, M. Sammeth, L. Schaffer, L. H. See, A. Shahab, J. Skancke, A. M. Suzuki, H. Takahashi, H. Tilgner, D. Trout, N. Walters, H. Wang, J. Wrobel, Y. Yu, X. Ruan, Y. Hayashizaki, J. Harrow, M. Gerstein, T. Hubbard, A. Reymond, S. E. Antonarakis, G. Hannon, M. C. Giddings, Y. Ruan, B. Wold, P. Carninci, R. Guigo and T. R. Gingeras (2012). "Landscape of transcription in human cells." Nature **489**(7414): 101-108.

Duvel, K., J. L. Yecies, S. Menon, P. Raman, A. I. Lipovsky, A. L. Souza, E. Triantafellow, Q. Ma, R. Gorski, S. Cleaver, M. G. Vander Heiden, J. P. MacKeigan, P.

M. Finan, C. B. Clish, L. O. Murphy and B. D. Manning (2010). "Activation of a metabolic gene regulatory network downstream of mTOR complex 1." Mol Cell **39**(2): 171-183.

Ebrahimi-Fakhari, D., A. Saffari, L. Wahlster, A. Di Nardo, D. Turner, T. L. Lewis Jr, C. Conrad, J. M. Rothberg, J. O. Lipton and S. Kölker (2016). "Impaired mitochondrial dynamics and mitophagy in neuronal models of tuberous sclerosis complex." Cell reports **17**(4): 1053-1070.

Egan, D., J. Kim, R. J. Shaw and K. L. Guan (2011). "The autophagy initiating kinase ULK1 is regulated via opposing phosphorylation by AMPK and mTOR." Autophagy **7**(6): 643-644.

Egan, D. F., D. B. Shackelford, M. M. Mihaylova, S. Gelino, R. A. Kohnz, W. Mair, D. S. Vasquez, A. Joshi, D. M. Gwinn, R. Taylor, J. M. Asara, J. Fitzpatrick, A. Dillin, B. Viollet, M. Kundu, M. Hansen and R. J. Shaw (2011). "Phosphorylation of ULK1 (hATG1) by AMP-activated protein kinase connects energy sensing to mitophagy." Science **331**(6016): 456-461.

Ehninger, D., S. Han, C. Shilyansky, Y. Zhou, W. Li, D. J. Kwiatkowski, V. Ramesh and A. J. Silva (2008). "Reversal of learning deficits in a Tsc2+/- mouse model of tuberous sclerosis." Nat Med **14**(8): 843-848.

El-Chemaly, S., A. Taveira-Dasilva, H. J. Goldberg, E. Peters, M. Haughey, D. Bienfang, A. M. Jones, P. Julien-Williams, Y. Cui, J. A. Villalba, S. Bagwe, R. Maurer, I. O. Rosas, J. Moss and E. P. Henske (2017). "Sirolimus and Autophagy Inhibition in Lymphangioleiomyomatosis: Results of a Phase I Clinical Trial." Chest **151**(6): 1302-1310.

Esquela-Kerscher, A. and F. J. Slack (2006). "Oncomirs - microRNAs with a role in cancer." Nat Rev Cancer **6**(4): 259-269.

Ess, K. C., C. A. Kamp, B. P. Tu and D. H. Gutmann (2005). "Developmental origin of subependymal giant cell astrocytoma in tuberous sclerosis complex." Neurology **64**(8): 1446-1449.

European Chromosome 16 Tuberous Sclerosis, C. (1993). "Identification and characterization of the tuberous sclerosis gene on chromosome 16." Cell **75**(7): 1305-1315.

Evron, E., Umbricht, C.B., Korz, D., Raman, V., Loeb, D.M., Niranjan, B., Buluwela, L., Weitzman, S.A., Marks, J., and Sukumar, S. (2001). Loss of cyclin D2 expression in the majority of breast cancers is associated with promoter hypermethylation. Cancer Res *61*, 2782-2787.

Falck, J., J. V. Forment, J. Coates, M. Mistrik, J. Lukas, J. Bartek and S. P. Jackson (2012). "CDK targeting of NBS1 promotes DNA-end resection, replication restart and homologous recombination." EMBO Rep **13**(6): 561-568.

Fang, F., S. Sun, L. Wang, J. L. Guan, M. Giovannini, Y. Zhu and F. Liu (2015). "Neural Crest-Specific TSC1 Deletion in Mice Leads to Sclerotic Craniofacial Bone Lesion." J Bone Miner Res **30**(7): 1195-1205.

Farmer, H., N. McCabe, C. J. Lord, A. N. Tutt, D. A. Johnson, T. B. Richardson, M. Santarosa, K. J. Dillon, I. Hickson, C. Knights, N. M. Martin, S. P. Jackson, G. C. Smith and A. Ashworth (2005). "Targeting the DNA repair defect in BRCA mutant cells as a therapeutic strategy." Nature **434**(7035): 917-921.

Feliciano, D. M., T. Su, J. Lopez, J. C. Platel and A. Bordey (2011). "Single-cell Tsc1 knockout during corticogenesis generates tuber-like lesions and reduces seizure threshold in mice." J Clin Invest **121**(4): 1596-1607.

Fernandez-Hernando, C., C. M. Ramirez, L. Goedeke and Y. Suarez (2013). "MicroRNAs in metabolic disease." Arterioscler Thromb Vasc Biol **33**(2): 178-185.

Ferrington, D. A., H. Roehrich, A. A. Chang, C. W. Huang, M. Maldonado, W. Bratten, A. A. Rageh, N. D. Heuss, D. S. Gregerson, E. F. Nelson and C. Yuan (2013). "Corneal wound healing is compromised by immunoproteasome deficiency." PLoS One **8**(1): e54347.

Fokkema, I. F., P. E. Taschner, G. C. Schaafsma, J. Celli, J. F. Laros and J. T. den Dunnen (2011). "LOVD v.2.0: the next generation in gene variant databases." Hum Mutat **32**(5): 557-563.

Fokkema, I. F., P. E. Taschner, G. C. Schaafsma, J. Celli, J. F. Laros and J. T. den Dunnen (2011). "LOVD v. 2.0: the next generation in gene variant databases." Human mutation **32**(5): 557-563.

Franz, D. N. and J. K. Capal (2017). "mTOR inhibitors in the pharmacologic management of tuberous sclerosis complex and their potential role in other rare neurodevelopmental disorders." Orphanet journal of rare diseases **12**(1): 51.

Friedman, R. C., K. K. Farh, C. B. Burge and D. P. Bartel (2009). "Most mammalian mRNAs are conserved targets of microRNAs." Genome Res **19**(1): 92-105.

Gagnon, J. A., E. Valen, S. B. Thyme, P. Huang, L. Ahkmetova, A. Pauli, T. G. Montague, S. Zimmerman, C. Richter and A. F. Schier (2014). "Efficient mutagenesis by Cas9 protein-mediated oligonucleotide insertion and large-scale assessment of single-guide RNAs." PloS one **9**(5): e98186.

Gaj, T., C. A. Gersbach and C. F. Barbas, 3rd (2013). "ZFN, TALEN, and CRISPR/Cas-based methods for genome engineering." Trends Biotechnol **31**(7): 397-405.

Gao, L., M. M. Yue, J. Davis, E. Hyjek and L. Schuger (2014). "In pulmonary lymphangioleiomyomatosis expression of progesterone receptor is frequently higher than that of estrogen receptor." Virchows Arch **464**(4): 495-503.

Garami, A., F. J. Zwartkruis, T. Nobukuni, M. Joaquin, M. Roccio, H. Stocker, S. C. Kozma, E. Hafen, J. L. Bos and G. Thomas (2003). "Insulin activation of Rheb, a mediator of mTOR/S6K/4E-BP signaling, is inhibited by TSC1 and 2." Mol Cell **11**(6): 1457-1466.

Gilbert, E. R., J. M. Eby, A. M. Hammer, J. Klarquist, D. G. Christensen, A. J. Barfuss, R. E. Boissy, M. M. Picken, R. B. Love and D. F. Dilling (2013). "Positioning ganglioside D3

as an immunotherapeutic target in lymphangioleiomyomatosis." The American journal of pathology **183**(1): 226-234.

Gilbert, L. A., M. H. Larson, L. Morsut, Z. Liu, G. A. Brar, S. E. Torres, N. Stern-Ginossar, O. Brandman, E. H. Whitehead, J. A. Doudna, W. A. Lim, J. S. Weissman and L. S. Qi (2013). "CRISPR-mediated modular RNA-guided regulation of transcription in eukaryotes." Cell **154**(2): 442-451.

Goncharova, E. A., D. A. Goncharov, A. Chisolm, M. S. Spaits, P. N. Lim, G. Cesarone, I. Khavin, O. Tliba, Y. Amrani, R. A. Panettieri, Jr. and V. P. Krymskaya (2008). "Interferon beta augments tuberous sclerosis complex 2 (TSC2)-dependent inhibition of TSC2-null ELT3 and human lymphangioleiomyomatosis-derived cell proliferation." Mol Pharmacol **73**(3): 778-788.

Goncharova, E. A., D. A. Goncharov, M. Fehrenbach, I. Khavin, B. Ducka, O. Hino, T. V. Colby, M. J. Merrilees, A. Haczku, S. M. Albelda and V. P. Krymskaya (2012). "Prevention of alveolar destruction and airspace enlargement in a mouse model of pulmonary lymphangioleiomyomatosis (LAM)." Sci Transl Med **4**(154): 154ra134.

Goto, J., D. M. Talos, P. Klein, W. Qin, Y. I. Chekaluk, S. Anderl, I. A. Malinowska, A. Di Nardo, R. T. Bronson and J. A. Chan (2011). "Regulable neural progenitor-specific Tsc1 loss yields giant cells with organellar dysfunction in a model of tuberous sclerosis complex." Proceedings of the National Academy of Sciences **108**(45): E1070-E1079.

Goudarzi, K. M. and M. S. Lindstrom (2016). "Role of ribosomal protein mutations in tumor development (Review)." Int J Oncol **48**(4): 1313-1324.

Granados-Aparici, S., Hardy, K., Franks, S., Sharum, I.B., Waite, S.L., and Fenwick, M.A. (2019). SMAD3 directly regulates cell cycle genes to maintain arrest in granulosa cells of mouse primordial follicles. Scientific Reports *9*, 6513.

Griffith, M., O. L. Griffith, A. C. Coffman, J. V. Weible, J. F. McMichael, N. C. Spies, J. Koval, I. Das, M. B. Callaway, J. M. Eldred, C. A. Miller, J. Subramanian, R. Govindan, R. D. Kumar, R. Bose, L. Ding, J. R. Walker, D. E. Larson, D. J. Dooling, S. M. Smith, T. J. Ley, E. R. Mardis and R. K. Wilson (2013). "DGIdb: mining the druggable genome." Nat Methods **10**(12): 1209-1210.

Grzegorek, I., D. Lenze, M. Chabowski, D. Janczak, M. SZOLKOWSKA, R. Langfort, A. Szuba and P. Dziegiel (2015). "Immunohistochemical evaluation of pulmonary lymphangioleiomyomatosis." Anticancer research **35**(6): 3353-3360.

Guertin, D. A. and D. M. Sabatini (2007). "Defining the role of mTOR in cancer." Cancer Cell **12**(1): 9-22.

Gunhanlar, N., G. Shpak, M. van der Kroeg, L. A. Gouty-Colomer, S. T. Munshi, B. Lendemeijer, M. Ghazvini, C. Dupont, W. J. G. Hoogendijk, J. Gribnau, F. M. S. de Vrij and S. A. Kushner (2018). "A simplified protocol for differentiation of electrophysiologically mature neuronal networks from human induced pluripotent stem cells." Mol Psychiatry **23**(5): 1336-1344.

Guvakova, M. A., W. S. Lee, D. K. Furstenau, I. Prabakaran, D. C. Li, R. Hung and N. Kushnir (2014). "The small GTPase Rap1 promotes cell movement rather than stabilizes adhesion in epithelial cells responding to insulin-like growth factor I." Biochem J **463**(2): 257-270.

Haeussler, M., K. Schönig, H. Eckert, A. Eschstruth, J. Mianné, J.-B. Renaud, S. Schneider-Maunoury, A. Shkumatava, L. Teboul and J. Kent (2016). "Evaluation of off-target and on-target scoring algorithms and integration into the guide RNA selection tool CRISPOR." Genome biology **17**(1): 148.

Hartman, J. L. t., B. Garvik and L. Hartwell (2001). "Principles for the buffering of genetic variation." Science **291**(5506): 1001-1004.

Hartwell, L. H., P. Szankasi, C. J. Roberts, A. W. Murray and S. H. Friend (1997). "Integrating genetic approaches into the discovery of anticancer drugs." Science **278**(5340): 1064-1068.

Henry, K. W., X. Yuan, N. J. Koszewski, H. Onda, D. J. Kwiatkowski and D. J. Noonan (1998). "Tuberous sclerosis gene 2 product modulates transcription mediated by steroid hormone receptor family members." J Biol Chem **273**(32): 20535-20539.

Henske, E. P. (2003). "Metastasis of benign tumor cells in tuberous sclerosis complex." Genes Chromosomes Cancer **38**(4): 376-381.

Henske, E. P. and F. X. McCormack (2012). "Lymphangioleiomyomatosis—a wolf in sheep's clothing." The Journal of clinical investigation **122**(11): 3807-3816.

Henske, E. P., B. W. Scheithauer, M. P. Short, R. Wollmann, J. Nahmias, N. Hornigold, M. van Slegtenhorst, C. T. Welsh and D. J. Kwiatkowski (1996). "Allelic loss is frequent in tuberous sclerosis kidney lesions but rare in brain lesions." Am J Hum Genet **59**(2): 400-406.

Hoeijmakers, J. H. (2009). "DNA damage, aging, and cancer." N Engl J Med **361**(15): 1475-1485.

Hoogeveen-Westerveld, M., L. van Unen, A. van den Ouweland, D. Halley, A. Hoogeveen and M. Nellist (2012). "The TSC1-TSC2 complex consists of multiple TSC1 and TSC2 subunits." BMC Biochem **13**: 18.

Hopkins, A. L. and C. R. Groom (2002). "The druggable genome." Nat Rev Drug Discov **1**(9): 727-730.

Housden, B. E., A. J. Valvezan, C. Kelley, R. Sopko, Y. Hu, C. Roesel, S. Lin, M. Buckner, R. Tao, B. Yilmazel, S. E. Mohr, B. D. Manning and N. Perrimon (2015). "Identification of potential drug targets for tuberous sclerosis complex by synthetic screens combining CRISPR-based knockouts with RNAi." Sci Signal **8**(393): rs9.

Howe, S. R., M. M. Gottardis, J. I. Everitt and C. Walker (1995). "Estrogen stimulation and tamoxifen inhibition of leiomyoma cell growth in vitro and in vivo." Endocrinology **136**(11): 4996-5003.

Hsu, P. D., D. A. Scott, J. A. Weinstein, F. A. Ran, S. Konermann, V. Agarwala, Y. Li, E. J. Fine, X. Wu, O. Shalem, T. J. Cradick, L. A. Marraffini, G. Bao and F. Zhang (2013). "DNA targeting specificity of RNA-guided Cas9 nucleases." Nat Biotechnol **31**(9): 827-832.

Iadevaia, V., R. Liu and C. G. Proud (2014). "mTORC1 signaling controls multiple steps in ribosome biogenesis." Semin Cell Dev Biol **36**: 113-120.

Inoki, K., Y. Li, T. Xu and K. L. Guan (2003). "Rheb GTPase is a direct target of TSC2 GAP activity and regulates mTOR signaling." Genes Dev **17**(15): 1829-1834.

Inoki, K., Y. Li, T. Zhu, J. Wu and K. L. Guan (2002). "TSC2 is phosphorylated and inhibited by Akt and suppresses mTOR signalling." Nat Cell Biol **4**(9): 648-657.

Inoki, K., H. Ouyang, T. Zhu, C. Lindvall, Y. Wang, X. Zhang, Q. Yang, C. Bennett, Y. Harada, K. Stankunas, C. Y. Wang, X. He, O. A. MacDougald, M. You, B. O. Williams and K. L. Guan (2006). "TSC2 integrates Wnt and energy signals via a coordinated phosphorylation by AMPK and GSK3 to regulate cell growth." Cell **126**(5): 955-968.

Inoki, K., T. Zhu and K. L. Guan (2003). "TSC2 mediates cellular energy response to control cell growth and survival." Cell **115**(5): 577-590.

Ionescu, L. I., R. S. Alphonse, N. Arizmendi, B. Morgan, M. Abel, F. Eaton, M. Duszyk, H. Vliagoftis, T. R. Aprahamian, K. Walsh and B. Thebaud (2012). "Airway delivery of soluble factors from plastic-adherent bone marrow cells prevents murine asthma." Am J Respir Cell Mol Biol **46**(2): 207-216.

Jinek, M., A. East, A. Cheng, S. Lin, E. Ma and J. Doudna (2013). "RNA-programmed genome editing in human cells." Elife **2**: e00471.

Johnson, C. E., E. A. Dunlop, S. Seifan, H. D. McCann, T. Hay, G. J. Parfitt, A. T. Jones, P. J. Giles, M. H. Shen and J. R. Sampson (2018). "Loss of tuberous sclerosis complex 2 sensitizes tumors to nelfinavir− bortezomib therapy to intensify endoplasmic reticulum stress-induced cell death." Oncogene **37**(45): 5913.

Jopling, C. L., M. Yi, A. M. Lancaster, S. M. Lemon and P. Sarnow (2005). "Modulation of hepatitis C virus RNA abundance by a liver-specific MicroRNA." Science **309**(5740): 1577-1581.

Julian, L. M., S. P. Delaney, Y. Wang, A. A. Goldberg, C. Dore, J. Yockell-Lelievre, R. Y. Tam, K. Giannikou, F. McMurray, M. S. Shoichet, M. E. Harper, E. P. Henske, D. J. Kwiatkowski, T. N. Darling, J. Moss, A. S. Kristof and W. L. Stanford (2017). "Human Pluripotent Stem Cell-Derived TSC2-Haploinsufficient Smooth Muscle Cells Recapitulate Features of Lymphangioleiomyomatosis." Cancer Res **77**(20): 5491-5502.

Kandt, R. S. (2003). "Tuberous sclerosis complex and neurofibromatosis type 1: the two most common neurocutaneous diseases." Neurol Clin **21**(4): 983-1004.

Karbowniczek, M., A. Astrinidis, B. R. Balsara, J. R. Testa, J. H. Lium, T. V. Colby, F. X. McCormack and E. P. Henske (2003). "Recurrent lymphangiomyomatosis after

transplantation: genetic analyses reveal a metastatic mechanism." Am J Respir Crit Care Med **167**(7): 976-982.

Kim, D., S. Bae, J. Park, E. Kim, S. Kim, H. R. Yu, J. Hwang, J. I. Kim and J. S. Kim (2015). "Digenome-seq: genome-wide profiling of CRISPR-Cas9 off-target effects in human cells." Nat Methods **12**(3): 237-243.

Kim, J., M. Kundu, B. Viollet and K. L. Guan (2011). "AMPK and mTOR regulate autophagy through direct phosphorylation of Ulk1." Nat Cell Biol **13**(2): 132-141.

Klarquist, J., A. Barfuss, S. Kandala, M. J. Reust, R. K. Braun, J. Hu, D. F. Dilling, M. D. McKee, R. E. Boissy and R. B. Love (2009). "Melanoma-associated antigen expression in lymphangioleiomyomatosis renders tumor cells susceptible to cytotoxic T cells." The American journal of pathology **175**(6): 2463-2472.

Kleinstiver, B. P., V. Pattanayak, M. S. Prew, S. Q. Tsai, N. T. Nguyen, Z. Zheng and J. K. Joung (2016). "High-fidelity CRISPR-Cas9 nucleases with no detectable genome-wide off-target effects." Nature **529**(7587): 490-495.

Klover, P. J., R. L. Thangapazham, J. Kato, J. A. Wang, S. A. Anderson, V. Hoffmann, W. K. Steagall, S. Li, E. McCart, N. Nathan, J. D. Bernstock, M. D. Wilkerson, C. L. Dalgard, J. Moss and T. N. Darling (2017). "Tsc2 disruption in mesenchymal progenitors results in tumors with vascular anomalies overexpressing Lgals3." Elife **6**.

Knudson, A. G., Jr. (1971). "Mutation and cancer: statistical study of retinoblastoma." Proc Natl Acad Sci U S A **68**(4): 820-823.

Kobayashi, T., O. Minowa, J. Kuno, H. Mitani, O. Hino and T. Noda (1999). "Renal carcinogenesis, hepatic hemangiomatosis, and embryonic lethality caused by a germ-line Tsc2 mutation in mice." Cancer Res **59**(6): 1206-1211.

Kobayashi, T., O. Minowa, Y. Sugitani, S. Takai, H. Mitani, E. Kobayashi, T. Noda and O. Hino (2001). "A germ-line Tsc1 mutation causes tumor development and embryonic lethality that are similar, but not identical to, those caused by Tsc2 mutation in mice." Proc Natl Acad Sci U S A **98**(15): 8762-8767.

Komili, S., N. G. Farny, F. P. Roth and P. A. Silver (2007). "Functional specificity among ribosomal proteins regulates gene expression." Cell **131**(3): 557-571.

Koyama-Nasu, R., Nasu-Nishimura, Y., Todo, T., Ino, Y., Saito, N., Aburatani, H., Funato, K., Echizen, K., Sugano, H., Haruta, R.*, et al.* (2013). The critical role of cyclin D2 in cell cycle progression and tumorigenicity of glioblastoma stem cells. Oncogene *32*, 3840-3845.

Krasinska, L., E. Besnard, E. Cot, C. Dohet, M. Mechali, J. M. Lemaitre and D. Fisher (2008). "Cdk1 and Cdk2 activity levels determine the efficiency of replication origin firing in Xenopus." EMBO J **27**(5): 758-769.

Krueger, D. A., M. M. Care, K. Holland, K. Agricola, C. Tudor, P. Mangeshkar, K. A. Wilson, A. Byars, T. Sahmoud and D. N. Franz (2010). "Everolimus for subependymal giant-cell astrocytomas in tuberous sclerosis." N Engl J Med **363**(19): 1801-1811.

Krutzfeldt, J., N. Rajewsky, R. Braich, K. G. Rajeev, T. Tuschl, M. Manoharan and M. Stoffel (2005). "Silencing of microRNAs in vivo with 'antagomirs'." Nature **438**(7068): 685-689.

Kumasaka, T., K. Seyama, K. Mitani, T. Sato, S. Souma, T. Kondo, S. Hayashi, M. Minami, T. Uekusa, Y. Fukuchi and K. Suda (2004). "Lymphangiogenesis in lymphangioleiomyomatosis: its implication in the progression of lymphangioleiomyomatosis." Am J Surg Pathol **28**(8): 1007-1016.

Kwiatkowski, D. J. (2010). "Animal models of lymphangioleiomyomatosis (LAM) and tuberous sclerosis complex (TSC)." Lymphatic research and biology **8**(1): 51-57.

Lam, J. K., M. Y. Chow, Y. Zhang and S. W. Leung (2015). "siRNA Versus miRNA as Therapeutics for Gene Silencing." Mol Ther Nucleic Acids **4**: e252.

Lamb, R. F., C. Roy, T. J. Diefenbach, H. V. Vinters, M. W. Johnson, D. G. Jay and A. Hall (2000). "The TSC1 tumour suppressor hamartin regulates cell adhesion through ERM proteins and the GTPase Rho." Nat Cell Biol **2**(5): 281-287.

Lee, D. F., H. P. Kuo, C. T. Chen, J. M. Hsu, C. K. Chou, Y. Wei, H. L. Sun, L. Y. Li, B. Ping, W. C. Huang, X. He, J. Y. Hung, C. C. Lai, Q. Ding, J. L. Su, J. Y. Yang, A. A. Sahin, G. N. Hortobagyi, F. J. Tsai, C. H. Tsai and M. C. Hung (2007). "IKK beta suppression of TSC1 links inflammation and tumor angiogenesis via the mTOR pathway." Cell **130**(3): 440-455.

Lee, G., S. M. Chambers, M. J. Tomishima and L. Studer (2010). "Derivation of neural crest cells from human pluripotent stem cells." Nat Protoc **5**(4): 688-701.

Leeman, D. S., K. Hebestreit, T. Ruetz, A. E. Webb, A. McKay, E. A. Pollina, B. W. Dulken, X. Zhao, R. W. Yeo and T. T. Ho (2018). "Lysosome activation clears aggregates and enhances quiescent neural stem cell activation during aging." Science **359**(6381): 1277-1283.

Lesma, E., S. M. Sirchia, S. Ancona, S. Carelli, S. Bosari, F. Ghelma, E. Montanari, A. M. Di Giulio and A. Gorio (2009). "The methylation of the TSC2 promoter underlies the abnormal growth of TSC2 angiomyolipoma-derived smooth muscle cells." Am J Pathol **174**(6): 2150-2159.

Li, C., P. S. Lee, Y. Sun, X. Gu, E. Zhang, Y. Guo, C. L. Wu, N. Auricchio, C. Priolo, J. Li, A. Csibi, A. Parkhitko, T. Morrison, A. Planaguma, S. Kazani, E. Israel, K. F. Xu, E. P. Henske, J. Blenis, B. D. Levy, D. Kwiatkowski and J. J. Yu (2014). "Estradiol and mTORC2 cooperate to enhance prostaglandin biosynthesis and tumorigenesis in TSC2-deficient LAM cells." J Exp Med **211**(1): 15-28.

Li, C., N. Li, X. Liu, E. Y. Zhang, Y. Sun, K. Masuda, J. Li, J. Sun, T. Morrison, X. Li, Y. Chen, J. Wang, N. A. Karim, Y. Zhang, J. Blenis, M. J. Reginato, E. P. Henske and J. J. Yu (2016). "Proapoptotic protein Bim attenuates estrogen-enhanced survival in lymphangioleiomyomatosis." JCI Insight **1**(19): e86629.

Li, W., J. Köster, H. Xu, C.-H. Chen, T. Xiao, J. S. Liu, M. Brown and X. S. Liu (2015). "Quality control, modeling, and visualization of CRISPR screens with MAGeCK-VISPR." Genome Biology **16**(1): 281.

Li, X. L., G. H. Li, J. Fu, Y. W. Fu, L. Zhang, W. Chen, C. Arakaki, J. P. Zhang, W. Wen, M. Zhao, W. V. Chen, G. D. Botimer, D. Baylink, L. Aranda, H. Choi, R. Bechar, P. Talbot, C. K. Sun, T. Cheng and X. B. Zhang (2018). "Highly efficient genome editing via CRISPR-Cas9 in human pluripotent stem cells is achieved by transient BCL-XL overexpression." Nucleic Acids Res **46**(19): 10195-10215.

Li, Y., J. Cao, M. Chen, J. Li, Y. Sun, Y. Zhang, Y. Zhu, L. Wang and C. Zhang (2017). "Abnormal neural progenitor cells differentiated from induced pluripotent stem cells partially mimicked development of TSC2 neurological abnormalities." Stem cell reports **8**(4): 883-893.

Li, Z. and T. M. Rana (2014). "Therapeutic targeting of microRNAs: current status and future challenges." Nat Rev Drug Discov **13**(8): 622-638.

Liang, N., C. Zhang, P. Dill, G. Panasyuk, D. Pion, V. Koka, M. Gallazzini, E. N. Olson, H. Lam, E. P. Henske, Z. Dong, U. Apte, N. Pallet, R. L. Johnson, F. Terzi, D. J. Kwiatkowski, J. Y. Scoazec, G. Martignoni and M. Pende (2014). "Regulation of YAP by mTOR and autophagy reveals a therapeutic target of tuberous sclerosis complex." J Exp Med **211**(11): 2249-2263.

Lieber, M. R. and Z. E. Karanjawala (2004). "Ageing, repetitive genomes and DNA damage." Nat Rev Mol Cell Biol **5**(1): 69-75.

Liu, F., E. P. Lunsford, J. Tong, Y. Ashitate, S. L. Gibbs, J. Yu, H. S. Choi, E. P. Henske and J. V. Frangioni (2012). "Real-time monitoring of tumorigenesis, dissemination, & drug response in a preclinical model of lymphangioleiomyomatosis/tuberous sclerosis complex." PLoS One **7**(6): e38589.

Liu, H. J., P. H. Lizotte, H. Du, M. C. Speranza, H. C. Lam, S. Vaughan, N. Alesi, K. K. Wong, G. J. Freeman, A. H. Sharpe and E. P. Henske (2018). "TSC2-deficient tumors have evidence of T cell exhaustion and respond to anti-PD-1/anti-CTLA-4 immunotherapy." JCI Insight **3**(8).

Lopes, M. B., H. J. Altermatt, B. W. Scheithauer, C. W. Shepherd and S. R. VandenBerg (1996). "Immunohistochemical characterization of subependymal giant cell astrocytomas." Acta Neuropathol **91**(4): 368-375.

Lou, D., N. Griffith and D. J. Noonan (2001). "The tuberous sclerosis 2 gene product can localize to nuclei in a phosphorylation-dependent manner." Mol Cell Biol Res Commun **4**(6): 374-380.

Love, M. I., W. Huber and S. Anders (2014). "Moderated estimation of fold change and dispersion for RNA-seq data with DESeq2." Genome biology **15**(12): 550.

Ludwig, N., P. Leidinger, K. Becker, C. Backes, T. Fehlmann, C. Pallasch, S. Rheinheimer, B. Meder, C. Stahler, E. Meese and A. Keller (2016). "Distribution of miRNA expression across human tissues." Nucleic Acids Res **44**(8): 3865-3877.

Ma, L., Z. Chen, H. Erdjument-Bromage, P. Tempst and P. P. Pandolfi (2005). "Phosphorylation and functional inactivation of TSC2 by Erk implications for tuberous sclerosis and cancer pathogenesis." Cell **121**(2): 179-193.

Magri, L., M. Cambiaghi, M. Cominelli, C. Alfaro-Cervello, M. Cursi, M. Pala, A. Bulfone, J. M. Garcìa-Verdugo, L. Leocani and F. Minicucci (2011). "Sustained activation of mTOR pathway in embryonic neural stem cells leads to development of tuberous sclerosis complex-associated lesions." Cell stem cell **9**(5): 447-462.

Magri, L., M. Cominelli, M. Cambiaghi, M. Cursi, L. Leocani, F. Minicucci, P. L. Poliani and R. Galli (2013). "Timing of mTOR activation affects tuberous sclerosis complex neuropathology in mouse models." Dis Model Mech **6**(5): 1185-1197.

Mahata, B., Sundqvist, A., and Xirodimas, D.P. (2012). Recruitment of RPL11 at promoter sites of p53-regulated genes upon nucleolar stress through NEDD8 and in an Mdm2-dependent manner. Oncogene *31*, 3060-3071.

Maisel, K., M. J. Merrilees, E. N. Atochina-Vasserman, L. Lian, K. Obraztsova, R. Rue, A. N. Vasserman, N. Zuo, L. F. Angel, A. J. Gow, I. Kang, T. N. Wight, E. Eruslanov, M. A. Swartz and V. P. Krymskaya (2018). "Immune Checkpoint Ligand PD-L1 Is Upregulated in Pulmonary Lymphangioleiomyomatosis." Am J Respir Cell Mol Biol **59**(6): 723-732.

Mak, B. C., H. L. Kenerson, L. D. Aicher, E. A. Barnes and R. S. Yeung (2005). "Aberrant beta-catenin signaling in tuberous sclerosis." Am J Pathol **167**(1): 107-116.

Mali, P., L. Yang, K. M. Esvelt, J. Aach, M. Guell, J. E. DiCarlo, J. E. Norville and G. M. Church (2013). "RNA-guided human genome engineering via Cas9." Science **339**(6121): 823-826.

Mandegar, M. A., N. Huebsch, E. B. Frolov, E. Shin, A. Truong, M. P. Olvera, A. H. Chan, Y. Miyaoka, K. Holmes, C. I. Spencer, L. M. Judge, D. E. Gordon, T. V. Eskildsen, J. E. Villalta, M. A. Horlbeck, L. A. Gilbert, N. J. Krogan, S. P. Sheikh, J. S. Weissman, L. S. Qi, P. L. So and B. R. Conklin (2016). "CRISPR Interference Efficiently Induces Specific and Reversible Gene Silencing in Human iPSCs." Cell Stem Cell **18**(4): 541-553.

Martin, K. R., W. Zhou, M. J. Bowman, J. Shih, K. S. Au, K. E. Dittenhafer-Reed, K. A. Sisson, J. Koeman, D. J. Weisenberger and S. L. Cottingham (2017). "The genomic landscape of tuberous sclerosis complex." Nature communications **8**: 15816.

Martina, J. A., Y. Chen, M. Gucek and R. Puertollano (2012). "MTORC1 functions as a transcriptional regulator of autophagy by preventing nuclear transport of TFEB." Autophagy **8**(6): 903-914.

Masel, J. and M. L. Siegal (2009). "Robustness: mechanisms and consequences." Trends Genet **25**(9): 395-403.

Mayshar, Y., U. Ben-David, N. Lavon, J. C. Biancotti, B. Yakir, A. T. Clark, K. Plath, W. E. Lowry and N. Benvenisty (2010). "Identification and classification of chromosomal aberrations in human induced pluripotent stem cells." Cell Stem Cell **7**(4): 521-531.

McCormack, F. X., Y. Inoue, J. Moss, L. G. Singer, C. Strange, K. Nakata, A. F. Barker, J. T. Chapman, M. L. Brantly and J. M. Stocks (2011). "Efficacy and safety of sirolimus in lymphangioleiomyomatosis." New England Journal of Medicine **364**(17): 1595-1606.

McCormack, F. X., Y. Inoue, J. Moss, L. G. Singer, C. Strange, K. Nakata, A. F. Barker, J. T. Chapman, M. L. Brantly, J. M. Stocks, K. K. Brown, J. P. Lynch, 3rd, H. J. Goldberg, L. R. Young, B. W. Kinder, G. P. Downey, E. J. Sullivan, T. V. Colby, R. T. McKay, M. M. Cohen, L. Korbee, A. M. Taveira-DaSilva, H. S. Lee, J. P. Krischer, B. C. Trapnell, C. National Institutes of Health Rare Lung Diseases and M. T. Group (2011). "Efficacy and safety of sirolimus in lymphangioleiomyomatosis." N Engl J Med **364**(17): 1595-1606.

McDowell, I. C., D. Manandhar, C. M. Vockley, A. K. Schmid, T. E. Reddy and B. E. Engelhardt (2018). "Clustering gene expression time series data using an infinite Gaussian process mixture model." PLoS computational biology **14**(1): e1005896.

McKenna III, J., D. Kapfhamer, J. M. Kinchen, B. Wasek, M. Dunworth, T. Murray-Stewart, T. Bottiglieri, R. A. Casero Jr and M. J. Gambello (2018). "Metabolomic studies identify changes in transmethylation and polyamine metabolism in a brain-specific mouse model of tuberous sclerosis complex." Human molecular genetics **27**(12): 2113-2124.

Medvetz, D., C. Priolo and E. P. Henske (2015). "Therapeutic targeting of cellular metabolism in cells with hyperactive mTORC1: a paradigm shift." Mol Cancer Res **13**(1): 3-8.

Mehlem, A., C. E. Hagberg, L. Muhl, U. Eriksson and A. Falkevall (2013). "Imaging of neutral lipids by oil red O for analyzing the metabolic status in health and disease." Nat Protoc **8**(6): 1149-1154.

Meikle, L., D. M. Talos, H. Onda, K. Pollizzi, A. Rotenberg, M. Sahin, F. E. Jensen and D. J. Kwiatkowski (2007). "A mouse model of tuberous sclerosis: neuronal loss of Tsc1 causes dysplastic and ectopic neurons, reduced myelination, seizure activity, and limited survival." J Neurosci **27**(21): 5546-5558.

Mi, R., J. Ma, D. Zhang, L. Li and H. Zhang (2009). "Efficacy of combined inhibition of mTOR and ERK/MAPK pathways in treating a tuberous sclerosis complex cell model." J Genet Genomics **36**(6): 355-361.

Moss, J., N. A. Avila, P. M. Barnes, R. A. Litzenberger, J. Bechtle, P. G. Brooks, C. J. Hedin, S. Hunsberger and A. S. Kristof (2001). "Prevalence and clinical characteristics of lymphangioleiomyomatosis (LAM) in patients with tuberous sclerosis complex." Am J Respir Crit Care Med **164**(4): 669-671.

Mosser, J. L., G. M. Herdrich and T. D. Brock (1976). "Temperature optima for bacteria and yeasts from cold-mountain habitats." Can J Microbiol **22**(2): 324-325.

Moury, J. D. and A. G. Jacobson (1990). "The origins of neural crest cells in the axolotl." Dev Biol **141**(2): 243-253.

Munkley, J., P. Rajan, N. P. Lafferty, C. Dalgliesh, R. M. Jackson, C. N. Robson, H. Y. Leung and D. J. Elliott (2014). "A novel androgen-regulated isoform of the TSC2 tumour suppressor gene increases cell proliferation." Oncotarget **5**(1): 131-139.

Murthy, V., L. A. Haddad, N. Smith, D. Pinney, R. Tyszkowski, D. Brown and V. Ramesh (2000). "Similarities and differences in the subcellular localization of hamartin and tuberin in the kidney." Am J Physiol Renal Physiol **278**(5): F737-746.

Muzykewicz, D. A., A. Sharma, V. Muse, A. L. Numis, J. Rajagopal and E. A. Thiele (2009). "TSC1 and TSC2 mutations in patients with lymphangioleiomyomatosis and tuberous sclerosis complex." J Med Genet **46**(7): 465-468.

Nadadhur, A. G., M. Alsaqati, L. Gasparotto, P. Cornelissen-Steijger, E. van Hugte, S. Dooves, A. J. Harwood and V. M. Heine (2019). "Neuron-Glia Interactions Increase Neuronal Phenotypes in Tuberous Sclerosis Complex Patient iPSC-Derived Models." Stem Cell Reports **12**(1): 42-56.

NCATS. (2018, 25.10.2018). "Inxight: Drugs." Retrieved 08.12.2019, 2019, from https://drugs.ncats.io/drug/44750KD9OE.

Nellist, M., M. A. van Slegtenhorst, M. Goedbloed, A. M. van den Ouweland, D. J. Halley and P. van der Sluijs (1999). "Characterization of the cytosolic tuberin-hamartin complex. Tuberin is a cytosolic chaperone for hamartin." J Biol Chem **274**(50): 35647-35652.

Neuman, N. A. and E. P. Henske (2011). "Non-canonical functions of the tuberous sclerosis complex-Rheb signalling axis." EMBO Mol Med **3**(4): 189-200.

Ngo, V. N., R. E. Davis, L. Lamy, X. Yu, H. Zhao, G. Lenz, L. T. Lam, S. Dave, L. Yang, J. Powell and L. M. Staudt (2006). "A loss-of-function RNA interference screen for molecular targets in cancer." Nature **441**(7089): 106-110.

Nguyen-Vu, P. A., I. Fackler, A. Rust, J. E. DeClue, C. A. Sander, M. Volkenandt, M. Flaig, R. S. Yeung and R. Wienecke (2001). "Loss of tuberin, the tuberous-sclerosis-complex-2 gene product is associated with angiogenesis." J Cutan Pathol **28**(9): 470-475.

Noonan, D. J., D. Lou, N. Griffith and T. C. Vanaman (2002). "A calmodulin binding site in the tuberous sclerosis 2 gene product is essential for regulation of transcription events and is altered by mutations linked to tuberous sclerosis and lymphangioleiomyomatosis." Arch Biochem Biophys **398**(1): 132-140.

Normand, E. A., S. R. Crandall, C. A. Thorn, E. M. Murphy, B. Voelcker, C. Browning, J. T. Machan, C. I. Moore, B. W. Connors and M. Zervas (2013). "Temporal and mosaic Tsc1 deletion in the developing thalamus disrupts thalamocortical circuitry, neural function, and behavior." Neuron **78**(5): 895-909.

O'Leary, M. N., K. H. Schreiber, Y. Zhang, A. C. Duc, S. Rao, J. S. Hale, E. C. Academia, S. R. Shah, J. F. Morton, C. A. Holstein, D. B. Martin, M. Kaeberlein, W. C. Ladiges, P. J. Fink, V. L. Mackay, D. L. Wiest and B. K. Kennedy (2013). "The ribosomal protein Rpl22 controls ribosome composition by directly repressing expression of its own paralog, Rpl22l1." PLoS Genet **9**(8): e1003708.

Ohsawa, M., T. Kobayashi, H. Okura, T. Igarashi, M. Mizuguchi and O. Hino (2013). "TSC1 controls distribution of actin fibers through its effect on function of Rho family of small GTPases and regulates cell migration and polarity." PLoS One **8**(1): e54503.

Onda, H., A. Lueck, P. W. Marks, H. B. Warren and D. J. Kwiatkowski (1999). "Tsc2+/– mice develop tumors in multiple sites that express gelsolin and are influenced by genetic background." The Journal of clinical investigation **104**(6): 687-695.

Oprescu, N., F. McCormack, S. Byrnes and B. Kinder (2013). "Clinical predictors of mortality and cause of death in lymphangioleiomyomatosis: a population-based registry." Lung **191**(1): 35-42.

Pacheco-Rodriguez, G., W. K. Steagall, D. M. Crooks, L. A. Stevens, H. Hashimoto, S. Li, J. A. Wang, T. N. Darling and J. Moss (2007). "TSC2 loss in lymphangioleiomyomatosis cells correlated with expression of CD44v6, a molecular determinant of metastasis." Cancer Res **67**(21): 10573-10581.

Page, D. B., M. A. Postow, M. K. Callahan, J. P. Allison and J. D. Wolchok (2014). "Immune modulation in cancer with antibodies." Annu Rev Med **65**: 185-202.

Palumbo, R. J., G. Fuchs, S. Lutz and M. J. Curcio (2017). "Paralog-Specific Functions of RPL7A and RPL7B Mediated by Ribosomal Protein or snoRNA Dosage in Saccharomyces cerevisiae." G3 (Bethesda) **7**(2): 591-606.

Pandey, U. B. and C. D. Nichols (2011). "Human disease models in Drosophila melanogaster and the role of the fly in therapeutic drug discovery." Pharmacol Rev **63**(2): 411-436.

Park, J., S. K. Yun, Y. S. Cho, K. H. Song and H. U. Kim (2014). "Treatment of angiofibromas in tuberous sclerosis complex: the effect of topical rapamycin and concomitant laser therapy." Dermatology **228**(1): 37-41.

Park, S. H., S. H. Pepkowitz, C. Kerfoot, M. J. De Rosa, V. Poukens, R. Wienecke, J. E. DeClue and H. V. Vinters (1997). "Tuberous sclerosis in a 20-week gestation fetus: immunohistochemical study." Acta Neuropathol **94**(2): 180-186.

Parkhitko, A., F. Myachina, T. A. Morrison, K. M. Hindi, N. Auricchio, M. Karbowniczek, J. J. Wu, T. Finkel, D. J. Kwiatkowski, J. J. Yu and E. P. Henske (2011). "Tumorigenesis in tuberous sclerosis complex is autophagy and p62/sequestosome 1 (SQSTM1)-dependent." Proc Natl Acad Sci U S A **108**(30): 12455-12460.

Parkhitko, A. A., C. Priolo, J. L. Coloff, J. Yun, J. J. Wu, K. Mizumura, W. Xu, I. A. Malinowska, J. Yu and D. J. Kwiatkowski (2014). "Autophagy-dependent metabolic reprogramming sensitizes TSC2-deficient cells to the antimetabolite 6-aminonicotinamide." Molecular Cancer Research **12**(1): 48-57.

Patil, V. S., R. Zhou and T. M. Rana (2014). "Gene regulation by non-coding RNAs." Crit Rev Biochem Mol Biol **49**(1): 16-32.

Patro, R., G. Duggal, M. I. Love, R. A. Irizarry and C. Kingsford (2017). "Salmon provides fast and bias-aware quantification of transcript expression." Nature methods **14**(4): 417.

Paul, P., A. Chakraborty, D. Sarkar, M. Langthasa, M. Rahman, M. Bari, R. S. Singha, A. K. Malakar and S. Chakraborty (2018). "Interplay between miRNAs and human diseases." J Cell Physiol **233**(3): 2007-2018.

Pfaffl, M. W. (2001). "A new mathematical model for relative quantification in real-time RT-PCR." Nucleic Acids Res **29**(9): e45.

Pietrobon, A., S. P. Delaney and W. L. Stanford (2018). "Could Immunotherapy Sink Its Teeth into Lymphangioleiomyomatosis?" Am J Respir Cell Mol Biol **59**(6): 663-665.

Plank, T. L., R. S. Yeung and E. P. Henske (1998). "Hamartin, the product of the tuberous sclerosis 1 (TSC1) gene, interacts with tuberin and appears to be localized to cytoplasmic vesicles." Cancer Res **58**(21): 4766-4770.

Porstmann, T., C. R. Santos, B. Griffiths, M. Cully, M. Wu, S. Leevers, J. R. Griffiths, Y. L. Chung and A. Schulze (2008). "SREBP activity is regulated by mTORC1 and contributes to Akt-dependent cell growth." Cell Metab **8**(3): 224-236.

Prabhakar, S., J. Goto, X. Zhang, M. Sena-Esteves, R. Bronson, J. Brockmann, D. Gianni, G. R. Wojtkiewicz, J. W. Chen, A. Stemmer-Rachamimov, D. J. Kwiatkowski and X. O. Breakefield (2013). "Stochastic model of Tsc1 lesions in mouse brain." PLoS One **8**(5): e64224.

Pradhan, S. A., M. I. Rather, A. Tiwari, V. K. Bhat and A. Kumar (2014). "Evidence that TSC2 acts as a transcription factor and binds to and represses the promoter of Epiregulin." Nucleic Acids Res **42**(10): 6243-6255.

Prizant, H., A. Sen, A. Light, S. N. Cho, F. J. DeMayo, J. P. Lydon and S. R. Hammes (2013). "Uterine-specific loss of Tsc2 leads to myometrial tumors in both the uterus and lungs." Mol Endocrinol **27**(9): 1403-1414.

Qi, L. S., M. H. Larson, L. A. Gilbert, J. A. Doudna, J. S. Weissman, A. P. Arkin and W. A. Lim (2013). "Repurposing CRISPR as an RNA-guided platform for sequence-specific control of gene expression." Cell **152**(5): 1173-1183.

Qin, J., Z. Wang, M. Hoogeveen-Westerveld, G. Shen, W. Gong, M. Nellist and W. Xu (2016). "Structural Basis of the Interaction between Tuberous Sclerosis Complex 1 (TSC1) and Tre2-Bub2-Cdc16 Domain Family Member 7 (TBC1D7)." J Biol Chem **291**(16): 8591-8601.

Qin, W., J. A. Chan, H. V. Vinters, G. W. Mathern, D. N. Franz, B. E. Taillon, P. Bouffard and D. J. Kwiatkowski (2010). "Analysis of TSC cortical tubers by deep sequencing of TSC1, TSC2 and KRAS demonstrates that small second-hit mutations in these genes are rare events." Brain Pathol **20**(6): 1096-1105.

Radzikowska, E. (2015). Lymphangioleiomyomatosis: New Treatment Perspectives. Lung *193*, 467-475.

Ran, F. A., P. D. Hsu, J. Wright, V. Agarwala, D. A. Scott and F. Zhang (2013). "Genome engineering using the CRISPR-Cas9 system." Nature protocols **8**(11): 2281.

Reid, R. J., X. Du, I. Sunjevaric, V. Rayannavar, J. Dittmar, E. Bryant, M. Maurer and R. Rothstein (2016). "A Synthetic Dosage Lethal Genetic Interaction Between CKS1B and PLK1 Is Conserved in Yeast and Human Cancer Cells." Genetics **204**(2): 807-819.

Rodgers, K. and M. McVey (2016). "Error-Prone Repair of DNA Double-Strand Breaks." J Cell Physiol **231**(1): 15-24.

Rosner, M., M. Hanneder, N. Siegel, A. Valli and M. Hengstschlager (2008). "The tuberous sclerosis gene products hamartin and tuberin are multifunctional proteins with a wide spectrum of interacting partners." Mutat Res **658**(3): 234-246.

Rosner, M. and M. Hengstschlager (2004). "Tuberin binds p27 and negatively regulates its interaction with the SCF component Skp2." J Biol Chem **279**(47): 48707-48715.

Rosset, C., C. B. O. Netto and P. Ashton-Prolla (2017). "TSC1 and TSC2 gene mutations and their implications for treatment in Tuberous Sclerosis Complex: a review." Genet Mol Biol **40**(1): 69-79.

Roux, P. P., B. A. Ballif, R. Anjum, S. P. Gygi and J. Blenis (2004). "Tumor-promoting phorbol esters and activated Ras inactivate the tuberous sclerosis tumor suppressor complex via p90 ribosomal S6 kinase." Proc Natl Acad Sci U S A **101**(37): 13489-13494.

Rupaimoole, R. and F. J. Slack (2017). "MicroRNA therapeutics: towards a new era for the management of cancer and other diseases." Nat Rev Drug Discov **16**(3): 203-222.

Sancak, Y., L. Bar-Peled, R. Zoncu, A. L. Markhard, S. Nada and D. M. Sabatini (2010). "Ragulator-Rag complex targets mTORC1 to the lysosomal surface and is necessary for its activation by amino acids." Cell **141**(2): 290-303.

Sancak, Y., T. R. Peterson, Y. D. Shaul, R. A. Lindquist, C. C. Thoreen, L. Bar-Peled and D. M. Sabatini (2008). "The Rag GTPases bind raptor and mediate amino acid signaling to mTORC1." Science **320**(5882): 1496-1501.

Sanjana, N. E., O. Shalem and F. Zhang (2014). "Improved vectors and genome-wide libraries for CRISPR screening." Nat Methods **11**(8): 783-784.

Sardiello, M., M. Palmieri, A. di Ronza, D. L. Medina, M. Valenza, V. A. Gennarino, C. Di Malta, F. Donaudy, V. Embrione, R. S. Polishchuk, S. Banfi, G. Parenti, E. Cattaneo and A. Ballabio (2009). "A gene network regulating lysosomal biogenesis and function." Science **325**(5939): 473-477.

Sato, T., K. Seyama, H. Fujii, H. Maruyama, Y. Setoguchi, S. Iwakami, Y. Fukuchi and O. Hino (2002). "Mutation analysis of the TSC1 and TSC2 genes in Japanese patients with pulmonary lymphangioleiomyomatosis." J Hum Genet **47**(1): 20-28.

Sato, Y., H. Matsui, R. Sato and H. Harashima (2018). "Neutralization of negative charges of siRNA results in improved safety and efficient gene silencing activity of lipid nanoparticles loaded with high levels of siRNA." J Control Release **284**: 179-187.

Saxton, R. A. and D. M. Sabatini (2017). "mTOR Signaling in Growth, Metabolism, and Disease." Cell **168**(6): 960-976.

Schindelin, J., I. Arganda-Carreras, E. Frise, V. Kaynig, M. Longair, T. Pietzsch, S. Preibisch, C. Rueden, S. Saalfeld and B. Schmid (2012). "Fiji: an open-source platform for biological-image analysis." Nature methods **9**(7): 676.

Segev, N. and J. E. Gerst (2018). "Specialized ribosomes and specific ribosomal protein paralogs control translation of mitochondrial proteins." J Cell Biol **217**(1): 117-126.

Seifert, U., L. P. Bialy, F. Ebstein, D. Bech-Otschir, A. Voigt, F. Schroter, T. Prozorovski, N. Lange, J. Steffen, M. Rieger, U. Kuckelkorn, O. Aktas, P. M. Kloetzel and E. Kruger (2010). "Immunoproteasomes preserve protein homeostasis upon interferon-induced oxidative stress." Cell **142**(4): 613-624.

Selleck, M. A. and M. Bronner-Fraser (1995). "Origins of the avian neural crest: the role of neural plate-epidermal interactions." Development **121**(2): 525-538.

Settembre, C., C. Di Malta, V. A. Polito, M. Garcia Arencibia, F. Vetrini, S. Erdin, S. U. Erdin, T. Huynh, D. Medina, P. Colella, M. Sardiello, D. C. Rubinsztein and A. Ballabio (2011). "TFEB links autophagy to lysosomal biogenesis." Science **332**(6036): 1429-1433.

Seyama, K., T. Kumasaka, S. Souma, T. Sato, M. Kurihara, K. Mitani, S. Tominaga and Y. Fukuchi (2006). "Vascular endothelial growth factor-D is increased in serum of patients with lymphangioleiomyomatosis." Lymphat Res Biol **4**(3): 143-152.

Shalem, O., N. E. Sanjana, E. Hartenian, X. Shi, D. A. Scott, T. S. Mikkelsen, D. Heckl, B. L. Ebert, D. E. Root, J. G. Doench and F. Zhang (2014). "Genome-scale CRISPR-Cas9 knockout screening in human cells." Science **343**(6166): 84-87.

Shannon, P., A. Markiel, O. Ozier, N. S. Baliga, J. T. Wang, D. Ramage, N. Amin, B. Schwikowski and T. Ideker (2003). "Cytoscape: a software environment for integrated models of biomolecular interaction networks." Genome Res **13**(11): 2498-2504.

Sherr, C. J. and J. M. Roberts (1999). "CDK inhibitors: positive and negative regulators of G1-phase progression." Genes Dev **13**(12): 1501-1512.

Shibata, A., S. Conrad, J. Birraux, V. Geuting, O. Barton, A. Ismail, A. Kakarougkas, K. Meek, G. Taucher-Scholz, M. Lobrich and P. A. Jeggo (2011). "Factors determining DNA double-strand break repair pathway choice in G2 phase." EMBO J **30**(6): 1079-1092.

Sicinski, P., Donaher, J.L., Geng, Y., Parker, S.B., Gardner, H., Park, M.Y., Robker, R.L., Richards, J.S., McGinnis, L.K., Biggers, J.D.*, et al.* (1996). Cyclin D2 is an FSH-responsive gene involved in gonadal cell proliferation and oncogenesis. Nature *384*, 470-474.

Silva, J. M., K. Marran, J. S. Parker, J. Silva, M. Golding, M. R. Schlabach, S. J. Elledge, G. J. Hannon and K. Chang (2008). "Profiling essential genes in human mammary cells by multiplex RNAi screening." Science **319**(5863): 617-620.

Siroky, B. J., H. Yin, J. T. Babcock, L. Lu, A. R. Hellmann, B. P. Dixon, L. A. Quilliam and J. J. Bissler (2012). "Human TSC-associated renal angiomyolipoma cells are hypersensitive to ER stress." Am J Physiol Renal Physiol **303**(6): F831-844.

Siroky, B. J., H. Yin, B. P. Dixon, R. J. Reichert, A. R. Hellmann, T. Ramkumar, Z. Tsuchihashi, M. Bunni, J. Dillon, P. D. Bell, J. R. Sampson and J. J. Bissler (2014). "Evidence for pericyte origin of TSC-associated renal angiomyolipomas and implications for angiotensin receptor inhibition therapy." Am J Physiol Renal Physiol **307**(5): F560-570.

Slaymaker, I. M., L. Gao, B. Zetsche, D. A. Scott, W. X. Yan and F. Zhang (2016). "Rationally engineered Cas9 nucleases with improved specificity." Science **351**(6268): 84-88.

Smith, I., P. G. Greenside, T. Natoli, D. L. Lahr, D. Wadden, I. Tirosh, R. Narayan, D. E. Root, T. R. Golub, A. Subramanian and J. G. Doench (2017). "Evaluation of RNAi and CRISPR technologies by large-scale gene expression profiling in the Connectivity Map." PLoS Biol **15**(11): e2003213.

Smith, M.A., and Houghton, P. (2013). A proposal regarding reporting of in vitro testing results. Clin Cancer Res *19*, 2828-2833.

Smolock, E.M., Korshunov, V.A., Glazko, G., Qiu, X., Gerloff, J., and Berk, B.C. (2012). Ribosomal protein L17, RpL17, is an inhibitor of vascular smooth muscle growth and carotid intima formation. Circulation *126*, 2418-2427.

Sulima, S. O., I. J. F. Hofman, K. De Keersmaecker and J. D. Dinman (2017). "How Ribosomes Translate Cancer." Cancer Discov **7**(10): 1069-1087.

Sun, H., A. E. Takesian, T. T. Wang, J. J. Lippman-Bell, T. K. Hensch and F. E. Jensen (2018). "Early seizures prematurely unsilence auditory synapses to disrupt thalamocortical critical period plasticity." Cell reports **23**(9): 2533-2540.

Sun, Y., X. Gu, E. Zhang, M. A. Park, A. M. Pereira, S. Wang, T. Morrison, C. Li, J. Blenis, V. H. Gerbaudo, E. P. Henske and J. J. Yu (2014). "Estradiol promotes pentose phosphate pathway addiction and cell survival via reactivation of Akt in mTORC1 hyperactive cells." Cell Death Dis **5**: e1231.

Usui, N., Watanabe, K., Ono, K., Tomita, K., Tamamaki, N., Ikenaka, K., and Takebayashi, H. (2012). Role of motoneuron-derived neurotrophin 3 in survival and axonal projection of sensory neurons during neural circuit formation. Development *139*, 1125.

Tam, R. Y., J. Yockell-Lelievre, L. J. Smith, L. M. Julian, A. E. G. Baker, C. Choey, M. S. Hasim, J. Dimitroulakos, W. L. Stanford and M. S. Shoichet (2019). "Rationally Designed 3D Hydrogels Model Invasive Lung Diseases Enabling High-Content Drug Screening." Adv Mater **31**(7): e1806214.

Taveira-DaSilva, A. M. and J. Moss (2012). "Optimizing treatments for lymphangioleiomyomatosis." Expert Rev Respir Med **6**(3): 267-276.

Tchieu, J., B. Zimmer, F. Fattahi, S. Amin, N. Zeltner, S. Chen and L. Studer (2017). "A modular platform for differentiation of human PSCs into all major ectodermal lineages." Cell stem cell **21**(3): 399-410. e397.

Terasaki, Y., K. Yahiro, G. Pacheco-Rodriguez, W. K. Steagall, M. P. Stylianou, J. F. Evans, A. M. Walker and J. Moss (2010). "Effects of prolactin on TSC2-null Eker rat cells and in pulmonary lymphangioleiomyomatosis." Am J Respir Crit Care Med **182**(4): 531-539.

Tiberio, D., D. N. Franz and J. R. Phillips (2011). "Regression of a cardiac rhabdomyoma in a patient receiving everolimus." Pediatrics **127**(5): e1335-1337.

Toledo, C. M., Y. Ding, P. Hoellerbauer, R. J. Davis, R. Basom, E. J. Girard, E. Lee, P. Corrin, T. Hart, H. Bolouri, J. Davison, Q. Zhang, J. Hardcastle, B. J. Aronow, C. L. Plaisier, N. S. Baliga, J. Moffat, Q. Lin, X. N. Li, D. H. Nam, J. Lee, S. M. Pollard, J. Zhu, J. J. Delrow, B. E. Clurman, J. M. Olson and P. J. Paddison (2015). "Genome-wide CRISPR-Cas9 Screens Reveal Loss of Redundancy between PKMYT1 and WEE1 in Glioblastoma Stem-like Cells." Cell Rep **13**(11): 2425-2439.

Trang, P., J. F. Wiggins, C. L. Daige, C. Cho, M. Omotola, D. Brown, J. B. Weidhaas, A. G. Bader and F. J. Slack (2011). "Systemic delivery of tumor suppressor microRNA mimics using a neutral lipid emulsion inhibits lung tumors in mice." Mol Ther **19**(6): 1116-1122.

Tsuchiya, H., K. Orimoto, K. Kobayashi and O. Hino (1996). "Presence of potent transcriptional activation domains in the predisposing tuberous sclerosis (Tsc2) gene product of the Eker rat model." Cancer Res **56**(3): 429-433.

Tyburczy, M. E., J. A. Wang, S. Li, R. Thangapazham, Y. Chekaluk, J. Moss, D. J. Kwiatkowski and T. N. Darling (2014). "Sun exposure causes somatic second-hit mutations and angiofibroma development in tuberous sclerosis complex." Hum Mol Genet **23**(8): 2023-2029.

Uhlmann, E. J., A. J. Apicelli, R. L. Baldwin, S. P. Burke, M. L. Bajenaru, H. Onda, D. Kwiatkowski and D. H. Gutmann (2002). "Heterozygosity for the tuberous sclerosis complex (TSC) gene products results in increased astrocyte numbers and decreased p27-Kip1 expression in TSC2+/- cells." Oncogene **21**(25): 4050-4059.

Ungrin, M. D., C. Joshi, A. Nica, C. Bauwens and P. W. Zandstra (2008). "Reproducible, ultra high-throughput formation of multicellular organization from single cell suspension-derived human embryonic stem cell aggregates." PLoS One **3**(2): e1565.

Valvezan, A. J. and B. D. Manning (2019). "Molecular logic of mTORC1 signalling as a metabolic rheostat." Nature Metabolism **1**(3): 321-333.

van Bakel, I., T. Sepp, S. Ward, J. R. Yates and A. J. Green (1997). "Mutations in the TSC2 gene: analysis of the complete coding sequence using the protein truncation test (PTT)." Hum Mol Genet **6**(9): 1409-1414.

van Scheppingen, J., D. W. Broekaart, T. Scholl, M. R. Zuidberg, J. J. Anink, W. G. Spliet, P. C. van Rijen, T. Czech, J. A. Hainfellner, M. Feucht, A. Muhlebner, E. A. van

Vliet and E. Aronica (2016). "Dysregulation of the (immuno)proteasome pathway in malformations of cortical development." J Neuroinflammation **13**(1): 202.

van Slegtenhorst, M., R. de Hoogt, C. Hermans, M. Nellist, B. Janssen, S. Verhoef, D. Lindhout, A. van den Ouweland, D. Halley, J. Young, M. Burley, S. Jeremiah, K. Woodward, J. Nahmias, M. Fox, R. Ekong, J. Osborne, J. Wolfe, S. Povey, R. G. Snell, J. P. Cheadle, A. C. Jones, M. Tachataki, D. Ravine, J. R. Sampson, M. P. Reeve, P. Richardson, F. Wilmer, C. Munro, T. L. Hawkins, T. Sepp, J. B. Ali, S. Ward, A. J. Green, J. R. Yates, J. Kwiatkowska, E. P. Henske, M. P. Short, J. H. Haines, S. Jozwiak and D. J. Kwiatkowski (1997). "Identification of the tuberous sclerosis gene TSC1 on chromosome 9q34." Science **277**(5327): 805-808.

Veres, A., B. S. Gosis, Q. Ding, R. Collins, A. Ragavendran, H. Brand, S. Erdin, C. A. Cowan, M. E. Talkowski and K. Musunuru (2014). "Low incidence of off-target mutations in individual CRISPR-Cas9 and TALEN targeted human stem cell clones detected by whole-genome sequencing." Cell Stem Cell **15**(1): 27-30.

Verhoef, S., L. Bakker, A. M. Tempelaars, A. L. Hesseling-Janssen, T. Mazurczak, S. Jozwiak, A. Fois, G. Bartalini, B. A. Zonnenberg, A. J. van Essen, D. Lindhout, D. J. Halley and A. M. van den Ouweland (1999). "High rate of mosaicism in tuberous sclerosis complex." Am J Hum Genet **64**(6): 1632-1637.

Villegas, F., D. Lehalle, D. Mayer, M. Rittirsch, M. B. Stadler, M. Zinner, D. Olivieri, P. Vabres, L. Duplomb-Jego and E. S. De Bont (2019). "Lysosomal signaling licenses embryonic stem cell differentiation via inactivation of Tfe3." Cell stem cell **24**(2): 257-270. e258.

Vincentz, J. W., B. A. Firulli, A. Lin, D. B. Spicer, M. J. Howard and A. B. Firulli (2013). "Twist1 controls a cell-specification switch governing cell fate decisions within the cardiac neural crest." PLoS Genet **9**(3): e1003405.

Wang, B., M. Wang, W. Zhang, T. Xiao, C. H. Chen, A. Wu, F. Wu, N. Traugh, X. Wang, Z. Li, S. Mei, Y. Cui, S. Shi, J. J. Lipp, M. Hinterndorfer, J. Zuber, M. Brown, W. Li and X. S. Liu (2019). "Integrative analysis of pooled CRISPR genetic screens using MAGeCKFlute." Nat Protoc **14**(3): 756-780.

Wang, S., P. Xia, B. Ye, G. Huang, J. Liu and Z. Fan (2013). "Transient activation of autophagy via Sox2-mediated suppression of mTOR is an important early step in reprogramming to pluripotency." Cell Stem Cell **13**(5): 617-625.

Wang, T., H. Yu, N. W. Hughes, B. Liu, A. Kendirli, K. Klein, W. W. Chen, E. S. Lander and D. M. Sabatini (2017). "Gene Essentiality Profiling Reveals Gene Networks and Synthetic Lethal Interactions with Oncogenic Ras." Cell **168**(5): 890-903 e815.

Way, S. W., J. McKenna, 3rd, U. Mietzsch, R. M. Reith, H. C. Wu and M. J. Gambello (2009). "Loss of Tsc2 in radial glia models the brain pathology of tuberous sclerosis complex in the mouse." Hum Mol Genet **18**(7): 1252-1265.

Wei, J., P. Li, L. Chiriboga, M. Mizuguchi, H. Yee, D. C. Miller and M. A. Greco (2002). "Tuberous sclerosis in a 19-week fetus: immunohistochemical and molecular study of hamartin and tuberin." Pediatr Dev Pathol **5**(5): 448-464.

Wienecke, R., A. Konig and J. E. DeClue (1995). "Identification of tuberin, the tuberous sclerosis-2 product. Tuberin possesses specific Rap1GAP activity." J Biol Chem **270**(27): 16409-16414.

Wienecke, R., J. C. Maize, Jr., F. Shoarinejad, W. C. Vass, J. Reed, J. S. Bonifacino, J. H. Resau, J. de Gunzburg, R. S. Yeung and J. E. DeClue (1996). "Co-localization of the TSC2 product tuberin with its target Rap1 in the Golgi apparatus." Oncogene **13**(5): 913-923.

Wong, N., and Wang, X. (2015). miRDB: an online resource for microRNA target prediction and functional annotations. Nucleic Acids Res *43*, D146-152.

Wu, H., Z. Wu, P. Li, Q. Cong, R. Chen, W. Xu, S. Biswas, H. Liu, X. Xia, S. Li, W. Hu, Z. Zhang, S. L. Habib, L. Zhang, J. Zou, H. Zhang, W. Zhang and B. Li (2017). "Bone Size and Quality Regulation: Concerted Actions of mTOR in Mesenchymal Stromal Cells and Osteoclasts." Stem Cell Reports **8**(6): 1600-1616.

Xiao, G. H., F. Shoarinejad, F. Jin, E. A. Golemis and R. S. Yeung (1997). "The tuberous sclerosis 2 gene product, tuberin, functions as a Rab5 GTPase activating protein (GAP) in modulating endocytosis." J Biol Chem **272**(10): 6097-6100.

Yamamoto, Y., K. A. Jones, B. C. Mak, A. Muehlenbachs and R. S. Yeung (2002). "Multicompartmental distribution of the tuberous sclerosis gene products, hamartin and tuberin." Arch Biochem Biophys **404**(2): 210-217.

Yang, L., J. L. Yang, S. Byrne, J. Pan and G. M. Church (2014). "CRISPR/Cas9-Directed Genome Editing of Cultured Cells." Curr Protoc Mol Biol **107**: 31 31 31-17.

Yao, R. W., Y. Wang and L. L. Chen (2019). "Cellular functions of long noncoding RNAs." Nat Cell Biol **21**(5): 542-551.

Yeung, R. S., G. H. Xiao, F. Jin, W. C. Lee, J. R. Testa and A. G. Knudson (1994). "Predisposition to renal carcinoma in the Eker rat is determined by germ-line mutation of the tuberous sclerosis 2 (TSC2) gene." Proc Natl Acad Sci U S A **91**(24): 11413-11416.

Yin, W. and M. Rogge (2019). "Targeting RNA: A Transformative Therapeutic Strategy." Clin Transl Sci **12**(2): 98-112.

Yong, W. H., M. Shabihkhani, D. Telesca, S. Yang, J. L. Tso, J. C. Menjivar, B. Wei, G. M. Lucey, S. Mareninov, Z. Chen, L. M. Liau, A. Lai, S. F. Nelson, T. F. Cloughesy and C. L. Tso (2015). "Ribosomal Proteins RPS11 and RPS20, Two Stress-Response Markers of Glioblastoma Stem Cells, Are Novel Predictors of Poor Prognosis in Glioblastoma Patients." PLoS One **10**(10): e0141334.

York, B., D. Lou and D. J. Noonan (2006). "Tuberin nuclear localization can be regulated by phosphorylation of its carboxyl terminus." Mol Cancer Res **4**(11): 885-897.

York, B., D. Lou, R. A. Panettieri, Jr., V. P. Krymskaya, T. C. Vanaman and D. J. Noonan (2005). "Cross-talk between tuberin, calmodulin, and estrogen signaling pathways." FASEB J **19**(9): 1202-1204.

You, L., R. Tong, M. Li, Y. Liu, J. Xue and Y. Lu (2019). "Advancements and Obstacles of CRISPR-Cas9 Technology in Translational Research." Mol Ther Methods Clin Dev **13**: 359-370.

Young, L., H. S. Lee, Y. Inoue, J. Moss, L. G. Singer, C. Strange, K. Nakata, A. F. Barker, J. T. Chapman, M. L. Brantly, J. M. Stocks, K. K. Brown, J. P. Lynch, 3rd, H. J. Goldberg, G. P. Downey, J. J. Swigris, A. M. Taveira-DaSilva, J. P. Krischer, B. C. Trapnell, F. X. McCormack and M. T. Group (2013). "Serum VEGF-D a concentration as a biomarker of lymphangioleiomyomatosis severity and treatment response: a prospective analysis of the Multicenter International Lymphangioleiomyomatosis Efficacy of Sirolimus (MILES) trial." Lancet Respir Med **1**(6): 445-452.

Yu, G., L.-G. Wang, Y. Han and Q.-Y. He (2012). "clusterProfiler: an R package for comparing biological themes among gene clusters." Omics: a journal of integrative biology **16**(5): 284-287.

Yu, J., A. Astrinidis, S. Howard and E. P. Henske (2004). "Estradiol and tamoxifen stimulate LAM-associated angiomyolipoma cell growth and activate both genomic and nongenomic signaling pathways." Am J Physiol Lung Cell Mol Physiol **286**(4): L694-700.

Yu, J. and E. P. Henske (2010). "mTOR activation, lymphangiogenesis, and estrogen-mediated cell survival: the "perfect storm" of pro-metastatic factors in LAM pathogenesis." Lymphat Res Biol **8**(1): 43-49.

Yumlu, S., S. Bashir, J. Stumm and R. Kuhn (2019). "Efficient Gene Editing of Human Induced Pluripotent Stem Cells Using CRISPR/Cas9." Methods Mol Biol **1961**: 137-151.

Yun, Y. S., K. H. Kim, B. Tschida, Z. Sachs, K. E. Noble-Orcutt, B. S. Moriarity, T. Ai, R. Ding, J. Williams, L. Chen, D. Largaespada and D. H. Kim (2016). "mTORC1 Coordinates Protein Synthesis and Immunoproteasome Formation via PRAS40 to Prevent Accumulation of Protein Stress." Mol Cell **61**(4): 625-639.

Yung, B. C., J. Li, M. Zhang, X. Cheng, H. Li, E. M. Yung, C. Kang, L. E. Cosby, Y. Liu, L. Teng and R. J. Lee (2016). "Lipid Nanoparticles Composed of Quaternary Amine-Tertiary Amine Cationic Lipid Combination (QTsome) for Therapeutic Delivery of AntimiR-21 for Lung Cancer." Mol Pharm **13**(2): 653-662.

Zeng, L. H., N. R. Rensing, B. Zhang, D. H. Gutmann, M. J. Gambello and M. Wong (2011). "Tsc2 gene inactivation causes a more severe epilepsy phenotype than Tsc1 inactivation in a mouse model of tuberous sclerosis complex." Hum Mol Genet **20**(3): 445-454.

Zhang, H., G. Cicchetti, H. Onda, H. B. Koon, K. Asrican, N. Bajraszewski, F. Vazquez, C. L. Carpenter and D. J. Kwiatkowski (2003). "Loss of Tsc1/Tsc2 activates mTOR and disrupts PI3K-Akt signaling through downregulation of PDGFR." J Clin Invest **112**(8): 1223-1233.

Zhang, Y., J. Nicholatos, J. R. Dreier, S. J. Ricoult, S. B. Widenmaier, G. S. Hotamisligil, D. J. Kwiatkowski and B. D. Manning (2014). "Coordinated regulation of protein synthesis and degradation by mTORC1." Nature **513**(7518): 440-443.

Zhang, Y., Wolf, G.W., Bhat, K., Jin, A., Allio, T., Burkhart, W.A., and Xiong, Y. (2003). Ribosomal protein L11 negatively regulates oncoprotein MDM2 and mediates a p53-dependent ribosomal-stress checkpoint pathway. Mol Cell Biol *23*, 8902-8912.

Zhou, J., G. Shrikhande, J. Xu, R. M. McKay, D. K. Burns, J. E. Johnson and L. F. Parada (2011). "Tsc1 mutant neural stem/progenitor cells exhibit migration deficits and give rise to subependymal lesions in the lateral ventricle." Genes Dev **25**(15): 1595-1600.

Zhou, X., T. Ikenoue, X. Chen, L. Li, K. Inoki and K.-L. Guan (2009). "Rheb controls misfolded protein metabolism by inhibiting aggresome formation and autophagy." Proceedings of the National Academy of Sciences **106**(22): 8923-8928.

Zhu, A., J. G. Ibrahim and M. I. Love (2018). "Heavy-tailed prior distributions for sequence count data: removing the noise and preserving large differences." Bioinformatics.

APPENDIX I

Supplementary Information

Where noted, supplementary information has been adapted from:

Delaney, S.P., Julian, L.M., Pietrobon, A., Yockell-Lelièvre, J., Doré, C., Wang, T.T., Doyon, V.C., Raymond, A., Patten, D.A., Harper, M.-E., Sun, H., Stanford W.L (2019). "TSC2-deficiency potentiates a catabolic signaling switch that differentiates neural and neural crest lineage development and progressive disease manifestations". bioRxiv, 683359. (Delaney et al., 2019)

Contributions to this chapter:
Sequencing of TSC2 exon3 loci and Cas9 off target loci was performed by VCD under the guidance of **SPD**. All other work presented was prepared by **SPD.**

Table S1: Primers and oligonucleotides utilized in this study
(GE: genome editing, PCR: polymerase chain reaction, NGS: next generation sequencing, RT-qPCR: reverse transcription quantitative PCR. Red highlighted bases indicate barcodes used for demultiplexing NGS data.) Portions adapted from Delaney et al. 2019, bioRxiv, 683359 (Delaney, Julian et al. 2019)

Name	Application	Manufacturer	DNA/Oligo sequence
TSC2 Exon3 sgRNA	GE	Invitrogen	TCATCCGGATGCGATTGTTG
TSC2 Exon3 stop codon donor ssODN	GE	Integrated DNA Technologies	AAATTTCTTGGTTTTTGCGACTTC ACAAATCTGCCCTATCCTACAAC AGCTTAATTAAGGTTTAAACGCC ATGACATCCGGATGCGATTGTTG AGGCCACATTCCATGCTCAGTT
TSC2 Exon3 PCR F	PCR	Invitrogen	TCCTCGGGATGGAGCAGTAA
TSC2 Exon3 PCR R	PCR	Invitrogen	TGCAAACCAGATCATCGGCA
AAVS1 gRNA	GE	Invitrogen	GTCACCAATCCTGTCCCTAG
TSC2 Exon11 5p sgRNA	GE	Invitrogen	GTTGCTGGTCTGTCCGAGTC
TSC2 Exon11 3p sgRNA	GE	Invitrogen	AGAGCATTGCCCCCGACCGC
TSC2 Exon11 PCR F	PCR	Invitrogen	GGCGGCTCTGTTTTGTCAAG
TSC2 Exon11 PCR R	PCR	Invitrogen	CCTCATGGGTTGAGACACCC
mCherry sgRNA 1	GE	Invitrogen	CAAGGGCGAGGAGGATAACA
GeCKO Master_F	NGS	Integrated DNA Technologies	AATGATACGGCGACCACCGAGAT CTACACTCTTTCCCTACACGACG CTCTTCCGATCTNNNNNNtcttgtgg aaaggacgaaacaccg
GeCKO R01	NGS	Integrated DNA Technologies	CAAGCAGAAGACGGCATACGAG ATAAGTAGAGGTGACTGGAGTTC AGACGTGTGCTCTTCCGATCTtTC TACTATTCTTTCCCCTGCACTGT
GeCKO R02	NGS	Integrated DNA Technologies	CAAGCAGAAGACGGCATACGAG ATACACGATCGTGACTGGAGTTC AGACGTGTGCTCTTCCGATCTatT CTACTATTCTTTCCCCTGCACTGT
GeCKO R03	NGS	Integrated DNA Technologies	CAAGCAGAAGACGGCATACGAG ATCGCGCGGTGTGACTGGAGTT CAGACGTGTGCTCTTCCGATCTg atTCTACTATTCTTTCCCCTGCAC TGT
GeCKO R04	NGS	Integrated DNA Technologies	CAAGCAGAAGACGGCATACGAG ATCATGATCGGTGACTGGAGTTC AGACGTGTGCTCTTCCGATCTcga tTCTACTATTCTTTCCCCTGCACT GT
GeCKO R05	NGS	Integrated DNA Technologies	CAAGCAGAAGACGGCATACGAG ATCGTTACCAGTGACTGGAGTTC AGACGTGTGCTCTTCCGATCTtcg atTCTACTATTCTTTCCCCTGCAC TGT
GeCKO R06	NGS	Integrated DNA Technologies	CAAGCAGAAGACGGCATACGAG ATTCCTTGGTGTGACTGGAGTTC AGACGTGTGCTCTTCCGATCTatc gatTCTACTATTCTTTCCCCTGCAC TGT

Table S1: Primers and oligonucleotides utilized in this study (continued)			
GeCKO R07	NGS	Integrated DNA Technologies	CAAGCAGAAGACGGCATACGAG ATTACGCATTGTGACTGGAGTTC AGACGTGTGCTCTTCCGATCTgat cgatTCTACTATTCTTTCCCCTGCA CTGT
GeCKO R08	NGS	Integrated DNA Technologies	CAAGCAGAAGACGGCATACGAG ATGCAGGTATGTGACTGGAGTTC AGACGTGTGCTCTTCCGATCTcga tcgatTCTACTATTCTTTCCCCTGC ACTGT
GeCKOv2 Adaptor_F	PCR	Invitrogen	AATGGACTATCATATGCTTACCG TAACTTGAAAGTATTTCG
GeCKOv2 Adaptor_R	PCR	Invitrogen	TCTACTATTCTTTCCCCTGCACTG TTGTGGGCGATGTGCGCTCTG
SOX2_F	RT-qPCR	Invitrogen	TACAGCATGTCCTACTCGCAG
SOX2_R	RT-qPCR	Invitrogen	GAGGAAGAGGTAACCACAGGG
PAX6_F	RT-qPCR	Invitrogen	CCAGAAAGGATGCCTCATAAA
PAX6_R	RT-qPCR	Invitrogen	TCTGCGCGCCCCTAGTTA
OTX_F	RT-qPCR	Invitrogen	CTTAAGCAACCGCCTTACGC
OTX_R	RT-qPCR	Invitrogen	AGGGGTGCAGCAAGTCCATA
GAPDH_F	RT-qPCR	Invitrogen	TTCTTTTGCGTCGCCAGCCG
GAPDH_R	RT-qPCR	Invitrogen	TGACCAGGCGCCCAATACGA
SNAI1_F	RT-qPCR	Invitrogen	ATGCCGCGCTCTTTCCTCGT
SNAI1_R	RT-qPCR	Invitrogen	AGGGCTGCTGGAAGGTAAACTCT GG
TWIST1_F	RT-qPCR	Invitrogen	GTCGCTGAACGAGGCGT
TWIST1_R	RT-qPCR	Invitrogen	CCGCCAGCTTGAGGGTCTG
SOX9_F	RT-qPCR	Invitrogen	TACGACTACACCGACCACC
SOX9_R	RT-qPCR	Invitrogen	GAGCGGGGTTCATGTAGGT
SNAI2_F	RT-qPCR	Invitrogen	CTCTCTCCTCTTTCCGGATACT
SNAI2_R	RT-qPCR	Invitrogen	GCTTGGACTGTAGTCTTTCCTC

Off-Target Mutation Analysis:

Off target loci for each gRNA sequence utilized in this study were identified using the CRISPOR algorithm (Haeussler, Schönig et al. 2016). The 3 highest scoring off target loci falling within an intron or exon were selected for PCR amplification of the off-target region followed by amplicon sequencing to identify potential off target mutations. No off-target cleavage induced indel mutations were detected across all CRISPR/Cas9 genome edited cell lines in this study.

Table S2: Off-target gene information and primer sequences.

CRISPR/Cas9 target Gene	Gene name	Genomic region	Feature	Primer	Primer sequence
AAVS1	TTN	chr2:179,467,749-179,467,771	Intron	Forward (w/M13)	GTAAAACGACGGCCAGTAAGCTGATGAAGTGCTGGAGTC
				Reverse	TGTAGACACTGATCCTGTCCCTAA
	APPL2	chr12:105,594,363-105,594,385	Intron	Forward (w/M13)	GTAAAACGACGGCCAGTAGGCAGCCTAAGCAAGTTCC
				Reverse	CACAGTGCAGAGGAACACCT
	CDK8	chr13:26,959,035-26,959,057	Intron	Forward (w/M13)	GTAAAACGACGGCCAGTAAACAGCCATGCCCGAATAA
				Reverse	ATGTGTCACCCCACCGTTAG
TSC2 Exon 3	PPAT	chr4:57,272,513-57,272,535	Intron	Forward (w/M13)	GTAAAACGACGGCCAGTGCTTTGAACATAGCAACAGAGTT
				Reverse	TTCATGGGAAGATAGCTGTGGC
	XKRX	chr1:89,353,000-89,353,022	Intron	Forward (w/M13)	GTAAAACGACGGCCAGTGCCTAATCGATTCCTCCCCAC
				Reverse	GGGCAAAGGAAGGCAGTTCA
	GTF2B	chrX:100,181,678-100,181,700	Exon	Forward	CCAAGCCACATTCAGGACAGA
				Reverse	AAGAGCACAAACTGGATGGTAA
				Reverse sequencing primer	CTACTTGCCAGTTACTAGCTGGAA

Table S3: Antibodies utilized in this study.
(WB: western blot, IF: immunofluorescence, IFC: imaging flow cytometry, FC: flow cytometry, IHC: immunohistochemistry)

Antibody	Manufacturer	Catalog #	Dilution/Conc. Used	Application
4E-BP1	Cell Signalling Technology	9452	1:1000	WB
Alpha-Smooth Muscle Actin	Millipore	CBL171	1:250	IF
AMPKα	Cell Signalling Technology	5832	1:1000	WB
Calponin	DAKO	M3556	1:250	IF
Cas9	Cell Signalling Technology	14697	1:100	IFC
CD271 (p75)	BD Biosciences	560326	1:20	FC
GAPDH	Abcam	ab8245	WB: 1:5000	WB
GFAP	ThermoFisher	MA5-12023	IF 1:40	IF
IgG1 κ Isotype control	BD Biosciences	55778	1:20	FC
LAMP1	Cell Signalling Technology	9091	1:400	IF/IFC
LC3B	Cell Signalling Technology	3868	1:200	WB
mTOR	Cell Signalling Technology	4517	1:1000	WB
NANOG	Cell Signalling Tecnology	4903	IF 1:200	IF
Nestin	Millipore	MAB5326	1:100	IF
OCT3/4	BD Biosciences	611203	IF 1:400	IF
p70 S6 Kinase (total)	Cell Signalling Technology	2708	1:1000	WB
PAX6	BD Biosciences	561462	1:200	IF/IFC
PAX6	Biolegend	901301	1:200	IF
Phospho-4E-BP1 (Thr37/46)	Cell Signalling Technology	2855	1:1000	WB
Phospho-AMPKα (Thr172)	Cell Signalling Technology	2535	1:500	WB
Phospho-mTOR (Ser 2448)	Cell Signalling Technology	5536	1:1000	WB
Phospho-mTOR (Ser2448)	Cell Signalling Technology	2971	1:1000	WB
Phospho-p70 S6 Kinase (Thr389)	Cell Signalling Technology	9205	WB: 1:1000	WB
Phospho-p70 S6 Kinase (Thr389)	Cell Signalling Technology	9206	1:1000	WB
Phospho-S6 (Ser235/236)	Cell Signalling Technology	2211	WB: 1:1000, IF 1:200	WB/IF/IHC
Phospho-ULK1 (Ser555)	Cell Signalling Technology	5869	1:500	WB
Phospho-ULK1 (Ser757)	Cell Signalling Technology	6888	1:1000	WB
PMEL (HMB45)	ThermoFisher	MA5-13232	1:50	IF
RFP	ROCKLAND	600-401-379	1:100	IF/IHC
S6 (total)	Cell Signalling Technology	2317	1:1000	WB
S6K1 (total)	Abcam	ab131440	1:1000	WB
SOX10	R&D Systems	MAB2864	1:200	IF/IFC

Table S3: Antibodies utilized in this study (continued)				
SOX2	Millipore	AB5603	IF 1:200	IF
Tuberin/TSC2	Cell Signalling Tecnology	4308	IF/IFC 1:100, WB 1:1000	IF/IFC/WB
Tubulin-β3 (Tuj1)	Biolegend	801201	1:100	IF
ULK1 (total)	Cell Signalling Technology	8054	1:1000	WB
β-Actin	Cell Signalling Technology	3700	1:1000	WB
DyLight 800 goat anti Ms IgG	Invitrogen	SA535521	1:10,000	WB
Alexa Fluor 680 goat anti rabbit IgG	Life Tech	A21076	1:10,000	WB
Alexa fluor 488 goat anti Ms IgM	Life Tech	A21042	1:1000	WB
Alexa Fluor 488 goat anti Ms IgG1	Life Tech	A21121	1:1000	IF
Alexa Fluor 488 goat anti Ms IgG	Life Tech	A11001	1:1000	IF
Alexa Fluor 488 goat anti Rb IgG	Life Tech	A11034	1:1000	IF/IFC
Alexa Fluor 647 goat anti Ms IgG	Life Tech	A21235	1:1000	IF
Alexa Fluor 647 goat anti Rb IgG	Life Tech	A21245	1:1000	IF
Alexa Fluor 647 goat anti Ms IgG1	Life Tech	A21240	1:1000	IF
Alexa Fluor 647 goat anti Ms IgG2A	Life Tech	A21241	1:1000	IF
Goat anti Ms IgG+IgM+IgA HRP	Abcam	ab2891	1:1	IHC

Supplementary Tables S4-12 can be found in the supplementary data files associated with this thesis.

List of supplementary files:

Table S4: Enrichment results relating to Figure 4.1.3A
(Table_S4_Figure_4-1-3A_EnrichResults.xlsx)

Table S5: Enrichment results relating to Figure 4.1.3B
(Table_S5_Figure_4-1-3B_EnrichResults.xlsx)

Table S6: MAGeCK MLE gene summary output
(Table_S6_MAGeCK_MLE_gene_summaru.xlsx)

Table S7: Enrichment results relating to Figure 5.1.4A
(Table_S7_Figure_5-1-4A_EnrichResults.xlsx)

Table S8: Enrichment results relating to Figure 5.1.4C
(Table_S8_Figure_5-1-4C_EnrichResults.xlsx)

Table S9: ClueGo enrichment results relating to Figure 5.2.1B
(Table_S9_Figure_5-2-1B.xlsx)

Table S10: Predicted synthetic lethal miRNA targets
(Table_S10_miRNA_Targets_miRDB_Results.xlsx)

Table S11: Enrichment results relating to Figure 5.2.1D
(Table_S11_Figure_5-2-1C_EnrichResults.xlsx)

Table S12: Enrichment results relating to Figure 5.2.2A
(Table_S12_Figure_5-2-2A_EnrichResults.xlsx)

Sequencing of TSC2 exon 3 target region of *TSC2*$^{-/-}$ hPSC cell lines:
Sanger sequencing was performed on all *TSC2*$^{-/-}$ hPSC cell lines to ensure proper integration of the 'stop-codon' donor sequence (highlighted in chromatograms).
H9 *TSC2*$^{-/-}$. Reprinted from Delaney et al. 2019, bioRxiv, 683359 (Delaney, Julian et al. 2019).

H9 *TSC2*$^{-/-}$

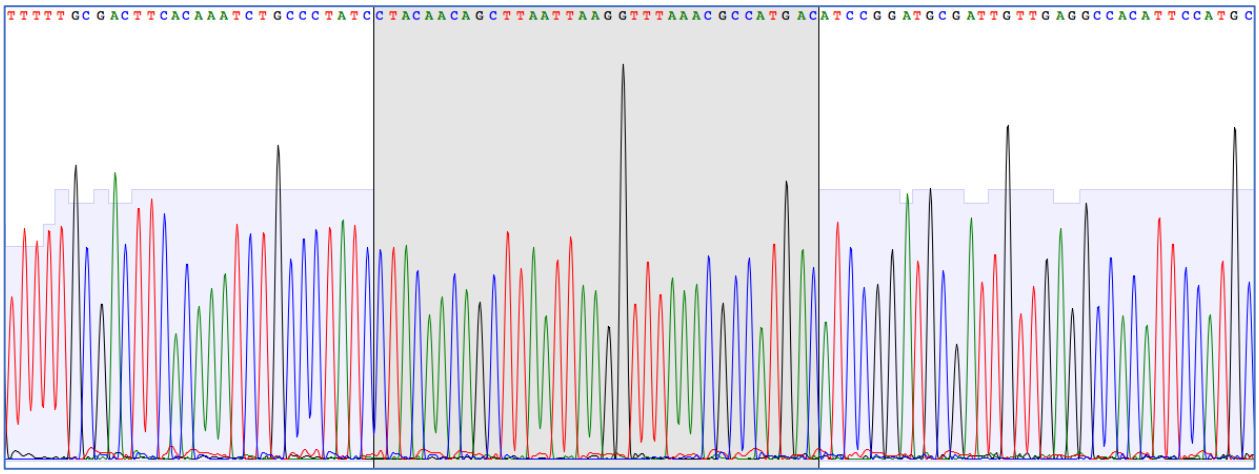

H7 *TSC2*$^{-/-}$

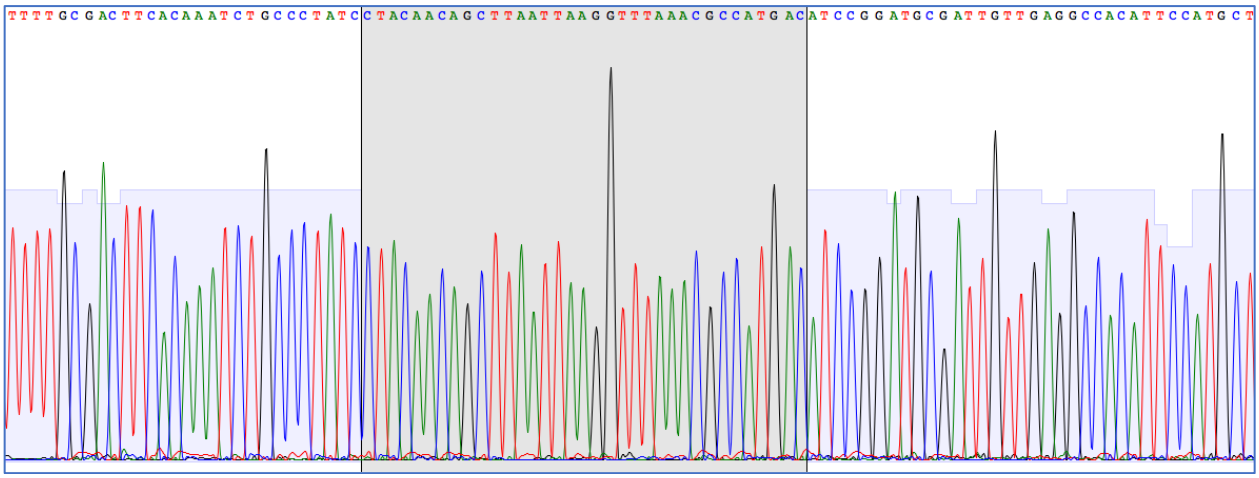

H1 *TSC2*$^{-/-}$

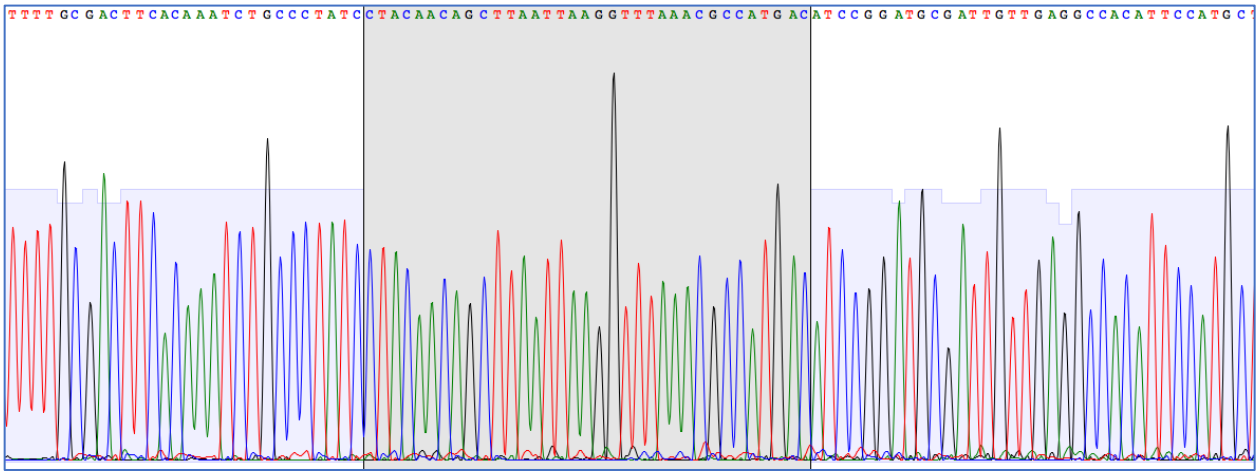

168 *TSC2*$^{-/-}$

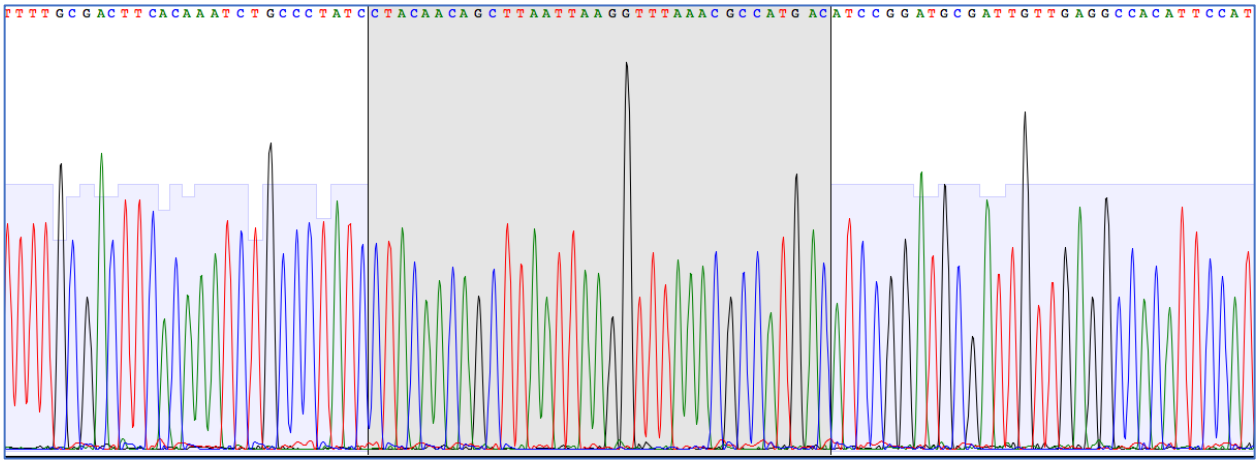

AAVS1 Donor Plasmid Sequence:

To aid in live cell assays and any potential in vivo studies, a CMV early enhancer/chicken β actin (CAG) promoter driven mCherry/Zeocin-resistance transgene was integrated into the AVVS1 locus. All cell lines utilized in this study, excluding 168 *TSC2*$^{-/-}$ cells, possess this transgene integration. Reprinted from Delaney et al. 2019, bioRxiv, 683359 (Delaney, Julian et al. 2019)

AAVS1: CAG-mCherry/T2A/ZeocinResistance donor plasmid sequence (in pUC19 backbone) and annotated map:

TCGCGCGTTTCGGTGATGACGGTGAAAACCTCTGACACATGCAGCTCCCGGAGAC
GGTCACAGCTTGTCTGTAAGCGGATGCCGGGAGCAGACAAGCCCGTCAGGGCGC
GTCAGCGGGTGTTGGCGGGTGTCGGGGCTGGCTTAACTATGCGGCATCAGAGCA
GATTGTACTGAGAGTGCACCATATGCGGTGTGAAATACCGCACAGATGCGTAAGGA
GAAAATACCGCATCAGGCGCCATTCGCCATTCAGGCTGCGCAACTGTTGGGAAGG
GCGATCGGTGCGGGCCTCTTCGCTATTACGCCAGCTGGCGAAAGGGGGATGTGCT
GCAAGGCGATTAAGTTGGGTAACGCCAGGGTTTTCCCAGTCACGACGTTGTAAAAC
GACGGCCAGTGAATTCCAGGAGAGCCAGGGGCATGAGATGGTGGACGAGGAAGG
GGGACAGGGAAGCCTGAGCGCCTCTCCTGGGCTTGCCAAGGACTCAAACCCAGAA
GCCCAGAGCAGGGCCTTAGGGAAGCGGGACCCTGCTCTGGGCGGAGGAATATGT
CCCAGATAGCACTGGGGACTCTTTAAGGAAAGAAGGATGGAGAAAGAGAAAGGGA
GTAGAGGCGGCCACGACCTGGTGAACACCTAGGACGCACCATTCTCACAAAGGGA
GTTTTCCACACGGACACCCCCCTCCTCACCACAGCCCTGCCAGGACGGGGCTGGC
TACTGGCCTTATCTCACAGGTAAAACTGACGCACGGAGGAACAATATAAATTGGGG
ACTAGAAAGGTGAAGAGCCAAAGTTAGAACTCAGGACCAACTTATTCTGATTTTGTT
TTTCCAAACTGCTTCTCCTCTTGGGAAGTGTAAGGAAGCTGCAGCACCAGGATCAG
TGAAACGCACCAGACGGCCGCGTCAGAGCAGCTCAGGTTCTGGGAGAGGGTAGC
GCAGGGTGGCCACTGAGAACCGGGCAGGTCACGCATCCCCCCCTTCCCTCCCACC
CCCTGCCAAGCTCTCCCTCCCAGGATCCTCTCTGGCTCCATCGTAAGCAAACCTTA
GAGGTTCTGGCAAGGAGAGAGATGGCTCCAGGAAATGGGGGTGTGTCACCAGATA
AGGAATCTGCCTAACAGGAGGTGGGGGTTAGACCCAATATCAGGAGACTAGGAAG
GAGGAGGCCTAAGGATGGGGCTTTTCTGTCACCAATCCTGTCCCGTCGACgcgttacat
aacttacggtaaatggcccgcctggctgaccgcccaacgacccccgcccattgacgtcaataatgacgtatgttcccatag
taacgccaatagggactttccattgacgtcaatgggtggactatttacggtaaactgcccacttggcagtacatcaagtgtatc
atatgccaagtacgccccctattgacgtcaatgacggtaaatggcccgcctggcattatgcccagtacatgaccttatggga
ctttcctacttggcagtacatctacgtattagtcatcgctattaccatgggtcgaggtgagccccacgttctgcttcactctcccc
atctccccccccctccccacccccaattttgtatttatttatttttttaattattttgtgcagcgatgggggcgggggggggggggggc
gcgcgccaggcggggcggggcggggcgaggggcggggcggggcgaggcggagaggtgcggcggcagccaatca
gagcggcgcgctccgaaagtttccttttatggcgaggcggcggcggcggccctataaaaagcgaagcgcgcggcg
ggcgggagtcgctgcgttgccttcgccccgtgccccgctccgcgccgcctcgcgccgcccgccccggctctgactgaccg
cgttactcccacaggtgagcgggcgggacggcccttctcctccgggctgtaattagcgcttggtttaatgacggctcgtttctttt
ctgtggctgcgtgaaagccttaaagggctccgggagggccctttgtgcgggggggagcggctcgggggtgcgtgcgtgt
gtgtgtgcgtggggagcgccgcgtgcggcccgcgctgcccggcggctgtgagcgctgcgggcgcggcgcggggctttgt
gcgctccgcgtgtgcgcgaggggagcgcggccgggggcggtgccccgcggtgcgggggggctgcgaggggaacaa
aggctgcgtgcggggtgtgtgcgtgggggggtgagcaggggggtgtgggcgcggcggtcgggctgtaacccccccctgca
ccccccctccccgagttgctgagcacggcccggcttcgggtgcggggctccgtgcggggcgtggcgcggggctcgccgtg
ccgggcgggggtggcggcaggtgggggtgccgggcggggcggggccgcctcgggccggggagggctcgggggga
ggggcgcggcggccccggagcgccggcggctgtcgaggcgcggcgagccgcagccattgccttttatggtaatcgtgcg
agagggcgcagggacttcctttgtcccaaatctggcggagccgaaatctgggaggcgccgccgcaccccctctagcggg
cgcgggcgaagcggtgcggcgccggcaggaaggaaatgggcggggagggccttcgtgcgtcgccgcgccgccgtcc

ccttctccatctccagcctcggggctgccgcaggggacggctgccttcgggggggacggggcagggcggggttcggctt
ctggcgtgtgaccggcggctctagagcctctgctaaccatgttcatgccttcttcttttttcctacagCTCGAGgccaccatg
gtgagcaagggcgaggaggataacatggccatcatcaaggagttcatgcgcttcaaggtgcacatggagggctccgtga
acggccacgagttcgagatcgagggcgagggcgagggccgcccctacgagggcacccagaccgccaagctgaaggt
gaccaagggtggccccctgcccttcgcctgggacatcctgtcccctcagttcatgtacggctccaaggcctacgtgaagca
ccccgccgacatccccgactacttgaagctgtccttccccgagggcttcaagtgggagcgcgtgatgaacttcgaggacg
gcggcgtggtgaccgtgacccaggactcctccctgcaggacggcgagttcatctacaaggtgaagctgcgcggcaccaa
cttcccctccgacggccccgtaatgcagaagaagaccatgggctgggaggcctcctccgagcggatgtaccccgagga
cggcgccctgaagggcgagatcaagcagaggctgaagctgaaggacggcggccactacgacgctgaggtcaagacc
acctacaaggccaagaagcccgtgcagctgcccggcgcctacaacgtcaacatcaagttggacatcacctcccacaac
gaggactacaccatcgtggaacagtacgaacgcgccgagggccgccactccaccggcggcatggacgagctgtacaa
gaccggtgagggcagaggaagtcttctaacatgcggtgacgtggaggagaatcccggcccttccggtatggccaaactc
acttctgcagtcccagtcctcacagcaagggatgttgcaggggctgtagagttctggactgacagattaggattctccagag
actttgttgaagatgattttgctggtgttgtcagagatgatgtcaccctcttcatctcagcagttcaggaccaagttgtccctgaca
acacccttgcttgggtctgggtcagaggcctagatgagctttatgcagaatggtcagaagtagtcagcacaaatttcaggga
tgcctctggcccagccatgacagaaattggtgaacaaccttggggaagggaatttgccctcagagaccctgctggaaattg
tgtccattttgtagctgaggaacaggactagaacttgtttattgcagcttataatggttacaaataaagcaatagcatcacaaa
tttcacaaataaagcatttttttcactgcattctagttgtggtttgtccaaactcatcaatgtatcttatcatgtctACGCGTTAG
TGGCCCCACTGTGGGGTGGAGGGGACAGATAAAAGTACCCAGAACCAGAGCCACA
TTAACCGGCCCTGGTAATATAAGGTGGTCCCAGCTCGGGGACACAGGATCCCTGG
AGGCAGCAAACATGCTGTCCTGAAGTGGACATAGGGGCCCGGGTTGGAGGAAGAA
GACTAGCTGAGCTCTCGGACCCCTGGAAGATGCCATGACAGGGGGCTGGAAGAGC
TAGCACAGACTAGAGAGGTAAGGGGGGTAGGGGAGCTGCCCAAATGAAAGGAGTG
AGAGGTGACCCGAATCCACAGGAGAACGGGGTGTCCAGGCAAAGAAAGCAAGAG
GATGGAGAGGTGGCTAAAGCCAGGGAGACGGGGTACTTTGGGGTTGTCCAGAAAA
ACGGTGATGATGCAGGCCTACAAGAAGGGGAGGCGGGACGCAAGGGAGACATCC
GTCGGAGAAGGCCATCCTAAGAAACGAGAGATGGCACAGGCCCCAGAAGGAGAAG
GAAAAGGGAACCCAGCGAGTGAAGACGGCATGGGGTTGGGTGAGGGAGGAGAGA
TGCCCGGAGAGGACCCAGACACGGGGAGGATCCGCTCAGAGGACATCACGTGGT
GCAGCGCCGAGAAGGAAGTGCTCCGGAAAGAGCATCCTTGGGCAGCAACACAGCA
GAGAGCAAGGGGAAGAGGGAGTGGAGGAAGACGGAACCTGAAGGAGGCGGCAG
GGAAGGATCTGGGCCAGCCGTAGAGGTGACCCAGGCCACAAGCTGCAGACAGAA
AGCGGCACAGGCCCAGGGGAGAGAATGCAGGTCAAAGCTTGGCGTAATCATGGTC
ATAGCTGTTTCCTGTGTGAAATTGTTATCCGCTCACAATTCCACACAACATACGAGC
CGGAAGCATAAAGTGTAAAGCCTGGGGTGCCTAATGAGTGAGCTAACTCACATTAA
TTGCGTTGCGCTCACTGCCCGCTTTCCAGTCGGGAAACCTGTCGTGCCAGCTGCAT
TAATGAATCGGCCAACGCGCGGGGAGAGGCGGTTTGCGTATTGGGCGCTCTTCCG
CTTCCTCGCTCACTGACTCGCTGCGCTCGGTCGTTCGGCTGCGGCGAGCGGTATC
AGCTCACTCAAAGGCGGTAATACGGTTATCCACAGAATCAGGGGATAACGCAGGAA
AGAACATGTGAGCAAAAGGCCAGCAAAAGGCCAGGAACCGTAAAAAGGCCGCGTT
GCTGGCGTTTTTCCATAGGCTCCGCCCCCCTGACGAGCATCACAAAAATCGACGCT
CAAGTCAGAGGTGGCGAAACCCGACAGGACTATAAAGATACCAGGCGTTTCCCCC
TGGAAGCTCCCTCGTGCGCTCTCCTGTTCCGACCCTGCCGCTTACCGGATACCTGT
CCGCCTTTCTCCCTTCGGGAAGCGTGGCGCTTTCTCATAGCTCACGCTGTAGGTAT
CTCAGTTCGGTGTAGGTCGTTCGCTCCAAGCTGGGCTGTGTGCACGAACCCCCCG
TTCAGCCCGACCGCTGCGCCTTATCCGGTAACTATCGTCTTGAGTCCAACCCGGTA
AGACACGACTTATCGCCACTGGCAGCAGCCACTGGTAACAGGATTAGCAGAGCGA
GGTATGTAGGCGGTGCTACAGAGTTCTTGAAGTGGTGGCCTAACTACGGCTACACT
AGAAGAACAGTATTTGGTATCTGCGCTCTGCTGAAGCCAGTTACCTTCGGAAAAAG
AGTTGGTAGCTCTTGATCCGGCAAACAAACCACCGCTGGTAGCGGTGGTTTTTTTG
TTTGCAAGCAGCAGATTACGCGCAGAAAAAAAGGATCTCAAGAAGATCCTTTGATCT

TTTCTACGGGGTCTGACGCTCAGTGGAACGAAAACTCACGTTAAGGGATTTTGGTC
ATGAGATTATCAAAAAGGATCTTCACCTAGATCCTTTTAAATTAAAAATGAAGTTTTA
AATCAATCTAAAGTATATATGAGTAAACTTGGTCTGACAGTTACCAATGCTTAATCAG
TGAGGCACCTATCTCAGCGATCTGTCTATTTCGTTCATCCATAGTTGCCTGACTCCC
CGTCGTGTAGATAACTACGATACGGGAGGGCTTACCATCTGGCCCCAGTGCTGCA
ATGATACCGCGAGACCCACGCTCACCGGCTCCAGATTTATCAGCAATAAACCAGCC
AGCCGGAAGGGCCGAGCGCAGAAGTGGTCCTGCAACTTTATCCGCCTCCATCCAG
TCTATTAATTGTTGCCGGGAAGCTAGAGTAAGTAGTTCGCCAGTTAATAGTTTGCGC
AACGTTGTTGCCATTGCTACAGGCATCGTGGTGTCACGCTCGTCGTTTGGTATGGC
TTCATTCAGCTCCGGTTCCCAACGATCAAGGCGAGTTACATGATCCCCCATGTTGT
GCAAAAAAGCGGTTAGCTCCTTCGGTCCTCCGATCGTTGTCAGAAGTAAGTTGGCC
GCAGTGTTATCACTCATGGTTATGGCAGCACTGCATAATTCTCTTACTGTCATGCCA
TCCGTAAGATGCTTTTCTGTGACTGGTGAGTACTCAACCAAGTCATTCTGAGAATAG
TGTATGCGGCGACCGAGTTGCTCTTGCCCGGCGTCAATACGGGATAATACCGCGC
CACATAGCAGAACTTTAAAAGTGCTCATCATTGGAAAACGTTCTTCGGGGCGAAAA
CTCTCAAGGATCTTACCGCTGTTGAGATCCAGTTCGATGTAACCCACTCGTGCACC
CAACTGATCTTCAGCATCTTTTACTTTCACCAGCGTTTCTGGGTGAGCAAAAACAGG
AAGGCAAAATGCCGCAAAAAAGGGAATAAGGGCGACACGGAAATGTTGAATACTCA
TACTCTTCCTTTTTCAATATTATTGAAGCATTTATCAGGGTTATTGTCTCATGAGCGG
ATACATATTTGAATGTATTTAGAAAAATAAACAAATAGGGGTTCCGCGCACATTTCC
CCGAAAAGTGCCACCTGACGTCTAAGAAACCATTATTATCATGACATTAACCTATAA
AAATAGGCGTATCACGAGGCCCTTTCGTC

Annotated map: